Frequency-domain quantum information processing with multimode quantum states of light from integrated sources at telecom wavelengths

Antoine Henry

To cite this version:

Antoine Henry. Frequency-domain quantum information processing with multimode quantum states of light from integrated sources at telecom wavelengths. Quantum Physics [quant-ph]. Institut Polytechnique de Paris, 2023. English. NNT : 2023IPPAT042 . tel-04513100

HAL Id: tel-04513100
https://theses.hal.science/tel-04513100v1

Submitted on 20 Mar 2024

INSTITUT
POLYTECHNIQUE
DE PARIS

NNT : 2023IPPAT042

Thèse de doctorat

TELECOM
Paris

IP PARIS

Frequency-domain quantum information processing with multimode quantum states of light from integrated sources at telecom wavelengths

Thèse de doctorat de l'Institut Polytechnique de Paris
préparée à Télécom Paris

École doctorale n°626 École doctorale de l'Institut Polytechnique de Paris (ED IP Paris)
Spécialité de doctorat : Physique

Thèse présentée et soutenue à Palaiseau, le 18/12/2023, par

ANTOINE HENRY

Composition du Jury :

Sara Ducci Professeure, Laboratoire Matériaux et Phénomènes Quantiques, Université Paris-Cité, CNRS	Présidente/Examinatrice
Yannick Dumeige Professeur, Université de Rennes 1- Institut FOTON, CNRS UMR	Rapporteur
Michael Kues Professeur, Leibniz University Hannover, Institute of Photonics	Rapporteur
Ségolène Olivier Ingénieure de recherche, CEA LETI	Examinatrice
Benoît Valiron Maître de conférences, CentraleSupelec	Examinateur
Isabelle Zaquine Professeure, Télécom Paris, Institut Polytechnique de Paris	Directrice de thèse
Nadia Belabas Chargée de recherche, Centre de Nanosciences et de Nanotechnologies, Université Paris-Saclay, CNRS	Co-directrice de thèse

Résumé

L'information quantique combine deux domaines scientifiques : la science de l'information, et la mécanique quantique. Le domaine de l'information quantique cherche à utiliser les propriétés de la mécanique quantique au service de l'encodage, de la manipulation et de la mesure d'information. Il est alors possible d'encoder des bits quantiques (qubits) en utilisant deux états quantiques pour encoder les état logiques $|0\rangle$ et $|1\rangle$. Il est également possible de produire des états de plus hautes dimensions, encodés sur un plus grand nombre d'états quantiques (qudits). Parmi les plateformes populaires pour l'encodage et la manipulation d'information quantique, l'utilisation du photon comme porteur de l'information quantique confère plusieurs avantages. Tout d'abord, la lumière peut se propager sur de grandes distances avec peu d'interaction avec l'environnement, tout en gardant ses qualités d'état quantique. De plus, le développement des communications optiques aux longueurs d'onde télécom est un atout permettant de mettre au service de l'information quantique différents outils et composantes optiques accessibles, ainsi que les réseaux de communications existants. Enfin, il est possible de s'appuyer sur la croissance du domaine de la nanophotonique afin de générer, manipuler ou bien mesurer des états quantiques. Le photon est également un candidat attractif, car il possède une variété de degrés de liberté sur lesquels il est possible d'encoder de l'information. Le degré de liberté pionnier pour cette tache est la polarisation, qui permet d'encoder le $|0\rangle$ et le $|1\rangle$ logique du qubit sur deux états de polarisation orthogonaux. L'utilisation des degrés de liberté temps et fréquence donne accès à un espace de Hilbert de grande dimension pour les états photoniques. Cela autorise l'encodage et le traitement en parallèle d'un grand nombre de qubits voire de qudits. Dans ce cas, les états logiques sont encodés chacun sur un état fréquentiel du photon (sa couleur), ou le temps d'arrivée du photon (le moment où la détection est effectuée). Le défi est alors de réussir à générer et de manipuler des états fréquentiels. C'est dans ce cadre que se situe cette thèse sur la génération et la manipulation d'états quantiques photoniques aux longueurs d'onde télécom. Nous présentons trois réalisations. La première est une réalisation expérimentale portant sur la génération efficace de paires de photons par processus non-linéaire du second et du troisième ordre dans des sources intégrées innovantes : un guide en niobate de lithium sur isolant, en couche mince et à inversion de domaines périodique, et

un micro-résonateur en silicium sur isolant possédant un intervalle spectral libre de 21 GHz. La deuxième est le développement de concepts, de modèles et d'optimisations numériques pour la manipulation de qubits et qudits photoniques dans les espaces-temps fréquence avec des éléments linéaires. Nous utilisons des filtres programmables (PF) et des modulateurs de phase électro-optiques (EOM). Nous comparons les performances théoriques de portes à 1 qubit pour deux configurations de composants [EOM-PF-EOM] et [PF-EOM-PF] dans les deux types d'encodage temps et fréquence. La troisième est la démonstration expérimentale de portes a un qubit permettant de manipuler des qubits encodés en fréquence ainsi que la parallélisation de ces portes à plusieurs qubits. Nous démontrons à l'aide de ces portes la manipulation de qubits fréquentiels issus du micro-résonateur en Silicium. Nous utilisons la configuration [EOM-PF-EOM] pour implémenter une porte quantique reconfigurable et accordable. Un seul paramètre variable permet de passer d'une porte identité à une porte Hadamard, ainsi qu'à un continuum de portes intermédiaires. Cette configuration nous permet également d'avoir un contrôle indépendant sur chacune des portes parallélisées. Nous démontrons la parallélisation de 34 de ces portes appliquées à 17 états à deux qubits intriqués en fréquence générés par le résonateur. Nous utilisons ensuite ces portes pour réaliser la tomographie quantique des états intriqués et pour mettre en oeuvre un protocole de distribution de clef quantique basé sur l'intrication des deux photons en fréquence. Nous faisons finalement la démonstration inédite d'un réseau multi-utilisateur sans nœuds sécurisés en encodage fréquentiel. Cette expérience constitue une preuve de principe pour la distribution de clé quantique dans le domaine fréquentiel avec un débit de 2 bits par seconde en simultané pour chacune des paires d'utilisateurs dans un réseau de 5 utilisateurs.

Abstract

Quantum information combines two fields of science: information science and quantum mechanics. Quantum information seeks to use the properties of quantum mechanics to encode, manipulate, and measure information. The logical states $|0\rangle$ and $|1\rangle$ of quantum bits (qubits) are encoded on . It is also possible to produce higher-dimensional states encoded over a larger number of quantum states (qudits). Among the popular platforms for encoding and manipulating quantum information, the use of the photon confers several advantages. First, light can propagate over great distances with limited interaction with the environment. Furthermore, development of optical communications at telecom wavelengths is an asset, enabling us to harness various optical tools and components accessible at telecom wavelengths and existing communications networks for quantum information. Finally, it is possible to build on the growth of the field of nanophotonics to generate, manipulate, or measure quantum states. The photon is also an attractive candidate, as it has a variety of degrees of freedom on which to encode information. Polarization is a pioneer degree of freedom, encoding the logical $|0\rangle$ and $|1\rangle$ of the qubit on two orthogonal polarization states. . Encoding in time and frequency degrees of freedom gives access to a high-dimensional Hilbert space for photonic states, enabling parallel processing of a large number of qubits or even qudits. This is the scope of our work on the generation and manipulation of photonic quantum states at telecom wavelengths with three main achievements. The first one is the efficient generation of photon pairs by second and third-order nonlinear processes in innovative integrated sources: a thin-film, periodically-poled lithium niobate-on-insulator waveguide, and a silicon-on-insulator micro-resonator with a free spectral range of 21 GHz. The second one is the development of concepts, models, and numerical optimizations for the manipulation of photonic qubits and qudits in time-frequency spaces with linear devices. We use programmable filters (PF) and electro-optical phase modulators (EOM). We compare the theoretical performance of 1-qubit gates for two configurations [EOM-PF-EOM] and [PF-EOM-PF] in both time and frequency encoding. The third one is the experimental demonstration of such manipulation of frequency qubits from the silicon microresonator. We use the [EOM-PF-EOM] configuration to implement a reconfigurable and tunable quantum gate. A single tunable parameter is used to go from an identity gate to a Hadamard gate, as well as to a

continuum of intermediate gates. We then use these gates to perform quantum tomography of entangled states and to implement a quantum key distribution protocol based on two-photon frequency entanglement. Finally, we demonstrate a frequency-encoded multi-user network without trusted nodes. This experiment constitutes a proof of principle for quantum key distribution in the frequency domain at a rate of 2 bits per second simultaneously for each pair of users in a 5-user network.

> *Parce que l'enfer c'est pas d'échouer, c'est de ne pas tout faire pour esssayer.*
>
> Ben Mazué, Gaël Faye, Grand Corps Malade, On a pris le temps, Ephèmère, 2022

Acknowledgements

Although this thesis bears my name, it would never have existed without the presence of the many people who took part, directly or indirectly, in this project.

First and foremost, I would like to express my gratitude to each of the jury members for reading and proofreading my Ph.D. thesis and for taking the time to attend my Ph.D. defense. Thank you to Michael Kues and Yannick Dumeige for reviewing this manuscript.

Isabelle and Nadia, I cannot express my thanks enough for accepting the challenge of transforming the student I was three years ago into the young researcher I am today. Thanks to your teaching, I have been able to grow both scientifically and as a person. Your rigor and your expectations in my regard have been essential to the course of these three years. I've learned a lot and no words could express how grateful I am. I hope I made you as proud as I was to have both of you as mentors.

Kamel, I shall thank you for your involvement in the success of my thesis. I learned a lot from you, and greatly appreciated all the time I spent in the lab.

Pascale, thank you very much for your implication in my project and for always seeking to make me become a better scientist. Thank you for pushing me forward.

Loïc and Olivier, thank you for your input, help, discussions, and overall wholesomeness. I learned from you a whole lot of traits that I believe make a good researcher.

I must also thank Carlos, Eric, and Laurent, as well as Frédéric and Stéphane. A lot of beautiful experiments would not have been possible without their expertise.

Dario, siete stati un fattore inestimabile per il successo di questa tesi. It was a pleasure working with you. You taught me so much about many things, I will always be thankful for all the support and help you provided throughout these past three years.

Juan, Muchas gracias por su amabilidad y su ayuda diaria. I learned a great deal with you, and thank you for the help during the defense.

George, I want to express my gratitude for allowing me to be your Ph.D. mentor. I truly believe that you have the potential to become an excellent researcher and I have no doubt that you will achieve great things in your career. I will always cherish the time we spent together in the lab and our lengthy discussions. Thank you for being a great person to work with.

Of course, I will never thank my office mates enough, Ilse, Nathan, Tim, and for a short time, Manuel. We spent great moments in the lab and at conferences, thank you for all of your interactions, cheer up, and kindness.

Andreas, you were the first intern I had the chance to teach, and possibly traumatize permanently. That is quite an accomplishment!

Thank you Valentin for the long conversations, and cheer-ups! Our time spent together in the lab and at conferences has been very valuable!

More generally, Thank you to all the GOSS group. Working, discussing, and creating ideas for most of my Ph.D. was amazing. You were wonderful colleagues and even greater scientists. This Ph.D. was memorable partly due to the time spent together, at the coffee machine, in the lab, in conferences, or the office. Prashant, for the music gigs and kind messages, Tim for the cheerful moments in the lab, Rita for the short but amazing time we worked together, Hubert and Adria for taking the time to come and see me playing music.

Thank you to Nicolas Glady, director of Telecom Paris, and Giancarlo Faini, director of C2N, as well as all the administrative teams of both laboratories. A special thanks to Françoise for always granting me access when I forgot my badge.

Sami et Rebecca, Je ne saurais jamais comment vous remercier de tout ce temps partagé. On a vécu la thèse de A à Z. Merci d'avoir été là à chaque moment de doute, pour tous les gentils mots d'encouragement, et ces souvenirs précieux qui resterons gravés à jamais.

À tous les amis du master LOM, avec qui j'ai partagé mes doutes et mes réussites. Merci Clarisse, Damien, Guillaume, Gustave, Hadriel, J-P, Laure et Sylvain pour ces moments passés et qui m'accompagneront. Vous m'avez fait aimer Paris, surtout la rue Mouffetard !

Bien qu'elle soit éparpillée aux quatre vents, jusqu'au pays des kiwis et des All Blacks au moment où j'écris ces lignes, je ne serais jamais la personne que je suis sans la bande de Binic/Saint-Brieuc. Sans cette joyeuse troupe, je n'aurais probablement pas tenu la longueur. Adrien, Alexandre, Dorian, Quentin, Matiss, Thomas, Vincent, vous resterez toujours prêt de moi malgré la distance qui peut nous séparer.

Ael et Lénaïg, je vous remercie de ne pas m'oublier. Nos conversations sont rares, mais nos retrouvailles sont toujours chères. Isaac, merci pour toutes ces discussions, ces partages de doutes et ces encouragements durant nos thèses respectives.

Je me dois bien évidemment de remercier ma famille, qui m'accompagne depuis 27 ans. Vous vous êtes battus pour moi, et avec moi pour que je puisse accomplir cet objectif. Merci pour le soutien quotidien. Sans vous, sans vos encouragements, sans votre aiguillage, sans les "*there is a will, there is a way*" de mes parents et de mon grand-père avant eux, je ne serais sûrement pas là où j'en suis aujourd'hui. Merci à Maman, Papa, Tatie, Mathieu, Pauline, Camille et Cécile, ainsi qu'à Antoine, Antoine, Emmanuelle, Thibaut de m'avoir soutenu sans vous en rendre compte. Chaque moment passé en votre compagnie, les restaurations de bateaux, anniversaires, courses à pied, et autres noëls m'ont rempli la tête de souvenirs, me permettant de parsemer cette thèse difficile de moments familiaux fabuleux.

Bien entendu, je me dois de remercier ma femme, Linda. Le soutien inconditionnel, l'amour apporté au quotidien, et les défis relevés ensemble sont un précieux carburant m'ayant permis de sereinement envisager cette thèse et d'avancer toujours plus loin. Merci d'être là et de m'épauler à chaque instant. Arriver au bout de cette thèse avec toi me fait présager de grandes années que nous allons affronter ensemble. Je suis heureux d'être avec toi, et d'avoir cette aide permanente à mes côtés. Merci du fond du cœur. (Merci également à Jojo, cette petite boule de bonheur qui m'a permis de me ressourcer tant de fois pendant cette thèse.)

Contents

List of Figures

List of Tables

Chapter 1

Introduction

1.1 General context in quantum information

Quantum information bridges two prominent fields of research: information science and quantum mechanics. Information science is dedicated to processing bits of data for communication and computation. Classical bits are the fundamental units for computing and communication tasks and are manipulated using logic gates, which perform operations on these bits of information. Quantum physics has been a revolution that brought new concepts to understand the behavior of systems at the level of single particles. Quantum information aims to harness the specifics of quantum mechanics to information science. Information can be encoded in quantum bits (qubits) i.e. quantum states evolving in a two-dimensional Hilbert space with two orthogonal basis states called $|0\rangle$ and $|1\rangle$. Contrary to its classical counterpart, the qubit can exist in an infinity of coherent linear superposition of $|0\rangle$ and $|1\rangle$, bringing the hope of massive parallelization and greatly increased computational power. As a result, numerous works investigate the realization of devices that can perform quantum information processing tasks.

Several quantum computing platforms have emerged as promising candidates for encoding and manipulating quantum information. Some examples of systems based on atoms, ions, or superconductors, have achieved remarkable results in the fields of quantum computing and quantum simulation [2, 3, 4]. In contrast with other approaches, the optical platform offers several key advantages such as low interaction with the environment, and applications such as quantum communication, quantum computing, and quantum sensing [5, 6, 7, 8, 9, 10, 11]. Capitalizing on technologies from optical telecommunications, single photons appear as good candidates for distributed applications and linking distant nodes.

Two key objectives for enabling a photonic quantum computing platform are the generation of photonic quantum states and their efficient and scalable processing.

A major technological effort has been put in the direction of controlling single quantum emitters, enabling the near-deterministic uniform flow of single photons, for instance in single atoms [12] 2D materials [13, 14, 15] and quantum dots [16, 17]. Such sources represent a prominent step toward the deterministic generation of single photons, with a near unity emission probability of high-quality single photons. The challenge for this platform is the control of the emission wavelength of the single photon sources, emitting mostly below 900 nm. To reach single photon emission at telecom wavelength, frequency conversion is possible through non-linear interaction [18, 19, 20]. Furthermore, the quality of the generated photons depends on the control of the environment around the quantum emitters. They generally necessitate particular working conditions of vacuum and temperature. Nonetheless, the performances achieved by these sources led to impressive results, and promising perspectives, placing single emitters as a highly competitive platform for quantum state generation [21, 22].

Alternatively, non-linear media can mediate interaction between light beams of different frequencies. Through spontaneous parametric down-conversion or four-wave-mixing, photon pairs can be emitted simultaneously and are correlated in time, space, and frequency. While the generated quantum state is not a single photon state *per se*, the use of temporal correlations can enable a *heralded single-photon source*. Measuring one photon heralds the presence of the second one, which can then be used for quantum computing or communication tasks. The photon pair generation via spontaneous processes has the advantage of functioning at room temperature. Furthermore, emission can be engineered to generate photons directly at telecom wavelength. While the process is probabilistic, the ability to integrate such sources provides a very efficient way to design standalone integrated quantum optics experiments, offering the possibility to generate and process quantum states in a single chip [23, 24].

When working with photonic qubits, an essential choice is the *degree of freedom* used to encode quantum information such as its polarization, space, orbital angular momentum (OAM), relative time, or frequency [25, 26]. Polarization only allows encoding a single qubit per spatial mode, and spatial qubits necessitate two spatial modes for one qubit. As a result, expanding the number of qubits means increasing the size of the experiments. An intrinsic advantage of time, frequency, and OAM is the access to a large dimensional space of states permitting the encoding of parallel qubits in a single beam of light. In comparison to OAM, multiple time and frequency-encoded qubits can coexist in a single spatial mode, making them more suitable for easy transport through single-mode optical fibers.

1.2 Integrated quantum photonics

Integrated photonics is a pivotal technology that miniaturizes and integrates complex optical systems onto a single chip. The optical confinement of light in a waveguide with a small cross-section enhances interactions with non-linear materials. Several platforms have emerged for photonic integration, such as silica [27], silicon nitride [28], gallium arsenide [29], lithium niobate [30, 31], and silicon carbide [32]. In particular, silicon photonics and lithium niobate are attractive platforms for integrated quantum photonics.

Silicon photonics has become a well-established platform for integrated photonics circuits as it inherits the mastered techniques from silicon electronics and industry-ready fabrication methods. Silicon is also a well-suited material for classical and quantum telecommunication, as the transparency window includes the telecom range. Silicon-on-insulator (SOI) in particular is very attractive as it allows the easy integration of various passive components. While limited by non-linear losses induced by two-photon absorption compared to silicon nitride, its higher third-order non-linear index makes it more efficient for photon pair generation. The first use of silicon for photon pair generation was reported in 2006 [33]. As SOI is now processed at an industrial scale, it is possible to harness this technology for the controlled and reproducible fabrication of photon pair sources [34], as well as quantum information processing [24]. SOI is thus a platform of choice for integrated quantum photonics [23].

Lithium niobate is also a material of choice for optical quantum information processing. Due to its high second-order non-linear index, it has been used in free space configuration in the form of bulk crystals to generate photon pairs [35, 36]. Its first use for generating photon pairs in waveguides has been reported in 2001 [31, 37]. Compared to silicon, it offers a wider transparency range that includes the visible spectrum and enables the integration of high-speed active optical components through electro-optic effects. Integrating waveguides in lithium niobate is intrinsically difficult, as it is hard to etch with common dry and wet etching methods, although possible through ion-beam enhanced etching [38, 39]. Yet, titanium indiffusion and ion implantation have shown to be very efficient alternatives for the fabrication of lithium niobate waveguides without etching, altering the refractive index of the material necessary for guiding light in the material [31, 37]. This technique however limits the confinement of light in the waveguide as the relative refraction index difference is relatively small. A key step for the efficient, compact, and scalable nanostructuring of lithium niobate is the processing of high-quality crystalline thin films. One very recent and promising approach for the creation of waveguides is the use of smart cut technology to produce sub-micrometer height thin films of lithium niobate with high crystalline purity. With such thin films, the difficulty of etching lithium niobate can be transferred to other materials for creating guiding structures. For instance, silicon nitride-loaded thin-film lithium niobate waveguide enables the guiding of light in lithium niobate without etching the lithium niobate itself. Recent progress has been reported regarding the high-quality integration of optical components on this platform [40]. For quantum photonics, this platform has the potential to serve numerous functions, such as photon pair generation [41, 42, 43], and quantum information processing [44, 45, 46]. Finally, a significant advantage of thin-film lithium niobate on insulator is its ability to integrate with CMOS-compatible materials, such as silicon, enabling hybrid applications for more scalable and standalone integrated architectures [47, 48, 49].

1.3 Frequency-domain encoding for quantum information

Frequency-bin encoding uses frequency modes of light to encode quantum information, which offers several advantages

- Harnessing a larger number of frequency modes enables us to encode several qubits in parallel using a pair of modes for the two states of each qubit
- These qubits can propagate contiguously in a single spatiotemporal mode.
- This encoding also offers an intrinsic robustness to environmental fluctuations.

Frequency-domain manipulation started to be investigated in 2005 and has gained a growing interest since. Table 1.1 presents a timeline of the works investigating frequency-domain manipulation through theoretical works, experimental demonstration, either classical for gates characterization, or applied to quantum experiments, and very recently on-chip design proposals. This table separates the theoretical works for the manipulation, classical experiments, proof-of-concept, and experiments realized on generated frequency-bin quantum states. The manipulation of frequency-bin qubits is not trivial as it necessitates frequency conversion. Two methods, recently investigated since 2005 have been proposed:

Non-linear optical interaction has been demonstrated to perform tunable frequency conversion between modes that can be separated by large frequency spacing [50, 51]. This method involving non-linear four-wave mixing requires the use of strong optical pump fields to tune the desired operation [52, 53].

Frequency conversion can also be achieved by using the electro-optic effect. In [54], a frequency-coded communication scheme was proposed, using an electro-optic phase modulator (EOM). In 2017, the seminal work in [55] introduces a theoretical framework for frequency bin qubits. Within this paper, numerical simulation demonstrates that EOMs and programmable filters (PF) can enable the realization of a universal set of single and two-qubit gates for performing quantum computing tasks. This achievement ultimately paves the way for universal quantum computing utilizing frequency-bin qubits.

Two main differences arise between these approaches: i) the qubit spacing: the non-linear method, enables the manipulation of frequency bins spaced by one order of magnitude higher than the electro-optic approach (hundreds of GHz with respect to tens of GHz), and ii) reconfigurability: the electro-optic approach, through electrical control of the EOMs and PFs, enable to easily program the devices for any desired operation, whereas non-linear transformations require a heavy setup for a limited reprogrammability.

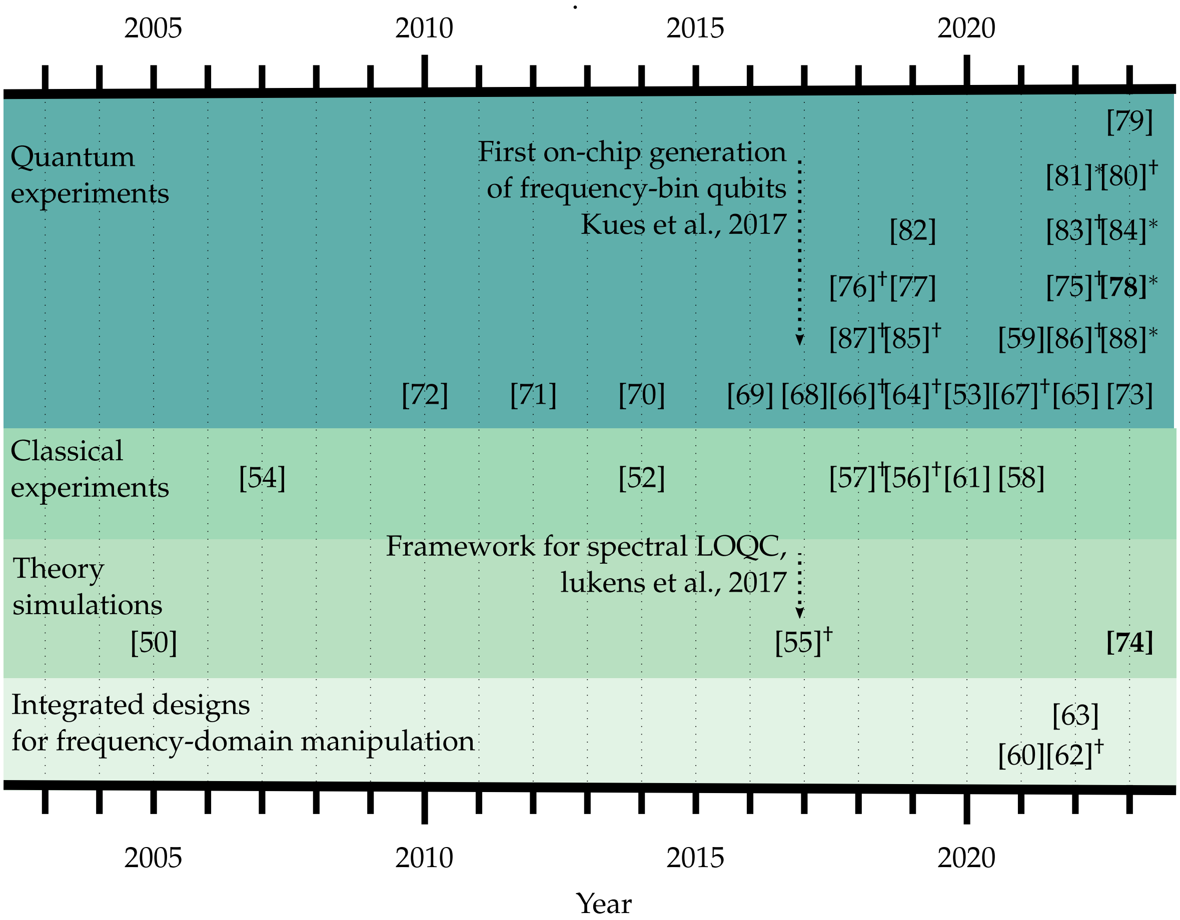

Figure 1.1: Timeline of the several works on frequency-domain manipulation.†: works from the team in Purdue/Oak-Ridge, *: work using silicon on insulator photon pair sources. Bold references represent works from our team.

An important challenge is the ability to generate frequency-bin quantum states. Seminal experiments in [70, 71, 72] used photon pairs generated from a bulk crystal through spontaneous parametric down conversion. The two photons spectrums were carved into frequency bins using a frequency demultiplexer, enabling pioneer results in the domain of frequency-bin quantum information, with a measure of Bell parameters for frequency-bin entangled qubits. Capitalizing on the progress of integrated quantum optics, frequency-bin quantum states can be generated at telecom wavelength, in straight waveguides, or micro-resonators. Waveguides can efficiently generate broadband photon pairs that can be carved into frequency bins with external filtering, and micro-resonators enable the on-chip generation of equispaced frequency combs.

Frequency-domain quantum information processing has been mainly investigated along two paths:

- **Generation of frequench-domain quantum states**. A key challenge for frequency-encoded information processing is the generation of frequency-bin qubits, with spacing fit for the manipulation with electro-optic devices. Furthermore, to harness the parallelization, the ability the generate an equispace comb of frequency-bin is necessary. Frequency-bin entangled state generated by photon pair sources has also been increasingly studied in lithium niobate waveguides [66, 75, 79, 87], silicon nitride [75, 76, 86] and hydex micro-resonators [68]. Very recently, silicon photonics has enabled, through the fabrication of complex nanostructures, the generatation of frequency-bin entangled states [81, 84, 88].
- **Processing of frequency-domain quantum information**. Several theoretical and experimental studies have demonstrated the manipulation of frequency-bin quantum states with EOMs and PFs. Arbitrary synthesis of single-qubit gates has been experimentally realized for frequency-bin qubits, reaching high-fidelities [57, 61]. Such qubit gates can be parallelized to independent frequency-bin qubits [57, 61, 67]. A post-selected controlled-not gate has been demonstrated [85]. The manipulation of qudits has also been investigated with an experimental realization of discrete Fourier transform gate up to three dimensions [57, 75]. As such, the use of EOMs and PFs offers a versatile approach to frequency-bin manipulation. Beyond the realization of specific quantum gates, an electro-optic approach could lead to the compact design of large-scale scale fully programmable interferometer in the frequency-domain [60], analogous to standard spatial approaches [89].

This Ph.D. work, conducted between Telecom Paris and the Center of Nanosciences and Nanotechnology (C2N), proposes to explore both building blocks, by exploiting two novel sources of light emitting at telecom wavelength, based on two attractive platforms: silicon-on-insulator, which has proven to be an enabling material for integrated quantum photonics, and lithium-niobate-on-insulator, a promising emerging platform. As the landscape of frequency-domain information has been increasingly growing, it is now possible to envision practical uses in quantum information processing. In this manuscript, we implement a quantum key distribution protocol as a concrete application of frequency-encoding to the domain of quantum communication.

In Chapter 2, we investigate **photon pair generation at telecom wavelength** of two novel integrated sources, based on two promising materials for integrated classical and quantum photonics: a silicon on insulator micro-resonator, and a periodically-poled thin-film lithium niobate waveguide on insulator. We first describe the non-linear processes of spontaneous parametric down-conversion and spontaneous four-wave-mixing. Then we describe both devices. For the silicon-on-insulator micro-resonator, we characterize the spectral properties of the micro-resonator. We assess, a small spectral spacing and low dispersion for the efficient generation of photon pairs at telecom wavelength. For the periodically poled thin-film lithium-niobate waveguides, we optimize the parameters for photon pair generation at telecom wavelength. Then for both sources, we characterize their performances as a heralded single photon source, by computing the emission statistics, heralding efficiencies, single photon purity, and spectral purity.

In Chapter 3, we describe the **theoretical and numerical tools enabling the manipulation of frequency-bin and time-bin encoded qubits** with electro-optic modulators (EOM) and programmable filters (PF). We investigate the synthesis of single qubit gates with time and frequency encoding, using two combinations of PFs and EOMs. We compare the results of both combinations and both encodings. Then, we investigate the parallelization of single-qubit gates. We discuss the limitations and the perspective of improvement through more complex RF driving of the EOMs. Some sections of Chapter 3 can be skipped for the understanding of the results in Chapter 4, only requiring the understanding of the functioning of the EOMs and PFs found in Section 3.2, and rationale behind single qubit gate synthesis in Section 3.3

In Chapter 4, we **experimentally realize a tunable single qubit gate for frequency-bin qubits**. We measure its performance and ability to be parallelized to several qubits. We then apply those gates to the photon pairs generated by the on-chip photon pair sources presented in Chapter 2. We **generate and manipulate frequency-bin entangled state**. Using two parallel single qubit gates, we perform frequency-bin Bell-like interferences and perform quantum state tomography on frequency-bin qubits, generated by the silicon on insulator micro-resonator. These parallel gates enable us to **realize a proof-of-concept of a frequency-domain version of a quantum key distribution protocol**. Finally, we perform a frequency-domain version of the Hong-Ou-Mandel experiment using a single qubit gate, for qubits generated by a periodically-poled thin-film lithium niobate waveguide.

We conclude in Chapter 5 and explore several paths for the continuation of the experiments. We give a tentative broad view of where the frequency-bin manipulation could be heading. Notably, we present preliminary results on an entanglement swapping protocol performed on frequency-bin entangled qubits.

The work is presented in the three main chapters, 2, 3, and 4, as well as Section 5.2.

Chapter 2

On-chip generation of photon pairs at telecom wavelength

The ability to generate photonic quantum states at telecom wavelengths is a pivotal resource in quantum information science and technologies. This capability combined with standard telecommunication infrastructures, will enable the creation of large-scale quantum networks between distant nodes [90]. Spontaneous parametric down-conversion (SPDC) and spontaneous four-wave mixing (SFWM) offer methods to produce, at telecom wavelength, photon pairs that exhibit correlation across various degrees of freedom. Exploiting these correlations, one can achieve a single photon source from such a two-photon state. As the two photons are created at the same time, a heralded single-photon source is achieved through the measurement of one herald photon.

Photonic quantum information processing requires efficient and high-quality heralded single-photon sources that need to exhibit efficient generation and high single-photon purity. Harnessing the recent progress in the domain of integrated quantum optics, various platforms emerged as promising candidates for such purposes [1]. The materials listed in Table 2.1 represent viable pathways for realizing integrated photon pair sources. Each of them offers specific advantages for their guiding properties, non-linear interaction, and transparency windows. We present in this chapter the experimental broadband generation of photon pairs in silicon and lithium niobate on insulator.

Silicon photonics is a well-established platform for integrated photonics. The ability to process at an industrial scale enables the production of large-scale integrated circuits, providing a versatile testbed for quantum photonic [89, 104, 105]. The lack of second-order coefficient however hinders the ability to integrate active devices. It is nonetheless an attractive platform for photon pair generation: the third-order non-linearity of silicon enables photon pair generation through spontaneous four-wave-mixing [34, 106, 107].

Material	n	d_{max} [pm/V] ($\chi^{(2)}$)	n_2 [m^{2}W^{-1}] at 1.55 μm	Transparency [μm]	loss [dB.cm^{-}1]
Si	3.8	15 (strained Si) [91]	4.5x10^{-18}[92]	1.1 - 9	0.026 [93]
Si_3N_4	2	-	2.6x10^{-19}[94]	0.4 - 4	0.01 [95]
GaAs	3.4	170 (d_{36} [96] at 1 μm)	1.6x10^{-17}[92]	1.0 - 10	0.2 [29]
AlN	2.1	23.2 [97]	2.3x10^{-19}[98]	0.2 - 5	0.6 [99]
$LiNbO_3$	2.21	25.2 [100]	9.1x10^{-20}[101]	0.5 - 4	0.042 [102]
Hydex	1.5-1.9	-	1.15x10^{-19} [103]	0.2 - 2	0.06 [103]

Table 2.1: Properties of material used for integrated photon pair sources, adapted from [1]. n: refraction index, d_{max} is the maximum second order non-linear coefficient, n_2 is the Kerr coefficient at 1.55 μm.

Micro-resonators are particularly interesting structures for photon pair generation. Such structures enable more intensity to build up, as light undergoes several round trips in the micro-cavity, thus facilitating more efficient nonlinear interactions with a reduced footprint. Additionally, photons are efficiently generated in spectral modes resonant with the cavity, enabling the generation of narrow-band single photons. Such narrow filtering is essential for the use of heralded single-photon sources [108]. The generation of photon pairs in silicon micro-resonator structures was first reported in [34]. Numerous works followed, enabling more efficient photon pair generation in micro-resonators leading to applications in quantum information [109, 110, 111, 112, 113, 114, 115, 116, 117, 118, 119, 120]. The typical free spectral range of such a structure is typically of the order of hundreds of GHz.

Lithium niobate (LN) has been a pioneeringly material for quantum optics [121]. Its nonlinear and electro-optical properties enable a plethora of applications such as polarization rotation or electro-optic phase modulation and frequency conversion [46, 122, 123, 124]. For photon pair generation periodically LN is a seminal material, as its strong second-order nonlinear coefficient enables the spontaneous generation of quantum states at telecom wavelength [31]. Recently, the smart-cut technology allowed the realization of high-quality thin-film from bulk crystal, harnessing the thin-film technology. As such, it places lithium niobate as a promising platform for integrated photonics and integrated quantum technologies. Especially, the confinement of light harnessed in those thin films has since 2019 enabled the efficient photon pair generation in waveguides, in etched LNOI waveguide [42, 43, 125], and more recently in micro-resonators [126], or in silicon-nitride-loaded waveguides [41].

Photon pairs generated in bulk crystals or waveguide structures produce a broad spectrum that can be divided into frequency bins using external filtering techniques, such as frequency demultiplexers or programmable filters. In the case of photon pairs generated

Work	year	**Frequency spacing**	**Platform**	Reference
Kues et al.	2017	200 GHz	hydex Single MR	[68]
Imany et al.†	2018	50 GHz	SiN Single MR	[76]
Lu et al.†	2022	40 GHz	SiN Single MR	[86]
Sabattoli et al.*	2022	15 GHz	**SOI** 2 MR	[81]
Borghi et al.*	2023	15 GHz	**SOI** 2 MR	[88]
Clementi et al.*	2023	19 GHz	**SOI** 4 MR	[84]
Mahmudlu et al.	2023	199 GHz	SiN Single MR	[73]
Henry et al.*	**2023**	**21 GHz**	**SOI** **Single MR**	[78]

Table 2.2: Frequency spacing achieved with micro-resonator structures for frequency-domain manipulations. MR: micro-resonators.†: works from the group of Purdue/Oak-Ridge, *: works using SOI micro-resonators.

in micro-resonator structures, the free spectral range (FSR) determines the frequency spacing. Table 2.2 displays the achieved frequency spacing for micro-resonator-based sources. With single micro-resonators, spacing has been achieved down to 40 GHz in SiN and hydex. Employing complex SOI structures can reduce the frequency spacing to as low as 15 GHz. However, in such structures, the FSR is not constant across the entire spectrum, reducing the ability to parallelize quantum gates to several qubits.

We aim in this chapter to introduce, and characterize two novel photon pair sources, emitting at telecom wavelength, and fit for frequency manipulation. This chapter is structured as follows: In Section 2.1, we **introduce the concepts of both spontaneous parametric down-conversion and spontaneous four-wave mixing** enabling the photon pair generation. We discuss the desired statistical properties of a heralded single-photon source. Then, in Section 2.2, we **describe the structures used for photon pair generation**: a silicon-on-insulator (SOI) micro-resonator, and a periodically-poled thin-film lithium niobate on insulator waveguide (LNOI). For the LNOI, we investigate the poling parameters and optimize them for photon pair generation at telecom wavelength. For the micro-resonator, we characterize the resonator structure and correlate the resonator properties with the photon pair emission. Then, in Section 2.3, we **characterize both photon pair sources** by assessing key metrics. We assess their efficiency, by measuring the number of generated pairs, and their quality by measuring the single photon statistics and their spectral purity.

2.1 Spontaneous parametric down-conversion and spontaneous four-wave-mixing processes

In this section, we investigate the two spontaneous processes for photon pair generation in second-order and third-order non-linear materials, namely spontaneous parametric down-conversion and spontaneous four-wave-mixing. We first explore the single mode case in section 2.1.1 and 2.1.2, before considering multimode spectral emission in Section 2.1.4. We then discuss the spectral purity and photon number statistics of a heralded single-photon source.

2.1.1 Interaction Hamiltonian for the SPDC process

Spontaneous parametric down-conversion is a non-linear process involving three interacting fields

- A pump photon of frequency ω_p and wavevector $\vec{k}_p$,
- A signal photon of frequency ω_s and wavevector $\vec{k}_s$,
- An idler photon of frequency ω_i and wavevector $\vec{k}_i$.

The Hamiltonian describing the non-linear interaction can be expressed in terms of creation and annihilation operators $\hat{a}_j^\dagger$ and $\hat{a}_j$, $k \in \{p,\ s,\ i\}$ as [127, 128]

$$\hat{H}_{SPDC} = i\hbar\kappa \left(\hat{a}_i \hat{a}_s \hat{a}_p^\dagger e^{i\vec{\Delta}_k.\vec{L} - i\Delta\omega.t} + \hat{a}_i^\dagger \hat{a}_s^\dagger \hat{a}_p e^{-i\vec{\Delta k}.\vec{L} + i\Delta\omega.t} \right). \tag{2.1}$$

Where κ incorporates the medium geometry and is proportional to the second-order coefficient d_{eff}. In Eq. 2.1, $\vec{\Delta k}$ and $\Delta\omega$ are respectively the phase and energy mismatches involving the energy and wavevectors of the three interacting fields, defined as

$$\begin{aligned} \vec{\Delta k} &= \vec{k}_p - \vec{k}_i - \vec{k}_s \\ \Delta\omega &= \omega_p - \omega_i - \omega_s \end{aligned} \tag{2.2}$$

A critical condition is the cancelation of the **phase mismatch** $\vec{\Delta k} = 0$. If this condition is respected, the energy build-up of the generated field increases monotonously with crystal length. In the presence of phase mismatch, power transfer from the pump to the generated field initially increases over a coherence length of $l_c = \frac{\pi}{\vec{\Delta k}}$, after which the energy exchange between the pump and the generated beam changes sign, causing the generated power to cancel out at $2 \times l_c$. Achieving $\vec{\Delta k} = 0$ depends on the ability to compensate for the dispersion in the medium. Such a condition can be achieved using the birefringence of the medium, and tuning the orientation of the non-linear medium with the interacting pump field [129]. Alternatively, quasi-phase matching (QPM) can be achieved with a non-zero $\vec{\Delta k}$. This technique consists of a periodic reversal of the ferroelectric domains, allowing to change the sign of the $\chi^{(2)}$. To achieve QPM, inversion must happen every lc. We can thus define a poling period, $\Lambda_{\text{poling}} = 2l_c$. Under these considerations, the condition to achieve quasi-phase matching becomes

$$k_p = k_i + k_s + \frac{2\pi}{\Lambda_{\text{poling}}}. \tag{2.3}$$

An interesting point is the possibility of compensating for any values of phase mismatch as long as the right poling can be engineered. We will see in Section 2.2.1.2 how the engineering of the poling period enables us to achieve QPM for the generation of photon pairs starting from a specific pump field. Experimentally, QPM can be achieved by stacking layers of non-linear medium with an inverse orientation direction [130], or directly changing the material's properties by applying a strong electric field, that changes the direction of polarization of the medium. Assuming $\vec{\Delta k} = 0$ and $\vec{\Delta \omega} = 0$, the Hamiltonian becomes

$$\hat{H}_{SPDC} = i\hbar\kappa \left(\hat{a}_i \hat{a}_s \hat{a}_p^\dagger + \hat{a}_i^\dagger \hat{a}_s^\dagger \hat{a}_p \right) \tag{2.4}$$

This Hamiltonian describes two non-linear processes. The first term of the sum corresponds to the sum-frequency generation: two photons of energy ω_i and ω_s are annihilated to create one photon of energy $\omega_p = \omega_i + \omega_s$. A particular case of this process is second harmonic generation (SHG), where the annihilated photons have the same energy $\omega_i = \omega_s = \omega_p/2$. The second term corresponds to the SPDC process, where one photon of energy ω_p is annihilated to create two photons of energy ω_i and ω_s. It is worth noting that SHG and SPDC both necessitate the same energy and momentum conservation relations.

Because of its high intensity compared to the spontaneously generated photons, the pump field can be treated as a coherent state of amplitude α_p. The interaction Hamiltonian can be rewritten as :

$$\hat{H}_{SPDC} = i\hbar\alpha_p\kappa \left(\hat{a}_i \hat{a}_s + \hat{a}_i^\dagger \hat{a}_s^\dagger \right) \tag{2.5}$$

Under these conditions, the two-photon state created by the SPDC process can be written as [127, 128]

$$|\psi\rangle = e^{\frac{1}{i\hbar}\hat{H}_{SPDC}} |0_i, 0_s\rangle \approx \zeta_{SPDC} |0_i, 0_s\rangle + \kappa\alpha_p |1_i, 1_s\rangle + \frac{(\kappa\alpha_p)^2}{2} |2_i, 2_s\rangle + \cdots \tag{2.6}$$

Where ζ_{SPDC} is the normalization coefficient. From Eq. 2.6, we see that spontaneously, a photon pair is created with a probability $|\kappa\alpha_p|^2$. $|\alpha_p|^2$ is proportional to the pump power

P_p. It also appears that double pairs can be created. These events are not desirable, as we are only interested in generating pairs of single photons.

2.1.2 Interaction Hamiltonian for the SFWM process

The SFWM process involves four interacting fields:

- Two pump photon of frequency ω_p and wavevector $\vec{k}_p$,
- A signal photon of frequency ω_s and wavevector $\vec{k}_s$,
- An idler photon of frequency ω_i and wavevector $\vec{k}_i$.

The Hamiltonian describing the non-linear interaction is [127, 128]

$$\hat{H}_{SFWM} = i\hbar\Gamma \left(\hat{a}_i\hat{a}_s\hat{a}_p^\dagger\hat{a}_p^\dagger e^{i\vec{\Delta}_k.\vec{L}-i\Delta\omega.t} + \hat{a}_i^\dagger\hat{a}_s^\dagger\hat{a}_p\hat{a}_p e^{-i\vec{\Delta k}.\vec{L}+i\Delta\omega.t}\right). \tag{2.7}$$

In Eq. 2.7, Γ englobes the third-order nonlinearity of the medium, $\vec{\Delta k}$ and $\Delta\omega$ are respectively the phase and energy mismatch, defined as

$$\begin{aligned} \vec{\Delta k} &= 2\vec{k}_p - \vec{k}_i - \vec{k}_s \\ \Delta\omega &= 2\omega_p - \omega_i - \omega_s \end{aligned} \tag{2.8}$$

As for SPDC, we wish to have $\vec{\Delta k} = \Delta\omega = 0$. Fulfilling $\vec{\Delta k} = 0$ depends on dispersion in the medium. As the four interacting fields are close in frequency: $\omega_p \approx \omega_i \approx \omega_s$, phase matching can thus be achieved by engineering the dispersion in the medium to obtain zero dispersion for a region centered on the pump wavelength. In integrated structures, this can be achieved by changing the width or height of the waveguide [131].

Treating the pump as a classical field, we can write the Hamiltonian for a strong pump pulse as

$$\hat{H}_{SFWM} = i\hbar\alpha_p^2\Gamma\left(\hat{a}_i\hat{a}_s + \hat{a}_i^\dagger\hat{a}_s^\dagger\right) \tag{2.9}$$

The generated bi-photon state can thus be written as

$$|\psi\rangle = e^{\frac{1}{i\hbar}\hat{H}_{SFWM}}|0_i, 0_s\rangle \approx \zeta_{SFWM}|0_i, 0_s\rangle + \Gamma\alpha_p^2|1_i, 1_s\rangle + \frac{(\Gamma\alpha_p^2)^2}{2}|2_i, 2_s\rangle + \cdots \tag{2.10}$$

Where ζ_{SFWM} is the normalization coefficient. From Eq. 2.6, we see that spontaneously, a photon pair is created with a probability $|\kappa\alpha_p|^4$. The photon pair generation probability is thus proportional to P_p^2.

2.1.3 Comparison of SPDC and SFWM

The two non-linear processes give rise to similar wavefunctions

$$|\psi_{SPDC}\rangle \approx \zeta_{SPDC}\,|0_i,0_s\rangle + \kappa\alpha_p\,|1_i,1_s\rangle + \frac{(\kappa\alpha_p)^2}{2}\,|2_i,2_s\rangle + \cdots \tag{2.11}$$

$$|\psi_{SFWM}\rangle \approx \zeta_{SFWM}\,|0_i,0_s\rangle + \Gamma\alpha_p^2\,|1_i,1_s\rangle + \frac{(\Gamma\alpha_p^2)^2}{2}\,|2_i,2_s\rangle + \cdots \tag{2.12}$$

With each process, we produce photon pairs, with a probability increasing with pump power P_p. The dependency is however different for SPDC and SFWM. The probability of generating a photon pair is expected to evolve as:

- P_p for photon pairs generated from SPDC,
- P_p^2 for photon pairs generated from SFWM.

To facilitate the reading, SPDC and SFWM Hamiltonians can be written generally as

$$\hat{H}_{PP} = i\hbar\xi\left(\hat{a}_i\hat{a}_s + \hat{a}_i^{\dagger}\hat{a}_s^{\dagger}\right) \tag{2.13}$$

Where $\xi = \kappa\alpha_p$ or $\xi = \Gamma\alpha_p^2$ respectively for SPDC and SFWM. This Hamiltonian leads to a wavefunction $|\psi\rangle$

$$|\psi\rangle \approx \xi_0\,|0_i,0_s\rangle + \xi\,|1_i,1_s\rangle + \xi^2\,|2_i,2_s\rangle + \cdots, \tag{2.14}$$

where ξ_0 is a different normalization coefficient for SPDC and SFWM.

The following section describes notions that are similar for both processes.

2.1.4 Spectral distribution of photon pairs

In previous sections, we assumed photon pair emissions to be in a single mode, with just one pair of signal and idler photons at frequencies ω_i and ω_s. However, in practice, photon pair generation is multimode, allowing signal and idler photons to be emitted across a range of frequencies, while still satisfying energy conservation relation and resulting in the following ω_i and ω_s relationships:

$$\begin{aligned}\omega_i &= \omega_d - \omega\\ \omega_s &= \omega_d + \omega\end{aligned} \tag{2.15}$$

where ω_d represents the degeneracy frequency. In the case of SPDC, $\omega_d = \omega_p/2$, and the case of SFWM, $\omega_d = \omega_p$. The Hamiltonian describing the multimode generation of photons can be defined as

$$\hat{H}_{PP} = \int_{\omega_i}\int_{\omega_s} d\omega_i d\omega_s\, A(\omega_i,\omega_s) i\hbar\xi\left(\hat{a}_{\omega_s}\hat{a}_{\omega_s} + \hat{a}_{\omega_s}^{\dagger}\hat{a}_{\omega_s}^{\dagger}\right), \tag{2.16}$$

Where

$$A(\omega_i, \omega_s) = \alpha(\omega_i, \omega_s)\Phi(\omega_i, \omega_s), \tag{2.17}$$

is the joint spectral amplitude describing spectral correlations between the signal and idler photon, and is the product of the pump spectral shape $\alpha(\omega_d - \omega, \omega_d + \omega)$ and the medium's phase matching function $\Phi(\omega_d - \omega, \omega_d + \omega)$, that determines the range of frequencies for which the phase matching is achieved [108, 132]. The multimode photon pair state is thus expressed as

$$|\psi\rangle \approx \int_{\omega_i}\int_{\omega_s} d\omega_i d\omega_s \, A(\omega_i, \omega_s)\xi \, |1_{\omega_i}, 1_{\omega_s}\rangle \, . \tag{2.18}$$

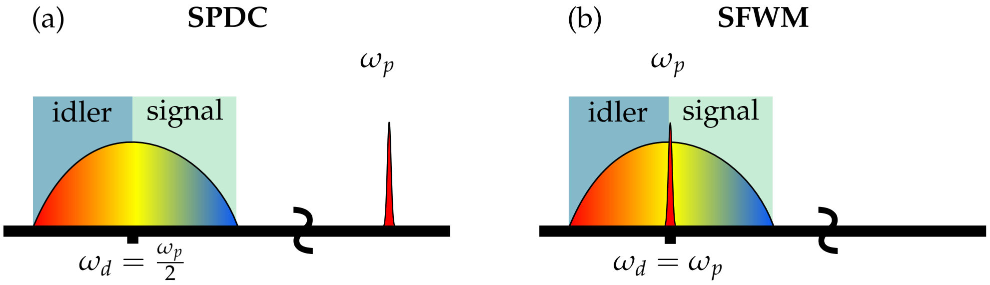

Figure 2.1: Representation of a photon pair spectrum generated by (a): SPDC and (b): SFWM.

In the next section, we describe how spectral correlations affect the purity of the generated quantum states.

2.1.5 Spectral purity

A pure photon state corresponds to a well-defined spatiotemporal mode. A high spectral purity (P_{spectral}) is essential to perform quantum experiments between independent heralded photon sources [108]. Photon pairs generated by SFWM or SPDC usually exhibit spectral correlation. The detection of the heralding signal projects the heralded idler into an incoherent mixture of states. As such, for use in heralded quantum experiments, it is essential to suppress those spectral correlations to achieve a high spectral purity.

Practically, a high purity can be achieved using spectral filtering on the signal and idler photon, to reduce the spectral correlations. However, this technique comes at the price of a lower photon rate [133]. Alternatively, engineering the joint spectral amplitude function can be achieved by using a pulsed pump field. The broadband of the pump reduces the demand on spectral filtering [108].

To see how spectral correlations affect the spectral purity of a heralded single photon, let us use the Schmidt decomposition and express Eq. 2.18 as a sum of signal idler quantum state generated at the frequencies $\omega_{i,n}$ and $\omega_{s,n}$ as [134]

$$|\psi\rangle = \sum_n \sqrt{\lambda_n}\, |\omega_{i,n}, \omega_{s,n}\rangle \,, \tag{2.19}$$

where $|\omega_{i,n}\rangle$ and $|\omega_{s,n}\rangle$ define two sets of eigenmodes. λ_n are the Schmidt coefficients, respecting the condition

$$\sum_n \lambda_n = 1 \tag{2.20}$$

The operation of heralding corresponds to tracing out one photon from the state. Considering heralding a signal photon with an idler, we can write the density matrix of a heralded signal photon as

$$\rho_s = Tr_i\left(|\psi\rangle\langle\psi|\right) = \sum_n \lambda_n\, |\omega_{s,n}\rangle\langle\omega_{s,n}| \,. \tag{2.21}$$

The degree of spectral correlations can be quantified by computing the Schmidt number, describing the effective number of populated eigenmodes [135]

$$K = \frac{1}{\sum_N \lambda_n^2} \tag{2.22}$$

The spectral purity of such a state is directly linked to the Schmidt number as [136]

$$P_{\text{spectral}} = \frac{1}{K} \tag{2.23}$$

From this equation, we thus see that to achieve a unit purity, it is necessary to harness $K = 1$, i.e., each photon populating a single spectral mode. Please note that the measurement of the spectral purity is described in Section 2.3.5

2.1.6 Photon number statistics

A light source emits photons with certain statistics:

- **Poissonian statistics**: Coherent light sources, e.g. laser
- **Super-Poissonian statistics**: Chaotic light sources, e.g. light spontaneously emitted from an atom
- **Sub-Poissonian statistics**: Quantum , e.g. single photon sources

Each of the three statistics exhibits specific intensity correlations, that are characterized by the second-order correlation function $g^{(2)}(0)$. For a light source radiating an electric field $\hat{E}$, with the complex components $\hat{E}^{(+)}(t)$ and its complex conjugate $\hat{E}^{(-)}(t)$, the second-order correlation function is written as [137, 138].

$$g^{(2)}(\tau) = \frac{\left\langle \hat{E}^{(-)}(t)\hat{E}^{(-)}(t+\tau)\hat{E}^{(+)}(t)\hat{E}^{(+)}(t+\tau)\right\rangle}{\left\langle \hat{E}^{(-)}(t)\hat{E}^{(+)}(t)\right\rangle \left\langle \hat{E}^{(-)}(t+\tau)\hat{E}^{(+)}(t+\tau)\right\rangle}, \tag{2.24}$$

Assuming quantized electro-magnetic fields, we can express the electric field $\hat{E}^{(+)}$ and $\hat{E}^{(-)}$ as creation and annihilation operators $\hat{a}$ and $\hat{a}^{\dagger}$. Eq. 2.24 becomes [137]

$$g^{(2)}(\tau) = \frac{\langle \hat{a}^{\dagger}\hat{a}^{\dagger}\hat{a}\hat{a}\rangle}{\langle \hat{a}^{\dagger}\hat{a}\rangle \langle \hat{a}^{\dagger}\hat{a}\rangle} = \frac{\langle \hat{n}(\hat{n}-1)\rangle}{\langle \hat{n}\rangle^{2}} = 1 + \frac{\langle(\Delta\hat{n})\rangle^{2} - \langle\hat{n}\rangle}{\langle\hat{n}\rangle^{2}} \tag{2.25}$$

In Eq. 2.25, $\langle\hat{n}\rangle$ and $\langle(\Delta\hat{n})\rangle^{2}$ are respectively the mean number of photon and the variance. The value of $g^{(2)}(\tau)$ remains theoretically constant for a photonic mode unaffected by decoherence. However, a realistic source has limited coherence time resulting in two limits for

$$\begin{aligned} g^{(2)}(\tau \to \pm\infty) &\to 1 \\ g^{(2)}(\tau \to 0) &\to 1 + \frac{\langle(\Delta\hat{n})\rangle^{2} - \langle\hat{n}\rangle}{\langle\hat{n}\rangle^{2}} \end{aligned} \tag{2.26}$$

Table 2.3 lists the expected values of $g^{(2)}(0)$ for several probability distributions P_n.

	Poissonian	Thermal	Single photon source
$P_{\hat{n}} =$	$\frac{\langle\hat{n}\rangle^{\hat{n}}}{\hat{n}!}e^{-\langle\hat{n}\rangle}$	$\frac{1}{(\langle\hat{n}\rangle+1)}\left(\frac{\langle\hat{n}\rangle}{\langle\hat{n}\rangle+1}\right)^{\hat{n}}$	$P_{\hat{n}=1} = 1$, $P_{\hat{n}\neq1} = 0$
$\langle(\Delta\hat{n})\rangle^{2}$=	$\langle\hat{n}\rangle$	$2\langle\hat{n}\rangle$	0
Expected $g^{(2)}(0)$	1	2	0

Table 2.3: Probability distribution and associated values of $g^{(2)}(0)$ for coherent, thermal and quantum light sources.

The second-order correlation function can be experimentally evaluated with a Hanbury-Brown and Twiss (HBT) interferometer, presented in Fig. 2.2. This interferometer consists only of a 50:50 beam splitter whose outputs are directed to two photon detectors. The intensity correlations are then measured by computing a histogram of relative arrival time at the two detectors. Intuitively, we can already understand the behavior of a single photon source plugged into this experiment. A single photon arriving at a beam splitter can only be transmitted or reflected. As such, it can only trigger one detector at a time. For a true single-photon source, the histogram of relative arrival time at the two detectors exhibits no simultaneous detection, hence a $g^{(2)}(0) = 0$. Please note that we use the HBT interferometer in Section 2.3.4 for measuring the single photon purity, as well as in Section 2.3.5 for measuring the spectral purity.

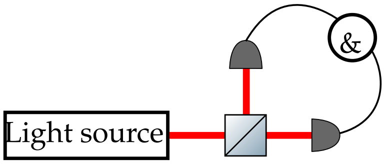

Figure 2.2: Experimental setup for the measurement of the second order correlation function.

2.2 Integrated sources for photon pair generation at telecom wavelength

In this section, we explore the experimental generation of photon pairs at telecom wavelength using two innovative integrated sources: a silicon-on-insulator micro-resonator and a periodically poled thin-film lithium niobate waveguide. Our approach begins with an introduction to these structures and their optimization for photon pair generation around 1550 nm. For the LNOI waveguide, we optimize the waveguide parameters and temperature, and for the SOI micro-resonator, we compare the spectral properties of the resonator with the photon pair emission. Following, we evaluate the performance of both sources, by assessing key metrics such as generation efficiency through the generated number of pairs, internal brightness, heralding efficiency, single photon purity, and spectral purity.

2.2.1 Periodically poled thin-film lithium niobate waveguides-on-insulator

2.2.1.1 Description of the waveguides

This section focuses on a chip comprised of periodically-poled thin-film lithium niobate waveguides, designed in C2N and fabricated at the Royal Melbourne Institute of Technology (RMIT). The wafer consists of a 300-nm-thick lithium niobate (LN) film bonded over a 2-μm-thick buried SiO_2 wafer using smart-cut technology. The waveguides consist of a 400 nm thick layer of silicon nitride (SiN) deposited on top of the LN layer and then partially etched to a depth of 350 nm. The refractive index of SiN (1.98) is slightly smaller than LN (2.13 for extraordinary mode at 1550 nm). As such, it laterally confines the optical mode while leaving most of the light in the lithium niobate layer [139]. A cross-section of the waveguide is shown in Fig. 2.3, with the simulated transverse profiles for the two wavelengths of interest, 780 nm for the pump wavelength, and 1550 nm for the photon pairs. Gold electrodes are deposited on both sides of the waveguide in a comb pattern as shown in Fig. 2.4 to realize the periodic poling. The teeth of the comb are spaced to match the desired poling period Λ_{poling} over a certain length L_{poling}. Three Λ_{poling} and four L_{poling} are designed, and listed in Table. 2.4. To achieve the periodic poling, electric pulses of 48 kV/mm are applied for a duration of 10 ms[139].

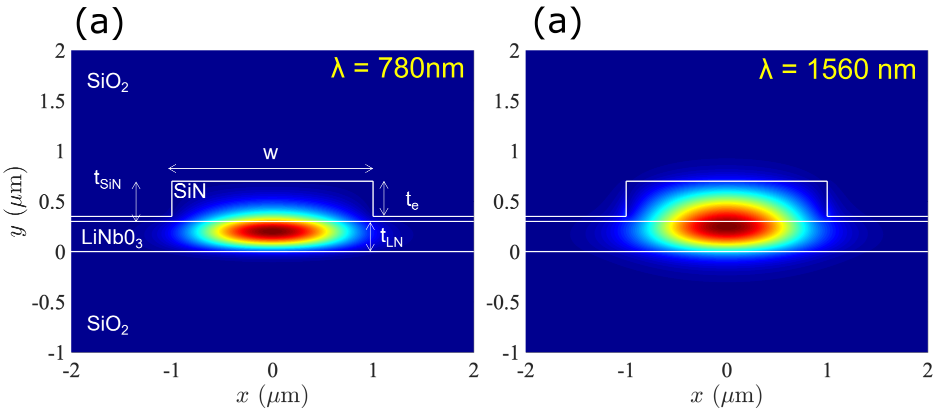

Figure 2.3: Scheme of the cross-section of the structure. Simulation of intensity mode profile calculated using Lumerical finite-difference eigenmode solver for (a): 780 nm light and (b): 1560 nm light. t_{SiN}= 400 nm, t_e= 350 nm, t_{LN}= 300 nm, w= 2 μm.

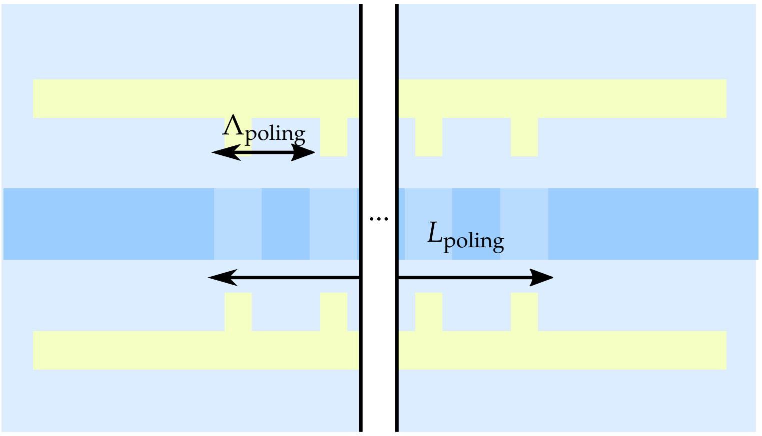

Figure 2.4: Drawing of a thin film lithium niobate waveguide. The waveguide is displayed in darker blue. The domain inversion is represented by a lighter shade of blue along the waveguide. Λ_{poling} corresponds to the poling period, while L_{poling} correspond to the length of the poling region.

The sample is divided into three groups of waveguides, one for each Λ_{poling}. The three groups are composed of 10 waveguides: 4 with a poling length of 4800 μm, 2 with a poling length of 3600 μm, 2 with a poling length of 2400 μm, 2 with a poling length of 1200 μm. Fig. 2.5.(a) shows a portion of the photonic chip, on which we observe 4 waveguides. Each waveguide is surrounded by arrays of electrodes. The squares correspond to the contact electrodes for the external wiring. Fig. 2.5.(b) shows a zoom-in of a waveguide,

Λ_{poling} (μm)	4.97	4.93	4.87	
L_{poling} (μm)	4800	3600	2400	1200

Table 2.4: Available poling periods (Λ_{poling}) and poling lengths (L_{poling}).

with combs of electrodes used for the poling.

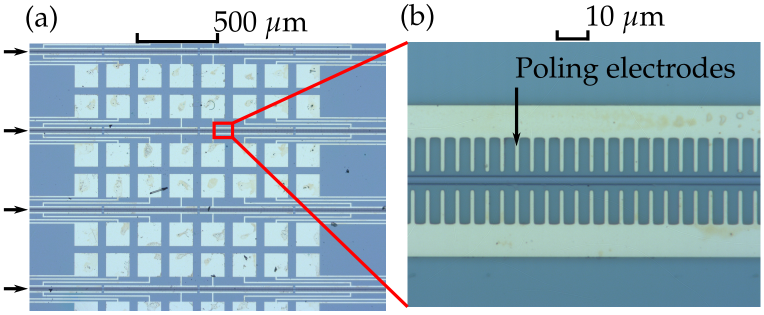

Figure 2.5: (a): Picture of a part of the device. the gold squares are contact electrodes for the external electrical signal. (b): zoom-in on a waveguide with two combs of electrodes around the waveguide used for poling.

2.2.1.2 Spontaneous parametric down-conversion in a periodically-poled thin-film lithium niobate waveguide

The process of photon pair generation in a second-order non-linear material has been described in Section 2.1.1. We recall here the condition for achieving quasi-phase-matching (QPM) presented in Eq. 2.3

$$\vec{k_p} = k_i + k_s + \frac{2\pi}{\Lambda_{\text{poling}}}. \tag{2.27}$$

As shown in Table 2.4, three poling periods are designed in the sample, which restricts the phase-matching possibilities. However, as the wavevectors's magnitude is temperature-dependent, it is possible to tune the temperature to gain flexibility in choosing the parameters for the pump, signal, and idler. In this section, we present the optimization of the poling period, and sample temperature, enabling the degenerate photon pair generation at telecom wavelength, from a pump laser situated at 780.24 nm.

Directly tuning the parameters based on the generated SPDC signal is challenging due to the extremely low generated power compared to the input pump. To overcome this difficulty, we use second-harmonic generation (SHG), which must satisfy the same phase-matching conditions. We wish to generate the photons using a pump laser Eylsa, from Quantel, operating at a fixed wavelength of 780.24 nm, and thus producing degenerate photons around 1560.48 nm. In this regard, we optimize the waveguide parameters for the second harmonic generation at 780.24 nm from a pump at 1560.48 nm. Fig. 2.6.(a) shows the setup used for second harmonic generation. A CW tunable laser at telecom wavelength (Tunics T100r) is modulated in intensity by a carrier wave at 80 KHz. This modulation enables the detection of the low-intensity SHG signal using a lock-in amplifier. The laser is then power-controlled using an erbium-doped fiber amplifier (FA) followed by a variable optical attenuator (VOA). The power is monitored using a 1:99 beam splitter, where the 1% is directed to a power meter. The polarization of the pump laser is controlled by a polarization controller. The light is coupled into and out of the waveguide using a microlensed fiber. A passive resistive heater is used to control the temperature of the sample. A collimator AR coated at 780 nm couples light out of the fiber. The second harmonic is separated from the fundamental pump by a dichroïc mirror (DM), before reaching a photodiode Newport 1801. The signal received by the photodiode is then mixed with the 80 kHz reference modulation signal from the laser and measured by the lock-in amplifier. While scanning the wavelength of the pump laser, we measure the second-harmonic intensity. Fig. 2.6.(b) shows a typical SHG spectrum. To find the parameters optimizing SHG at 780.24 nm, we measure the central wavelength of the SHG spectrum as a function of the tuning parameters.

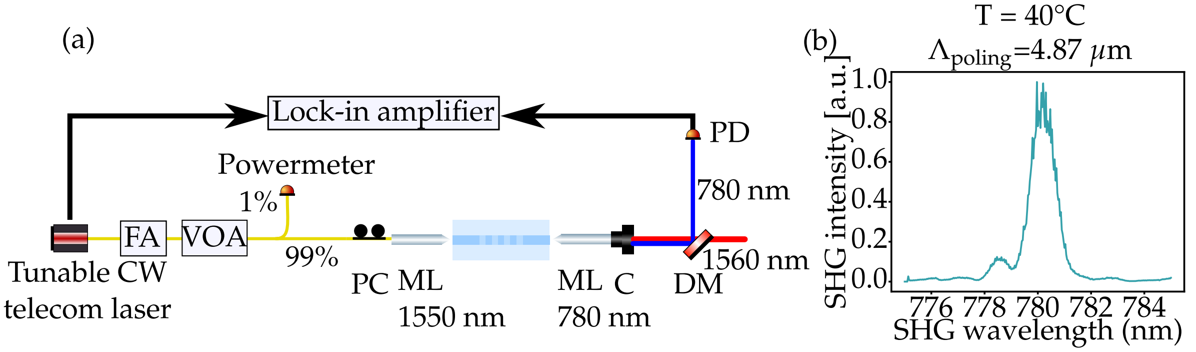

Figure 2.6: (a):Setup for the second harmonic generation. FA: fiber amplifier, VOA: variable optical attenuator, PC: polarization controller, ML: microlensed fiber, C: collimator, DM: dichroïc mirror. (b): Typical SHG spectrum.

Fig. 2.7.(a) shows the measured SHG maxima as a function of Λ_{poling}. The SHG wavelength variations are fitted with linear regression, showing an increase of 19 nm per 0.1 μm of the poling period. A poling period of 4.87 allows SHG close to 780 nm. Choosing this particular poling period, we vary the temperature to observe the behavior of the SHG spectrum. Results are shown in Fig. 2.7.(b). The SHG wavelength increases with the temperature, with a variation of 0.3 nm/C°. Increasing the waveguide temperature to 53°C allows us to tune the SHG wavelength to the desired value of 780.24 nm.

It is worth noting that by cooling the sample, it would be possible to generate SHG using the other available poling periods. For Λ_{poling} = 4.93 μm which is the next accessible poling period, at 40°C, the SHG wavelength is 787.71 nm. Achieving second harmonic generation at 780.24 nm would require cooling the waveguide at a temperature T = -6 °C and a more complex infrastructure.

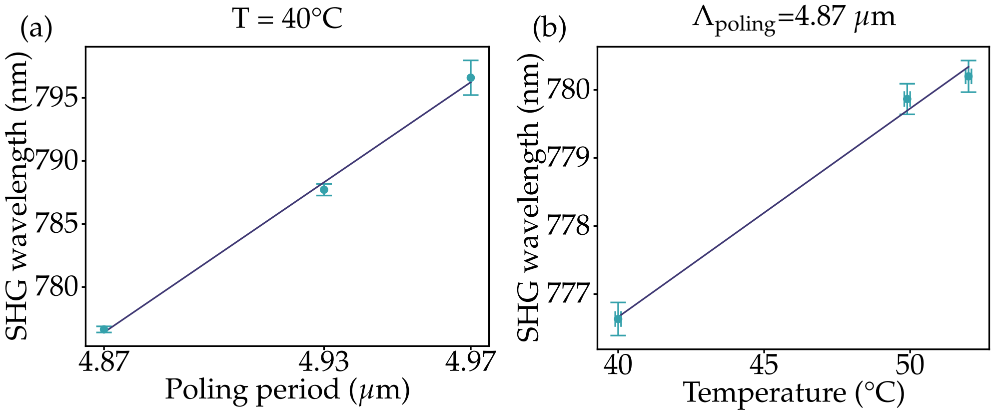

Figure 2.7: Central wavelength of the SHG spectrum for (a): the three available poling periods for waveguides at a temperature of 40°C, and (b): three waveguide temperatures a poling period Λ_{poling}=4.87 μm.

The poling length was not studied here as it is not a critical parameter for tuning the second-harmonic generation. However, a longer poling length leads to a more efficient generation [140] up to a certain saturation limit. We use the longest poling length available. To achieve SHG at 780 nm, we therefore use the parameters described in Table 2.5. We obtain the second-harmonic efficiency by computing the ratio of the second harmonic and fundamental wave power, correcting from losses throughout the setup, and find a maximum value of 230 %.W^{-1}.cm^{2}.

Λ_{poling} (μm)	L_{poling} (μm)	T (°C)
4.87	4800	53

Table 2.5: Poling and temperature parameters used for SPDC with LNOI waveguides.

Having optimized the phase matching condition for second harmonic generation at 780.24 nm, we now investigate spontaneous parametric down-conversion starting from this wavelength.

Fig. 2.8 shows the setup used to observe the SPDC spectrum with an optical spectrum analyzer. A laser Eylsa Quantel, emitting light at 780.24 nm, is power-controlled with

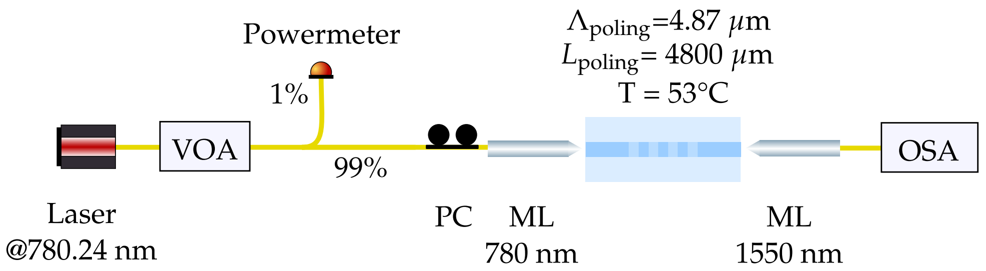

Figure 2.8: Setup for the measurement of the SPDC spectrum. VOA: variable optical attenuator, PC: polarization controller, ML: micro lensed fiber, OSA: optical spectrum analyzer.

the help of a variable optical attenuator and monitored with a 1:99 beam splitter. Before the waveguide, the polarization is controlled using paddles. Light is coupled into and out of the waveguide using a microlensed fiber. The generated SPDC spectrum is filtered by two RG1000 filters, that suppress the pump wavelength and is then directed to a Princeton Instrument spectrometer. Fig. 2.9 shows the results of the experiment at three different sample temperatures: $T = 53°\text{C}$, $T = 65°\text{C}$, $T = 80°\text{C}$. As expected from

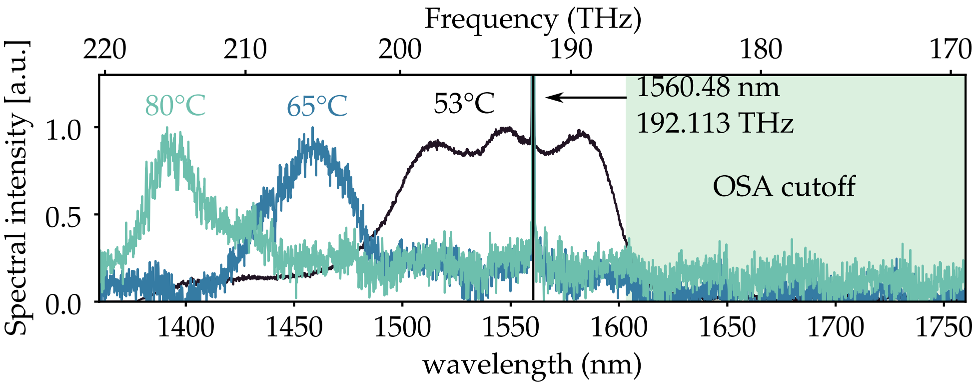

Figure 2.9: Normalized measured SPDC spectra for sample temperatures T=53, 65, and 80 °C. The black vertical line shows the degeneracy point.

the SHG measurements, the degeneracy point is found at 53°C at twice (half) the pump wavelength (frequency), i.e.: 1560.48 nm (192.113 THz). For the non-degenerate photon pairs obtained at higher temperatures, we can only measure the signal photon due to detector cutoff.

In Section 2.3, we characterize the efficiency and quality of this photon pair source.

2.2.2 Silicon-On-Insulator micro-resonator

In this section, we explore photon pair generation in a silicon-on-insulator micro-resonator. We describe the micro-resonator structure, followed by a characterization of its spectral properties. This characterization includes an analysis of the resonance modes, their linewidth and quality factor, and measurement of the free spectral range. Then, we explore the broadband photon pairs emission and compare it to the previously measured characteristics of the resonator.

2.2.2.1 Description and characterization of the resonator and parameter optimization

This silicon-on-insulator micro-resonator was designed at C2N and fabricated at ST microelectronics. A 3D representation of the sample is shown in Fig. 2.10. The resonator is designed in a folded configuration to limit the footprint of the device to below 0.05 mm^2, and the shape of the curves has been optimized to limit the bending loss. Grating couplers present at both ends of the bus waveguide couple light in and out of the sample. The waveguides consist of an etched layer of silicon with a height of 300 nm over a 350 nm layer of buried oxide layer. The 700 nm width of the waveguides has been chosen to reach the anomalous dispersion regime and achieve a zero dispersion. The bus waveguide is evanescently coupled to the cavity on a length of 10 μm.

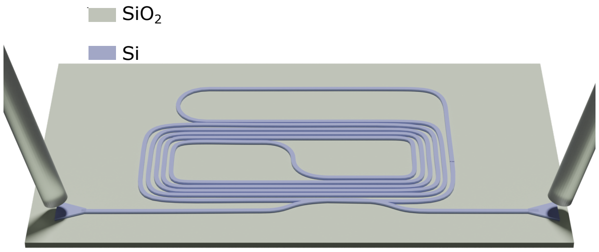

Figure 2.10: 3D drawing of the micro-resonator. Fibers couples light in and out of the bus waveguide through grating couplers. The bus waveguide is evanescently coupled to a folded cavity.

We measure the spectrum of the cavity using the setup described in Fig. 2.11.(a). The spectral analysis is performed using a tunable laser injected into the bus waveguide through the input grating coupler, from 1526.83 nm to 1554.12 nm with a 1 pm resolution. Light is outcoupled into fiber through the output grating coupler of the bus waveguide, and measured on a powermeter HP437B. As the laser tunes on a cavity mode, light couples into the ring, resulting in a drop of the signal measured by the photodetector. Fig. 2.11.(b). shows a portion of the spectrum, from 1537 nm to 1543 nm.

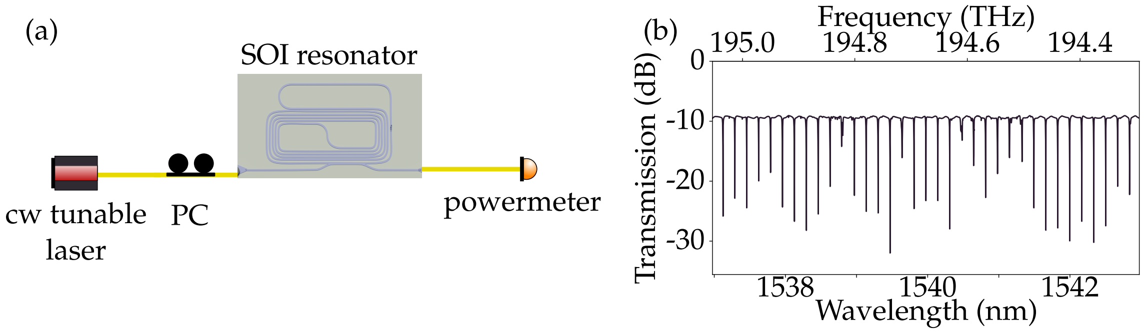

Figure 2.11: (a): Experimental setup and (b): Measured transmission spectrum of the cavity.

Looking individually at each cavity mode, we can examine their respective characteristics. We fit each resonance with a Lorentzian function to measure the full-width-half-maximum (FWHM) Δf, and central frequency f_0 as

$$L(f, f_0, \Delta f) \propto \frac{\Delta f}{(f - f_0)^2 + \Delta f^2}. \tag{2.28}$$

Fig. 2.12 shows an example of a Lorentzian fit on a cavity mode centered at 1537.974 nm. The measured resonance linewidth Δf can then be used to compute the external quality

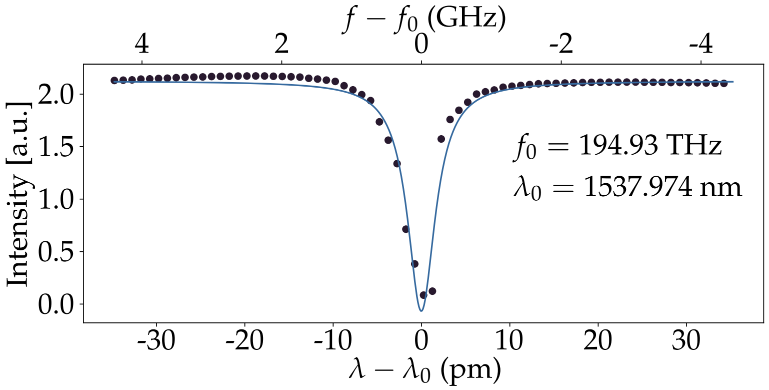

Figure 2.12: Lorentzian fit of a measured cavity mode.

factor for each cavity mode as

$$Q = \frac{f_0}{\Delta f}. \tag{2.29}$$

Fig. 2.13.(a) shows the measured FWHM, with a mean value of 430 ± 240 MHz. Fig. 2.13.(b) the corresponding quality factors. The values vary from 2×10^5 to 8×10^5, with a mean quality factor around 1540 of $4.75\text{x}10^5$.

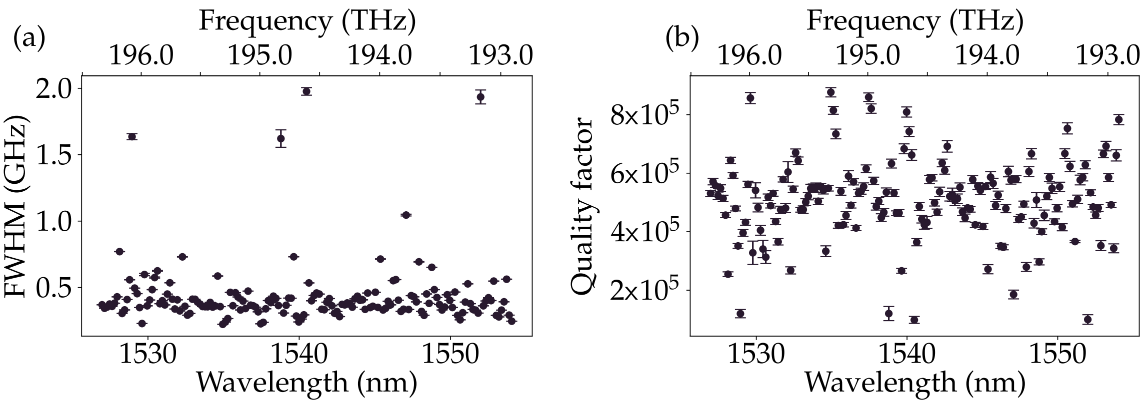

Figure 2.13: (a): Measured FWHM of the cavity modes. (b): Corresponding quality factors.

We then measure the free spectral range (FSR), spectral spacing between two adjacent cavity modes, linked to the cavity perimeter L, expressed in frequency as

$$FSR = \frac{c}{n_g L}. \tag{2.30}$$

Where c is the speed of light, and n_g is the group index of the waveguide. The cavity was designed with a perimeter $L = 3.54$ mm, targeting an FSR of 21 GHz. Experimentally, we measure the FSR by looking at the difference in wavelength or frequency of two consecutive modes n and n+1. Taking into account its significance in frequency units for our subsequent analysis, we measure the FSR as

$$FSR = f_{n+1} - f_n. \tag{2.31}$$

Fig. 2.14 shows the measured free spectral range as a function of the wavelength. The solid black line shows the mean value of the FSR of 21.25 GHz. The shaded green area highlights the region where the FSR remains within a deviation from its mean value of less than the mean cavity linewidth of 0.43 GHz, encompassing 85% of all the FSR values.

In the next section, we discuss the SFWM process in this structure. We investigate how the measured properties of the ring influence the photon pair emission.

2.2.2.2 Spontaneous four-wave-mixing in a silicon-on-insulator micro-resonator

In Section 2.1.2, we introduced SFWM and discussed the energy conservation relation and phase matching conditions. SFWM generates a pair of signal-idler photons, with their frequencies symmetrically distributed around a degeneracy frequency ω_d, equal to

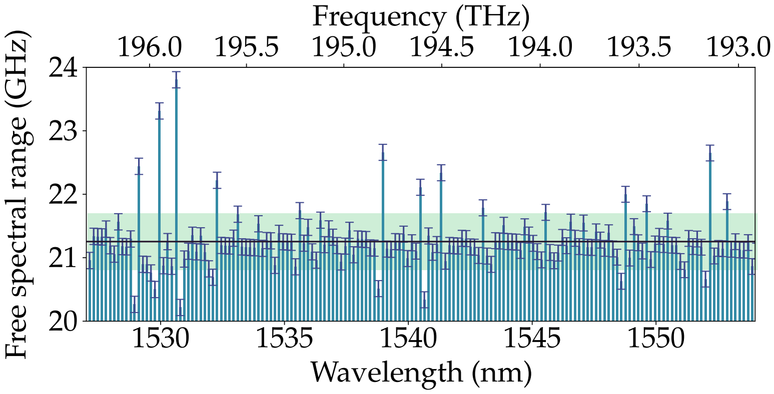

Figure 2.14: Free-spectral range as a function of the optical wavelength and frequency. the solid black line represents the mean free spectral range = 21.25 GHz.

the pump frequency ω_p. These signal and idler photons can be emitted at frequencies $\omega_d - \omega$ and $\omega_d + \omega$. However, in our case, photon pair generation takes place within a micro-resonator characterized by a discretized spectrum. In this context, the pump is tuned to a cavity mode, and the signal and idler photons are emitted on frequency modes $|I_N\rangle$ and $|S_N\rangle$ and defined as

$$\begin{aligned} |I_N\rangle &= |\omega_d - 2\pi N \times FSR\rangle \\ |S_N\rangle &= |\omega_d + 2\pi N \times FSR\rangle . \end{aligned} \tag{2.32}$$

where $N \in \mathbb{N}^*$. Each signal and idler mode corresponds to a resonator mode symmetrically positioned with respect to the pump frequency mode, as illustrated in Fig. 2.15. The two-photon state generated by the micro-resonator cavity is then represented as

$$|\phi\rangle = \sum_{N=1}^{D} A_N e^{i\alpha_N} |I_N, S_N\rangle , N \in \mathbb{N} \tag{2.33}$$

where D is the maximum value of N, limited by either the bandwidth of the devices or the phase matching, and α_N is defined as the biphoton phase associated with each eigenstate $|I_N, S_N\rangle$ [76]. The coefficients A_N correspond to the probability amplitudes of finding a photon pair in the N$^{\text{th}}$ signal-idler eigenstate related to the quality factor and the symmetry between signals and idler, which in turn depends on the fluctuations of the FSR. In this section, we measure the photon pair generation for several $|I_N, S_N\rangle$, and correlate the measurement with the spectral properties of the resonator previously measured.

Our analysis begins by investigating the number of spontaneously emitted photons in each reachable frequency mode $|I_N\rangle$ or $|S_N\rangle$ and comparing them with the quality factors of the corresponding frequency resonances defined as Q_I^N or Q_S^N. Subsequently, we assess

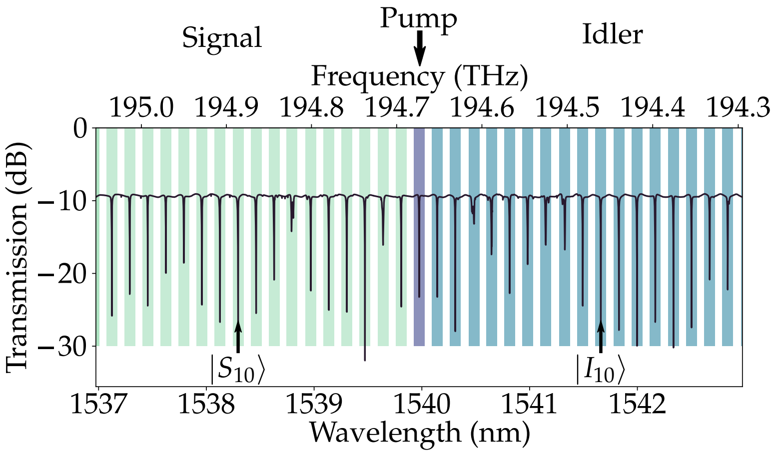

Figure 2.15: Solid line : transmission spectrum from Fig. 2.11. The purple bar corresponds to the cavity mode on which the pump is tuned. The blue(green) bars correspond to the cavity modes on which the idler(signal) photons are generated.

the number of correlated signal and idler emitted in symmetrical $|I_N\rangle$ and $|S_N\rangle$ modes. This evaluation involves comparing the joint detection of two signal and idler photons in each eigenstate $|I_N, S_N\rangle$, with both Q_S^N and Q_I^N, as well as considering the symmetry between the frequencies of the $|I_N\rangle$ and $|S_N\rangle$ modes relative to the degeneracy frequency ω_d. We introduce the frequency $\delta\omega_N$ mismatch between each $|I_N\rangle$ and $|S_N\rangle$ as

$$\delta\omega_N = \omega_i + \omega_s - 2\omega_d, \tag{2.34}$$

where ω_i and ω_s are the central frequencies of two symmetric signal and idler modes, derived from the measured transmission spectrum of Fig. 2.15. We compare the measured number of signal-idler pairs using

- The product of the quality factors of correlated signal and idler $Q_I^N \times Q_S^N$
- A figure of merit associated with the difference in frequency $f_{diff}^N = 1 - \frac{\delta\omega_N}{\max \delta\omega_N}$
- The product of both aforementioned factors $Q_I^N \times Q_S^N \times f_{diff}^N$

We perform these characterizations using the setup described in Fig. 2.16(a). The pump consists of a tunable tunics laser T100r tuned on cavity mode ω_p= 1540 nm (194.67 THz), with a nominal power of 10 mW, leading to an on-chip power of 1.1±0.2 mW. A bandpass filter suppresses the spontaneous emission from the laser with an exfo XTM-50 bandpass filter (BP). The filtered laser inputs the bus waveguide from a flat-cleaved fiber through a grating coupler. The photons generated in the resonator exit the chip to a flat-cleaved fiber via the output grating coupler. We set the angle of the fiber of 15° to the vertical axis to maximize transmission at 1540 nm. Two notch filters from AOS suppress the pump laser light from the output signal. The characteristics of the notch filter are given in Appendix B.2. A tunable programmable filter (PF) WaveShaper 4000A from Finisar selectively isolates an idler and a signal cavity mode ($|I_N\rangle$ and $|S_N\rangle$) by applying two bandpass filters with a 21 GHz bandwidth (see Fig. 2.16(b)) and separates them by sending them into distinct fibers. The PF also serves as a pump rejection filter. Altogether, the notch filters and the PF allow a pump rejection larger than 100 dB. A 900 nm notch filter eliminates undesired calibration light coming from the PF. The photons are detected with SNSPDs from Single Quantum. We process the measured counts and coincidences with a time tagger Ultra from Swabian Instruments.

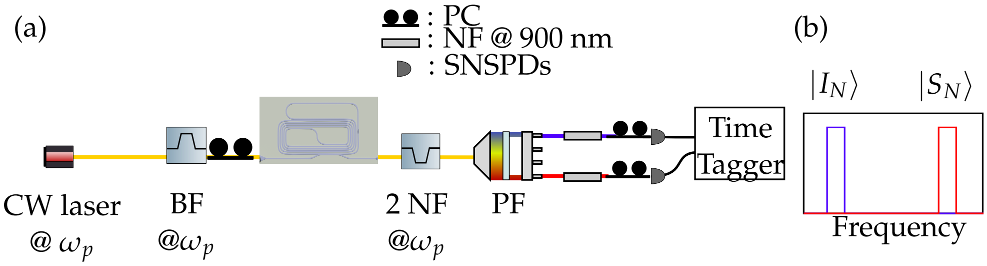

Figure 2.16: (a): Setup for detecting single counts and coincidences from the SOI microresonator. BP: bandpass filter, NF: notch filter, PC: polarization controller. (b): The programmable filter applies two 21 GHz bandpass filters to select specific signal and idler mode $|I_N\rangle$ and $|S_N\rangle$. The two photons are then spatially separated into two distinct fibers.

Fig. 2.17 shows the measured number of single counts in all frequency modes. The single photon emission is maximal near the pump and decreases as we move away from degeneracy. We observe up to 50% variations in the measured photon rates. In Fig. 2.18, we then correlate the results with the corresponding quality factors, which also exhibit strong variations. The comparison confirms that the frequency modes with the lowest quality factors are also the ones with fewer single counts.

We now compare the emission of two-photon coincidences associated with each signal idler pair $|I_N, S_N\rangle$. We count as coincidences two signal and idler photons detected within a coincidence window of 1 ns.

Fig. 2.19 shows the coincidence for the generated state $|\phi\rangle$ projected on the eigenstates $|I_N, S_N\rangle$, for N=3 to 83. As for the single photon spectrum, we observe a maximal number of coincidences for signal-idler pair near the degeneracy and decreasing as N increases. As mentioned earlier, we wish to compare the coincidences with the quality factors, and signal idler frequency-mismatch. Figure 2.20 presents the experimentally measured values of $\delta\omega_N$. For most signal-idler pairs, $\delta\omega_N$ is close to 0, indicating a good degree of symmetry. However, as N increases, the frequency difference increases, implying that the

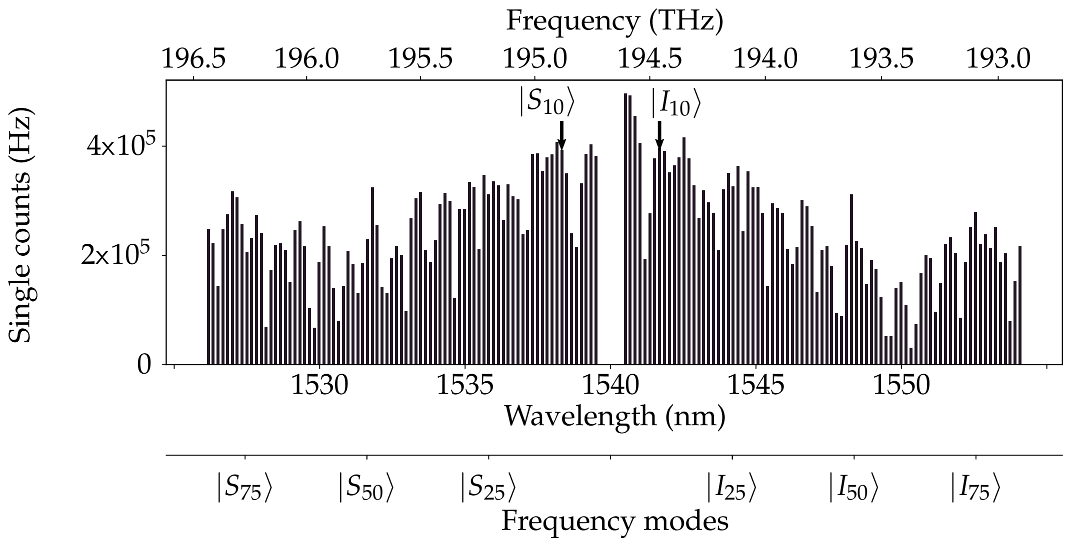

Figure 2.17: Measured single count rate for each cavity mode. as a function of the frequency, wavelength, and signal and idler frequency modes.

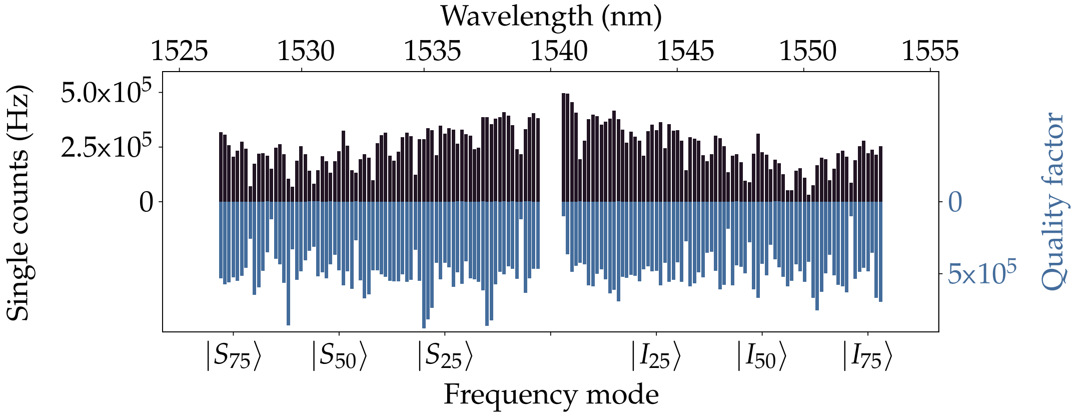

Figure 2.18: Black bars: single counts measured for cavity modes N compared to the pump cavity mode N_P. Blue bars: corresponding Q factors.

resonance frequencies ω_i and ω_s are not entirely symmetrical.

Fig. 2.21 finally compares the coincidences with various properties of the resonator: Fig. 2.21.(a), the product of the quality factors, Fig. 2.21.(b,) the figure of merit for the detuning f^N_{diff}, and finally, Fig. 2.21.(c) the product of the two previous indicators, showing a very clear correlation.

This figure shows that the quality factor of the resonances and the fluctuation of the free

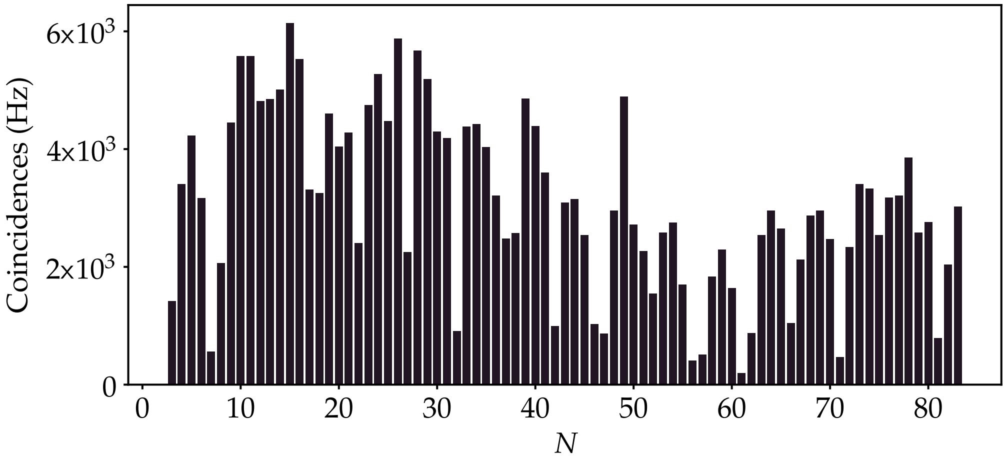

Figure 2.19: Measured two-photon coincidences as a function of N going from 3 to 83.

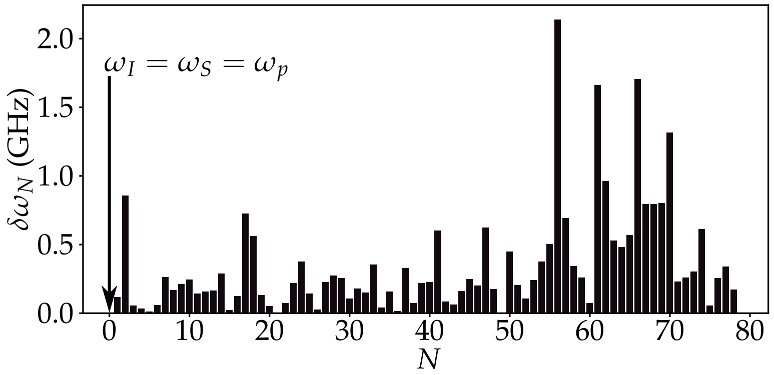

Figure 2.20: Detuning between the signal and idler frequency modes as a function of the spacing from the pump resonance.

spectral range play a great role in the photon pair generation process in the cavity. For the experiments involving the micro-resonator, the difference in coincidence rate between two signal idler pairs affects the quality of the generated frequency-bin entangled state. The results allow us to identify the resonator parameters that should be optimized for quantum information processing applications. Our structure allows the emission of photon pairs on more than 70 narrow signal-idler frequency modes.

In the next section, we focus on characterizing the two photon pair sources. We first investigate the efficiency of the photon pair emission by estimating the number of generated pairs, heralding efficiency, and internal brightness of the two previously introduced photon pair sources. Then, we investigate the statistics of the sources by examining the single

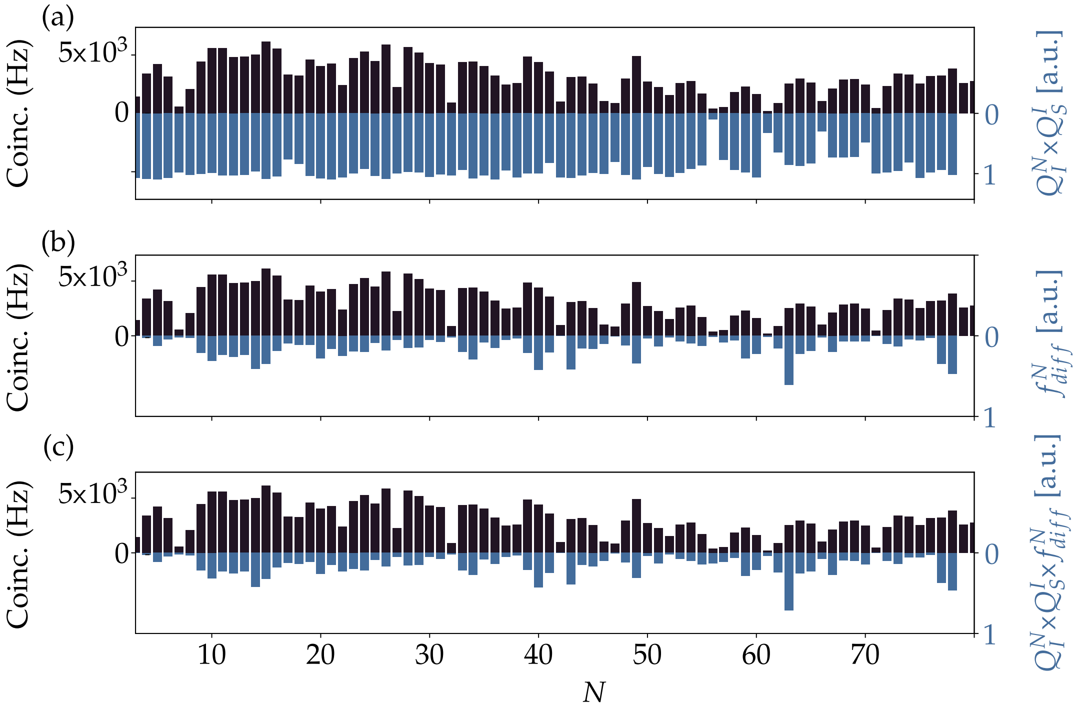

Figure 2.21: Correlation between the measured coincidences as a function of N and (a): the product of the quality factors of the signal and idler cavity modes, (b) the detuning between signal and idler frequencies, (c): the product of the quality factors and the detuning.

photon purity and spectral purity.

2.3 Heralded single-photon sources

The emission of a photon pair source can be characterized by the following

- The number of generated pairs N_p as a function of input power
- The number of detected pairs, compared to the number of single counts from which we can derive the signal and idler heralding efficiency γ_I and γ_S.
- The normalized internal Brightness B, enabling the comparison of our photon pair sources to the state of the art, independently of the on-chip power and single photon bandwidth.

Each of these figures of merit is defined and assessed in Section 2.3.3. Working as heralded photon pair sources, two parameters are important:

- The single photon purity, assessing the number of photons heralded. This measurement is performed in section 2.3.4
- The spectral purity, assessing the number of frequency modes populated by the heralded photons. This measurement is performed in section 2.3.5

Before delving into these characterizations, we first present the experimental setup in section 2.3.1, and investigate the temporal correlations between the generated twin photons in section 2.3.2.

2.3.1 Experimental characterization setup

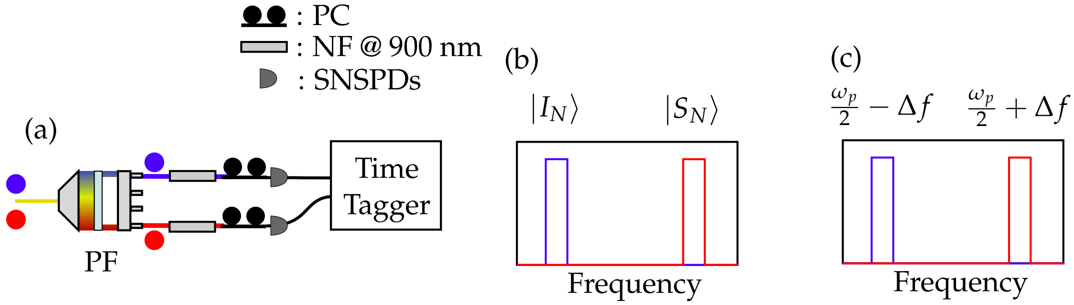

Figure 2.22: Experimental setup for the brightness measurement, PC: polarization controller, NF: notch filter, PF: programmable filter, SNSPDs: single photon detectors.

To perform the subsequent measurement, we use the setup described in Fig. 2.22. In order to spatially separate the two photons from a photon pair, we use wavelength demultiplexing, which is performed by a PF (see Fig. 2.23). The input bi-photon spectrum enters the PF, which applies symmetrical bandpass filters on the signal and idler part of the spectrum. The device then separates the filtered photons into two distinct outputs. For a continuous spectrum (Fig. 2.23.(a)), the filtering applied by the PF directly shapes the photons with the chosen bandwidth. For a comb spectrum (Fig. 2.23.(b)), the programmed filtering selects the modes to be transmitted. The bandwidth for a single transmitted mode is dictated by the linewidth of the cavity mode. For the subsequent experiments, we program the PF so that it applies filters with settings described in Table 2.6. The bandwidth of 21 GHz ensures to select a single cavity mode for the SOI micro-resonator. The bandwidth of 160 GHz for the LNOI waveguide is chosen arbitrarily.

After the filtering stage, the separated signal and idler photons are directed into two superconducting single-photon detectors from single quantum, and the single counts and coincidences are computed using a time tagger from Swabian instrument.

The next section investigates the signal-idler temporal correlations.

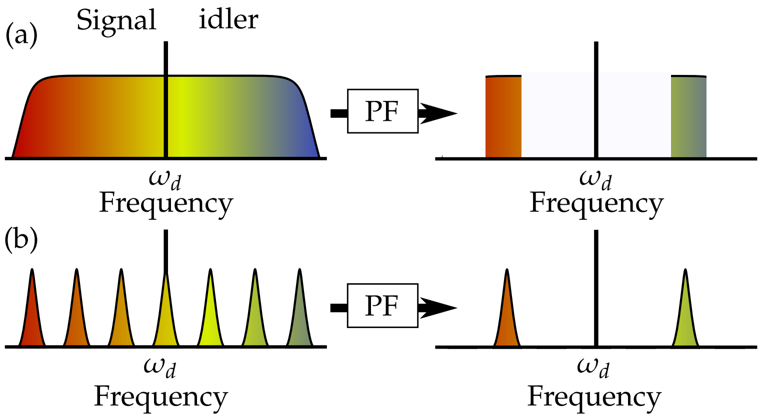

Figure 2.23: Filtering performed by the PF for (a): a continuous photon-pair spectrum and (b): a frequency-comb spectrum. The PF then outputs the filtered signal and idler in two distinct outputs.

Source	Central frequencies	Filter bandwidth	Single photon bandwidth
LNOI	192.113±0.8 THz	160 GHz	160 GHz
SOI	194.670±15×FSR THz	21 GHz	0.43 GHz

Table 2.6: Setting of the filters applied by the programmable filter and final bandwidth of the photons generated by the LNOI waveguide and the SOI micro-resonator.

2.3.2 Temporal correlation of photon pairs and choice of the coincidence window

The detection of two correlated signal and idler photons results in coincident detection on two detectors. However, the signal and idler are generated together within a coherence time of the photon wavepacket, τ_c, directly linked to the spectral bandwidth δf of the photons as [141]

$$\tau_c = \frac{1}{\pi\delta f}. \tag{2.35}$$

A coincident detection of correlated signal and idler can thus happen with a relative delay within this coherence time. To account for this, we define a coincidence window, t_{cw}: two events recorded within this time window will be considered as a coincidence, as shown in Fig. 2.24.

To measure the coherence time, and determine the coincidence window, we measure time histograms based on the time interval between the detections of the two photons. The timing of the detected click is limited by the electronic jitter of both the detector and the time tagger, summing up to 120 ps. Fig. 2.25 shows the time delay histogram between the detection of a signal and idler photon, generated from (a): The SOI micro-resonator and (b): the LNOI waveguide, where events are binned in time bins of 20 ps. One noticeable aspect is the difference in the temporal width between Fig. 2.25.(a) and Fig. 2.25.(b), mostly due to their different spectral bandwidth, c.f. Table 2.6. The SOI micro-resonator exhibits, as expected, a coherence time of 530 ps, which is larger than the system jitter. We observe therefore the Lorentzian temporal shape, corresponding to the Fourier transform of the cavity mode's Lorentzian spectral shape. For photons generated by the LNOI waveguide, the 160 GHz bandwidth results in an expected coherence time of 2 ps, one order of magnitude smaller than the combined jitter of the devices. In this case, the coincidence window is determined by the resolution of the measurement system.

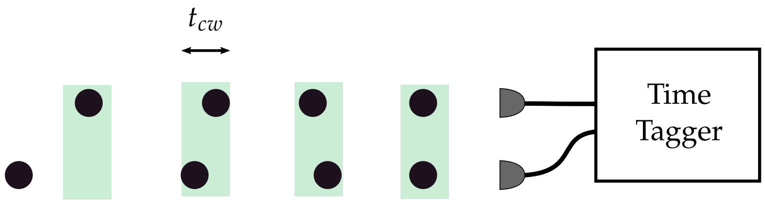

Figure 2.24: Principle of the measure of the relative time between two detectors.

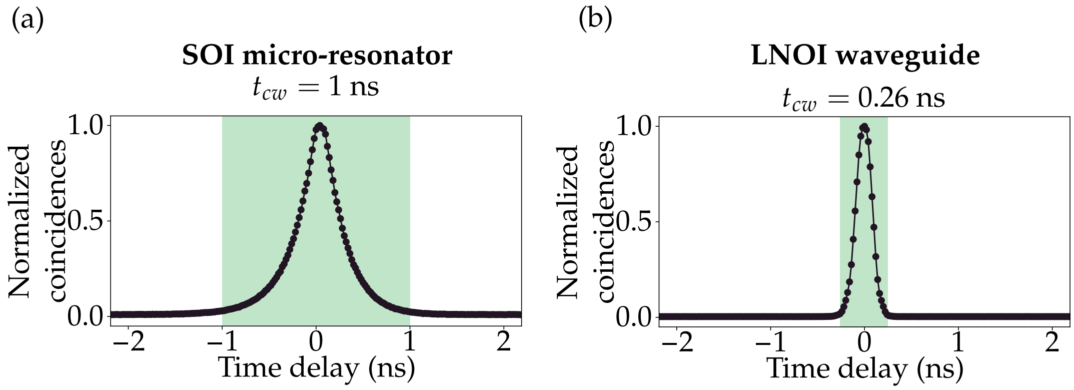

Figure 2.25: Normalized histogram of the relative arrival time of photons at the signal and idler detectors for (a): the SOI micro-resonator and (b): the LNOI waveguide.

The time width of the coincidence window t_{cw} is thus not the same for the two sources and is listed in Table. 2.7. Throughout this manuscript, we keep these values of coincidence windows.

Source	t_{cw} (ns)
SOI	1
LNOI	0.26

Table 2.7: Time width of the coincidence window t_{cw} for the SOI resonator and LNOI waveguide.

2.3.3 Relation between photon pairs and heralded single photon performances

The photon pair sources yield an average rate of N_P pairs per second. Each signal and idler photon goes through an optical system characterized by respective transmission γ_I and γ_S [1], and are detected with efficiencies η_I and η_S. In addition to the photons originating from the pairs, the detectors can register background counts, represented as BC_I and BC_S. The photons detected by respective detectors D_I and D_S are [127]

$$\begin{aligned} D_I &= \gamma_I \eta_I N_P + BC_I, \\ D_S &= \gamma_S \eta_S N_P + BC_S. \end{aligned} \tag{2.36}$$

Subtracting the background counts we access the signal and idler counts N_I and N_S

$$\begin{aligned} N_I &= \gamma_I \eta_I N_P \\ N_S &= \gamma_S \eta_S N_P. \end{aligned} \tag{2.37}$$

Losses impact the measured counts and coincidences. A single photon detected by one detector may not lead to coincidences if its twin is lost. The average number of coincidences per second N_C is written as a function of transmission, detection efficiency, and N_P as [127]

$$N_C = \gamma_I \gamma_S \eta_I \eta_S N_P. \tag{2.38}$$

Fig. 2.26 and 2.27 show the measured single counts (a) and coincidences (b), respectively, for the LNOI resonator and SOI waveguide. We observe that the measured quantities evolve linearly as a function of the power for photons generated by the LNOI and quadratically for the photons generated from the SOI resonator. To estimate the on-chip power, we compute the loss from the laser source to the chip using the transmission of the fiber elements and the on-chip couplings. The on-chip coupling is 3.8 dB for the SOI micro-resonator and 13 dB for the LNOI waveguide.

In both measurements, the background count rate remains constant: $BC_I = BC_S = 800$ Hz, representing only 1% of the measured single count rate. The background noise level

---

[1] Please note that throughout this chapter, we refer to γ_i and γ_s as both the **transmission of the setup** and the **heralding efficiency**

remains negligible in the coincidence measurement, as a background count rate of 800 Hz for each detector results in background coincidences of 1×10^{-4} Hz and 6×10^{-4} Hz for coincidence windows of 1 ns and 0.23 ns, respectively.

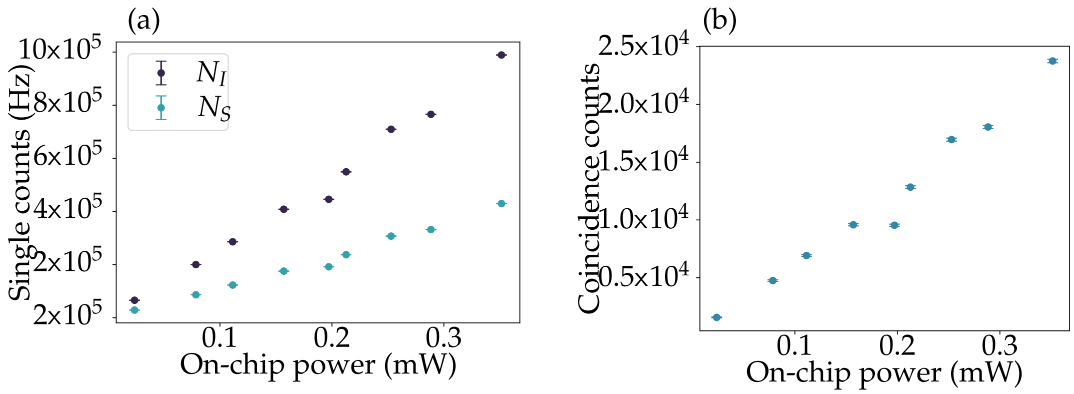

Figure 2.26: Measured (a): single counts and (b): coincidences from the signal-idler pair by the PPLN LNOI waveguide as a function of on-chip power.

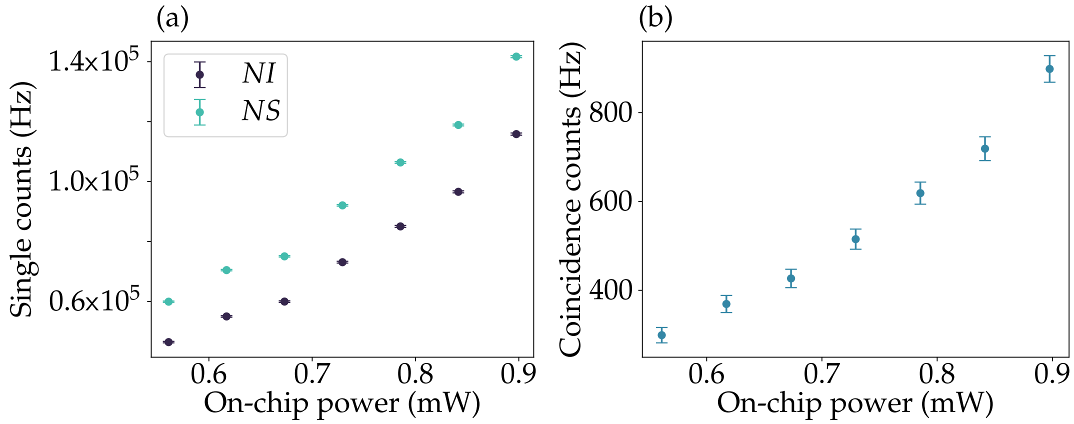

Figure 2.27: Measured (a): single counts and (b): coincidences from the signal-idler pair from the SOI resonator as a function of on-chip power.

The heralding efficiencies γ_I and γ_S can be deduced by two methods: (i) by measuring the insertion loss of each optical component of the setup, and (ii) through the numbers of single counts and coincidences as :

$$\begin{aligned} \frac{N_C}{N_S} &= \frac{\gamma_I \gamma_S \eta_I \eta_S N_P}{\gamma_S \eta_S N_P} = \gamma_I \eta_I \Rightarrow \gamma_I = \frac{N_C}{N_S \times \eta_I} \\ \frac{N_C}{N_I} &= \frac{\gamma_I \gamma_S \eta_I \eta_S N_P}{\gamma_I \eta_I N_P} = \gamma_S \eta_S \Rightarrow \gamma_S = \frac{N_C}{N_I \times \eta_S} \end{aligned} \tag{2.39}$$

Detector efficiencies Sample	η_I	η_S
SOI	0.7 ± 0.03	0.7 ± 0.03
LNOI	0.7 ± 0.03	0.3 ± 0.03

Table 2.8: Efficiency of the signal and idler detectors for experiments realized with the LNOI waveguide and SOI micro-resonator.

The results of the two measurements of γ_I and γ_S are compared in Table 2.9, with a good agreement. As we observe from the table, there is an order of magnitude difference between the resonator and the waveguide, due to the ring-to-waveguide coupling of the SOI micro-resonator.

Based on the measurement shown in Figure 2.19, we expect higher coincidence rates than what was measured in Fig. 2.27 for a similar on-chip power. This is attributed to additional experimental loss, mainly due to the mechanical alignment of the coupling fibers. Comparing the expected number of counts to the one measured in Fig. 2.27 for a similar on-chip power, we found that the transmission was reduced by a factor of $\frac{145000}{345000} \approx 0.41 \pm 0.02$. This excess loss caused a 0.16 ± 0.02 reduction in the expected coincidences, which matches our observation.

	SOI resonator	**LNOI waveguide**
Output coupling	-3.7 ±0.1 dB	-5.6 ±0.1 dB
PF	-3.3±0.2 dB	-3.3 ±0.2 dB
Additional setup losses	-1.5±0.5 dB	-1.5 ±0.5 dB
Resonator-waveguide coupling (idler ; signal)	-11.79 ; -13.78 ±0.2 dB	-
$\mathbf{10 \times \log_{10}(fl_I)}$ **;** $\mathbf{10 \times \log_{10}(fl_S)}$ from loss budget	**-20.29 ; -22.2 ±0.9 dB**	**-10.3 ± 0.8 dB**
$\mathbf{10 \times \log_{10}(fl_I)}$ **;** $\mathbf{10 \times \log_{10}(fl_S)}$ from single counts and coincidences	**-20.9 ; -19.9 dB ± 1.2**	**-11.02 ; -10.96 ±1.2 dB**

Table 2.9: Comparison between the values of γ_I and γ_S for the two sources, derived either from the loss budget or from counts and coincidences.

We now access the generated number of pairs through the measured single counts and coincidences as [127]

$$N_P = \frac{N_I \times N_S}{N_C} \tag{2.40}$$

As it is independent of the setup transmission and detector efficiency, no correction is

---

[1] Please note that the measurement with the LNOI waveguide was made first and that one detector was upgraded before measuring with the SOI micro-resonator.

needed to access the N_P. Fig. 2.28 shows the number of generated pairs N_P for (a): the LNOI waveguide and (b): the SOI micro-resonator. The number of pairs generated on the chip depends on input power and single photon bandwidth. To compare the efficiency of our source with other works, we use the internal brightness B. The definition of B differs for SPDC and SFWM due to distinct power scaling in these processes. They are defined as follows

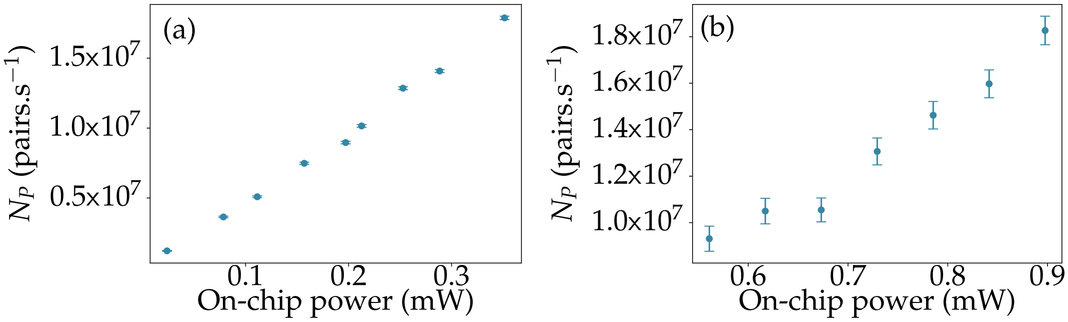

Figure 2.28: Generated number of pairs per second N_P as a function of the input power for (a): the LNOI waveguide and (b): the SOI micro-resonator.

$$\begin{aligned} B_{\text{SPDC}} &= \frac{N_P}{\delta f \times P_{pump}}, \text{ [pairs.s}^{-1}\text{.mW}^{-1}\text{.GHz}^{-1}\text{]} \\ B_{\text{SFWM}} &= \frac{N_P}{\delta f \times P_{pump}^2}, \text{ [pairs.s}^{-1}\text{.mW}^{-2}\text{.GHz}^{-1}\text{]} \end{aligned} \tag{2.41}$$

Where P_{pump} is the on-chip power and δf is the bandwidth of the photons, that can be found for both sources in Table 2.6

Work	B_{SPDC} (pairs.s^{-1}.mW^{-1}.GHz^{-1})
Zhao et al.[43]	4.6×10^5
Chen et al. [125]	5.6×10^5
Elkus e al. [42]	3.4×10^4
This work [41]	$(3 \pm 0.1) \times 10^5$

Table 2.10: [LNOI]: Comparison of normalized brightness between our source and several LNOI sources from in the literature.

While we cannot compare directly the two sources to each other, we compare the measured values to similar structures in the literature in the tables Table 2.10 and Table 2.11. The obtained brightness for the LNOI waveguide is of the order of magnitude of similar works in LNOI waveguide. For the Silicon resonator, we managed to reach some of the highest values of Brightness. This is partly due to the high-quality factor harnessed by our resonator, as shown in Table 2.11.

Work	B_{SFWM} (pairs.s^{-1},mW^{-2}GHz^{-1})	Q
Oser et al. [142]	5×10^5	3x10^4
Mazeas et al.[143]	1.6×10^6	4x10^4
Jiang et al.[144]	6.24×10^7	3.47/4.94x10^5
This work [78]	$(5.1 \pm 3) \times 10^7$	4.75x10^5

Table 2.11: [SOI]: Comparison of normalized brightness between our source and several SOI micro-resonator sources from in the literature.

2.3.4 Single photon purity

We defined earlier the second-order correlation function $g^{(2)}(\tau)$, and how its measurement enables us to distinguish between several classes of light sources. For a single photon source, we expect to measure $g^{(2)}(0) = 0$. We thus experimentally assess the $g^{(2)}(0)$ for our sources as heralded single photon sources. The experimental setup for performing this measurement is presented in Fig. 2.29. Photons are filtered and separated by a PF. One photon goes through a HBT interferometer, consisting of a fibered beam splitter, with one detector placed at each output. As our source is a heralded single-photon source, we herald the $g^{(2)}(0)$ measurement with the twin photon, directly routed to a third detector.

In this experiment, we record the single counts detected on the heralding detector (blue path) N_H and on the heralded detectors (red paths), N_{S1} and N_{S2} . Using the time tagger, we also record the two-photon coincidences between the heralding detectors and the signal photons leading to two figures: $N_{H,S1}$ and $N_{H,S2}$, and the three-photon coincidences between the herald, and the two signal detectors, leading to $N_{H,S1,S2}$ three-photon coincidences per second.

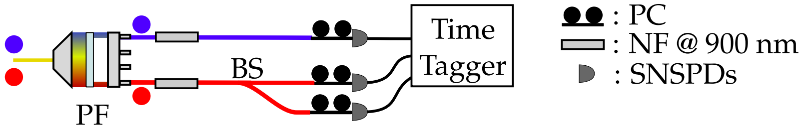

Figure 2.29: Setup for $g^{(2)}$ measurement. PF: programmable filter, BS: 50:50 beam splitter, PC: polarization controller, NF: Notch filters, SNSPDs: single photon detectors.

We use the method presented in [145, 146], where the value of $g^{(2)}(0)$ is expressed as

$$g^{(2)}(0) = \frac{2P_{n\geq 2}}{P_{n=1}^2}, \tag{2.42}$$

where $P_{n=1}$ and $P_{n\geq 2}$ are the probabilities that, given the detection of a heralding photon, n heralded single photons are detected. These probabilities are expressed as a function of the single and coincidence counts as [127, 146]:

$$\begin{aligned} P_{n=1} &= \frac{N_{H,S1} + N_{H,S2}}{N_H}, \\ P_{n\geq 2} &= \frac{N_{H,S1,S2}}{N_H}. \end{aligned} \tag{2.43}$$

Fig. 2.30 shows the variation of $P_{n=1}$ and $P_{n\geq 2}$ as a function of on-chip power for (a): the SOI micro-resonator, and (b): the LNOI waveguide. For both sources, there are four orders of magnitude of difference between the two probabilities. Furthermore, we observe that the probability $P_{n\geq 2}$ decreases faster than $P_{n=1}$ with decreasing power.

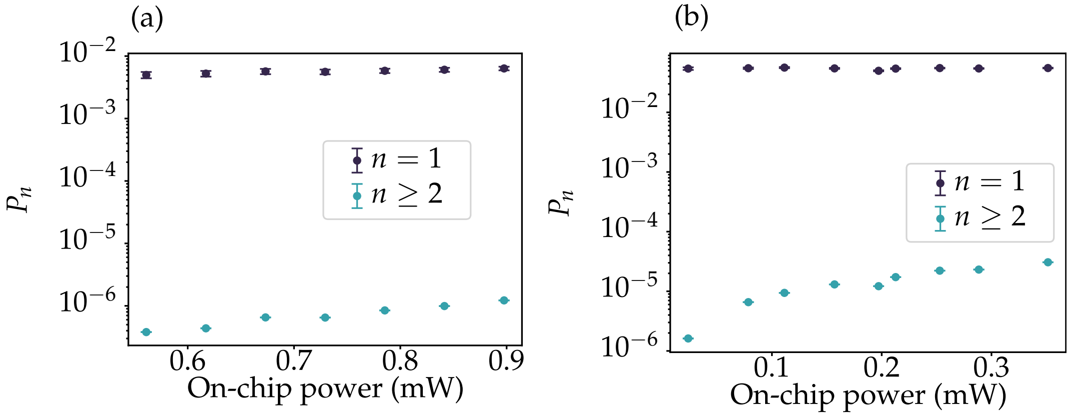

Figure 2.30: Measured probabilities to obtain n heralded photons for (a): the SOI micro-resonator and (b): the LNOI waveguide as a function of on-chip power.

Fig. 2.31 finally shows the measured values of the heralded $g^{(2)}(0)$ for the two photon pair sources. For both sources, the value decreases with decreasing power and can reach $g^{(2)}(0) = 0.03$. By measuring for lower power, it is possible to reach lower values, at the price of a lower heralded single-photon rate.

An interesting characterization is the comparison between the obtained values of the heralded $g^{(2)}(0)$ and the associated generated number of pairs N_P. We plot in Fig. 2.32 the measured $g^{(2)}(0)$ versus N_P divided by the single photon bandwidth δf, to compare the two sources.

2.3.5 Spectral purity

As discussed in Section 2.1.5, spectral purity is an important parameter of a heralded single-photon source. It measures the number of frequency modes populated by the heralded single photon, determined by the Schmidt number K. K can be obtained through a

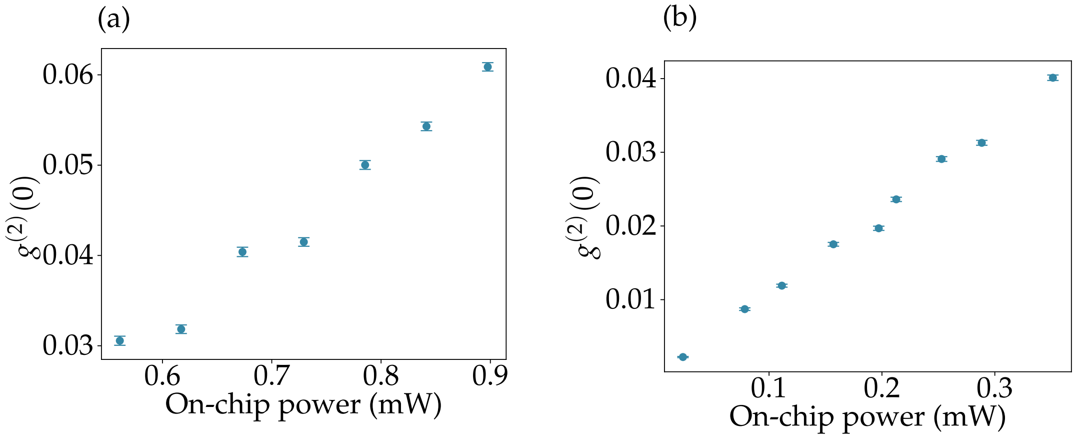

Figure 2.31: Experimental measurement of heralded $g^{(2)}(0)$ for (a): the SOI resonator and (b): the LNOI waveguides, as a function of on-chip power.

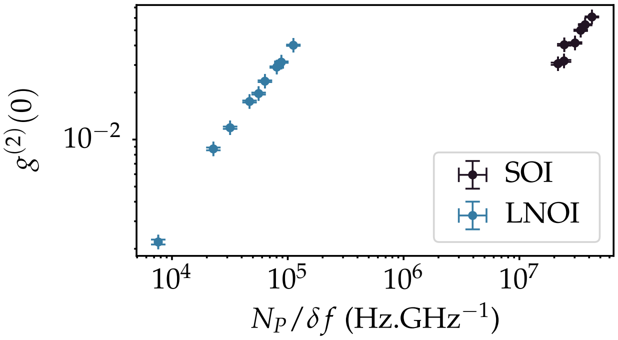

Figure 2.32: Heralded $g^{(2)}(0)$ as a function of N_P divided by the single photon bandwidth δf for both sources. For LNOI, δf= 160 GHz, For SOI, δf= 0.43 GHz.

non-heralded second-order correlation measurement, as its value is directly linked to the non-heralded $g^{(2)}(0)$ [108]

$$g^{(2)}(0) = 1 + \frac{1}{K}. \tag{2.44}$$

From Eqs. 2.44 and 2.23, it comes that the spectral purity P_{spectral} is related to $g^{(2)}(0)$ as

$$P_{\text{spectral}} = g^{(2)}(0) - 1. \tag{2.45}$$

The experimental setup is presented in Fig. 2.33. One photon from a photon pair is selected and filtered using a programmable filter. It goes through a fibered beam splitter, with one detector placed at each output.

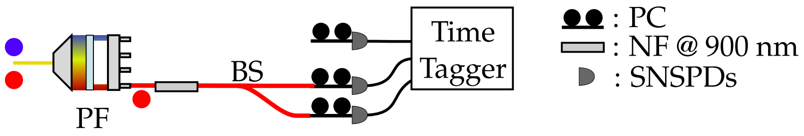

Figure 2.33: Setup for measurement of the non-heralded $g^{(2)}(0)$ of the signal photon. PF: programmable filter, PC: polarization controller, NF: notch filter, SNSPDs: single photon detectors.

Fig. 2.34 presents the experimental results for the SOI micro-resonator. For a given number of modes D transmitted by the PF, we plot the associated second-order correlation function. As expected, the maximum value of the non-heralded $g^{(2)}(0)$ is 2 in the single mode case, which characterizes thermal statistics. $g^{(2)}(0)$ decreases as we transmit a larger number of frequency modes.

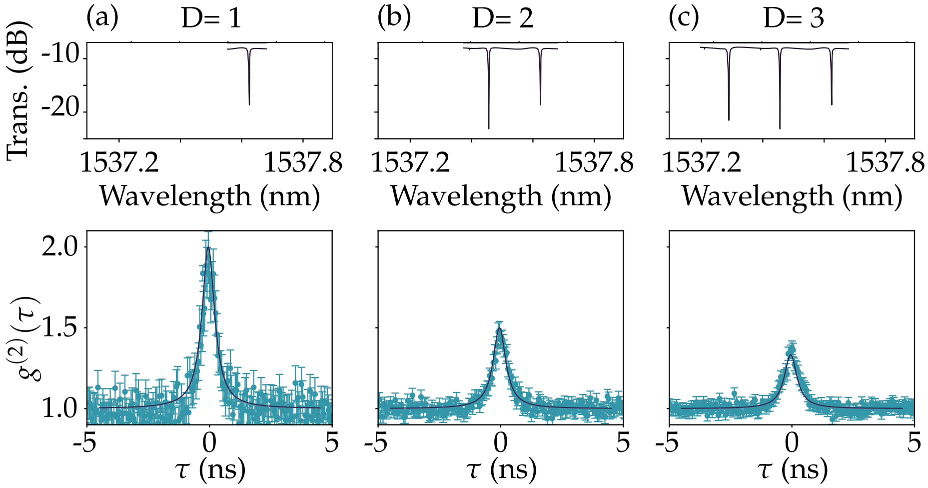

Figure 2.34: Signal photon spectrum filtered by the programmable filter and associated non-heralded $g^{(2)}(\tau)$ for (a): 1,(b): 2, and (c): 3 transmitted frequency modes. Black solid line correspond to the expected $g^{(2)}(\tau)$.

Fig. 2.35 shows the measured (blue dots) and the expected values (black dots) of the non-heralded $g^{(2)}(0)$ and inferred spectral purities as a function of the number of frequency modes transmitted by the programmable filter. We remark a good agreement between the measured and expected values.

Fig. 2.36 finally presents the results for the photons generated by the LNOI waveguide, filtered by the PF using the smallest achievable bandwidth of 10 GHz. The value of the non-heralded $g^{(2)}(0)$ only reaches 1.19± 0.02, and hence a spectral purity of $P_{\text{spectral}} = 0.19 \pm 0.02$.

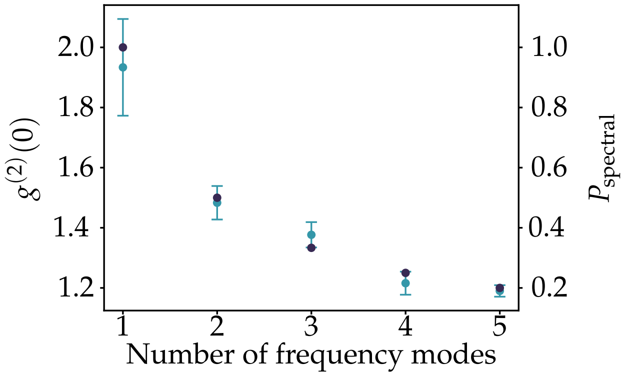

Figure 2.35: Non-heralded $g^{(2)}(0)$ as a function of the number of transmitted frequency modes. Light blue dots: measured data, dark blue dots: expected from theory.

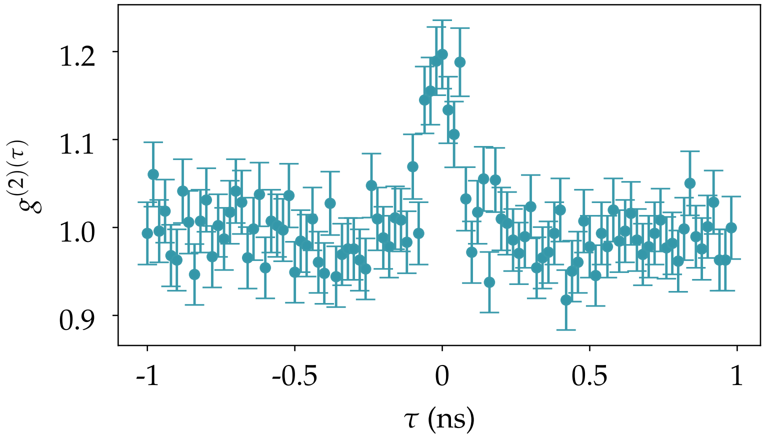

Figure 2.36: measured non-heralded $g^{(2)}(\tau)$ for a photon generated by the LNOI waveguide and filtered by a 10 GHz bandwidth filter.

It is worth noting that, as discussed in Section 2.1.5, engineering the pump spectrum, for instance using a pulsed pump laser with a broader bandwidth, can enable to achieve a higher value of purity even with a single photon bandwidth of the order of tens of GHz [68, 108, 147].

Table 2.12 compares our experimental results with works from literature, and the associated single photon bandwidth and pump bandwidth. A single photon filtering of 20 GHz would enable a 0.99 spectral purity if pumped by a 200 GHz bandwidth laser.

Work	**MR: Micro-resonator** **WG: waveguide**	**single photon bandwidth**	**Pump bandwidth**	$P_{\textbf{spectral}}$
Oser et al. [146]	**Silicon MR**	1.3 GHz	$\sim$100 MHz	**0.5**
Kues et al. [68]	**Hydex MR**	800 MHz	800 MHz	**0.92**
Samara et al. [148]	**Silicon Nitride MR**	300 MHz	300 MHz	**0.97**
Hua et al. [147]	**PPLN WG**	25 GHz	142 GHz	**0.96**
Khodadad [59]	**PPLN WG**	20 GHz	200 GHz	**0.99**
This work	**Silicon MR**	430 MHz	$\sim$100 MHz	**0.92**
	PPLN waveguide	10 GHz	2.5 MHz	**0.19**

Table 2.12: Comparison of our measured values of P_{spectral} with results in similar or related structures.

2.4 Conclusion on integrated photon pair generation

In this Chapter, we investigated photon pair generation at telecom wavelength using two state-of-the-art integrated sources, based on two promising materials for integrated quantum photonics :

- A periodically-poled thin-film lithium niobate waveguide

We chose the optimal poling period and waveguide temperature for second-harmonic generation at 780 nm and photon pair generation at 1560 nm. We investigated the SPDC degeneracy as a function of the waveguide temperature

- A Silicon-On-Insulator micro resonator

We measured a free spectral range of 21.25 GHz and quality factors of 4.75×10^5. We investigated how these parameters influence the photon pair generation. We will see in Chapter 4 that this small value of FSR is an advantage compared to other works for the frequency-bin qubit manipulation.

We measured for both sources key parameters for evaluating a photon pair source: the number of generated pairs, the heralding efficiency, and the single photon purity as a function of power, assessing internal brightnesses of 3×10^5 pairs.s^{-1}.mW^{-1}.GHz^{-1} for the LNOI waveguides, and 5×10^7 pairs.s^{-1}.mW^{-2}.GHz^{-1} for the SOI micro-resonator, both comparable to the state of the art. We assessed values of $g^{(2)}(0) = 0.03$ for both sources with a generated number of pairs of $\approx 10^5$ pairs per second for the LNOI waveguide and $\approx 10^7$ pairs per second for the SOI micro-resonator. For the SOI micro-resonator, we also measured a spectral purity of 0.93, necessary for applications involving heralded single photon sources.

In this chapter, we provided the way to generate photon pairs at telecom wavelength. Chapter 3 introduces the theoretical models and simulation for the manipulation of single photons with time and frequency encoding. In Chapter 4, we utilize the introduced photon pair sources, together with the manipulation scheme in the frequency domain to perform quantum optics experiments with these photon pair sources.

Chapter 3

Parallelizable synthesis of arbitrary single-qubit gates with linear otics and time-frequency encoding

Single qubit gates are important elements for quantum information [149]. In quantum communication, they allow for instance the preparation and measurement of quantum states to perform quantum key distribution protocols [150]. For quantum computation, they are applied independently to several qubits, together with two-qubit gates to perform quantum algorithms [151].

A single qubit gate is a linear and unitary transformation $\hat{U}$ that, when applied to an input qubit $|\Psi\rangle$, transforms it into an output state $|\Phi\rangle$, such that

$$|\Phi\rangle = \hat{U}\,|\Psi\rangle\,. \tag{3.1}$$

The Bloch sphere representation in Fig. 3.1, gives an intuitive way to visualize a single qubit state and single qubit rotation. Each point on the surface of the sphere represents a possible qubit state. The north and south poles represent the two logical basis states $|0\rangle$ and $|1\rangle$ used for encoding, and the points on the equator represent all possible equal superpositions of $|0\rangle$ and $|1\rangle$. An arbitrary qubit state is represented by a vector $|\Psi\rangle$, and the action of a single qubit gate $\hat{U}$ is represented by the dashed line, transforming the input state into the output state $|\Phi\rangle$.

For universal quantum information processing, the fourth Di Vincenzo criterium states the need for a *universal* set of quantum gates that enables the realization of any quantum circuit [152]. Such a set can be composed of a limited number of single and two-qubit gates [153, 154]. However, for physical implementations, such small sets of gates can

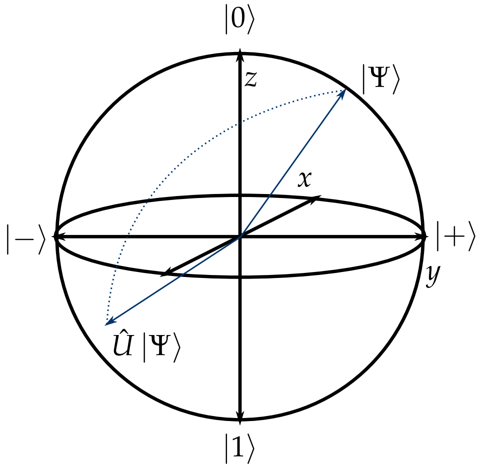

Figure 3.1: Representation on the Bloch sphere of the action of a single qubit rotation $\hat{U}$ on an input single qubit state $|\Psi\rangle$. $|+\rangle$ and $|-\rangle$ are the superposition states defined as $|+\rangle = |0\rangle + |1\rangle$ and $|-\rangle = |0\rangle - |1\rangle$

be inefficient if the gate performances are not ideal, as a targeted quantum circuit might necessitate a large combination of these universal gates.

Alternatively, using arbitrary single-qubit gates enables the reduction of the number of gates in the circuit. Such a quantum gate should be able to rotate the qubit around the three axes of the Bloch sphere, for which the three generic rotation matrices $\hat{U}_x$, $\hat{U}_y$, $\hat{U}_z$ are expressed as

$$\hat{U}_x = \begin{pmatrix} \cos(\frac{\theta}{2}) & \sin(\frac{\theta}{2}) \\ \sin(\frac{\theta}{2}) & \cos(\frac{\theta}{2}) \end{pmatrix}, \hat{U}_y = \begin{pmatrix} \cos(\frac{\theta}{2}) & -i\sin(\frac{\theta}{2}) \\ i\sin(\frac{\theta}{2}) & \cos(\frac{\theta}{2}) \end{pmatrix}, \hat{U}_z = \begin{pmatrix} 1 & 0 \\ 0 & e^{i\phi} \end{pmatrix}. \tag{3.2}$$

In practice, qubit gates are implemented by a series of devices, each device performing a rotation along one of the three axes. For photonic qubits, several degrees of freedom can be used to encode information, each harnessing different devices to implement these rotations. Table 3.1 lists several degrees of freedom of the photon, and devices needed for the realization of rotations with respect to axes of the Bloch sphere. The rotations are classified into two categories: rotation around the $\vec{z}$ axis, which corresponds physically to a phase shift between the qubit modes, and the rotations along the $\vec{x}$ and $\vec{y}$, for which a controlled coupling is required between the two-qubit modes.

The choice of a degree of freedom used for encoding the $|0\rangle$ and $|1\rangle$ determines the ability to encode qubits in parallel. Time and frequency, degrees of freedom of interest, enable the encoding of several qubits in a single spatial mode. Scaling the number of qubits therefore does not require scaling up the setup complexity required for qubit transport. The ability

Degree of freedom	$\vec{X}/\vec{Y}$ **rotations**	$\vec{Z}$ **rotations**
Polarization [155]	Half and quarter waveplates combination	
Path [89]	Directional couplers	Phase shifters
Orbital angular momentum [18, 156]	Spatial light modulators, q-plates	
Time-bin (1) [157]	Directional couplers/ Delay lines	Phase shifters
Time-bin (2) [74]	**PF**	**EOM**
Frequency-bin [55, 74]	**EOMs**	**PF**

Table 3.1: Experimental devices used for the manipulation of qubits encoded in different degrees of freedom of the photon. PF: programmable filter, EOM: electro-optic modulator.

to manipulate each qubit independently in a single spatial mode is very interesting for the scalable processing of such parallel qubits. A framework for universal computing using frequency-bin qubits has been proposed in [55], using optical linear devices acting on time and frequency domain. The elements used for the manipulation are electro-optic phase modulators (EOM) and programmable filters (PF). They demonstrate how to use these devices in serial to synthesize a set of single and two-qubit gates.

In this chapter, we investigate further the synthesis of a single qubit gate with EOMs and PF, by comparing the performances of the gate synthesis for two configurations of devices acting on time-bin and frequency-bin qubits. We assess and demonstrate as well their ability to be parallelized to independent qubits.

We start in Section 3.1, by introducing the Fourier transform relations linking time and frequency. We define the two spaces of states that will allow us to encode time and frequency qubits. In Section 3.2, **we present a model for the action of EOMs and PF acting on time and frequency modes**. We theoretically demonstrate how a PF can be used to obtain a two-scattering matrix in the time domain. In Section 3.3, we demonstrate **the synthesis of single qubit gates with time and frequency encoding**, with two combinations of devices : [EOM-PF-EOM] and [PF-EOM-PF]. We compare our findings to the literature findings. In Section 3.4, we investigate **the parallelization of single-qubit gates** with both configurations in the two encodings. We discuss the limitations of the parallelization and explore the evolution of the performances for more complex RF driving of the EOMs on time-domain single qubit gates.

3.1 Time-frequency Fourier relations

Time and frequency are conjugate variables. As a result, they are linked by the Fourier transform. While the space of state is naturally continuous, it is possible to discretize the time and frequency spaces in bins. At the quantum level, each frequency bin j and time bin k are quantum states $|\omega_j\rangle$ centered at a frequency $\omega_j/2\pi$ and $|t_k\rangle$ centered on an arrival time t_k. We define M as the number of frequency bins and time bins on the respective bases. Two consecutive bins are separated by a spacing $\delta\omega$ for the frequency bins and δt for the time bins. Physically, the M frequency bins correspond to a total spectral bandwidth $\Delta\omega = M\delta\omega$, and the M time bins to a temporal bandwidth of $\Delta t = M\delta t$. From the experimental point of view, the total spectral bandwidth will be limited either by the source or the processing devices.

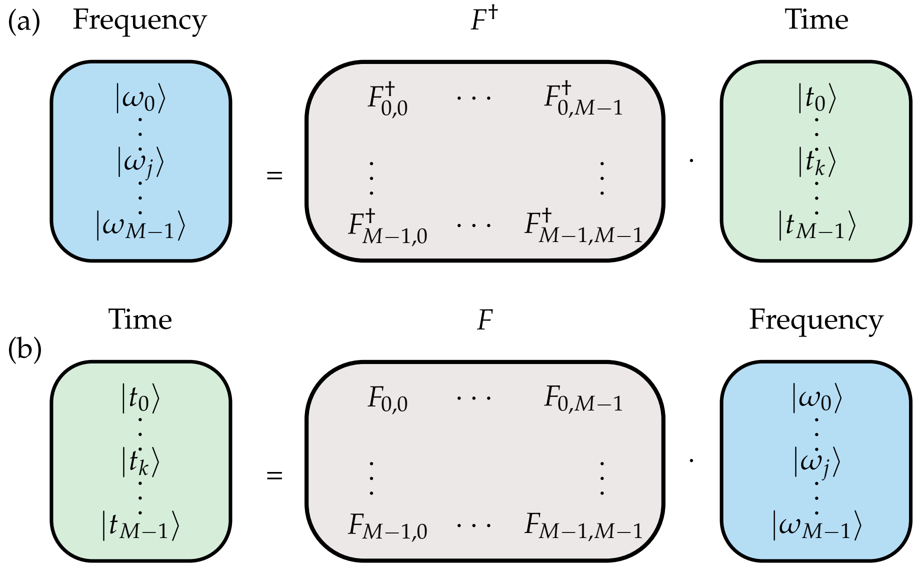

Figure 3.2: Representation of the time-frequency relation through Fourier transform. (a): A frequency bin is expressed as a superposition of time bins. (b): A time bin is expressed as a superposition of frequency bins.

As we work with discrete spaces of state, we can use the Discrete Fourier transform (DFT) to link the two conjugate spaces. Each element of the DFT $F_{k,m}$ is expressed as

$$F_{j,k} = \exp\left(i\frac{2\pi}{M}jk\right) \tag{3.3}$$

$|t_k\rangle$

Using this expression, a time bin can be written as a superposition of frequency bins, and

$\tilde{U}_{EOM}$ U_{FT} $\tilde{U}_{EOM}$

$\vdots$

$|t_{k+\frac{M}{2}}\rangle$

conversely for frequency bins as

$$\begin{aligned} |t_k\rangle &\approx \frac{1}{\sqrt{M}} \sum_{j=0}^{M-1} F_{j,k} |\omega_j\rangle \\ |\omega_j\rangle &\approx \frac{1}{\sqrt{M}} \sum_{k=0}^{M-1} F^{\dagger}_{j,k} |t_k\rangle \end{aligned} \tag{3.4}$$

Fig. 3.2 shows a graphical visualization of the matrix. Throughout this chapter for easier reading, we will use colors to represent the several spaces and useful matrices. The color blue represents the frequency space, and green the time space. The FDT matrix is represented in grey. We label the operators in the time domain with "˜"

Because of the Fourier transform relation, it is worth noting the link between the bin separation of one space, and the size of the conjugate space:

$$\begin{aligned} \delta\omega &= \frac{2\pi}{\Delta t} \\ \delta t &= \frac{2\pi}{\Delta\omega} \end{aligned} \tag{3.5}$$

The following section describes the theoretical model for the manipulation of time and frequency bins using electro-optic phase modulators and programmable filters. With these devices, we aim to implement arbitrary single-qubit gates acting on frequency and time-bin qubits.

3.2 Time and frequency domain manipulation with electro-optic modulators and programmable filters

3.2.1 Programmable Filter

General action of the programmable filter on time and frequency bins

In this section, we introduce the programmable filter (PF). Such a device enables one to act independently on every frequency bin, to apply an arbitrary attenuation and phase, enabling a wide range of applications. Throughout this manuscript, this device serves as a tunable filter and wavelength demultiplexer, properties that use the ability to control spectral attenuation.

Here, we wish to realize unitary transformations. We thus consider only the ability to apply arbitrary phase shifts independently on frequency modes. The action U_{PF} of a PF acting on a frequency mode ω_j is expressed as

$$U_{PF}|\omega_j\rangle = e^{i\varphi_j}|\omega_j\rangle. \tag{3.6}$$

Using DFT, it is possible to express the PF action on a time bin. We define $\tilde{U}_{PF} = FU_{PF}F\dagger$ as the transfer matrix of the PF in the time domain. Its action on a time bin is then

$$\tilde{U}_{PF}|t_k\rangle = \frac{1}{M}\sum_{k'=0}^{M-1}\sum_{j=0}^{M-1}\exp\left(i\frac{2\pi}{M}(k'-k)j+\varphi_j\right)|t_{k'}\rangle\,, \tag{3.7}$$

where the full calculations are done in A.1. Fig 3.3 shows a visual representation of the action of the PF in the spectral and temporal domain.

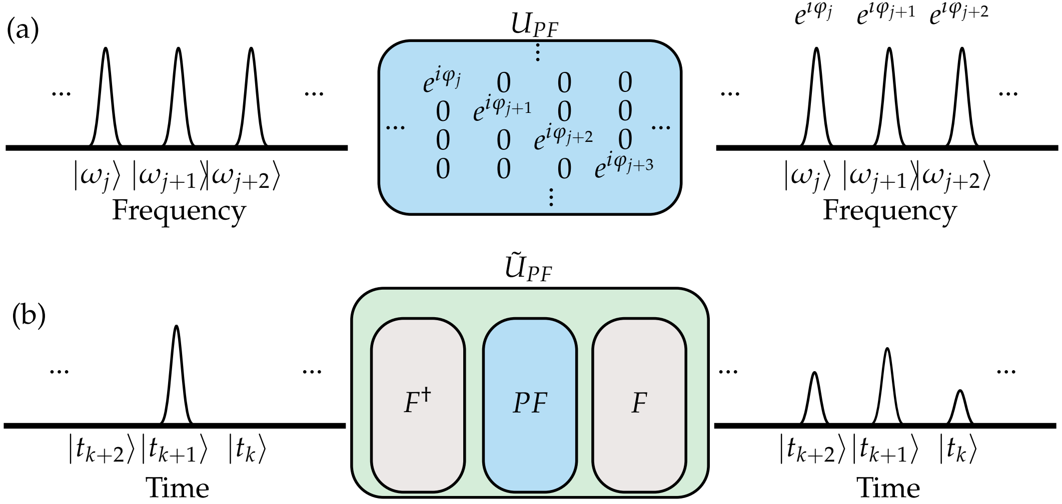

Figure 3.3: (a): Action of U_{PF} on frequency modes. (b): Action of $\tilde{U}_{PF}$ on temporal modes.

The PF is therefore a scatterer in the time basis, entirely controlled by the phases applied to the frequency modes.

Two-scattering operation of the PF in the time domain

Our goal is to use this device to act on single qubits. For frequency-bin qubits encoded on two frequency modes $|\omega_j\rangle$ and $|\omega_{j'}\rangle$, U_{PF} intrinsically acts as a phase gate. For time-bin qubits, $\tilde{U}_{PF}$ scatters light on several time bins. Our goal here is to control the scattering in the time domain so that for a qubit encoded on two time bins $|t_k\rangle$ and $|t_{k'}\rangle$, $\tilde{U}_{PF}$ becomes a **two-scattering matrix**: a matrix that effectively couples modes in pairs. The action of such a matrix on a time-bin $|t_k\rangle$ should be of the form

$$\tilde{U}_{PF}\,|t_k\rangle = \alpha\,|t_k\rangle + \beta\,|t_{k'}\rangle\,, \alpha,\beta\in\mathbb{C}, \tag{3.8}$$

with $|\alpha|^2+|\beta|^2=1$, $(\alpha,\beta)\in\mathbb{C}^2$. We start with no assumption on the ”distance” $k-k'$ between the two vectors of the qubit subspace. The coefficients α and β can be derived from the generalized action of the PF in the time domain

$$\forall (k,k') \in \{[0, M-1]\}^2, \tilde{P}_{k',k} = \langle t_{k'}|\tilde{U}_{PF}|t_k\rangle = \frac{1}{M}\sum_j \exp\left(i\frac{2\pi}{M}(k'-k)j + i\varphi_j\right). \tag{3.9}$$

Accordingly with Eq. A.5, we set

$$\begin{aligned} \langle t_k|\tilde{U}_{PF}|t_k\rangle &= \alpha \\ \langle t_{k'}|\tilde{U}_{PF}|t_k\rangle &= \beta \end{aligned} \tag{3.10}$$

Replacing $\langle t_k|\tilde{U}_{PF}|t_k\rangle$ $\langle t_{k'}|\tilde{U}_{PF}|t_k\rangle$ by their expression gives

$$\begin{cases} & \frac{1}{M}\sum_{j=0}^{M-1} e^{i\varphi_j} = \alpha, \\ & \frac{1}{M}\sum_{j=0}^{M-1} e^{i2\pi\frac{mj}{M}} e^{i\varphi_j} = \beta, \\ \forall (p,q) \neq (k,k),(k+m,k), & \frac{1}{M}\sum_{j=0}^{M-1} e^{i2\pi\frac{(p-q)j}{M}} e^{i\varphi_j} = 0. \end{cases} \tag{3.11}$$

The full detail for solving Eq. 3.11 is given in Appendix A.2. We demonstrate that it is possible to program the PF so that it only couples two time bins $|t_k\rangle$ and $|t_{k'}\rangle$, provided the distance between k and k' is M/2. As a result, the action of the PF on a time bin $|t_k\rangle$ can finally be expressed as

$$\begin{aligned} &\text{for } k \in \{0, \frac{M}{2}-1\},\ \tilde{U}_{PF}|t_k\rangle = |\alpha|\,|t_k\rangle \pm i|\beta|\,|t_{k+\frac{M}{2}}\rangle,\ |\alpha|,|\beta| \in \mathbb{R}, \\ &\text{for } k \in \{\frac{M}{2}, M-1\},\ \tilde{U}_{PF}|t_k\rangle = |\alpha|\,|t_k\rangle \pm i|\beta|\,|t_{k-\frac{M}{2}}\rangle,\ |\alpha|,|\beta| \in \mathbb{R}. \end{aligned} \tag{3.12}$$

To achieve this, the action of the PF on a frequency mode $|\omega_j\rangle$ should be programmed such that

$$U_{PF}|\omega_j\rangle = \left[|\alpha| + |\beta|e^{-i\pi j}\right]|\omega_j\rangle. \tag{3.13}$$

Subsequently, the PF matrix in the temporal basis takes the form

$$\tilde{U}_{PF} = e^{i\gamma}\begin{pmatrix} |\alpha|I & \pm i|\beta|I \\ \pm i|\beta|I & |\alpha|I \end{pmatrix}, \tag{3.14}$$

where I is the identity matrix of dimension $M/2$.

These results show that using a programmable filter, we can successfully couple two time bins, without coupling to other modes. Furthermore, the coupling between the modes is tunable to perform an arbitrary rotation around the y axis of the Bloch sphere.

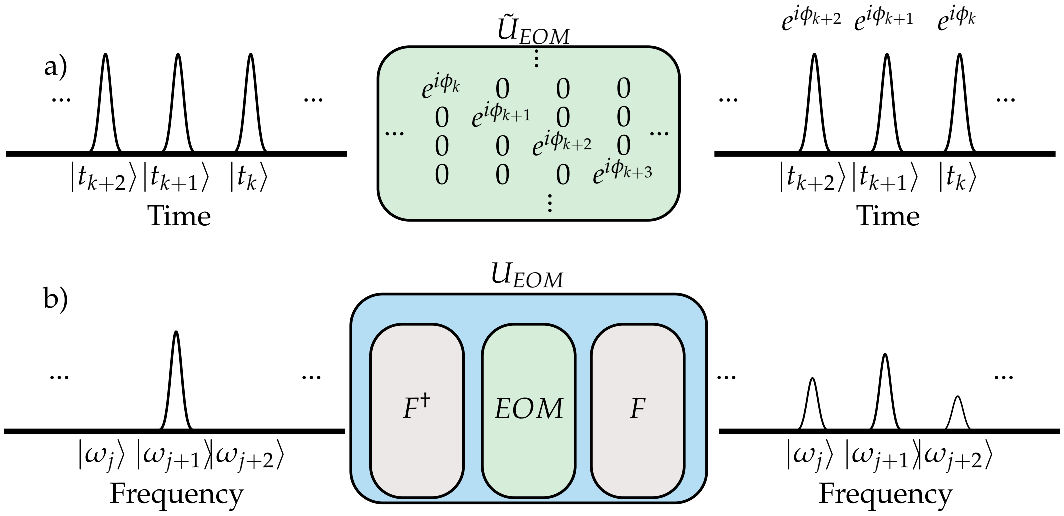

Figure 3.4: (a): Action of the $\tilde{U}_{EOM}$ on temporal modes (b): Action of U_{EOM} on frequency modes.

3.2.2 Electro-optic phase modulator

The electro-optic modulator applies a time-dependent phase to the temporal modes. Its action on a temporal mode $|t_k\rangle$ is

$$\tilde{U}_{EOM}\,|t_k\rangle = e^{i\phi(t_k)}\,|t_k\rangle \tag{3.15}$$

Where $\phi(t_k)$ is a phase applied to the corresponding time-bin k. In practice, this phase is set by a radio frequency (RF) driving applied to the modulator. The Fourier transform defines the unitary action of the electro-optic modulator in the frequency domain as $U_{EOM} = F\tilde{U}_{EOM}F^\dagger$. From this calculation, the action of $\tilde{E}$ on a frequency mode $|\omega_j\rangle$ is

$$U_{EOM}\,|\omega_j\rangle = \frac{1}{M}\sum_{j'=0}^{M-1}\sum_{k=0}^{M-1}\exp\left(i\frac{2\pi}{M}(j'-j)k + \phi_k\right)|\omega_{j'}\rangle\,. \tag{3.16}$$

Fig. 3.4 shows the visualization of the action of the electro-optic modulator on time and frequency bins. We thus see that the EOM is a scatterer in the frequency domain. Engineering the phase applied to each temporal mode $|t_k\rangle$ would allow us to manipulate this scattering. Realistically, the phase is determined by the EOM RF driving. In this work, we consider sine waves:

$$\phi(t_k) = \mu\cos(\Omega t_k + \theta). \tag{3.17}$$

Here, μ is the phase amplitude of the modulation wave. The modulation frequency sets the spacing of the frequency modes $\Omega = \delta\omega = 2\pi/M\delta t$. In this case, 3.16 can be approximated by Bessel functions as [158]

$$U_{EOM} \left|\omega_j\right\rangle = e^{i\phi_c} \sum_{k=-\lceil\mu\rceil-1}^{k=\lceil\mu\rceil+1} (e^{i\theta})^k J_k(\mu) \left|\omega_{j+k}\right\rangle . \tag{3.18}$$

For sinusoidal driving, the modulator couples nearby frequency modes. The weight of the coupling depends on the amplitude μ of the modulation signal.

In the following section, we define the encoding of frequency-bin and time-bin qubits. We describe the performance metrics assessing the realization of single-qubit gates. We then investigate two combinations of EOMs and PFs, [EOM-PF-EOM] and [PF-EOM-PF], for realizing single qubit gates for time and frequency encoding.

3.3 Synthesis of single-qubit gates

3.3.1 Time-bin and frequency-bin qubits

The frequency-bin and time-bin qubits are in a superposition of two quantum states. When working with individual qubits, we separate our M-dimensional Hilbert space, into $M/2$ distinct subspaces. This division is based on the choice of qubit encoding, which is noted $\mathcal{H}_j^\omega$ in the frequency domain, using two adjacent frequency bins, and $\mathcal{H}_k^t$ in the time domain, using modes separated by $M/2$ time bins with $j, k \in [0, M/2-1]$.

$$\begin{aligned} \mathcal{H}_j^\omega &= \left\{\left|\omega_{2j}\right\rangle, \left|\omega_{2j+1}\right\rangle, j \in [0, M/2-1]\right\}, \; \omega_{2j+1} - \omega_{2j} = \delta\omega, \\ \mathcal{H}_k^t &= \left\{\left|t_k\right\rangle, \left|t_{k+M/2}\right\rangle, k \in [0, M/2-1]\right\}, \; t_{k+M/2} - t_k = \frac{M}{2}\delta t, \end{aligned} \tag{3.19}$$

For frequency-bin qubits, the encoding choices are based on the physical limitations of the devices. An electro-optic modulator couples neighbor modes (see section 3.2.2). For time-bin qubits, we showed in Section 3.2.1 that the PF can be programmed to achieve a tunable superposition of two time bins that are M/2 time bins apart, which justifies the choice of the encoding here.

A single qubit gate is defined as a 2x2 unitary matrix acting on the two modes of the qubits $\left|0\right\rangle_L$ and $\left|1\right\rangle_L$, defined for a time-bin and a frequency-bin qubit as

$$\begin{aligned} \left|0\right\rangle_L = \left|\omega_j\right\rangle \; \left|1\right\rangle_L = \left|\omega_{j+1}\right\rangle, &\text{ for frequency-bin qubits,} \\ \left|0\right\rangle_L = \left|t_k\right\rangle \; \left|1\right\rangle_L = \left|t_{k+M/2}\right\rangle, &\text{ for time-bin qubits.} \end{aligned} \tag{3.20}$$

In this chapter, we aim to realize arbitrary single qubit gates. Such arbitrary unitary can be written as

$$\hat{U}(a,b,c,d) = e^{ia} \begin{pmatrix} \cos\left(\frac{c}{2}\right) e^{-i\left(\frac{b}{2}+\frac{d}{2}\right)} & \sin\left(\frac{c}{2}\right) e^{-i\left(\frac{b}{2}-\frac{d}{2}\right)} \\ \sin\left(\frac{c}{2}\right) e^{i\left(\frac{b}{2}-\frac{d}{2}\right)} & \cos\left(\frac{c}{2}\right) e^{i\left(\frac{b}{2}+\frac{d}{2}\right)} \end{pmatrix}_{\{\left|0_L\right\rangle, \left|1_L\right\rangle\}} \tag{3.21}$$

Where a, b, c, and d are free parameters. Choosing the set of parameters enables one to realize a particular quantum gate. For instance, the set of parameters $\{a = \pi/2, b = 0, c = \pi/2, d = \pi/2\}$ generates the Hadamard gate

$$H = \frac{1}{\sqrt{2}}\begin{pmatrix} 1 & 1 \\ 1 & -1 \end{pmatrix}. \tag{3.22}$$

We wish to synthesize such an arbitrary single-qubit gate using a combination of PF and EOM in serial. For a given configuration, we define the $M \times M$ transfer matrix V for the frequency domain and $\tilde{V}$ for the time domain, as the product of n PF and n' EOMs, depending on many parameters that we globally denote as
$\Phi \equiv (\varphi_{1,0}, \ldots, \varphi_{n,M-1}, \mu_{1,0}, \theta_{1,0}, \phi_{c_{1,0}} \ldots \mu_{n',M-1}, \theta_{n',M-1}, \phi_{c_{n',M-1}})$.

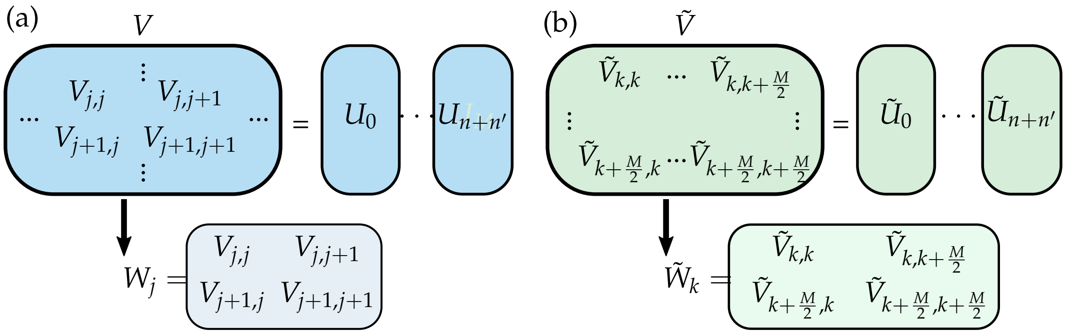

Figure 3.5: $M \times M$ transfer matrices in the (a): frequency and (b): time domain for a combination of n PF and n' EOMs.

For each qubit encoded on a pair of modes, we define a submatrix W_j for frequency-bin qubits and W_k for a time bin qubit k such that

$$\begin{aligned} W_j(\Phi) &= \begin{pmatrix} \langle\omega_j|\,\hat{V}(\Phi)\,|\omega_j\rangle & \langle\omega_j|\,\hat{V}(\Phi)\,|\omega_{j+1}\rangle \\ \langle\omega_{j+1}|\,\hat{V}(\Phi)\,|\omega_j\rangle & \langle\omega_{j+1}|\,\hat{V}(\Phi)\,|\omega_{j+1}\rangle \end{pmatrix} \\ \tilde{W}_k(\Phi) &= \begin{pmatrix} \langle t_k|\,\tilde{V}(\Phi)\,|t_k\rangle & \langle t_k|\,\tilde{V}(\Phi)\,|t_{k+\frac{M}{2}}\rangle \\ \langle t_{k+\frac{M}{2}}|\,\tilde{V}(\Phi)\,|t_k\rangle & \langle t_{k+\frac{M}{2}}|\,\tilde{V}(\Phi)\,|t_{k+\frac{M}{2}}\rangle \end{pmatrix}. \end{aligned} \tag{3.23}$$

Fig. 3.5 visually presents the parametrization of a 2x2 submatrix W_j for frequency bin qubits and $\tilde{W}_k$ for time-bin qubits. The matrix V is the matrix product of several unitary matrices U_x or $\tilde{U}_x$, $x = \{\text{PF, EOM}\}$.

3.3.2 Performance metrics

We aim to evaluate the performance of a synthesized single-qubit operation W, compared to a target operation T. We define two figures of merit, the probability of success and fidelity, enabling us to determine how well our synthesized gate approximates the ideal target.

The probability of success measures the probability that the photon remains in the computation space $\{|0_L\rangle, |1_L\rangle\}$. Any possibility of photon conversion outside this computational space will result in a decrease in the probability of success. It is defined as a function of W and T as

$$\mathcal{P}(W,T) = \frac{Tr(W^{\dagger}W)}{Tr(T^{\dagger}T)}. \tag{3.24}$$

$\mathcal{P}(W,T)$ essentially measures the unitarity of the synthesized matrix.

The fidelity $\mathcal{F}$ measures the accuracy of the synthesis of the target single-qubit gate. and is defined as

$$\mathcal{F}(W,T) = \frac{Tr(W^{\dagger}T)Tr(T^{\dagger}W)}{Tr(W^{\dagger}W)Tr(T^{\dagger}T)}. \tag{3.25}$$

3.3.3 Frequency encoding

We summarize recently reported results on the [EOM-PF-EOM] configuration [57, 61, 67, 75]. We provide an exhaustive study of both [EOM-PF-EOM] and [PF-EOM-PF] configurations and compare their performances for single-qubit gate synthesis.

3.3.3.1 [EOM-PF-EOM] configuration

The [EOM-PF-EOM] configuration has been investigated for single qubit gate synthesis in [57, 61]. In these studies, the experimental realization of the qubit gates involves electro-optic modulators driven by single-tone RF sine waves. The work in [57] experimentally demonstrates a frequency-domain Hadamard gate, harnessing an experimental fidelity $\mathcal{F} > 0.999$. A more exhaustive study of this configuration for arbitrary single-qubit gate has been investigated in [61]. In this work, they report the ability to perform an arbitrary single-qubit gate experimentally with fidelities $\mathcal{F} > 0.99$ and probability of success $\mathcal{P} > 0.85$.

3.3.3.2 [PF-EOM-PF] configuration

The [PF-EOM-PF] configuration has been investigated with spectral encoding implementing Hadamard gates for quantum state tomography and probabilistic Hong-Ou-Mandel [59, 68, 76, 83, 87]. Here, we aim to investigate this configuration further for arbitrary single-qubit gate synthesis. For this configuration, the transfer matrix V is

$$V = U_{PF}U_{EOM}U_{PF}. \tag{3.26}$$

For a qubit j, $\forall j \in [0, M/2-1]$ encoded over modes $|\omega_j\rangle$ and $|\omega_{j+1}\rangle$, the synthetized unitary is

$$W_j = e^{i\phi_c}\begin{pmatrix} J_0(\mu)e^{i(\varphi_{1,2j}+\varphi_{2,2j})} & e^{-i\theta}J_1(\mu)e^{i(\varphi_{1,2j+1}+\varphi_{2,2j})} \\ -e^{i\theta}J_1(\mu)e^{i(\varphi_{1,2j}+\varphi_{2,2j+1})} & J_0(\mu)e^{i(\varphi_{1,2j+1}+\varphi_{2,2j+1})} \end{pmatrix}, \tag{3.27}$$

Let $\hat{U}(a,b,c,d)$ be the matrix of an arbitrary unitary as given in Eq. 3.21. One can achieve an exact synthesis of U over qubit j **iff** parameters φ match the following set of conditions:

$$\begin{cases} J_0(\mu) = \cos(c/2) \\ J_1(\mu) = \sin(c/2) \end{cases} \quad \begin{cases} \varphi_{1,2j} = \frac{-d-\theta+\pi+s_j}{2} \mod \pi \\ \varphi_{2,2j} = -\frac{b+d}{2} + \varphi_{1,2j} \mod \pi \\ \varphi_{1,2j+1} = s_j - \varphi_{1,2j} \mod \pi \\ \varphi_{2,2j+1} = -s_j + \left(\frac{b-d}{2} + \varphi_{1,2j}\right) \mod \pi. \end{cases} \tag{3.28}$$

If the parameters of the programmable filter satisfy the second set of equations, then fidelity and success probability do not depend on the qubit number j and are given by

$$\mathcal{P} = J_0(\mu)^2 + J_1(\mu)^2, \tag{3.29}$$

$$\mathcal{F} = \frac{\left[J_0(\mu)\cos\left(\frac{c}{2}\right) + J_1(\mu)\sin\left(\frac{c}{2}\right)\right]^2}{J_0(\mu)^2 + J_1(\mu)^2}. \tag{3.30}$$

We obtain the following results

$$\begin{cases} \mathcal{P} = 1 \Leftrightarrow \mu = 0 \\ \mathcal{F} = 1 \Leftrightarrow J_0(\mu)\sin(\frac{c}{2}) = J_1(\mu)\cos(\frac{c}{2}) \\ \mathcal{P} = \mathcal{F} = 1 \Leftrightarrow \mu = c = 0. \end{cases} \tag{3.31}$$

Unit success probability and unit fidelity can only be obtained for phase gates. Fig. 3.6, displays the performances as a function of the modulation index μ. As expected, increasing μ means increasing the coupling between the two-qubit modes, until eventually reaching the bit-flip gate for μ=2.405 rad. μ=1.435 rad corresponds to an equal splitting between the two-qubit modes, realizing the Hadamard gate with unit fidelity.

3.3.4 Time encoding

In this section, we examine the synthesis of arbitrary single qubit gates with time-bin encoding.

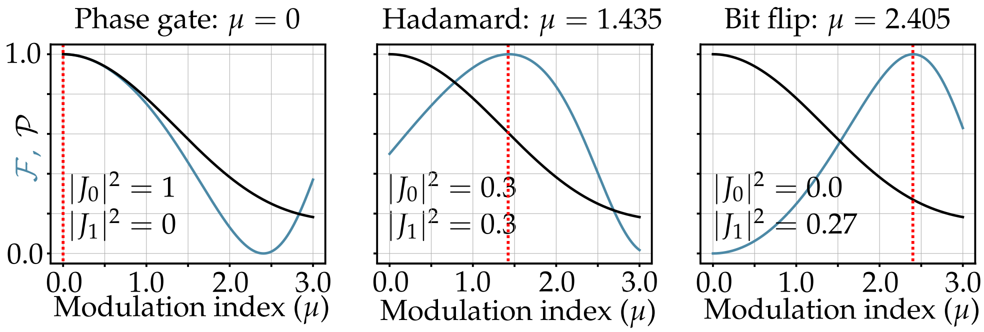

Figure 3.6: Fidelity and probability of success for (a): phase gate, (b): Hadamard gate, (c): Bit flip (X) gate. Fidelity is the blue line, and the probability of success is the black line.

As a reminder, the matrix of the programmable filter and electro-optic phase modulator for time encoding are noted below as

$$\tilde{U}_{PF} = e^{i\gamma}\begin{pmatrix} |\alpha|I & \pm i|\beta|I \\ \pm i|\beta|I & |\alpha|I \end{pmatrix};\ \tilde{U}_{EOM} = e^{i\phi_c}\begin{pmatrix} diag\{e^{\phi_k}\}_{0\leq k\leq \frac{M}{2}-1} & 0 \\ 0 & diag\{e^{-\phi_k}\}_{0\leq k\leq \frac{M}{2}-1} \end{pmatrix}, \tag{3.32}$$

The qubit is encoded over two time bins separated by $M/2$ modes

$$|0_L\rangle_k = |t_k\rangle \qquad |1_L\rangle_k = |t_{k+M/2}\rangle\,. \tag{3.33}$$

We investigate in the following sections the conditions needed to realize an arbitrary single-qubit unitary with both [EOM-PF-EOM] and [PF-EOM-PF] configurations.

3.3.4.1 [EOM-PF-EOM] configuration

This configuration consists of two EOMs with a PF in between. The two EOMs act as phase shifters in the time domain, i.e.: rotation around the z axis of the Bloch sphere, whereas the PF acts as a rotation around the x axis. Taking the matrix forms of the PF and EOM for time encoding in Eq. 3.32, we can compute the matrix product

$$\tilde{V} = \tilde{U}_{EOM2}\cdot\tilde{U}_{PF}\cdot\tilde{U}_{EOM1} \tag{3.34}$$

Using Eq. 3.23, the 2x2 matrix for the qubit $\{|t_k\rangle\,, |t_{k+M/2}\rangle\}$ is

$$\forall k \in [0, M/2-1], \mathbf{W_k} = e^{i(\phi_{c,1}+\phi_{c,2}+\gamma)}\begin{pmatrix} |\alpha|e^{i(\phi_{1,k}+\phi_{2,k})} & \pm i|\beta|e^{i(-\phi_{1,k}+\phi_{2,k})} \\ \pm i|\beta|e^{i(\phi_{1,k}-\phi_{2,k})} & |\alpha|e^{-i(\phi_{1,k}+\phi_{2,k})} \end{pmatrix}. \tag{3.35}$$

Identification with $\mathcal{M}(a,b,c,d)$ yields the following set of conditions for qubit k

$$\left\{\begin{array}{l} |\alpha| = \cos(c/2) \\ |\beta| = \sin(c/2) \end{array}\right. \quad \left\{\begin{array}{c} \phi_{1,k} + \phi_{2,k} = \frac{-b-d}{2} \mod 2\pi \\ -\phi_{1,k} + \phi_{2,k} + \pi/2 = \frac{-b+d}{2} + \pi \mod 2\pi \\ \phi_{1,k} - \phi_{2,k} + \pi/2 = \frac{b-d}{2} \mod 2\pi \\ -\phi_{1,k} - \phi_{2,k} = \frac{b+d}{2} \mod 2\pi, \end{array}\right. \tag{3.36}$$

which finally gives

$$\left\{\begin{array}{c} |\alpha| = \cos(c/2); \qquad |\beta| = \sin(c/2) \\ \phi_{1,k} = \frac{-d}{2} - \pi/4 \mod \pi \\ \phi_{2,k} = \frac{-b}{2} + \pi/4 \mod \pi. \end{array}\right. \tag{3.37}$$

As we consider a sinusoidal RF driving, the dephasing applied by the EOM to each temporal mode $|t_k\rangle$ is $\phi_k = \mu \sin(\frac{2k\pi}{M} + \theta)$, ($\forall k \in \{0, M/2-1\}$), which gives

$$\left\{\begin{array}{c} |\alpha| = \cos(c/2); \qquad |\beta| = \sin(c/2); \qquad \text{with } c \in [0,\pi] \\ \phi_{1,k} = \mu_1 \sin(\frac{2k\pi}{M} + \theta_1) = -\frac{d}{2} - \frac{\pi}{4} \mod \pi \\ \phi_{2,k} = \mu_2 \sin(\frac{2k\pi}{M} + \theta_2) = -\frac{b}{2} + \frac{\pi}{4} \mod \pi. \end{array}\right. \tag{3.38}$$

Under these conditions, we can realize an arbitrary single-qubit gate with the [EOM-PF-EOM] configuration for time-bin qubits. The two-scattering operation realized by the PF guarantees a unit success probability as $|\alpha|^2 + |\beta|^2 = 1$ for all targeted gates. Achieving unit fidelity then only relies on achieving the phase conditions. These conditions are easily fulfilled as $\phi_{1,k}$ and $\phi_{2,k}$ can be chosen independently. Performing an arbitrary unitary quantum gate with unit fidelity and success probability is then possible with the [EOM-PF-EOM] configuration acting on time-bin qubits.

3.3.4.2 [PF-EOM-PF] configuration

Undergoing the same reasoning as in the previous section, we compute the transfer matrix $\tilde{V}$ for the [PF-EOM-PF] configuration

$$\tilde{V} = \tilde{U}_{PF2} \cdot \tilde{U}_{EOM} \cdot \tilde{U}_{PF1} \tag{3.39}$$

$$\tilde{V} = \tilde{U}_{PF2} \cdot \tilde{U}_{EOM} \cdot \tilde{U}_{PF1} = e^{i(\gamma_2 + c + \gamma_1)}$$
$$\begin{pmatrix} A\, diag\{e^{i\phi_k}\} - B\, diag\{e^{-i\phi_k}\} & \pm iC\, |diag\{e^{i\phi_k}\} \pm iD\, diag\{e^{-i\phi_k}\} \\ \pm iC\, diag\{e^{-i\phi_k}\} \pm iD\, diag\{e^{i\phi_k}\} & A\, diag\{e^{-i\phi_k}\} - B\, diag\{e^{i\phi_k}\} \end{pmatrix}, \tag{3.40}$$

Where

$$A = |\alpha_1||\alpha_2|, B = |\beta_1||\beta_2|, C = |\alpha_2||\beta_1|, D = |\alpha_1||\beta_2| \tag{3.41}$$

Using Eq. 3.23, the 2x2 matrix for the qubit $\{|t_k\rangle, |t_{k+M/2}\rangle\}$ is

$$\forall k \in [0, M/2-1], \mathbf{W_k} = e^{i(\phi_{c,1}+\phi_{c,2}+\gamma)} \begin{pmatrix} A\,e^{i\phi_k} - B\,e^{-i\phi_k} & \pm iC\,e^{i\phi_k} \pm iD\,e^{-i\phi_k} \\ \pm iC\,e^{-i\phi_k} \pm iD\,e^{i\phi_k} & A\,e^{-i\phi_k} - B\,e^{i\phi_k} \end{pmatrix}, \tag{3.42}$$

Based on the two-scattering property demonstrated in section 3.2.1, a PF acts as a beamsplitter in the time basis. The following EOM then introduces an arbitrary phase shift between the two modes of the qubit subspace while the final PF of this configuration acts as a second arbitrary beamsplitter, completing a Mach-Zehnder interferometric device. The spatial version of such a Mach-Zehnder has been shown to achieve arbitrary unitary qubit synthesis [159].

3.3.5 Summary on the single qubit gate synthesis

In Table 3.2, we summarize and compare our findings [74] to results of the literature on the synthesis of single qubit gates, for two configurations of devices and for time and frequency encoding.

Arbitrary unitary synthesis for a single qubit		
Configuration	Frequency-encoding $\{|\omega_j\rangle, |\omega_{j+1}\rangle\}$	Time encoding $\{|t_k\rangle, |t_{k+M/2}\rangle\}$
[EOM-PF-EOM] Driving at Ω	[57, 61] Phase gate : $\mathcal{F}=1, \mathcal{P}=1$ H gate: $\mathcal{F}=1, \mathcal{P}=0.98$ Flip gate: $\mathcal{F}=1, \mathcal{P}=0.81$	[74] $\mathcal{F}=1, \mathcal{P}=1$ $\forall$ gates
[PF-EOM-PF] Driving at Ω	[59, 68, 74, 76, 79, 87] Phase gate : $\mathcal{F}=1, \mathcal{P}=1$ H gate: $\mathcal{F}=1, \mathcal{P}=0.60$ Flip gate: $\mathcal{F}=1, \mathcal{P}=0.27$	[74] $\mathcal{F}=1, \mathcal{P}=1$ $\forall$ gates

Table 3.2: Performances of single qubit gate synthesis for time and frequency encoding, considering two configurations of EOM and PF, driven by a single RF signal at frequency Ω.

For the frequency encoding, the EOM is essential to realize rotation around the x or y axis of the Bloch sphere. However, the larger the rotation angle, the higher the probability of scattering our photon out of the qubit space. This is visible by the decrease of the probability of success going from phase to Hadamard, and to bit flip gate. Phase gates are trivial, only necessitating a single PF whereas bit flip gates are the most demanding. For the [EOM-PF-EOM] configuration, the presence of a second EOM allows for control of the scattering of the photon in order to limit the loss in unwanted modes. Adding a second harmonic to the fundamental RF signal also allows more controls and an increase in the probability of success [61]. In the case of the [PF-EOM-PF], increasing the number of tones driving the EOM does not directly improve the performances. This is due to the fact that higher RF harmonics couple modes that are farther in frequency.

For the time encoding, both configurations enable the arbitrary synthesis of unitary single qubit gates, due to the two-scattering operation performed on the time-bin qubits by the programmable filter. This is a concrete advantage compared to frequency encoding.

In the next section, we investigate the ability to parallelize these single qubit gates.

3.4 Parallelization of single-qubit gates

Time and frequency offer the ability to produce a large number of modes, encoding as many qubits as the number of available pairs of modes. Considering our initial system of M=128 modes, it is possible to define M/2= 64 qubits.

In this section, we investigate the number of single-qubit gates that can be parallelized for each configuration and encoding. The case of the Hadamard gate is particularly examined for time-bin encoding, where we study the achieved performances with more elaborate RF driving.

3.4.1 Frequency encoding

3.4.1.1 Problematic for the parallelization of frequency-bin qubits

The idea of parallelization is to apply frequency-domain single qubit gates to adjacent qubits. This is possible only if the realized transformation does not induce any coupling between the two neighbor qubits. We thus define crosstalk as the probability of finding the initial photon in a frequency mode outside the computational space. Such crosstalk is unavoidable for frequency-bin quantum gates, as the EOM couples several neighbor modes. It is interesting to find out how many frequency modes should be left unused between two qubits to reduce crosstalk to an acceptable value. These unused modes are often called guard modes.

Two qubits separated by k guard modes will then be encoded on frequency modes $\{|\omega_j\rangle, |\omega_{j+1}\rangle\}$ for the first qubit and $\{|\omega_{j\pm k}\rangle, |\omega_{j+1\pm k}\rangle\}$ for the second one. Let us compare in the following sections the minimum amount of guard modes needed for the parallelization of two adjacent quantum gates, with the two configurations.

3.4.1.2 [EOM-PF-EOM] configuration

The parallelization of synthesized Hadamard gate as a function of the number of guard modes has been experimentally investigated with a single sine wave RF driving in [57].

Two-mode spacing is sufficient to keep a fidelity $\mathcal{F} > 0.99$ and probability $\mathcal{P} > 0.97$, ensuring a probability of finding a photon out of the computational space below 3%.

In [67], it is shown that adding a second harmonic to the RF driving signal allows to parallelize two Hadamard gates with no guard modes between them. To realize this operation, the PF must act on a larger number of modes: 10 modes have to be added before and after the two Hadamard gates for the interferences to happen, requiring a total of 24 frequency modes. For a space of state of M=128 frequency modes, 10 Hadamard gates are parallelized.

3.4.1.3 [PF-EOM-PF] configuration

Let us define a threshold for the crosstalk we tolerate. We consider that two qubits are independent if the crosstalk between them is lower than 10^{-3}.

The number of guard modes needed to achieve this crosstalk threshold depends on the considered operation. For a phase gate necessitating no coupling between the qubit modes, no guard modes are necessary. For other gates, the number of guard modes increases with the modulation index of the EOM. As such, we compute the number of guard modes needed for the gate demanding the highest modulation index: the bit flip gate.

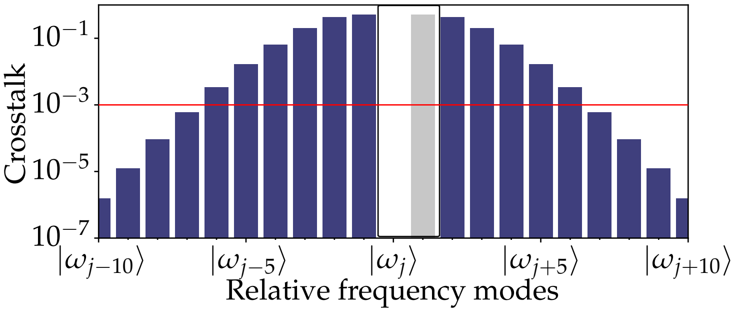

Figure 3.7: Probability distribution of a photon initially in $|\omega_j\rangle$ after a bit-flip gate. The horizontal red line corresponds to a crosstalk threshold of 10^{-3}.

Fig. 3.7 shows the probability distribution of the light in the modes neighboring ω_j. The computational space is represented by the grey bars. As anticipated with a bit flip gate, when a photon is initially in state $|\omega_j\rangle$, it predominantly transitions to the frequency mode $|\omega_{j+1}\rangle$. The blue bars correspond to the crosstalk which decreases as we move away from the qubit space. The red horizontal line delimits the 10^{-3} threshold and shows that 6 frequency modes are necessary to isolate two qubits for this bit-flip gate. Considering both the computational space and guard modes needed, one qubit takes an effective range of 8 frequency modes. For a system of 128 modes, it is then possible to parallelize 16 quantum gates.

3.4.2 Time-encoding

3.4.2.1 Problematic for the parallelization of time-bin qubits

To parallelize single qubit gates, we need the processing devices (EOM and PF) to act similarly on all parallel qubits. The PF allows a tunable two-mode splitting between modes $|t_k\rangle$ and $|t_{k+M/2}\rangle$. The sine wave driving the EOM cannot apply the same phase value to each temporal mode $|t_k\rangle$. As such, for single-qubit gates necessitating given phase conditions, only a limited number of qubits can reach maximum fidelity. Fig. 3.8 illustrates the phase pattern applied by the EOM driven by a single RF tone to the time bins (black line). The dark blue line corresponds to an arbitrary target phase. For a single RF tone, the EOM can apply the target phase value to only two qubits.

To increase the tolerance on the performances of parallel gates, we introduce a fidelity threshold $\mathcal{F}_{th}$. We will consider that a qubit gate is successfully realized if $\mathcal{F} \geq \mathcal{F}_{th}$. In Fig. 3.8, this notion of threshold is graphically shown with the light blue region around the targeted ϕ. This region corresponds to the phases allowing it to reach a fidelity above the threshold. The more tolerance we have on this threshold, the more qubits satisfy this condition. In this work, we choose a fidelity threshold of $\mathcal{F}_{th} = 0.99$. With time-bin qubits, we investigate the ability to parallelize two particular single-qubit gates: the phase gate and the Hadamard gate.

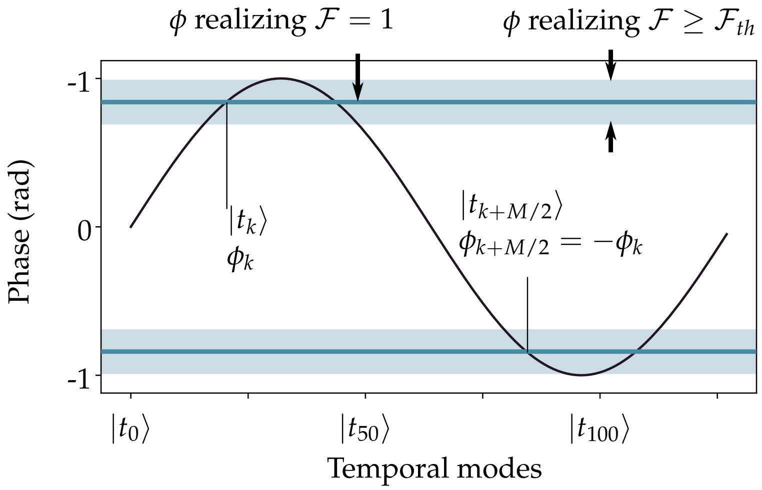

Figure 3.8: Phase applied by the EOM to each temporal modes $|t_k\rangle$. Two qubits are encoded over the modes $|t_k\rangle$ and $|t_{k+M/2}\rangle$. The solid blue represents the phase condition needed to achieve maximal fidelity for a given operation. The light blue area corresponds to the phase leading to the same operation with a fidelity $> \mathcal{F}_{th}$.

3.4.2.2 Parallelization of phase gates

In this section, we aim to compute the maximal number of gates whose fidelities reach the fidelity threshold. We start by recalling the matrix form of a phase gate

$$\mathcal{M}(\nu) = \begin{pmatrix} 1 & 0 \\ 0 & e^{-i\nu} \end{pmatrix}. \tag{3.43}$$

As the phase gate corresponds to a relative phase between the qubit modes, a single modulator alone can carry this operation. When considering both [PF-EOM-PF] and [EOM-PF-EOM] configurations, we derive the set of parameters needed to synthesize the phase gate. We use the synthesized matrix in Eq. 3.35 and Eq. 3.42, and derive the following sets of parameters for performing a phase gate

$$\begin{cases} |\alpha| = 1; \qquad |\beta| = 0, \\ \forall k \in [0, M/2-1] \qquad \phi_{1,k} + \phi_{2,k} = \frac{\nu}{2} \mod 2\pi, \\ \forall k \in [0, M/2-1] \qquad \phi_{1,k+M/2} + \phi_{2,k+M/2} = -\frac{\nu}{2} \mod 2\pi, \\ \phi_{c_1} + \phi_{c_2} + \gamma = -\frac{\nu}{2} \mod 2\pi, \end{cases} \tag{3.44}$$

for the [EOM-PF-EOM] configuration, and

$$\begin{cases} |\alpha_1| = 1; \qquad |\beta_1| = 0, \\ \forall k \in [0, M/2-1] \qquad \phi_k = \mu \sin\left(\frac{2k\pi}{M} + \theta\right) = \frac{\nu}{2} \mod 2\pi, \\ \phi_c + \gamma_1 + \gamma_2 = -\frac{\nu}{2} \mod 2\pi, \end{cases} \tag{3.45}$$

or

$$\begin{cases} |\alpha_1| = |\alpha_2| = 0; \qquad |\beta_1| = |\beta_2| = 1, \\ \forall k \in [0, M/2-1] \qquad \phi_k = \mu \sin\left(\frac{2k\pi}{M} + \theta\right) = -\frac{\nu}{2} \mod 2\pi, \\ \phi_c + \gamma_1 + \gamma_2 = -\frac{\nu}{2} \mod 2\pi, \end{cases} \tag{3.46}$$

for the [PF-EOM-PF] configuration. These three sets of equations lead to the same synthesized matrix and thus lead to the same performances. The fidelity of a phase gate applied to a qubit k can be computed $\forall \nu$ using Eq. 3.25 (c.f. Appendix A.3), and expressed as

$$\forall k \in [0, M/2-1] \qquad \mathcal{F}_k = \cos^2\left(\phi_k - \frac{\nu}{2}\right). \tag{3.47}$$

The number of qubits $\mathcal{N}$ for which $\mathcal{F}_k \geq \mathcal{F}_{th}$ is given by (see Appendix A.3)

$$\mathcal{N} = \left\lfloor \frac{M}{2\pi} \left[\frac{\pi}{2} - \arcsin\left(\frac{\frac{\nu}{2} - \arccos\left(\sqrt{\mathcal{F}_{th}}\right)}{\frac{\nu}{2} + \arccos\left(\sqrt{\mathcal{F}_{th}}\right)} \right) \right] \right\rfloor. \tag{3.48}$$

$\mathcal{N}$ depends on the desired phase ν, and increases when the threshold decreases.

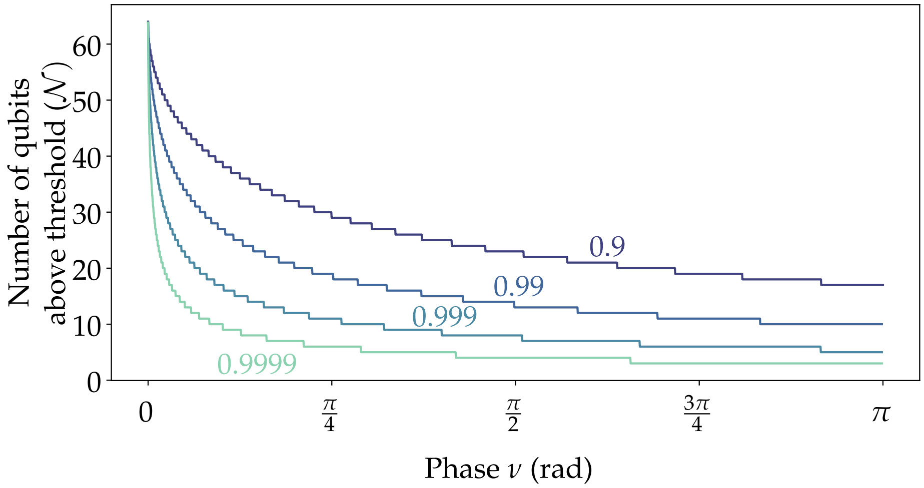

Figure 3.9: Phase gates parallel synthesis with time encoding: maximum number of gates synthesized in parallel with a fidelity better than $\mathcal{F}_{th}$ for four levels of accuracy as a function of the required gate z-rotation angle. This dependency holds for both [EOM-PF-EOM] and [PF-EOM-PF] configurations. Phase step is $\pi \cdot 10^{-4}$.

3.4.2.3 Parallelization of Hadamard gate

In the case of the Hadamard gate, the matrix form is :

$$H = \frac{1}{\sqrt{2}} \begin{pmatrix} 1 & 1 \\ 1 & -1 \end{pmatrix}. \tag{3.49}$$

As this gate requires coupling between the two-qubit modes, the [EOM-PF-EOM] and [PF-EOM-PF] configurations will not give the same results. The parameters corresponding to a single Hadamard gate for a qubit k are

$$\begin{cases} & |\alpha| = |\beta| = \frac{1}{\sqrt{2}} \\ \forall k \in [0, M/2-1] & \phi_k = \mu \sin\left(\frac{2k\pi}{M} + \theta\right) = \frac{\pi}{4} \mod \pi. \end{cases} \tag{3.50}$$

To simplify notations, we index the parameters corresponding to the two configurations, [EOM-PF-EOM] and [PF-EOM-PF], by EPE and PEP, respectively in the following equations. We define $\mathcal{F}_k^{(EPE)}$ $\mathcal{F}_k^{(PEP)}$ as the fidelity of a gate applied to a qubit k for the two configurations. The calculation, found in Appendix A.4, leads to the following

$$\forall k \in [0, M/2-1] \qquad \mathcal{F}_k^{(EPE)} = \sin^4\left(\phi_k + \frac{\pi}{4}\right) \tag{3.51}$$

for the [EOM-PF-EOM] configuration, and

$$\forall k \in [0, M/2-1] \qquad \mathcal{F}_k^{(PEP)} = \sin^2\left(\phi_k + \frac{\pi}{4}\right) \tag{3.52}$$

for the [PF-EOM-PF] configuration. The fidelity of the gate is higher than $\mathcal{F}_{th}$ only for certain values of ϕ_k:

$$\frac{\pi}{4} - \Delta\nu_{EPE} \leq \phi_k \leq \frac{\pi}{4} + \Delta\nu_{EPE}, \qquad \frac{\pi}{4} - \Delta\nu_{PEP} \leq \phi_k \leq \frac{\pi}{4} + \Delta\nu_{PEP}. \tag{3.53}$$

For the [EOM-PF-EOM] and [PF-EOM-PF] configuration, where $\Delta\nu_{EPE} = \frac{\pi}{2} - \arcsin\left(\mathcal{F}_{th}{}^{1/4}\right)$ and $\Delta\nu_{PEP} = \frac{\pi}{2} - \arcsin\left(\mathcal{F}_{th}{}^{1/2}\right)$.

The corresponding number of qubits realizing the Hadamard gate with a fidelity above $\mathcal{F}_{th}$ are respectively $\mathcal{N}_{EPE}$ and $\mathcal{N}_{PEP}$ for the two configurations (see Appendix A.4)

$$\begin{aligned} \mathcal{N}_{EPE} &= \frac{M}{\pi}\left\lfloor \frac{\pi}{2} - \arcsin\left(\frac{\frac{\pi}{4} - \Delta\nu_{EPE}}{\frac{\pi}{4} + \Delta\nu_{EPE}}\right)\right\rfloor + 1; \\ \mathcal{N}_{PEP} &= \frac{M}{\pi}\left\lfloor \frac{\pi}{2} - \arcsin\left(\frac{\frac{\pi}{4} - \Delta\nu_{PEP}}{\frac{\pi}{4} + \Delta\nu_{PEP}}\right)\right\rfloor + 1. \end{aligned} \tag{3.54}$$

Fig. 3.10 displays $\mathcal{N}_{PEP}$ and $\mathcal{N}_{EPE}$ as a function of $\mathcal{F}_{th}$. We note that the performance is slightly better for the [PF-EOM-PF] configuration than the [EOM-PF-EOM].

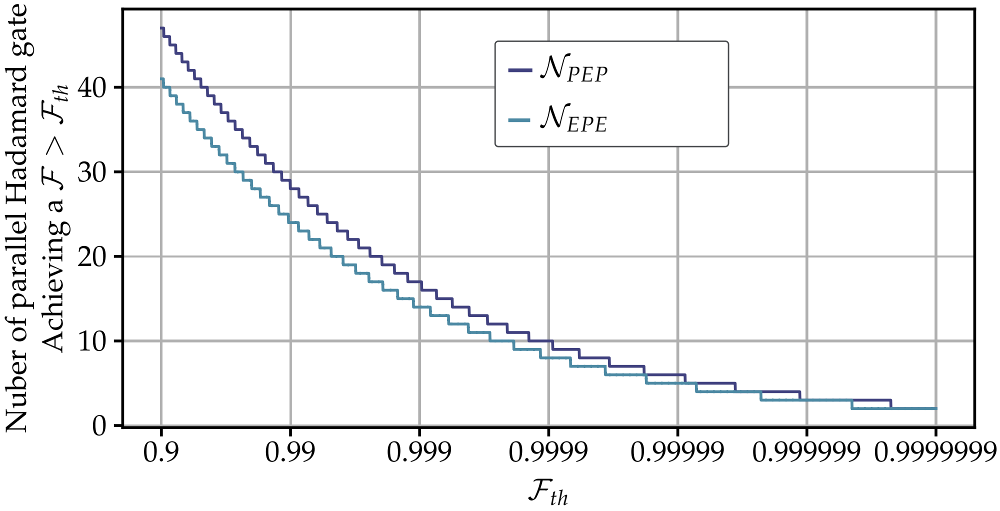

Figure 3.10: Number of gates realizing Hadamard operation with a fidelity above threshold as a function of $\mathcal{F}_{th}$.

3.4.2.4 Improving the parallelization of Hadamard gate with more complex RF driving

The number of gates realizing an operation with a fidelity above $\mathcal{F}_{th}$ can be improved by adding more RF harmonics of the fundamental frequency Ω in the signal driving the

EOM. As stated at the beginning, we need the electro-optic modulator to act similarly for each qubit. A square signal allowing to apply a phase ϕ from mode t_0 to $t_{M/2-1}$ and a phase $-\phi$ from mode $t_{M/2}$ to t_M would achieve such a function. The Fourier decomposition of this signal is

$$\phi(t) = \sum_{m=0}^{N} \frac{\mu}{2m+1} \sin\left((2m+1)\Omega t\right) \tag{3.55}$$

The limited bandwidth of the EOM implies truncating this series. We compare the exact truncature of a square signal to an approximated one, where the amplitude of the sine waves is chosen freely.

$$\phi(t) = \sum_{m=0}^{N} \mu_n \sin\left((2m+1)\Omega t\right) \tag{3.56}$$

Using a minimization algorithm, we optimize the amplitudes μ_n of the sine waves in order to maximize the number of parallel quantum gates that achieve the Hadamard operation with maximum fidelity.

Fig. 3.11 shows the number of parallel Hadamard gates, as a function of the number of tones driving the electro-optic modulators. The light blue lines correspond to the number of Hadamard achieving a fidelity above F_{th} for an exact truncature of a square, and the dark blue lines correspond to the approximated optimized truncature. The solid and dashed lines correspond respectively to the [PF-EOM-PF] and [EOM-PF-EOM] configurations.

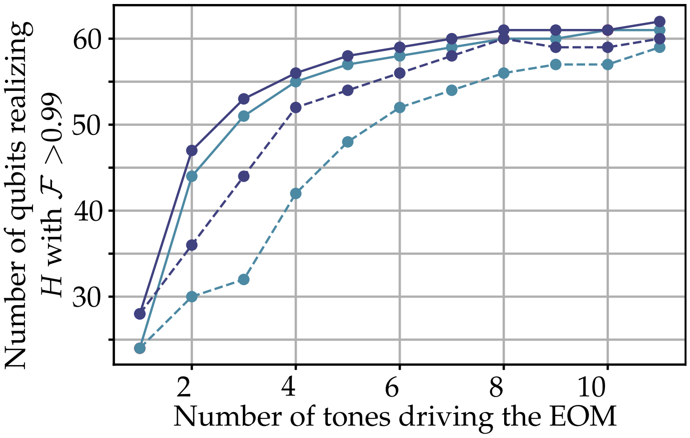

Figure 3.11: Number of qubits with fidelity above threshold as a function of fidelity threshold for [EOM-PF-EOM] (light blue) and [PF-EOM-PF] (dark blue) configurations with a single frequency RF modulation.

When driving with more than one tone, the performances are better for the optimized square truncature, especially for the [EOM-PF-EOM] configuration. Realistically, as this optimization considers adding odds harmonics, adding two tones is challenging with available commercial devices. With a qubit spacing of 20 GHz, it would require driving the EOMs at a RF frequency of 60 GHz.

3.4.3 Summary on the parallelization

In this section, we investigated the parallelization of single-qubit gates to frequency-bins and time-bin qubits qubits. We summarize the results in Table. 3.3.

Arbitrary unitary synthesis for a single qubit		
Configuration	Frequency-encoding $\{\|\omega_j\rangle, \|\omega_{j+1}\rangle\}$	Time encoding $\{\|t_k\rangle, \|t_{k+M/2}\rangle\}$
[EOM-PF-EOM]	$\mathcal{N}$=16	$\mathcal{N}$ **with** $\mathcal{F} > 0.99$**,** $\mathcal{P} = 1$
Driving at Ω	Phase gate : $\mathcal{F} = 1, \mathcal{P} = 1$ H gate: $\mathcal{F} = 1, \mathcal{P} = 0.98$ X gate: $\mathcal{F} = 1, \mathcal{P} = 0.81$	$\mathcal{N}_H$**=24** $\mathcal{N}_X$**=64**
Driving at 2Ω (Freq) Driving at 3Ω (Time)	Success probability improved	$\mathcal{N}_H$**=44** $\mathcal{N}_X$**=64**
[PF-EOM-PF]	$\mathcal{N}$**=16**	$\mathcal{N}$ **with** $\mathcal{F}$ **>0.99,** $\mathcal{P}$**=1**
Driving at Ω	H **gate:** $\mathcal{F}$**=1,** $\mathcal{P}$**=0.60** X **gate:** $\mathcal{F}$**=1,** $\mathcal{P}$**=0.27**	$\mathcal{N}_H$**=28** $\mathcal{N}_X$**=64**
Driving at 2Ω (Freq) Driving at 3Ω (Time)	**No improvement**	$\mathcal{N}_H$**=47** $\mathcal{N}_X$**=64**

Table 3.3: Comparison of the success probabilities of single qubit arbitrary unitary synthesis with [EOM-PF-EOM] and [PF-EOM-PF] configurations for single tone driving at Ω of the EOMs and for two encodings, with unit fidelities. The bold characters corresponds to **our results reported in this work**.

For frequency encoding, as stated in Section 3.4.1.1, the parallelization is limited by the ability of the electro-optic modulator to keep light in the computational space. As such, the number of qubits that can be processed in parallel depends on the number of guard modes needed between qubits. For both configurations the number of guard modes needed for parallelizing two gates is found to be 8, leading to the parallelization of 16 Hadamard gates, for a system of 128 frequency modes.

For time encoding, crosstalk is not a limiting parameter, as the two-scattering matrix performed by the PF ensures a deterministic coupling between only two time bins. As such, every qubit will operate with a unit probability of success. Fidelity is the limiting parameter. We find that the [PF-EOM-PF] configuration performs better than the [EOM-PF-EOM] configuration, allowing to parallelize 28 quantum gates with a fidelity exceeding the fidelity threshold, $\mathcal{F}_{th} \geq 0.99$, compared to 24 for the [EOM-PF-EOM] configuration.

When comparing the two encoding methods, it is intriguing to note that in both cases, parallelization is solely restricted by the electro-optic phase modulator (EOM). Another notable aspect is that the capacity to parallelize gates is constrained through the probability of success in the frequency domain, and the fidelity in the time domain. It is possible to get unit fidelity for each parallelized gate in the frequency domain, with a probability of success that depends on the gate. Conversely, for the time domain, it is possible to get a unit probability of success, for each parallelized gate, with a fidelity that depends on the gate.

3.5 Conclusion on the synthesis of single-qubit gates for time and frequency encoding

This chapter described the theoretical framework for the manipulation of frequency-bin and time-bin qubits.

The EOM is a diagonal matrix in the time domain, and the PF is a diagonal matrix in the frequency. Through the Fourier transform relation, each component is a scatterer in the conjugate space. The modulator has a programmability limited by the RF bandwidth. With a single sine way driving, the scattering of the EOM in the frequency domain is modeled by Bessel functions, coupling neighbor frequency bins. For time encoding, we show that the PF can act as a unitary beam splitter between two time bins separated by M/2 time bins. As a result, we encode frequency-bin qubits over two adjacent spectral modes, and time-bin qubits over two time bins separated by M/2 temporal modes.

We compare the performances of two device configurations, [EOM-PF-EOM] and [PF-EOM-PF]. For frequency encoding, we compare our results with the literature. For time-bin encoding, we obtain a unit probability of success and fidelity for any arbitrary unitary for both configurations.

We focused on the parallelization of such single qubit gates. We define for both encoding the limitation on the parallelization, both rising from the limited bandwidth of the EOM. For frequency-bin qubits, scattering of the EOM introduces crosstalk in modes close to the qubit space. As such, we find it sufficient to keep six guard modes between two qubits to ensure crosstalk below 10^{-3} between two qubits. For time encoding, the limit on the bandwidth of the EOM constrains the number of gates reaching a fidelity above a given threshold $\mathcal{F}_{th}$. We investigate the driving of the modulator with a single sine wave, and then with a more complex driving. For $\mathcal{F}_{th}$=0.99, we assess the parallelization of 24 and 28 Hadamard gates for respectively the [EOM-PF-EOM] and the [PF-EOM-PF] configuration with single tone RF driving. This result increased to respectively 44 and 47 with dual-tone RF driving.

We have noticed interesting works that go further than single qubit gates. In the frequency domain, a heralded controlled-Z gate has been proposed in [55]. More recently in [85], a frequency-encoded controlled-not gate has been implemented using the [EOM-PF-EOM] configuration. With this method, they realize a post-selected controlled-not gate with a fidelity of 0.99 and a probability of success of 0.04.

Another way of exploration is the use of qudits for quantum information processing [160]. In the frequency domain, a discrete Fourier transform gate for a qudit of dimension 3 has been realized in [57]. More recently, in [75], numerical solutions have been found to enable such a discrete Fourier transform gate for qudits of dimension up to d=10. For time-bin encoding, replacing the 2-scattering operation with a scattering extended to more modes would enable the manipulation of higher-dimensional time-bin quantum states.

Chapter 4

Experimental processing of frequency-bin qubits

Frequency-domain quantum information processing has gained a lot of interest in the past years, due to the programmability offered by off-the-shelf fibered PFs and EOMs. In Chapter 3, we introduced the theoretical and numerical models for the synthesis of single-qubit gates. At the beginning of this Ph.D. thesis, in 2020, only two groups were investigating frequency-domain information processing with electro-optics modulators and programmable filters, in Oak Ridge/Purdue (United States) and Varennes (Canada). The experimental investigations were mainly directed toward the manipulation of frequency-bin qubits and qutrits (qudit of dimension three) [57, 61]. These manipulation schemes enabled realization of Hong-Ou-Mandel experiments (HOM) with photons generated from commercial lithium niobate waveguides [66, 87], quantum state tomography of frequency-bin entangled states generated by silicon nitride micro-resonators and hydex micro-resonators [68, 76], two-qubit gates [85], and deterministic two-qudit gates [64], where the action of a time-bin qudit is controlled with a frequency-bin qudit.

The interest in frequency-domain quantum information processing has been steadily growing since 2020, with the emergence of new groups in Hanover [59, 73] and Jena [79] (Germany), Pavia (Italy) [81, 84, 88], and us (France) [74, 78], as well as ongoing works from the team in Oak Ridge/Purdue [67, 75, 86]. The experimental demonstrations have been directed toward the efficient generation and characterization of higher-dimensional quantum states [75, 79, 86, 88], heralded Hong-Ou-Mandel experiments and Bell-state analyzers [59, 67]. As the landscape of frequency-domain information has been increasingly growing, it is now possible to envision practical uses in quantum information processing.

One mature application of quantum information processing is quantum key distribution

Work	**Configuration**	**Dimensionality**	**Demonstrations**
Kues et al. [68]	PF-EOM-PF	2 to 4	Tomography, Bell-like interferences
Lu et al. [57] †	**EOM-PF-EOM**	2 to 3	Gate characterization
Imany et al. [76]†	PF-EOM-PF	2 to 3	Tomography, Bell-like interferences
Lu et al. [66]†	EOM-PF-EOM	2	HOM, Tomography
Imany et al. [87]	**PF-EOM-PF**	2	HOM
Lu et al. [85]†	EOM-PF-EOM	2	Two-qubit gate
Imany et al. [64]†	**PF (frequency) delay lines (time)**	32 (frequency) 3 (time)	Deterministic hyper-encoded two-qudit gates
Lu et al. [61]†	**EOM-PF-EOM**	2	Arbitrary single-qubit rotation
Khodadad et al. [59]	PF-EOM-EOM	2	HOM between heralded single photons
Lingaraju et al. [67]†	**EOM-PF-EOM**	2	Bell state measurement
Lu et al. [75]†	**EOM-PF-EOM**	2 to 3 exp. 2 to 9 sim.	gate characterization qudit manipulation
Lu et al. [86]†	PF-EOM-PF	2 to 8	Tomography
Sabattoli et al. [81]*	EOM	2	Tomography
Clementi et al. [84]*	EOM	2	Tomography
Mahmudlu et al. [73]	PF-EOM-PF	2 to 4	Tomography
Ponce et al. [79]	PF-EOM-PF	2 to 6	Bell-like interferences
Borghi et al. [88]*	EOM	2 to 4	Tomography
This work *	**EOM-PF-EOM**	**2**	**Parallelization of 34 single qubit gates**
			Bell-like interferences
			Tomography
			QKD protocol
			Proof-of-concept of quantum network
			HOM

Table 4.1: List of the experimental works performed with frequency-encoding using fibered EOMs and PFs. The double line separates works published before and after this Ph.D. thesis. HOM: Hong-Ou-Mandel. †: works from the team in Purdue/Oak Ridge, *: frequency-domain experiments on photons generated by SOI micro-resonator structures.

(QKD) protocols. Most QKD protocols rely on the distribution of single photons [150] or entangled states [161]. Usual implementations of such QKD protocols use polarization and time-bin entanglement. However, in practical implementations, environmental fluctuations can induce uncontrolled change in the quantum states. Tackling this problem usually requires an active stabilization scheme. The intrinsic quantum state stability offered by frequency encoding suppresses the need for such stabilization schemes.

However, realizing such a protocol requires two major elements: experimental realization of single-qubit operations acting independently on frequency bin qubits, measuring the state of the qubits, and generating frequency-encoded qubits adequate for such manipulation.

This chapter uses the results presented in the two previous chapters. We perform an experimental synthesis of a tunable single qubit gate for frequency-bin qubits, using the formalism introduced in Chapter 3. We then conduct experiments with these synthesized quantum gates applied to the photons generated by the integrated sources described in Chapter 2. In section 4.1, we investigate the **experimental realization and characterization with classical light of a tunable single qubit gate**. Then, in section 4.2, **we assess the parallelization of these single qubit gates**, and the experimental considerations to achieve this goal. We investigate the number of guard modes needed for the parallelization of two adjacent single qubit gates. We furthermore explore the parallelization of Hadamard gates applied to two contiguous qubits. In section 4.3, **we report the generation of frequency-entangled qubit pairs** from the silicon on insulator ring resonator introduced in Chapter 2. We perform Bell-like interference and quantum state tomography, and we parametrize the four Bell states using the frequency-domain qubit gates introduced in Chapter 3. In section 4.4, **we investigate the broadband frequency-bin qubit generation**, allowed by the broadband spectrum and low-FSR of our photon pair source. We parallelize the quantum state tomography to 17 parallel frequency-bin entangled qubit pairs and perform a proof-of-concept of a fully connected network. With our source, we show the ability to generate a five-user trusted-node free connected network, where each pair of users exchange secret keys with a local rate of 1 bit per second. We use photon pairs generated by the LNOI waveguide, to perform a frequency-domain version of the Hong-Ou-Mandel experiment. Finally, section 4.6 provides a conclusion to this chapter.

4.1 Tunable single qubit gate

We present in this section the frequency manipulation possibilities of an increasing number of devices. We start by characterizing a single EOM. Then, we investigate the temporal synchronization between two EOMs in series. Then, we investigate the EOM-PF-EOM for the realization of a tunable single qubit gate and assess its performance, by measuring the fidelity and success probability of the realized operation. We then utilize this single qubit gate in a frequency-version of the Mach-Zehnder interferometer.

4.1.1 Characterization of a single electro-optic phase modulator

In Chapter 2, we introduced the electro-optic phase modulator (EOM) as a device that applies a time-dependent phase shift to the optical field. The Fourier transform of a time-domain dependent phase shift leads to frequency domain scattering. Physically, this phase change is induced by applying a time-dependent voltage $V(t)$ with a RF generator. The applied voltage changes the refractive index of the electro-optic material and, thus, the path length seen by the optical field. If $V(t)$ is a sine wave with a peak voltage V_0 at a frequency Ω_m, the time-dependent RF sine wave can be written as

$$V(t) = V_0 \cos\left(\Omega_m t + \theta\right). \tag{4.1}$$

The time-dependent phase imprinted on the optical field is then

$$\phi(t) = \mu \cos\left(\Omega_m t + \theta\right). \tag{4.2}$$

This equation is similar to the equation presented in 3.17. The relation between the applied voltage and the obtained modulation index μ is

$$\mu = V_0 \frac{\pi}{V_\pi}. \tag{4.3}$$

The proportionality factor $\frac{\pi}{V_\pi}$ between V_0 and μ incorporates various aspects, including the non-linear efficiency and the geometry of the modulators. In our analysis, the voltage V_0 is the nominal voltage set on the generator. V_π is the voltage that must be applied by the generator to achieve $\mu = \pi$, accounting for the losses in the RF setup.

We must measure the V_π, in order to map the input voltage to the modulation index. We use the setup presented in Fig. 4.1.(a). A continuous wave laser is sent into a modulator, driven by an RF sine wave of amplitude V_0. We use a programmable filter as a 21 GHz bandpass filter tuned successively at the frequencies $\omega_0 + n \cdot \Omega_m$, for n $\in$ {-2,-1,0,1,2}, where ω_0 is the frequency of the laser. The light intensity I_n of each frequency mode $\omega_0 + n \times \Omega_m$ is then measured by a photodiode. We repeat this measurement for several nominal peak voltages. Fig. 4.1.(b) shows the experimental results (dots) and fit to Bessel functions using Eq. 3.18. The measured intensity is normalized with respect to the intensity at the frequency mode ω_0 when no voltage is applied to the modulator. As the voltage of the RF sine wave increases, the fraction of light in the initial mode ω_0 decreases to populate the neighboring modes. The solid line corresponds to fits with the Bessel function, with V_π as the adjustable parameter. For this particular modulator, the determined value is V_π = 11.28± 0.08 V, for a modulation frequency Ω_m= 21 GHz.

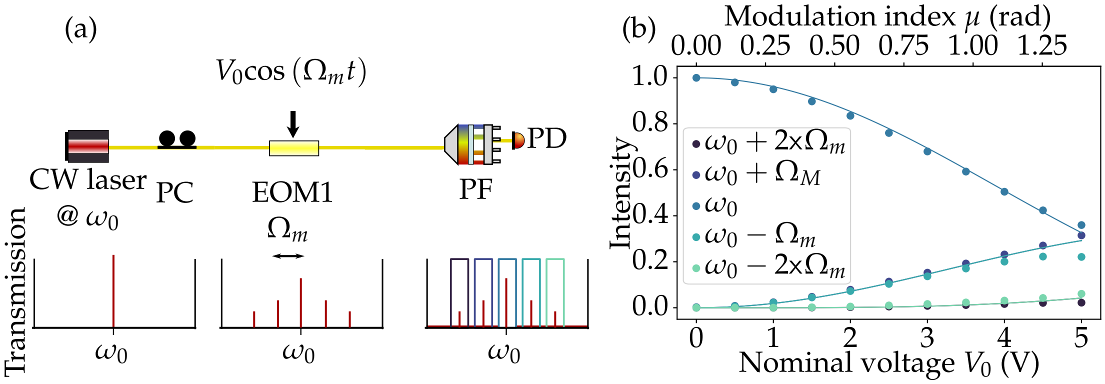

Figure 4.1: (a): Setup for the characterization of an EOM. CW laser: continuous wave laser, PC: polarization controller, EOM: electro-optic modulator, PF: programmable filter, PD: photodetector, with the spectra corresponding to each steps. (b) Variation of the intensity at frequencies $\omega_0 + n\Omega_m$ for n$\in$ $\{-2, \cdots, 2\}$, as a function of the nominal voltage. Dots are experimental results, and solid lines are simulations using Eq. 3.18.

From the theory, we expect the light intensity to be converted symmetrically to the modes around ω_0, i.e. $I_n = I_{-n}$. However, we experimentally observe an asymmetry between light converted in the upper and lower modes. The possible explanation for this asymmetry is the strain applied to the modulator for high RF power. To quantify this effect, we measure the ratio between the intensities of light in the symmetric modes I_{-1}/I_{+1}, as shown in Fig. 4.2. The dots represent the experimental data, and the solid line corresponds to the expected symmetry $I_{-1}/I_{+1} = 1$. At low voltages, the low measured intensities lead to high uncertainties. The ratio is close to 1 for voltage values under 2 V and decreases for higher values. This effect is a source of imperfection and leads to a reduction of the performances of the synthesized gates presented in section 4.1.3.

Throughout this manuscript, we use the EOMs to reach specific values μ. As the modulators have different values of V_π, we adapt the nominal voltage of the driving RF signal for each modulator to obtain a specific modulation index. We only give the targeted modulation index needed for the experiments. We list in Appendix B.1 the correspondence between the modulation index and nominal voltage for each modulator. In the following section, we focus on a system composed of two modulators in series. As these devices apply time-dependent phase shifts, we investigate the synchronization between two EOMs.

4.1.2 Two daisy-chained EOMs

If we consider two modulators EOM1 and EOM2 in series, each applies a time-dependent phase shift to an incoming photonic field, respectively $\phi_1(t) = \mu_1 \cdot \cos(\Omega_m t + \theta_1)$ and $\phi_2(t) = \mu_2 \cdot \cos(\Omega_m t + \theta_2)$. The light exits the second modulator acquiring an overall

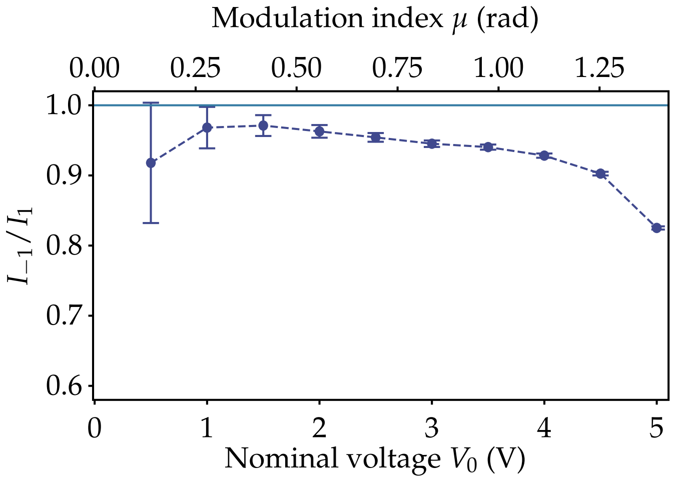

Figure 4.2: Ratio between the intensity of the light converted in the frequency band $\omega_0 - 1 \times \Omega_m$ and the band $\omega_0 + 1 \times \Omega_m$. Dots are experimental points, and the solid line is the expected constant value.

phase

$$\Phi(t) = \phi_1(t) + \phi_2(t). \tag{4.4}$$

By adjusting the relative phase between the two modulators ($\theta_2 - \theta_1$), we can control the amplitude of the overall modulation phase from 0 to $\mu_1 + \mu_2$. As it is similar to changing either θ_1 or θ_2, we set $\theta_1 = 0$, and define the relative phase as θ, applied by the second modulator. If the two time-dependent phase shifts have the same amplitude ($\mu_1 = \mu_2 = \mu$) and are in phase ($\theta = 0°$), the two phases add up, resulting in the optical phase gaining twice the RF signal applied by one modulator. If the two signals are out of phase ($\theta = 180°$), they cancel each other out, and the optical field experiences no phase change. However, experimentally, while traveling through the optical fiber linking two EOMs, an optical field acquires an additional phase that needs to be accounted for.

To investigate this behavior, we use the setup in Fig. 4.3.(a) A continuous wave laser is injected at frequency $\omega_0 = 194$ THz into the two modulators system. We drive both modulators with the respective RF driving amplitudes V_1 and V_2 so that the modulation index seen by the optical field is $\mu = 0.816$ for both devices. We control the synchronization of both EOMs by changing the phase between both RF signals θ, which can be arbitrarily set by the RF driver. A PF is used as a 21 GHz bandpass filter to select the laser frequency ω_0. The intensity is measured by a photodiode Newport 1811. Fig. 4.3.(b) shows the experimental results (dots) and simulated results (dashed line). When the two modulators are in phase, the optical field is modulated with a sine wave of amplitude 2μ, resulting in most of the light converted in neighbor modes. When the two modulators are out of

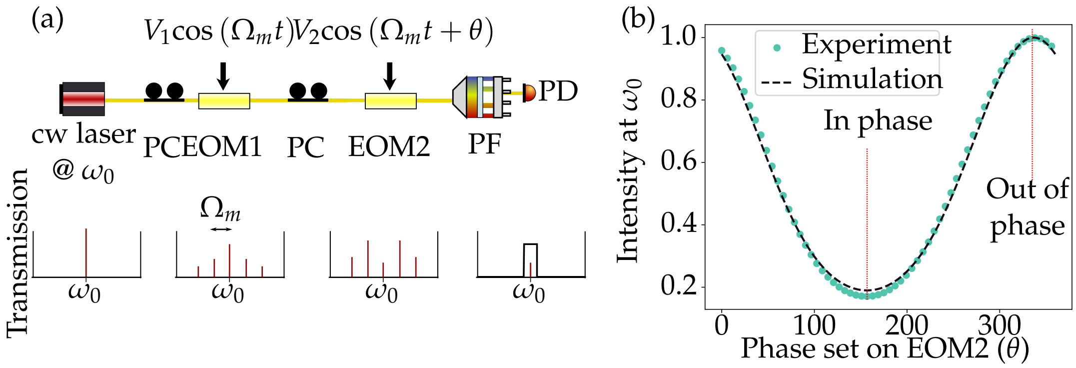

Figure 4.3: a. : Experimental setup for the characterization of the temporal phase dependence of two daisy-chained EOMs. PC: polarization controller, PF, programmable filter, PD: photodiode. b. : Experimental results and fit to the theory of the intensity of light in the mode ω_0 varying with the phase θ set on the RF generator.

phase, the two modulations cancel out and a maximum intensity is observed at ω_0. The phase needed to be applied to EOM2 for the modulators to be out of phase is $\theta = 337.7° \pm 0.1°$. Compared to the expected value of 180°, it means that the fiber induces an additional phase of 157.7°. This phase is also dependent on the optical frequency, as chromatic dispersion occurs in the fibers, as further discussed in 4.2. In the next section, we will complete our daisy-chained EOMs with a programmable filter placed between the two modulators to synthesize a tunable frequency-domain quantum gate.

4.1.3 Experimental synthesis of a tunable single qubit gate

In this section, we characterize a configuration of two electro-optic phase modulators and one programmable filter in a [EOM-PF-EOM] configuration to perform quantum gates on frequency-bin qubits. This set of devices acts as a multipath frequency-domain interferometer, where the PF allows tuning the interferences between the several frequency-bins, achieving controlled single qubit operations [55, 74]. While it is possible to realize an arbitrary unitary with this combination, in this section we are interested in synthesizing a tunable operation that can smoothly go from Identity (I) to Hadamard (H) operation, for which the matrix form is

$$I = \begin{pmatrix} 1 & 0 \\ 0 & 1 \end{pmatrix}, \; H = \frac{1}{\sqrt{2}} \begin{pmatrix} 1 & 1 \\ 1 & -1 \end{pmatrix}. \tag{4.5}$$

For this particular configuration, the only tunable parameter controlling the performed operation is the relative phase between the frequency modes applied by a PF. The RF frequency is equal to the qubit spacing chosen to be 21 GHz. It is worth noting that this scheme works for any qubit spacing larger than the programmable filter resolution, and lower than the RF bandwidth of the devices. Fig. 4.4 shows the phase imprinted by

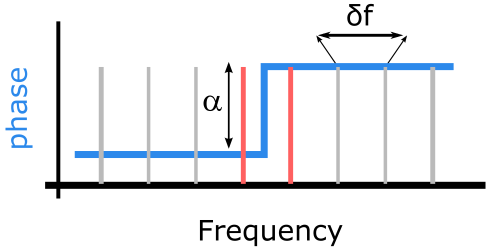

Figure 4.4: Representation of the phase mask that needs to be applied by the programmable filter to realize a tunable operation. The red bars represent the qubit modes, and the grey bars represent neighbor frequency modes.

the programmable filter. The qubit is encoded on two frequency modes: ω_0 and $\omega_1 = \omega_0 + \Omega_m$, here represented by the red bars. As the modulators have the same amplitude and are out of phase, we expect that no modulation appears when α=0. As we raise α, the interference pattern changes, up to $\alpha = \pi$ rad, where we expect an equal splitting between the two qubit modes.

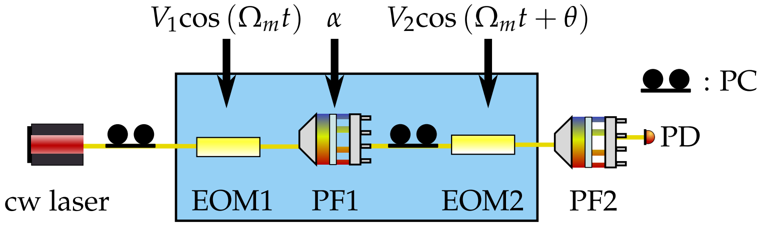

Figure 4.5: Setup for the characterization of the tunable quantum gate. CW laser: continuous wave laser. PC: polarization controller, PD : photodetector. EOM: electro-optic modulators, PF: programmable filters.

To characterize the behavior of the [EOM-PF-EOM] configuration for realizing a tunable quantum gate, we utilize the experimental setup depicted in Fig. 4.5. A continuous wave laser at frequency ω_0 emulates a qubit in the logical 0. The electro-optic modulators (EOMs) are driven by signals with the following parameters according to previous implementations [57, 61]

$$\mu = 0.816 \text{ rad}, \theta = 180 \text{ deg}. \tag{4.6}$$

PF1 imprints the phase mask shown in Fig. 4.4, with the parameter α tunable from 0 to 2π radians. Downstream of the [EOM-PF-EOM] elements, another programmable filter acts as a tunable bandpass filter to sequentially measure the light intensity in the frequency modes ω_0 and ω_1. We normalize the measured intensities by a reference value obtained when the modulators are off, and the PF applies a flat phase. This normalization allows us to characterize the performances of the gates independently from the insertion loss of the devices. Although it will not change the fidelity, insertion loss impacts the probability of success. With 3.5 dB of insertion loss for the PF and 2.5 dB for the EOMs, the transmission of the [EOM-PF-EOM] configuration is ≈11%.

The experimental results are presented in Fig. 4.6. In Fig. 4.6.a., we observe the normalized intensity transmitted in the two qubit modes as a function of α. As expected, when $\alpha = 0$, most of the light is transmitted in the frequency mode ω_0, realizing the Identity transformation, and when $\alpha = \pi$, the intensity is evenly split between the two frequency modes, realizing the Hadamard transformation. All intermediate operations can be controlled. The Identity operation is obtained for all $\alpha = 2n\pi$, $n \in \mathbb{N}$.

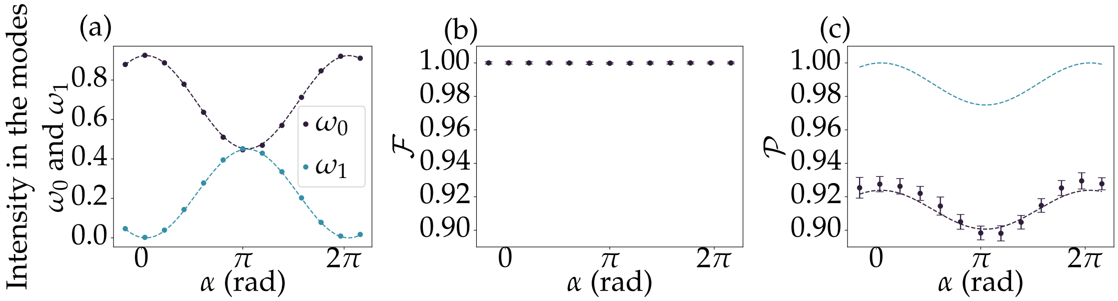

Figure 4.6: a.: Normalized intensity transmission in the frequency modes ω_0 and $\omega_1 = \omega_0 + \Omega_m$ as a function of the tuning parameter α. b.: fidelity of each realized rotation to simulated ones. c.: black dots: measured success probability of the gate, blue dashed line: theoretical success probability, black dashed line: theoretical success probability corrected to fit the experimental points.

Fig. 4.6.b. shows the fidelity of each realized rotation compared to the ideal ones. Each gate exceeds a fidelity of 0.9997 ± 0.0006. Fig. 4.6.c. shows the measured success probability (dots), numerical simulations (dashed blue line), and numerical simulations multiplied by 0.93, to fit the experimental results (dashed dark line). We compute the fidelity and probability of each gate using Eq. 3.25 and Eq. 3.24. From the simulation, we observe that the Identity operation (α=0) should lead to a unit fidelity and probability of success, and the Hadamard operation (α=π) should lead to a unit fidelity and a success probability of 0.9748 [61]. We experimentally do not reach the expected success probabilities, as shown by the difference between the simulated results (dashed light blue line) and experimental points (dots). The measured success probability only reaches ≈ 0.93 for Identity. One explanation for this diminution is the imperfect behavior of the modulators: asymmetry in the distribution of light in the symmetric modes observed in Fig. 4.2. This results in imperfect interferences which impacts the performance of the synthetized gate.

The theoretical limit of 0.9748 for the success probability of the Hadamard operation is due to light scattering in modes outside of the qubit space. It is then interesting to look at how much light is lost. We examine the crosstalk for the Hadamard operation, for which it is maximal. Using the same setup as in Fig. 4.5, we measure the 14x14 transfer matrix of a Hadamard gate applied to a qubit and the 6 neighbor modes on each side. Each matrix coefficient $C_{i,j}$ is measured by tuning the laser on the frequencies $\omega_0 + i\Omega_m$, and applying a bandpass filter on PF2 centered at $\omega_0 + j\Omega_m$, with $i, j \in \{-6, \cdots, 7\}$.

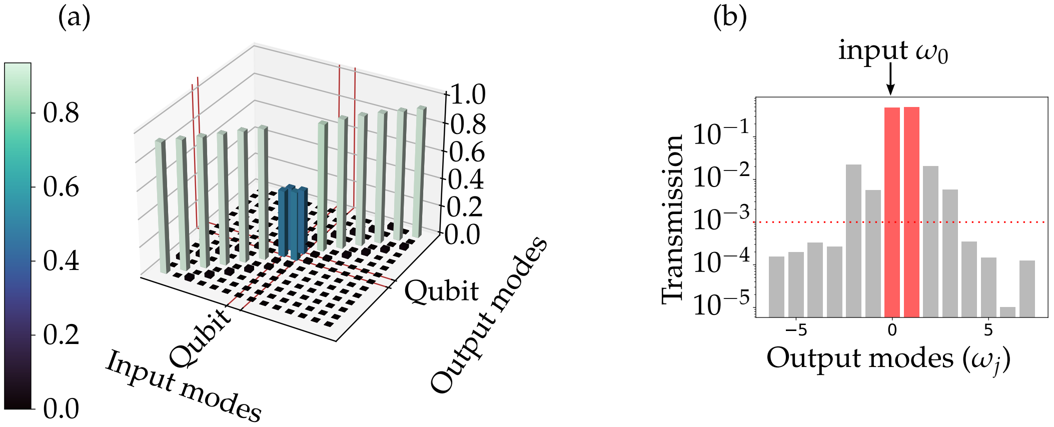

Figure 4.7: (a): Measured normalized transfer matrix for a 14x14 frequency space. (b): Distribution of the transmission on frequency modes $\omega_0 + j\Omega_m$ when light is injected in the frequency modes ω_0.

Fig. 4.7.(a) displays the measured intensity transfer matrix, where a Hadamard operation is applied to a qubit. Each row represents the normalized intensities measured in the frequency modes $\omega_0 + j\Omega_m$, when light is injected in mode $\omega_0 + i\Omega_m$. $j \in \{-6, \cdots, 7\}$.

We examine experimentally the crosstalk, as defined in 3.4.1.1. In this regard, we look at the normalized intensity distribution in each frequency mode $\omega_j = \omega_0 + j\Omega_M$, when injecting light in the frequency mode ω_0. The experimental measure of the crosstalk is presented in Fig. 4.7.(b). In the computational space, we find most of the light, equally distributed between the two computational modes, as expected from the action of the Hadamard gate. Crosstalk can be observed in the modes outside the computational space. By maintaining two guard modes between two qubits, the crosstalk can be reduced to below 10^{-3}.

In this section, we explore how setting the [EOM-PF-EOM] configuration to a Hadamard gate can be utilized to construct a MZI interferometer in the frequency domain.

4.1.4 Frequency-domain Mach-Zehnder interferometer

A Mach-Zehnder interferometer is a spatial domain interferometer, consisting of two 50:50 beam splitters, and a phase shifter present in one arm. A scheme of principle is presented in Fig. 4.8. This structure is very useful for path-encoded quantum information, as one Mach-Zehnder implements an operation tunable from Identity ($\phi = 0$) to the bit-flip gate ($\phi = \pi$), with the Hadamard gate ($\phi = \pi/2$) in between.

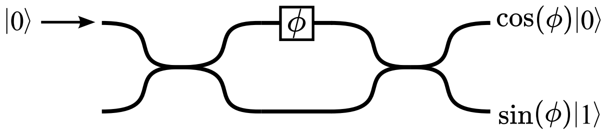

Figure 4.8: Scheme of a spatial Mach-Zehnder interferometer. Light input in the upper path and the output is a superposition of the upper and lower path, controlled by the phase ϕ.

In terms of logic gates, this structure requires two Hadamard gates for the beam splitters and a phase gate. It is possible to implement this interferometer, using frequency-domain qubit gates. Because of the limited available resources at the time of the experiment, we could not use [EOM-PF-EOM] setups for both Hadamard gates. A simple setup was used for the input of the interferometer, with just one EOM and one PF [59, 87]. Fig. 4.9 presents the setup of the experiment and the representation of the action of devices in the frequency domain along the experiment. A CW laser generates light in a single frequency mode at ω_0. An EOM creates a frequency-bin superposition, and the PF filters out the undesired frequencies. Using a modulation index of $\mu = 1.435$ would result in a probabilistic Hadamard gate [87]. However, we can only experimentally drive our EOM with a maximal modulation index of $\mu \approx 1.3$, c.f. Fig. 4.1. We must apply an additional attenuation with PF1 to create a true equal splitting between the two frequency modes. This PF also applies a relative phase ϕ between the two frequency modes. The [EOM-PF-EOM] configuration acts as the second 50:50 beam splitter. PF2 selects the measured frequency mode, ω_0 or ω_1, and we measure the output signal with a power meter. Fig. 4.10 shows the experimental result. Looking at the light output in both frequency modes, we change the relative phase applied by PF1 to tune the superposition from 100:0 to 0:100. The visibility of the interference is 0.98. As we measure a fidelity above 0.99 for the [EOM-PF-EOM] configuration performing 50:50 beam splitting, the limitation on the visibility could come from the first 50:50 beam splitter realized with EOM1 and PF1.

We have shown that with our choice of parameters, the [EOM-PF-EOM] setup enables a smooth tuning from Identity to Hadamard. Using a different combination of parameters for the EOMs and PF, it is possible to realize an arbitrary rotation over the whole Bloch Sphere i.e.: go beyond the Hadamard gate, up to a bit flip. However, a bit flip would require a modulation index of $\mu = 3.28$ rad, which is twice the maximum modulation

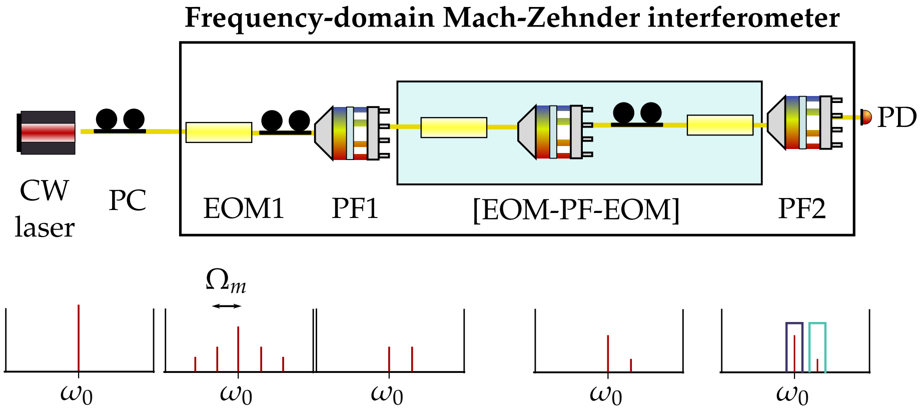

Figure 4.9: Experimental setup for the frequency-domain Mach-Zehnder interference with classical light, and associated spectrums. PC: polarization controller, PF: programmable filter, EOM: electro-optic modulator, PD: photodetector.

index that we can reach ($\mu \approx 1.3$).

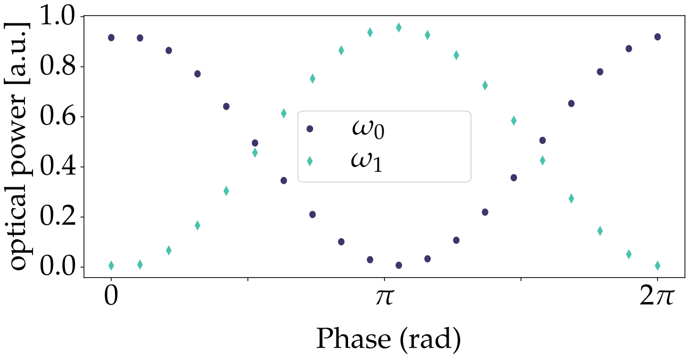

Figure 4.10: Experimental measurement of Mach-Zehnder interferences.

This [EOM-PF-EOM-PF-EOM] configuration of Fig. 4.9 requires however more devices and is thus more lossy (18 dB) than the [EOM-PF-EOM] configuration alone (9.5 dB) This tremendously hinders the performances for single photon applications.

This section focussed on the experimental synthesis of single-qubit gates. In the next section, we investigate the parallelization of these single qubit gates, using the same set of devices.

4.2 Parallelization of single-qubit gates

We now explore the parallelization of Hadamard gates to independent qubits. First, we verify that two guard modes are indeed sufficient for separating two neighbor qubits, as investigated in Section. 4.1.3. Then, we investigate the broadband parallelization of such a single qubit gate. We show that chromatic dispersion in the fibers needs to be compensated. We then look at the performances of Hadamard gates functioning throughout the C-band. Finally, we perform numerical simulations to explore the parallelization of the Hadamard gate on two contiguous frequency-bin qubits.

4.2.1 Independent tunable single-qubit gates

It is desirable to manipulate independently many qubits with a single set of devices. In section 4.1.3, we determined that a two-mode spacing between qubits could provide a crosstalk $\leq 10^{-3}$. Fig. 4.11.a. shows the square pattern is repeated so that the same quantum gate is performed on all the qubits processed in parallel. Fig. 4.11.b. shows how to implement different quantum gates for each qubit independently.

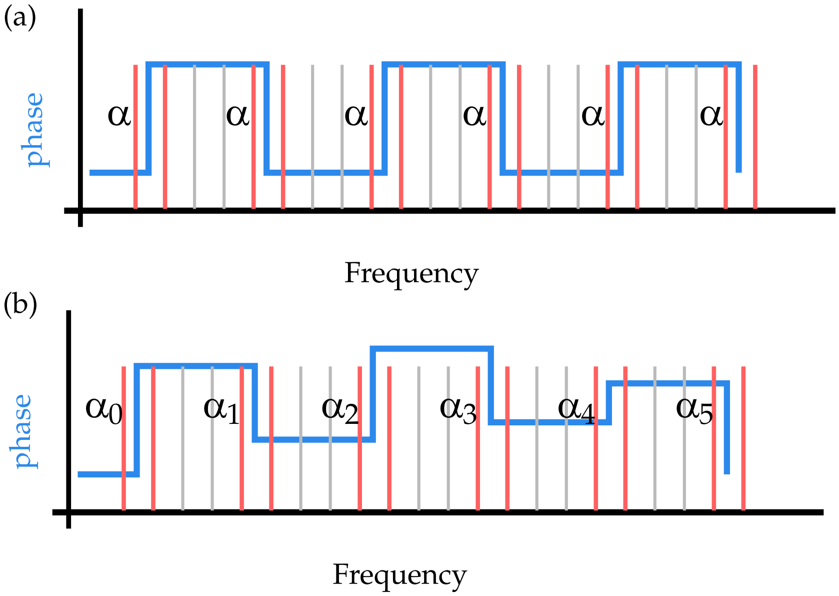

Figure 4.11: Phase pattern (blue) applied by the programmable filter of the [EOM-PF-EOM] configuration. The qubit modes (red) are separated by two guard modes (grey). (a): the same quantum gate is performed for all the considered qubits. (b): every qubit undergoes a different transformation.

To investigate the parallelization ability of our [EOM-PF-EOM] configuration, we experimentally implement a similar phase mask as Fig. 4.11.a. with the PF. We chose $\alpha = \pi$ rad thus applying three Hadamard gates to three independent qubits. Using the setup in Fig. 4.5, we measure the intensity transfer matrix of a 14x14 frequency space, comprising the three qubits. Fig. 4.12 shows the intensity transfer matrix. We observe the three Hadamard operations for which the fidelity exceeds 0.999.

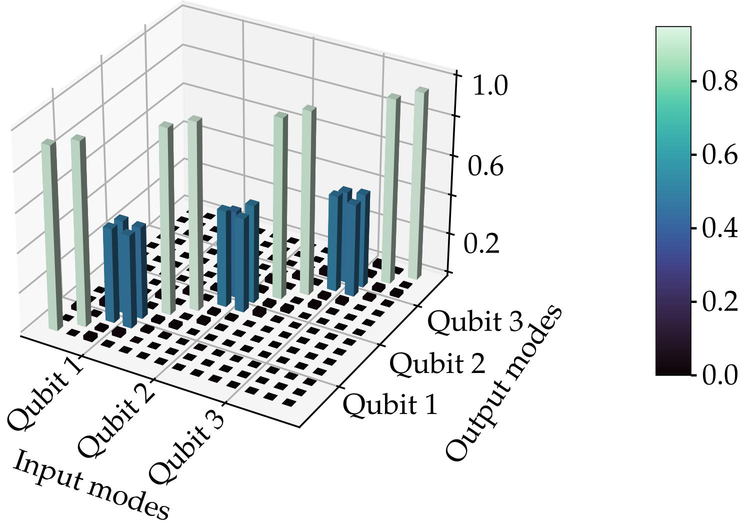

Figure 4.12: Measured normalized intensity transfer matrix of a 14x14 frequency space, where three Hadamard gates are applied to three qubits, separated by two guard modes.

It is important to verify whether the crosstalk between qubits separated by two guard modes remains below 10^{-3} while applying the three Hadamard gates. For this purpose, we examine the intensity distribution on each frequency mode by injecting light into the logical 0 of qubit 2. As qubit 2 is surrounded by two neighboring qubits it allows us to investigate the crosstalk from qubit 2 to its closest neighbors. The intensity distribution in Fig. 4.13 is similar to the one displayed in Fig. 4.7. The crosstalk below 10^{-3} is preserved in qubits 1 and 3. A tradeoff needs to be made between crosstalk and the number of qubits processed in parallel. The closer the qubits, the more processed qubits in a given bandwidth, but also the higher the crosstalk. In this experiment, the three qubits subspace uses 10 frequency modes, with each mode spaced by 21 GHz. The total frequency span amounts to 210 GHz (1.57 nm).

We showed that it is possible to parallelize quantum gates by changing the phase mask of the programmable filter. However, this holds only if all other parameters of the quantum gate remain fixed for every optical frequency. For instance, the modulation index is independent of the wavelength, but the relative phase between the two modulators is impacted by chromatic dispersion, which causes a frequency-dependent temporal phase. As

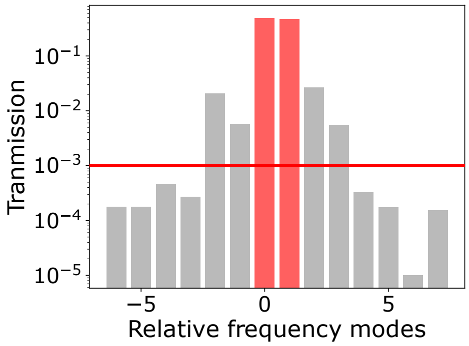

Figure 4.13: distribution of the transmission surrounding qubit 2 (grey bars) measured when injecting light into logical 0 of qubit 2 state. X-axis: frequency modes relative to qubit 2's logical 0.

we require the temporal phase between the EOMs to be fixed at 180°, we need to compensate for this dispersion. To measure the amount of chromatic dispersion D in our system, we use the setup depicted in Fig. 4.14. A tunable laser is sent into the [EOM-PF-EOM] group. The modulators are driven by sine waves. The voltages are chosen so that the modulation index is μ=0.816 rad for both modulators. PF2 applies a passband a 21 GHz filter at the laser frequency. For each optical frequency, the relative phase θ of the modulators is tuned from 0 to 360°, by the RF Generator. Fig. 4.15 shows the experimental

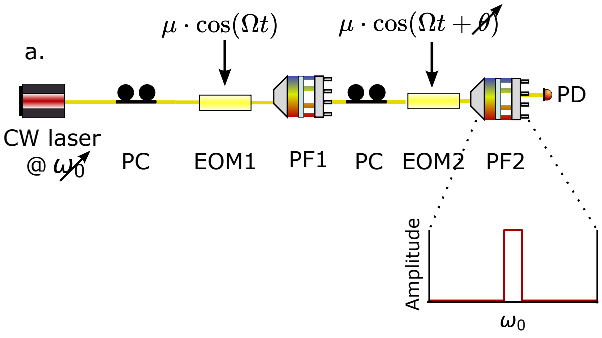

Figure 4.14: Setup for the measure of the achromatic dispersion in the [EPE] configuration.

results. In Fig. 4.15.a. we observe for each optical frequency an interference pattern, similar to Fig. 4.3.(b). Dispersion adds an extra phase that shifts the position of the maximum and minimum. This phase is related to the dispersion term as

$$\theta_{\text{disp}}(f) = \theta_0 + 360 \times \frac{c \times D}{T} \left(\frac{1}{f} - \frac{1}{f_0} \right) \tag{4.7}$$

Where $\theta_{\text{disp}}(f)$ is the extra frequency-dependent phase, θ_0 is the phase leading to the maxima for the interference pattern at frequency f_0, D is the amount of dispersion in the system, c is the speed of light and $T = \frac{2\pi}{\Omega_m}$ is the RF modulation period. Fig. 4.15.b. shows the phase θ that needs to be applied to reach the maximum, i.e. perfectly synchronize the two modulators out of phase. We can fit this variation with a dispersion of 0.4 ps/nm, using Eq. 4.7.

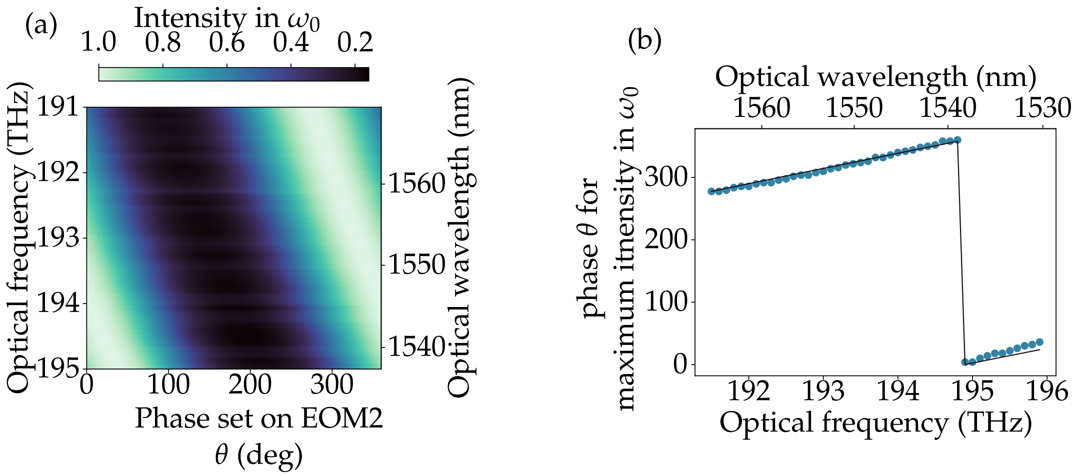

Figure 4.15: (a): Variation of the intensity in the mode ω_0 with the relative phase on EOM2, as shown in Fig. 4.3, for several optical frequencies. (b): phase value corresponding to the maximum of the interference for each optical frequency (dots), fitted with a dispersion of 0.4 ps/nm (solid line).

With the programmable filter of the [EOM-PF-EOM] configuration, we apply a negative dispersion phase mask to correct for this positive dispersion. We repeat the experiment with the applied negative dispersion of -0.4 ps/nm. The results of this experiment are shown in Fig. 4.16. Fig. 4.16.a. shows the interference pattern for each optical frequency. It is clear in this plot that the maximum is reached for a stable value θ for each optical frequency. Again, we can look at the position of the maxima for each wavelength, shown in Fig. 4.16.(b). It corresponds to a residual dispersion of 0.032 ps/nm. Using this -0.4 ps/nm negative dispersion correction, we have suppressed chromatic dispersion by one order of magnitude.

For any phase pattern necessary for the tunable quantum gates, this dispersion correction is taken into account as a phase background. Fig. 4.17 shows how this affects the phase pattern applied to a qubit (red vertical bars) in the case of the Hadamard gate. The black dashed line represents the dispersion correction, while the solid blue line corresponds to a phase mask producing a π rad phase shift between the qubit modes. Using this compensation scheme, we evaluate the fidelity and success probability of a Hadamard

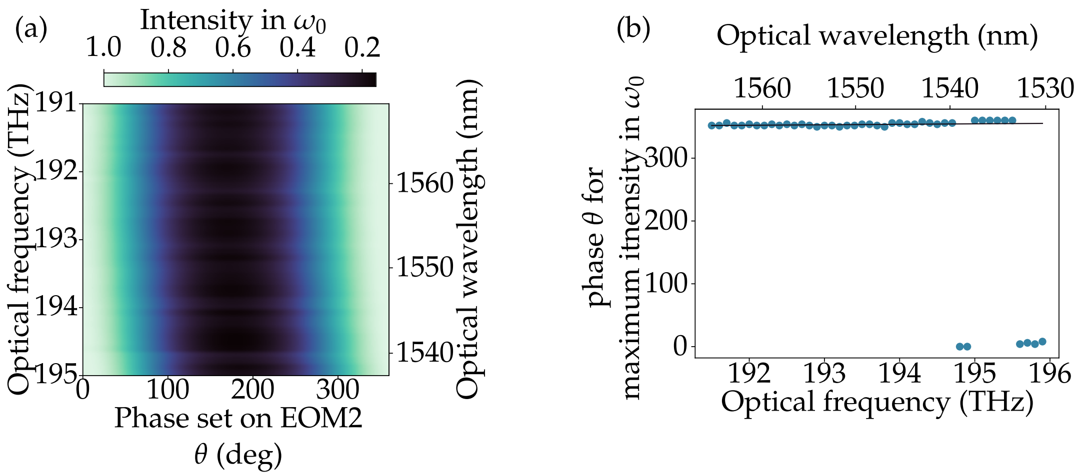

Figure 4.16: (a): Variation of the intensity in the mode ω_0 with the relative phase on EOM2, as shown in Fig. 4.3, for several optical frequencies with a negative dispersion of -0.4 ps/nm is applied by the programmable filter of the [EOM-PF-EOM] configuration. (b): phase value corresponding to the maxima of the interference for each optical frequency (dots), fit with a dispersion of 0.032ps/nm (solid line).

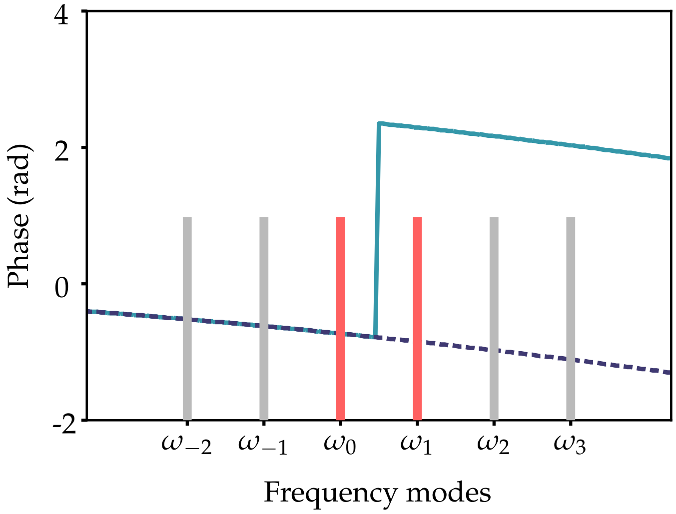

Figure 4.17: Solid line: phase pattern that needs to be applied by the quantum gate to apply a Hadamard gate on a qubit, taking into account the dispersion (dashed line). The red (greys) bars correspond to modes inside (adjacent to) the computational space. Frequency of the qubit modes are ω_0 =195 THz and ω_1 =195+Ω_m THz.

gate applied on frequency bins qubit over all the C band. The results are shown in Fig. 4.18, where we obtain fidelities $\geq 0.999 \pm 0.002$ and success probabilities $\geq 0.942 \pm 0.002$. The lower success probabilities compared to the state-of-the-art ($\mathcal{P}$=0.9748) are attributed to the imperfections of the modulators. We also notice that the probability is 2% higher than experiments in section 4.1.3, attributed to a better tuning of the EOMs parameters.

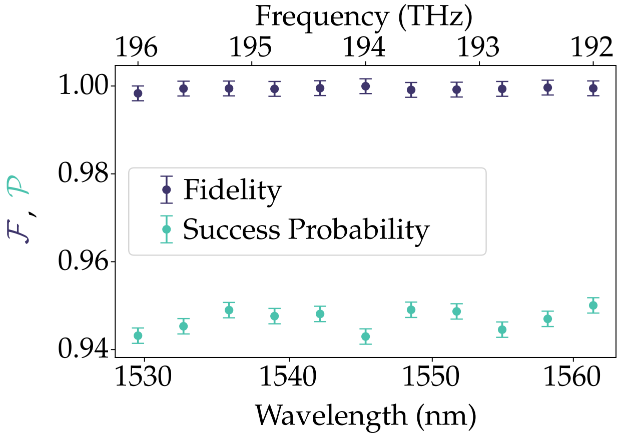

Figure 4.18: Success probability and fidelity of the Hadamard gate performed on 11 frequency-bin qubits distributed all over the PF bandwidth.

In this section, we showed the parallelization of independent Hadamard gates. These gates need a minimal amount of 2 guard modes to be isolated from each other by at least 30 dB. However, it is interesting to investigate the case of two Hadamard gates with no guard modes. The next section focuses on the parameters optimization of the quantum gate, for the same set of devices, and a single-frequency RF sine wave.

4.2.2 Hadamard gates with no guard modes

It is possible to synthesize such contiguous Hadamard gates with the [EOM-PF-EOM] configuration using multi-tone RF driving [67]. In this paper, the two transformations exhibit a fidelity $\mathcal{F}$ = 0.999999 and a success probability of $\mathcal{P}$ = 0.9310. Here, we aim to synthesize this transformation by driving the EOM with a single RF tone at frequency Ω_m. The [EOM-PF-EOM] combination has several free parameters that we can optimize: two modulation indices and two phases for the EOMs ($\mu_1, \theta_1, \mu_2, \theta_2$), and 18 phases for the PF ($\phi_0, \cdots, \phi_{17}$).

We numerically simulate the devices using tools developed in Chapter 3 on an 18x18 frequency space centered on the two Hadamard gates. Therefore, for the optimization process, a Particle Swarm Optimization algorithm was used, as it gave the best results, and is similar to the work reported in [61]. We use the bi-stage optimization function as in [61]

$$F(x) = \begin{cases} \mathcal{P}\log_{10}(1-\mathcal{F}) \text{ if } \mathcal{F} \leq 0.99 \\ -4 \times \mathcal{P} \text{ if } \mathcal{F} \geq 0.99 \end{cases} \tag{4.8}$$

This objective function optimizes both the fidelity and success probability of the operation. In the first stage, the optimization highly concentrates on optimizing the fidelity until $\mathcal{F} > 0.99$. When the fidelity reaches this threshold, the function maximally optimizes the probability of success. We target the following amplitude transfer matrix

$$T = \frac{1}{\sqrt{2}} \begin{pmatrix} 1 & 1 & 0 & 0 \\ 1 & -1 & 0 & 0 \\ 0 & 0 & 1 & 1 \\ 0 & 0 & 1 & -1 \end{pmatrix}, \tag{4.9}$$

corresponding to two Hadamard gates applied on two frequency qubits with no guard modes in between. Fig.4.19 shows the optimum parameters for the phase applied by the PF (a) and for the EOMs settings (b). The simulated transfer matrix is presented in Fig. 4.20. The black outlines represent the ideal values of Eq. 4.9. The numerical optimization leads to a fidelity of 0.92 to the targeted matrix and a success probability of 0.97. We then apply these settings to the experimental setup and measure the experimental intensity transfer matrix of the gate.

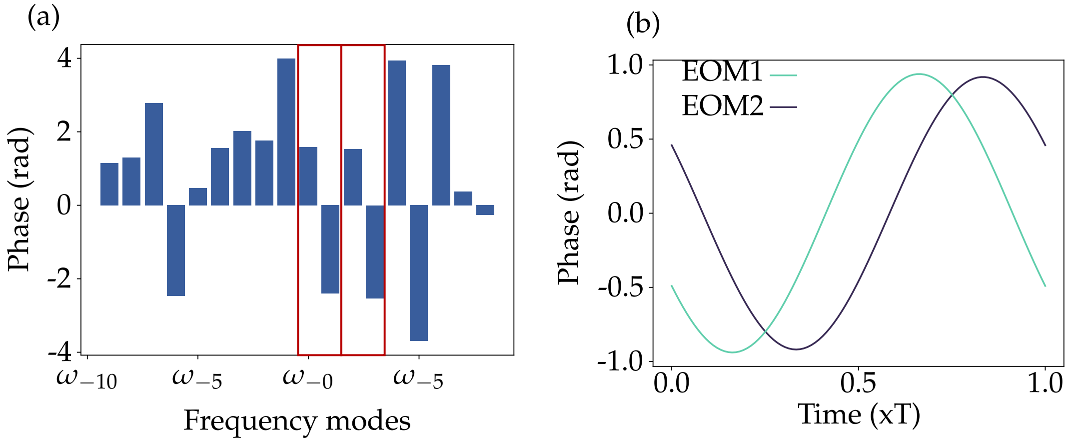

Figure 4.19: Optimized phases of the PF (a.) and parameters of the EOMs (b.) for the synthesis of two side-by-side Hadamard gates. In b. T is the period of the the RF wave T= $\frac{2\pi}{\Omega_m}$.

Fig. 4.21 compares the numerical simulation to the experimental data. As we experimentally measure an intensity, we plot in Fig. 4.21.(a) the simulated intensity transfer matrix, and Fig. 4.21.(b) shows the measured intensity transfer matrix. The black outlines correspond to the theoretical values. For intensity, we expect values of 0.5 for each bar. The fidelity to the target transformation in Eq. 4.9 is $\mathcal{F} = 0.94$ and the success probability is $\mathcal{P} = 0.95$ for the 4-dimensional transformation. Individually, the fidelity and probability of success for the two 2x2 operations are $\mathcal{F}_1 = 0.999 \pm 0.002$ and $\mathcal{F}_2 = 0.999 \pm 0.002$. The success probabilities are $\mathcal{P}_1 = 0.912 \pm 0.002$ and $\mathcal{P}_2 = 0.882 \pm 0.002$. These results show a slight improvement in performances for two adjacent Hadamards compared to [57], where a fidelity of 0.983 and a probability of success of 0.86 with a single sine wave driving of the EOMs were reported. With the same set of devices, we can find solutions that exhibit better performances both numerically and experimentally. As expected, driving the modulators with a sum of two RF harmonics exhibits better performance [67] with a higher fidelity ($\mathcal{F} = 0.99999$) and the same order of success probability ($\mathcal{P} = 0.9310$). However such realization necessitates a higher bandwidth RF generator to drive the second harmonics and a high bandwidth modulator.

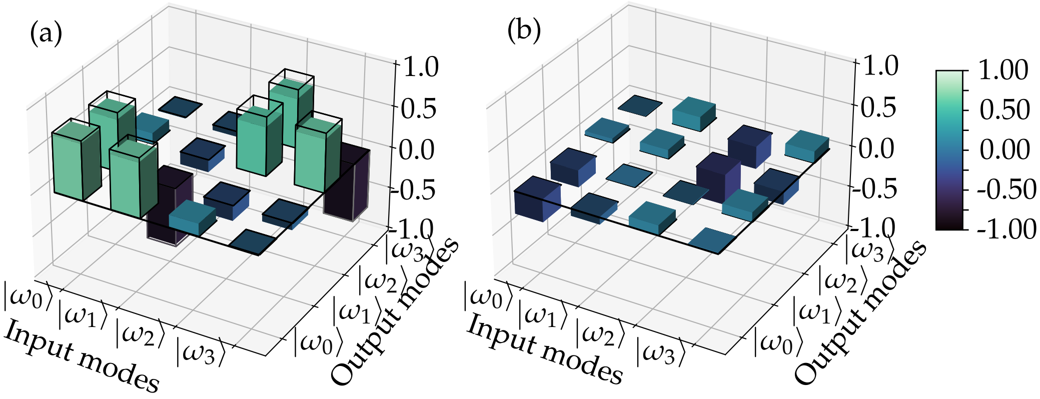

Figure 4.20: Numerical results of the simulation of two side-by-side Hadamard gates. (a): Real part of the matrix, (b): imaginary part of the matrix. Black outlines correspond to the expected values.

As investigated in the previous section, it is important to look at the crosstalk between the two gates. We infer the isolation of the two qubits of 13 dB. It's important to mention that our experiment only needs one RF sine wave. This method can be used to perform two Hadamard with no guard modes when the second harmonics cannot be generated easily by generator.

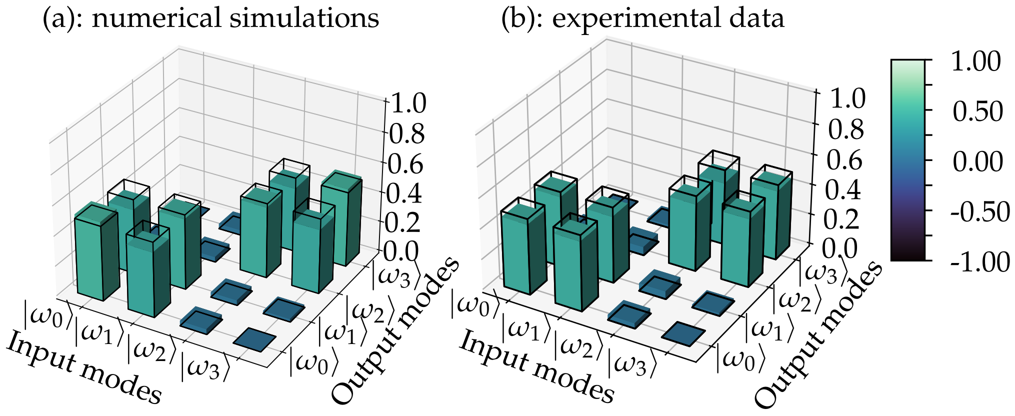

Figure 4.21: (a): Intensity transfer matrix of the numerically simulated transformation of the two side-by-side Hadamard gates. (b): Experimentally measured Intensity transfer matrix. Outlines correspond to expected values from Eq. 4.9.

4.3 Frequency entangled qubit pairs

4.3.1 Entangled state parametrization

In chapter 2, we studied the photon pair generation in a SOI micro-resonator. The generated photon pairs are emitted symmetrically around the pump frequency in a coherent superposition described by the state

$$|\phi\rangle = \frac{1}{\sqrt{D}} \sum_{N=1}^{D} A_N e^{i\alpha_N} |I_N, S_N\rangle \, . \tag{4.10}$$

This is a D-dimensional frequency-bin entangled state. We choose to parametrize frequency-entangled qubit pair states using the principle depicted in Fig. 4.22. Out of all the possible resonances in which a signal and idler can be simultaneously emitted, we use a programmable filter to keep only two adjacent pairs and encode our signal and idler qubits.

The two qubits are encoded on adjacent frequency modes $|I_{N=n}\rangle$ and $|I_{N=n+1}\rangle$ for the idler qubit, and $|S_{N=n}\rangle$ and $|S_{N=n+1}\rangle$ for the signal qubit. For convenience, It is useful to define a logical $|0\rangle$ and $|1\rangle$ for each qubit, with n being the signal idler pair $|S_n\rangle$ and $|I_n\rangle$. For the following experiment, we chose n=34. The encoding of the following

$$\begin{aligned} |0_n^I\rangle &= |I_n\rangle \\ |1_n^I\rangle &= |I_{n+1}\rangle \\ |0_n^S\rangle &= |S_n\rangle \\ |1_n^S\rangle &= |S_{n+1}\rangle \, . \end{aligned} \tag{4.11}$$

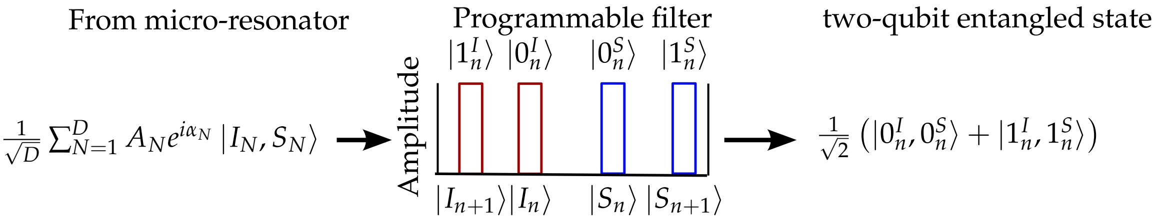

Figure 4.22: Preparation of a two-qubit entangled state from the high dimensional entangled state generated by the SOI micro-resonator. A programmable filter applies passband filters centered on 4 resonator modes and with a bandwidth $\Delta\omega$=FSR. We encode the $|0\rangle$ s and $|1\rangle$s of the two qubits on the $N = n$ and $N = n + 1$ modes respectively.

Taking this encoding into account, we define the two-qubit entangled state as

$$|\phi_n\rangle = A_0^n |0_n^I, 0_n^S\rangle + e^{i\Delta\alpha_n} A_1^n |1_n^I, 1_n^S\rangle , \tag{4.12}$$

$\Delta\alpha_n$ represents the difference between the biphoton phases α_n and α_{n+1}, while A_0^n and A_1^n represent A_n and A_{n+1}, respectively.

When we introduced the SOI micro-resonator, we noticed a variation in the number of coincidences between contiguous signal-idler pairs. To generate a maximally entangled state, we need to ensure that A_0^n is equal to A_1^n. To do this, we correct the contributions of each qubit in the following way [76]:

- if $A_0^n > A_1^n$, we attenuate A_0^n,
- if $A_1^n > A_0^n$, we attenuate A_1^n,

so that ultimately, $A_0^n = A_1^n$. The adjustments are done using a programmable filter, which applies the necessary attenuation to the signal and idler of the photon pair that requires it. It is worth noting that applying attenuation does not change the intrinsic purity of the generated states, as we post-select two-photon events. Therefore, if both coefficients are equal, we can represent the generated state as

$$|\phi_n\rangle = \frac{1}{\sqrt{2}} \left(|0_n^I, 0_n^S\rangle + e^{i\Delta\alpha_n} |1_n^I, 1_n^S\rangle\right) , \tag{4.13}$$

4.3.2 Using parallelizable frequency-domain quantum gates to parametrize the four Bell states

We first want to check that the two generated photons are indeed entangled in frequency. To this end, we first perform Bell-like two-photon interferences. Contrary to Hong-Ou-

Mandel interferences, where the two photons interact at a beam splitter, used to characterize their indistinguishability, these interferences assess the non-local property and give us a lower bound on the entanglement of the corresponding photons.

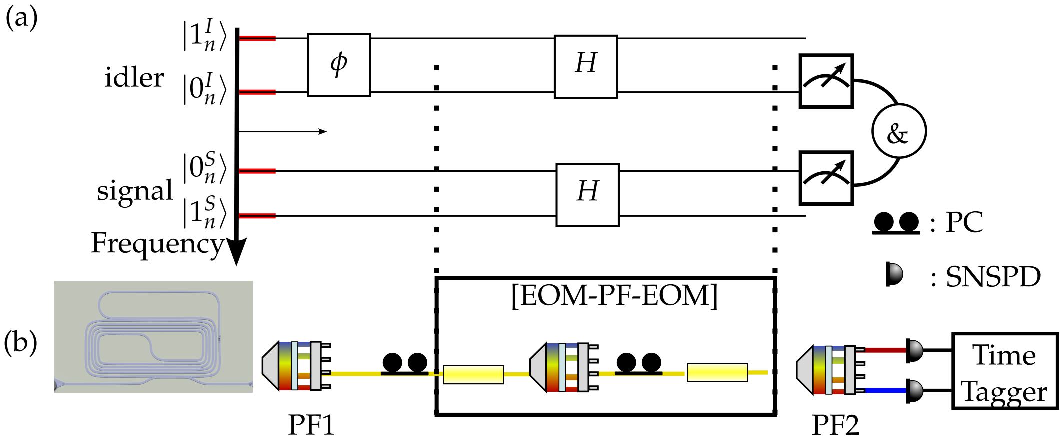

Figure 4.23: (a): Quantum gate representation of the two-photon interferences. The qubit modes 0 and 1 are encoded on adjacent resonance modes. A phase gate applies a phase ϕ between the idler qubit modes to control the interferences. The Hadamard gate allows the measurement of qubits on the superposition basis. we project each qubit on the qubit mode 0. (b): experimental setup for the two-photon interferences. PF: Programmable filter, EOM: electro-optic modulator, SNSPD: single-photon detectors, PC: polarization controller.

A scheme of the principle of the experiment is presented in Fig. 4.23.a. and the associated setup in Fig. 4.23.b. The state generated by the resonator is carved by a first programmable filter PF1 to parametrize the entangled qubit pair state as

$$|\phi_n\rangle = \frac{1}{\sqrt{2}}\left(|0_n^I, 0_n^S\rangle + e^{i\Delta\alpha_n}|1_n^I, 1_n^S\rangle\right). \tag{4.14}$$

PF1 applies a relative phase ϕ between the two idler qubit modes. The generated state thus becomes:

$$|\phi_n\rangle = \frac{1}{\sqrt{2}}\left(|0_n^I, 0_n^S\rangle + e^{i(\Delta\alpha_n+\phi)}|1_n^I, 1_n^S\rangle\right). \tag{4.15}$$

Then, the [EOM-PF-EOM] group is programmed to perform a Hadamard operation on both qubits. From Fig. 4.23, we see that the state $|1_n^S\rangle$ is higher in frequency than the state $|0_n^S\rangle$. For the idler qubit, the logical state $|1_n^I\rangle$ is lower in frequency than state $|0_n^I\rangle$. This creates a difference in how the Hadamard operation must be applied to each qubit. In the previous sections, the encoding method was chosen such that $\omega_1 = \omega_0 + \Omega_m$. An inverse encoding means switching the rows and columns of the Hadamard gate. We define a

Hadamard gate for the signal (H_S) and the idler (H_I) qubit as

$$H_S = \frac{1}{\sqrt{2}} \begin{pmatrix} 1 & 1 \\ 1 & -1 \end{pmatrix} \; H_I = \frac{1}{\sqrt{2}} \begin{pmatrix} -1 & 1 \\ 1 & 1 \end{pmatrix}. \tag{4.16}$$

Applying these two transformations to their respective qubits gives

$$\begin{aligned} H_I \otimes H_S \left|\phi_n\right\rangle = \frac{1}{2\sqrt{2}} \Big[& \left(- \left|0_n^I, 0_n^S\right\rangle + \left|1_n^I, 0_n^S\right\rangle - \left|0_n^I, 1_n^S\right\rangle + \left|1_n^I, 1_n^S\right\rangle\right) \\ & + e^{i(\Delta\alpha_n + \phi)} \left(- \left|1_n^I, 1_n^S\right\rangle - \left|0_n^I, 1_n^S\right\rangle + \left|1_n^I, 0_n^S\right\rangle + \left|0_n^I, 0_n^S\right\rangle\right) \Big]. \end{aligned} \tag{4.17}$$

A last programmable filter (PF2) projects the qubit pair on the two-photon state $\left|0_n^I\right\rangle \left|0_n^S\right\rangle$.

$$\left\langle 0_n^I, 0_n^S \right| H_I \otimes H_S \left|\phi_n\right\rangle = \frac{1}{\sqrt{2}} \frac{-1 + e^{i(\Delta\alpha_n + \phi)}}{2}. \tag{4.18}$$

The corresponding probability evolves as a function of the phase applied on the idler photon as

$$\left| \left\langle 0_n^I, 0_n^S \right| H_I \otimes H_S \left|\phi_n\right\rangle \right|^2 = \frac{1}{2} \left(1 - \cos(\Delta\alpha_n + \phi)\right). \tag{4.19}$$

Such interferences are the witness of frequency-bin entanglement.

PF2 also spatially separates the two-photon modes and sends them to two distinct SNSPDs. The two-photon measurement is done by recording the coincident clicks between the two detectors within a 1 ns coincidence window. The coincidences are processed using a Swabian Time Tagger Ultra. Fig. 4.24 shows the measured variation of two-photon coincidences as a function of the relative phase applied to the idler qubit. We fit the experimental points with a formula adapted from Eq. 4.19 as

$$\bar{N} \left(1 - V_0 \cos(\phi + \Delta\alpha)\right) \tag{4.20}$$

Where $\bar{N}$ is the mean number of coincidences, and V_0 is the visibility of the interference. We obtain V_0=0.85. The minimum number of coincidences was experimentally reached at a phase $\phi = -0.27$ rad (-15°) corresponding to $-\Delta\alpha_n$.

The setup presented in Fig. 4.23 can be seen in two ways. First, as the measurement of the quantum states, where the photons are sent to two parties who measure each of them independently. This is the usual point of view used for quantum key distribution. Another way of seeing this experiment is that it allows the parametrization of any of the four Bell states. Starting from a $\left|\phi^+\right\rangle$ state, applying a phase gate on one of the qubits allows us to change the initial state from $\left|\phi^+\right\rangle$ to $\left|\phi^-\right\rangle$. Moreover, the combined actions of

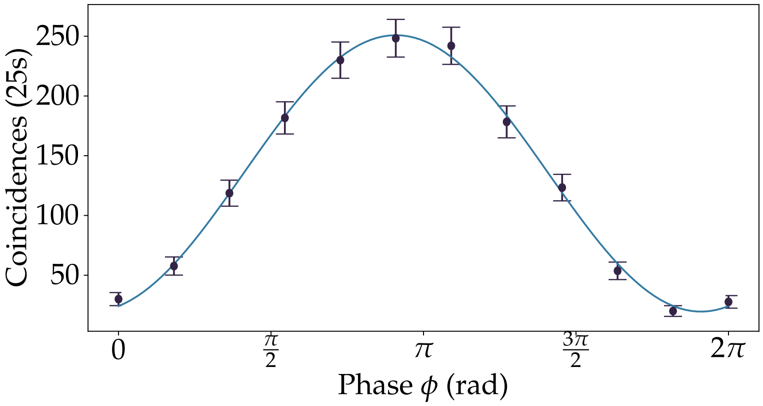

Figure 4.24: Two photon interferences for frequency-entangled qubits. The experimental points (dot) are fitted with a sine curve (refer to text).

the phase and the Hadamard gates allow to generate anti-symmetric $|\psi^-\rangle$ state. We can see from Eq. 4.17 that if we take the particular case of $\phi = 0$, we find

$$\begin{aligned} H_I \otimes H_S |\phi_n\rangle = \frac{1}{2\sqrt{2}} \Big[&(-|0_n^I, 0_n^S\rangle + |1_n^I, 0_n^S\rangle - |0_n^I, 1_n^S\rangle + |1_n^I, 1_n^S\rangle) \\ &- |1_n^I, 1_n^S\rangle - |0_n^I, 1_n^S\rangle + |1_n^I, 0_n^S\rangle + |0_n^I, 0_n^S\rangle \Big] . \end{aligned} \tag{4.21}$$

As the $|0_n^I, 0_n^S\rangle$ and $|1_n^I, 1_n^S\rangle$ terms cancels out, which leaves us with

$$H_I \otimes H_S |\phi_n\rangle = \frac{1}{\sqrt{2}} \left(|1_n^I, 0_n^S\rangle - |0_n^I, 1_n^S\rangle \right) = |\psi^-\rangle \tag{4.22}$$

In the following section, we perform quantum state tomography on a prepared $|\phi^+\rangle$. To parametrize this state, we consider that we initially compensate for any phase shift coming from the bi-photon phase, or the asymmetric action of H_I and H_S, by automatically adding a phase of $\pi + \Delta\alpha_n$ between the idler qubit modes of each considered $|\phi_n^+\rangle$ states. For the particular case of the two-qubit state $|\phi_{n=34}^+\rangle$, the initial phase to apply, to create the desired state is 3.41 rad (195°).

4.3.3 Quantum State Tomography of a frequency-entangled qubit pair

The generated quantum state can be further characterized by reconstructing the experimental density matrix, using quantum state tomography. The principle of the experiment is to perform a series of projective measurements of the generated state. From these measurements, we reconstruct the density matrix of an input quantum state. Here we focus on a particular $|\phi^+\rangle$ entangled state written as

$$|\phi_n^+\rangle = \frac{1}{\sqrt{2}}\left(|0_n^I, 0_n^S\rangle + |1_n^I, 1_n^S\rangle\right). \tag{4.23}$$

The corresponding density matrix in the $\{|0_n^I, 0_n^S\rangle, |0_n^I, 1_n^S\rangle, |1_n^I, 0_n^S\rangle, |1_n^I, 1_n^S\rangle\}$ basis is then

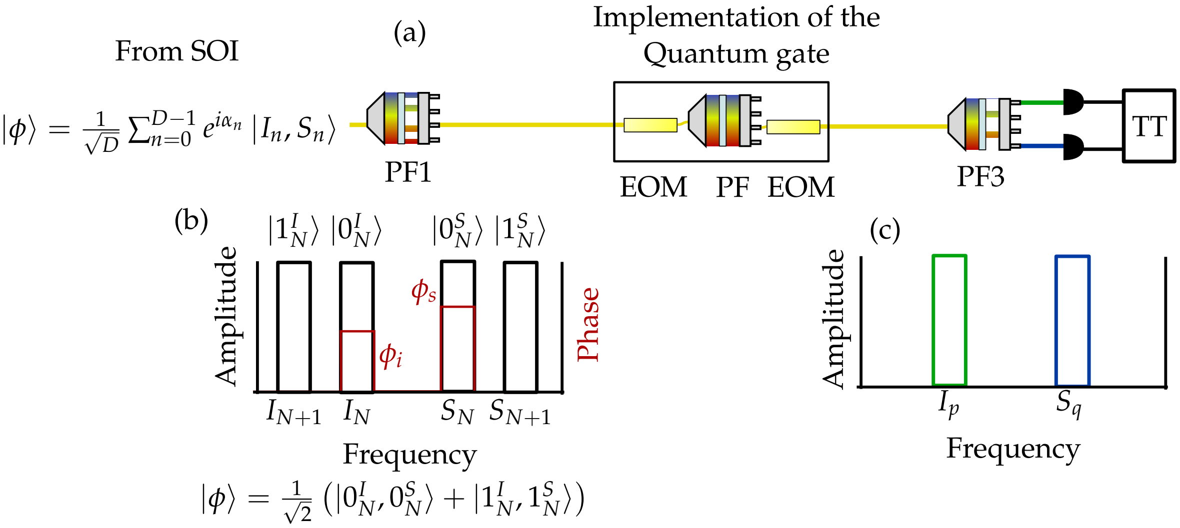

Figure 4.25: (a): Experimental setup for the quantum state tomography. PF1 parametrizes the entangled photon pair state and applies the phase mask shown in red in (b). The [EOM-PF-EOM] configuration applies either Hadamard or Identity on the qubits. The two photons are projected on one basis states selected by PF3, as shown in (c), where p,q$\in \{N, N+1\}$.

$$\hat{\rho} = |\phi_n^+\rangle\langle\phi_n^+| = \begin{pmatrix} 0.5 & 0 & 0 & 0.5 \\ 0 & 0 & 0 & 0 \\ 0 & 0 & 0 & 0 \\ 0.5 & 0 & 0 & 0.5 \end{pmatrix}. \tag{4.24}$$

To experimentally reconstruct the density matrix of a quantum state, we perform projections on four basis states among six vectors of the three orthogonal bases that we recall here

$$\begin{gathered}\mathbb{Z} : \{|0_n^x\rangle\,,\,|1_n^x\rangle\} \\ \mathbb{X} : \left\{|+\rangle = \frac{1}{\sqrt{2}}\left(|0_n^x\rangle + |1_n^x\rangle\right), |-\rangle = \frac{1}{\sqrt{2}}\left(|0_n^x\rangle - |1_n^x\rangle\right)\right\} \\ \mathbb{Y} : \left\{|+i\rangle = \frac{1}{\sqrt{2}}\left(|0_n^x\rangle + i\,|1_n^x\rangle\right), |-i\rangle = \frac{1}{\sqrt{2}}\left(|0_n^x\rangle - i\,|1_n^x\rangle\right)\right\} \\ . \end{gathered} \tag{4.25}$$

Where $x \in \{S, I\}$. Fig.4.25 depicts the setup for the experiment. The setup is similar to the two-photon interferences. However, in this case, the first PF also applies a phase gate on the signal photon. The combination of the phase gate and tunable gate allows one to choose the basis states on which to project. Using the parameters from Table 4.2, we project the state of the photon pair in all possible products of the four states

phase gate (ϕ)	Parametrized operation	Measurement basis	vector used for tomography
0	Identity	$\mathbb{Z}$	$\|0_n^x\rangle, \|1_n^x\rangle$
0	Hadamard	$\mathbb{X}$	$\|+_n^x\rangle$
$\frac{\pi}{2}$	Hadamard	$\mathbb{Y}$	$\|+i_n^x\rangle$

Table 4.2: Parameters of the phase gate and tunable gate to project the photon state on the three measurement bases.

$$|0\rangle\,,\,|1\rangle\,,\,|+\rangle\,,\,|+i\rangle\,. \tag{4.26}$$

We report the results of the 16 projective measurements (two photons and four possible states) in Table 4.3.

Projections	Coinc.	Projections	Coinc.
$C_{0,0}$	1548	$C_{+,0}$	716
$C_{0,1}$	36	$C_{+,1}$	767
$C_{0,+}$	622	$C_{+,+}$	1275
$C_{0,+i}$	663	$C_{+,+i}$	608
$C_{1,0}$	22	$C_{+i,0}$	837
$C_{1,1}$	1553	$C_{+i,1}$	695
$C_{1,+}$	692	$C_{+i,+}$	723
$C_{1,+i}$	664	$C_{+i,+i}$	42

Table 4.3: Coincidences for the two-photon projections $C_{a,b}$ integrated for 125 seconds, in a coincidence window of 1 ns, corresponding to the temporal width of the photon wavepacket.

Fig. 4.26 shows the density matrix reconstructed using Maximum likelihood estimation methods [162]. Comparing it to the density matrix of a maximally entangled state $|\phi^+\rangle = \frac{1}{\sqrt{2}}\left(|0^S_{34}\rangle\,|0^I_{34}\rangle + |1^I_{34}\rangle\,|1^I_{34}\rangle\right)$ we obtain a fidelity $\mathcal{F} = 0.961 \pm 0.007$.

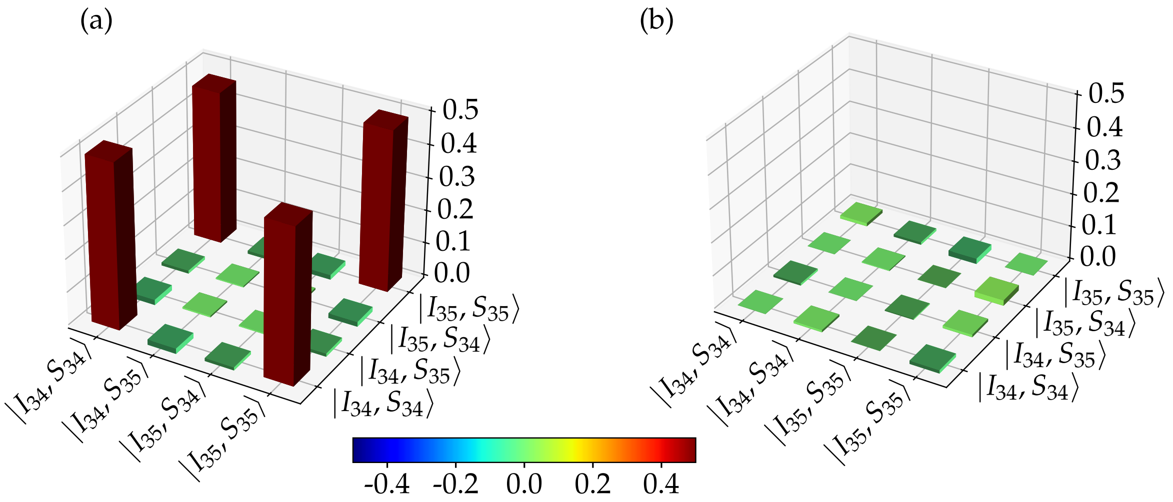

Figure 4.26: Experimental reconstruction of the density matrix of a $|\phi^+\rangle$ frequency-bin entangled state. (a): real part, (b): imaginary part.

To calculate the error bar on the fidelity, a Monte Carlo process is used. The noise is assumed to be Poissonian, which means the total number of coincidences registered for each measurement can be associated with a Poisson distribution with an average N. We attribute to each measurement a Poisson distribution associated with a standard deviation. We sample over multiple distributions and compute the fidelity for each iteration. The standard deviation gives us the error bar on our fidelity.

4.4 Frequency-entanglement-based fully-connected quantum networks

In this section, we provide a concrete application of frequency-domain information processing for a proof of concept of a trusted-node-free fully connected network. We use the broadband photon-pair generation from the SOI micro-resonator to encode 17 frequency-bin entangled qubit pairs. Using 34 parallel single qubit gates previously introduced, we assess their fidelity to $|\phi^+\rangle$ entangled state. Then, we measure the performances of each entangled qubit pair for a BBM92 quantum key distribution protocol used to link pairs of users in a quantum network.

A quantum network is represented as a graph, where vertices correspond to quantum nodes i.e.: users, and edges are quantum links i.e.: quantum optical channels, as illustrated in Fig. 4.27. A fully connected network is a configuration in which every user is connected to every other user as shown in Fig. 4.27.

Here each link consists of a photon pair shared between two users. If each link is established by an independent photon source, the number of sources scales quadratically with the number of users [163, 164]. Active time switching can be employed to consecutively create a link between each user [165, 166] for a limited time, and thus lower the demand on resources.

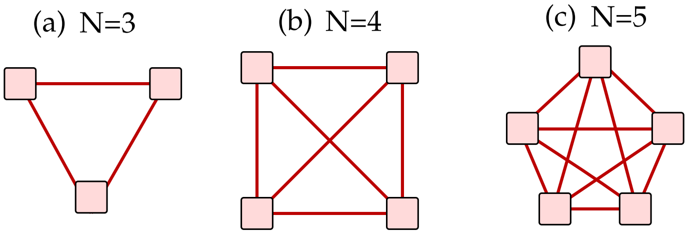

Figure 4.27: Representation of a quantum network. The squares represent the quantum nodes, and the red lines represent the quantum links.

Frequency demultiplexing is a technique that can harness this challenge. A broadband photon pair source correlated in frequency can be used to generate all the necessary links of a quantum network. Using demultiplexing, frequency channels are allocated to each user pair. As no switching is required, the communication between two parties can be done continuously.

Fig. 4.28 displays the rationale behind a fully connected network. The communication protocol between two parties is based on the BBM92 protocol [161]. In this protocol, each party receives one photon originating from an entangled photon pair source. Fig. 4.28.(a) shows the bandwidth allocation for three entangled photon pairs. Two spectrally correlated photons are emitted symmetrically around the degeneracy and represented by signal and idler bars with the same color. Fig. 4.28.(b) shows the physical implementation of the quantum links. The source generates the two-photon states, and the channels are demultiplexed and sent to each user so that every user shares a photon pair with every other user. Fig. 4.28.(c) shows the communication layer, where each node corresponds to a user and each edge is an entanglement link corresponding to a distributed photon pair.

In previous implementations or proofs of the concept of a fully connected network, entanglement is based on either polarization [167, 168, 169] or time-bin [170, 171, 172]. As stated in the introduction, the frequency domain provides a unique advantage that would prevent the need for active stabilization in real implementations. In this section, we thus aim to practically use frequency encoding and the parallelization of single-qubit gates permitted by the [EOM-PF-EOM] configuration to realize a proof-of-concept of a fully-connected

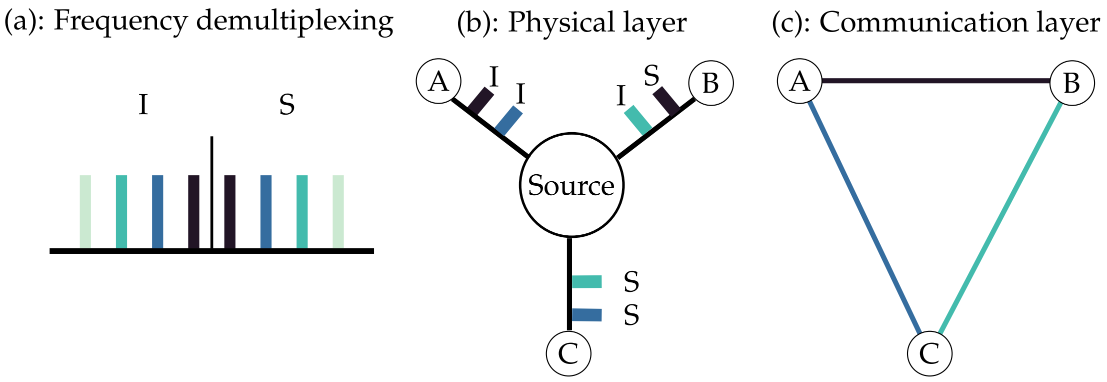

Figure 4.28: (a): A photon pair source produces spectrally correlated entangled photons. (b): physical layer: These photons, can be demultiplexed and distributed among users. (c): Communication layer: Each user is connected by links corresponding to two photons from the same entangled pair.

network.

4.4.1 Parallel encoding of 17 frequency-bin entangled photon pairs

In our proof of concept of a fully connected network, the users share frequency-entangled qubit pairs and perform measurements using the [EOM-PF-EOM] configuration. Each qubit is encoded on pairs of resonances. To comply with the results of section 4.2 on parallelization, each qubit needs to be separated by two guard modes.

Fig. 4.29 shows single count rates for cavity modes around the pump frequency, from N=3 to N=25 for each side. The frequency-bin qubits are encoded in two adjacent frequency modes, as depicted by the colored bars. A frequency-bin entangled state is represented by a signal and idler qubit with the same color. The black bars correspond to guard modes modes. The ideal states we wish to parametrize are $|\phi^+\rangle$ states of the form

$$|\phi_n^+\rangle = \frac{1}{2}(|0_n^I, 0_n^S\rangle + |1_n^I, 1_n^S\rangle\,. \tag{4.27}$$

We parametrize each frequency-bin entangled pair using the method in section 4.3.1. To specifically generate $|\phi^+\rangle$ states, we correct for the bi-photon phases, where the correction to apply for each qubit pair is displayed in Fig. 4.31. Each value is measured by performing Bell-like interferences.

We now perform quantum state tomography to measure the fidelity to the targeted state, following the method in Section 4.3.3, for each qubit pair. The experimentally measured fidelities are depicted in Fig. 4.32. $\mathcal{F} geq 0.8$ for 12 out of 17 entangled qubit pairs. The lower fidelities for the five remaining qubit pairs correlate with the signal-idler pairs with

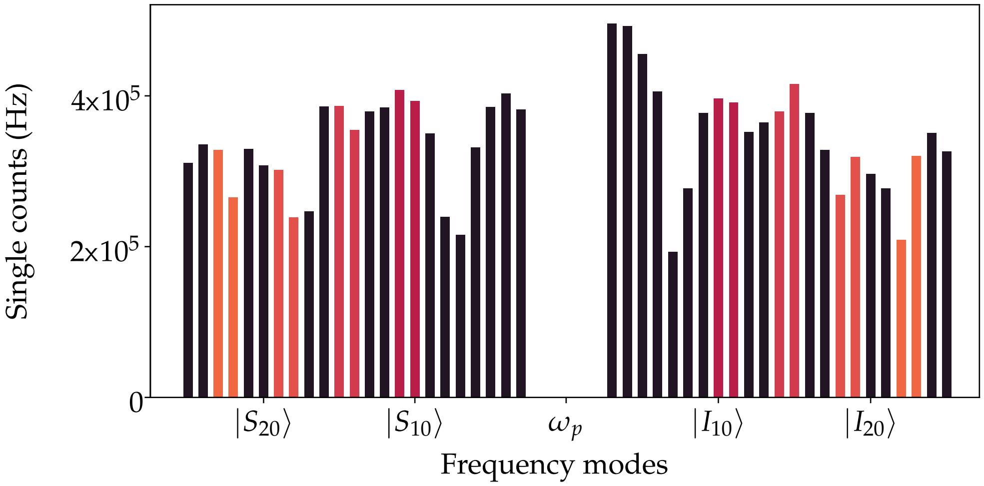

Figure 4.29: Single count spectrum as a function of the frequency modes. We encode the qubits on adjacent frequency modes. The four modes corresponding to an entangled pair have the same color. The black bars represent the modes that are not used for the encoding.

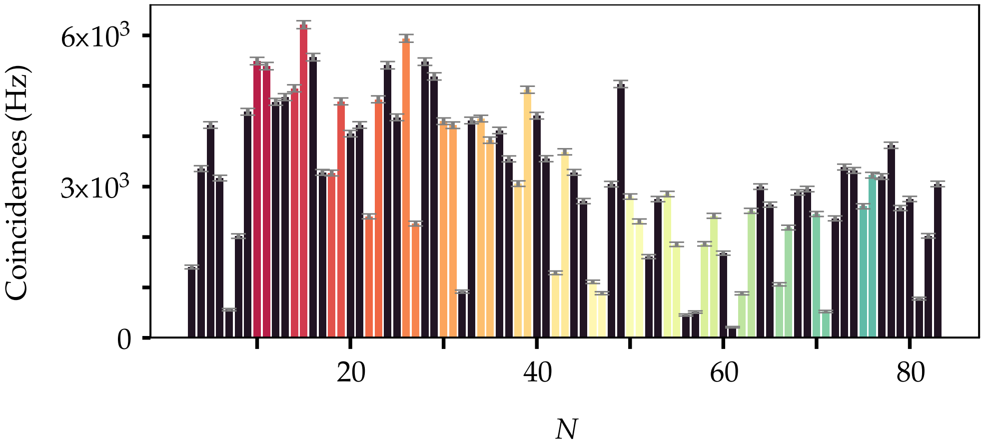

Figure 4.30: Coincidence rate for the two-photon state projected on $\langle I_N, S_N|$ for values of N from $N = 3$ to $N = 83$. Two bars with the same color correspond to signal idler mode pairs used for encoding. The black lines correspond to the guard modes, or modes not used to encode the two-qubit states.

the lowest coincidence rates in Fig. 4.30. Due to the low signal-to-noise ratio in these regions, more errors were induced leading to low fidelities.

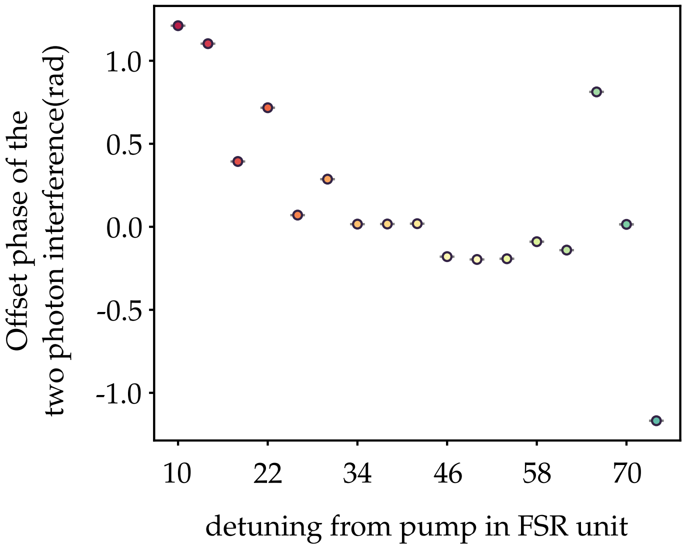

Figure 4.31: Experimental measured offset phase of the two-photon state for the 17 entangled qubit pairs.

4.4.2 Performances estimation of the BBM92 protocol in a frequency-entanglement based QKD network

Having parametrized 17 frequency-bin entangled qubit pairs, we assess their performances under a frequency-domain version of a BBM92 protocol. The two users of a link choose independently and randomly to measure the photon in two bases out of the three defined in 4.25.

- the $\mathbb{Z}$ basis : $|0\rangle$, $|1\rangle$
- the $\mathbb{X}$ basis : $|+\rangle$, $|-\rangle$

As a measurement is only valid if the two photons are measured on the same basis, we look at the quantum correlation in the $\mathbb{Z}$ and the $\mathbb{X}$ basis. For each projection, we measure several coincidences $C_{i,j}$ where i and $j \in \{0, 1, +, -\}$ are the states on which the photons are projected. The number of coincidences per basis is [173]

$$C_{\mathbb{Z}} = C_{0,0} + C_{0,1} + C_{1,0} + C_{1,1} \tag{4.28}$$

$$C_{\mathbb{X}} = C_{+,+} + C_{+,-} + C_{-,+} + C_{-,-}. \tag{4.29}$$

The raw coincidence rate exchanged by two parties is equal to [173]

$$R_{raw} = \frac{1}{2}\frac{(C_{\mathbb{Z}} + C_{\mathbb{X}})}{\tau}. \tag{4.30}$$

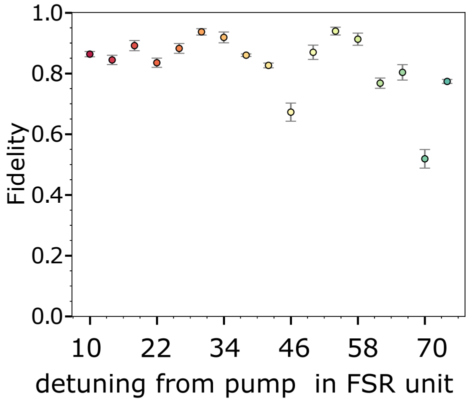

Figure 4.32: Measured fidelity to a $|\phi^+\rangle$ state for each frequency-bin entangled qubit pair state.

where τ is the integration time. The qubit error rate (QBER) is the ratio of accidental to total coincidences over the two bases. In the case of a $|\phi^+\rangle$ entangled state, the QBER is expressed as

$$e = \frac{C_{0,1} + C_{1,0} + C_{+,-} + C_{-,+}}{C_{\mathbb{Z}} + C_{\mathbb{X}}} \tag{4.31}$$

Finally, we can compute the sifted key rate between two users as [174, 175]

$$R_{sift} = \frac{1}{2} R_{raw} \left(1 - f(e)H_2(e) - H_2(e)\right). \tag{4.32}$$

R_{raw} is the total number of coincidences exchanged by the two users. The factor $\frac{1}{2}$ accounts for the fact that the two users choose on average the same basis half of the time. $f(e)H_2(e) + H_2(e)$ corresponds to the fraction of the key that needs to be discarded as a result of noise, coming from either environment or eavesdropping. $f(e)$ corresponds to the efficiency of the error correction code [175]. $H_2(e)$ is the binary entropy function $H_2(e) = -e \times log_2(e) - (1-e)log_2(1-e)$

In Fig. 4.33.(a), we can see the number of raw coincidences R_{raw} and the qubit error rate QBER for each accessible pair. To be useful, a given pair must have a QBER lower than 11% [175]. Out of the 17 accessible pairs, only 12 satisfy this condition.The sifted key rate between each user pair is derived from the raw coincidences R_{raw}, and the QBER using the method in [173]. Fig. 4.33.(b) displays the measured sifted key rate for each pair of users for each usable pair. The inset in Fig. 4.33.(b) illustrates how the distribution of 10 photon pairs can be used to create a node-free quantum network of 5 users.

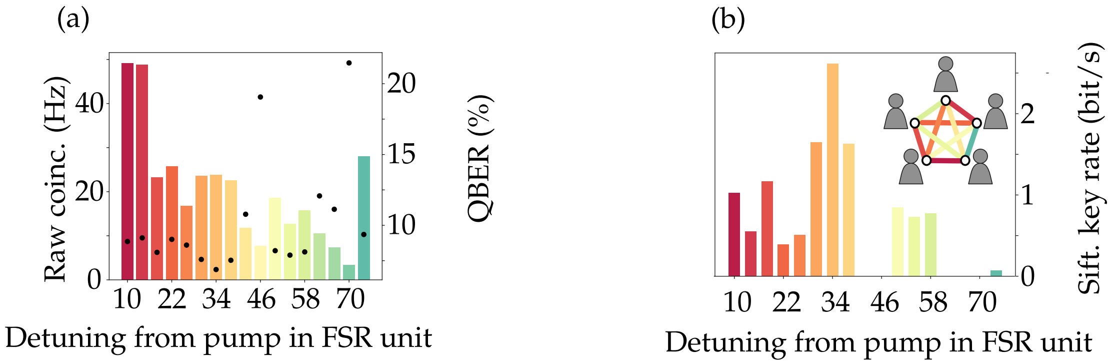

Figure 4.33: (a): Raw coincidences (bars) and qubit error rate (QBER) (dots) between two users, and (b): sifted key rate as a function of n, spectral detuning from the pump.

4.4.3 Scalability and possible improvements

In this proof of principle experiment, the achieved key rates (0.5 to 2.5 bits/second) are limited by the performances of the source, as well as the insertion loss of the devices (14 dB for the 3 PFs and the 2 EOMs). Integrating these components on the same chip would help to limit losses and improve overall performance. This particular way of improvement is discussed in section 5.5.

A real-world realization would necessitate an upgrade of the available equipment. In our laboratory, we possess 4 detectors. If U users want to communicate simultaneously, they need to register both basis states of each received qubit, which requires two detectors per qubit. Therefore, the number of detectors required scales as $2U \times (U-1)$. To reduce this demand to just one detector per user, we can use frequency-to-time mapping. Instead of resolving frequencies, we would look at the time of arrival of each photon and allocate one time bin for each frequency bin. This technique leverages the scalability of frequency encoding and measurement scalability of time encoding. To achieve this, we could use dispersive fibers to delay frequencies relative to each other. For this scheme to eliminate reliance on polarization, both involved parties must have measurement systems that are polarization-independent. The modulator currently used in our experiments is polarization-dependent. Nonetheless, a polarization-insensitive electro-optic modulator that combines two polarizing beam splitters and two modulators to achieve polarization-insensitive electro-optic modulation has already been demonstrated in [176].

A perspective of this work is to encode information into higher-dimensional entangled quantum states, which can readily be produced from our SOI micro-resonator. We discuss this in the perspectives section 5.4.

4.5 Hong-Ou-Mandel in the frequency domain

We also use the [EOM-PF-EOM] setup to perform a Hong-Ou-Mandel interference on photon pairs generated by the LNOI waveguide presented in chapter 2. The Hong-Ou-Mandel (HOM) [177] measures the degree of indistinguishability of two single photons. Usually, the HOM experiment consists in injecting two photons on the two inputs of a beamsplitter. If they are indistinguishable except for their spatial mode, they exhibit bunching and exit at the same output. Here we perform this experiment with photons encoded in frequency bins.

Frequency-domain Hong-Ou-Mandel experiments have been performed using different configurations. In [66], the mixing was achieved by employing the [EOM-PF-EOM] configuration. Alternatively, a single EOM was utilized [59, 87]. In another approach, third-order non-linear methods for frequency mixing were implemented [53]. Here, we utilize the [EOM-PF-EOM]. An EOM can also be used to translate the frequency of one photon with respect to the other, by using spectral sheering as in [178], instead of a frequency beam splitter that translates the frequency of both photons.

In the frequency version of the HOM experiment, the two photons are initially in two distinct frequency modes. The two-photon state is written as

$$|\Psi\rangle = |1_{\omega_0}\rangle\,|1_{\omega_1}\rangle = \hat{a}^{\dagger}_{\omega_0}\hat{a}^{\dagger}_{\omega_1}\,|0_{\omega_0}\rangle\,|0_{\omega_1}\rangle\,, \tag{4.33}$$

If we apply a Hadamard gate, programmed with the [EOM-PF-EOM] on the two frequency modes ω_0 and ω_1, the two photons output the configuration in the following state

$$|\Psi\rangle = \frac{1}{2}\left(|2_{\omega_0}\rangle\,|0_{\omega_1}\rangle + |0_{\omega_0}\rangle\,|2_{\omega_1}\rangle\right) \tag{4.34}$$

As we observe, both photons output in the same frequency mode. As such, the coincidences between the two output modes, exhibit a dip.

We realize the experiment using the setup shown in Fig. 4.34.(a) The frequency beam splitter is realized using the [EOM-PF-EOM] configuration.

To comply with the limitations on the frequency spacing allowed by the modulators, we choose a frequency spacing of $\delta\omega = 2\pi \times 25$ GHz lower than the maximum frequency of the RF generator (33 GHz), allowing us to perform the frequency conversion used for the Hong-Ou-Mandel. Consequently, using a first PF, we carve the signal and idler photons to parametrize them in frequency modes $|\omega_0\rangle$ and $|\omega_1\rangle$ situated at $\omega_d \mp \delta\omega/2$ GHz, as shown in Fig. 4.34.(b). Both selected spectral bands have a bandwidth of 13 GHz and are separated by 25 GHz.

The two photons output the first PF in the same fiber, directed into the [EOM-PF-EOM] configuration, performing a tunable quantum gate over the two frequency modes ω_0 and

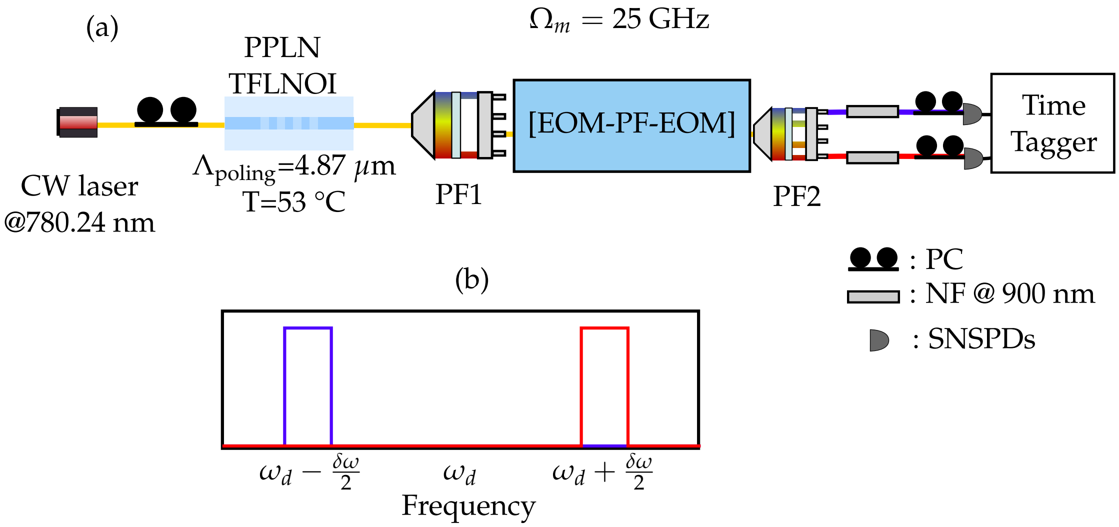

Figure 4.34: (a).: Setup for the frequency-domain Hong-Ou-Mandel experiment between correlated photons generated from the LNOI waveguide. (b): Filters applied on the two photons, defining two frequency bins placed at frequencies $\omega_d - \frac{\delta\omega}{2}$ and $\omega_d + \frac{\delta\omega}{2}$ with a bandwidth of 17 GHz.

ω_1. A final PF separates the two modes and sends them in two fibers, directed to single photon detectors. The coincidences are then computed using a time tagger.

The HOM interference is controlled by the tuning parameter α of the quantum gate. When $\alpha = 0$ rad, the operation performed is Identity. Therefore, the two photons remain in their respective frequency mode. When $\alpha = \pi$, we create a 50:50 frequency beam splitter, similar to a 50:50 beam splitter. In that case, we expect to observe a bunching of the two photons in one of the frequency modes. At this point, we do not expect to observe coincidences between the two outputs.

Fig. 4.35 shows the evolution of the number of coincidences between the two spectral modes as a function of the tuning parameter α. The decrease of the coincidences proves on the one hand that the source operates in a regime where the double pairs are negligible and on the other hand, that the operation performed by the quantum gate, when $\alpha = \pi$, is indeed a Hadamard operation. We observe a visibility of 0.98 ± 0.01

Table 4.4 compares our results with the previous realizations of this experiment. Our experiment shows that our experiment performs similarly to the state of the art, with a better coincidence rate than in [66] with the same configuration.

This experiment was only performed with photons generated by the lithium niobate waveguide. It would not be possible with the SOI micro-resonator, as the pump contami-

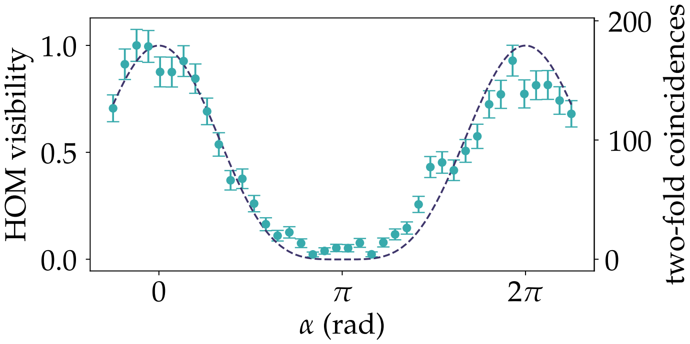

Figure 4.35: Measuremeent of the Hong-Ou-Mandel interference in the frequency domain using a tunable frequency-domain quantum gate. Dots are experimental points, and the dashed line corresponds to the expected values calculated with the model presented in Chapter 3.

Work	**HOM visibility**	**Method**	Coinc. per seconds
Lu et al. [66]	0.971 ± 0.007	EOM-PF-EOM	1.3
Imany et al. [87]	0.84 ± 0.02	EOM	0.6
Joshi et al. [53]	0.90 ± 0.04	Third-order non-linear conversion	0.75
Wright et al. [178]	0.93 ± 0.02	EOM : spectral shearing	200
This work	$\mathbf{0.98 \pm 0.02}$	EOM-PF-EOM	3

Table 4.4: Several methods used to perform a frequency-domain Hong-Ou-Mandel experiment, and the associated measured visibilities.

nates frequency modes close to the degeneracy, $\omega_d = \omega_p$. On the contrary, the degeneracy frequency for the SPDC process is $\omega_d = \omega_p/2$, far enough from the pump frequency.

4.6 Conclusion on the experimental manipulation of frequency-bin qubits

In this chapter, we synthesize a tunable, single qubit gate acting on frequency-bin qubits. With this quantum gate, we performed a frequency-domain version of a Mach-Zehnder interferometer. Concerning the parallelization of such frequency-bin quantum gates. We showed that by controlling the PF, it is possible to apply independent quantum gates to different qubits. We show that two guard modes between two qubits are sufficient to ensure a crosstalk lower than 10^{-3} between two neighbor qubits.

We used two of these parallelizable quantum gates to characterize a two-qubit entangled state, generated from a SOI micro-resonator. We performed quantum state tomography and assessed a fidelity of $\mathcal{F} = 0.961 \pm 0.007$. Thanks to the small FSR of our resonator (21 GHz) we generalized the encoding method, and the parallelization of quantum gates allowed us to generate several frequency-bin entangled two-qubit pairs, and perform quantum state tomography on each pair, ensuring a fidelity $\mathcal{F}$ $\geq$0.8 for 12 frequency-bin entangled states.

Using these 12 frequency-bin entangled pairs, we perform a proof-of-concept of a fully connected network. By performing correlation measurement, we can infer an exchanged coincidence rate and a qubit error rate, leading to an average sifted key rate of 1 bit/s for each link of the network, successfully creating a 5-users fully connected network.

Finally, using a tunable single qubit gate, we realize a Hong-Ou-Mandel experiment on photons generated by the LNOI waveguides. The access to frequency modes near the degeneracy of the SPDC process enables us to encode the signal and idler photons on two frequency bins separated by 25 GHz. Tuning the [EOM-PF-EOM] to apply a tunable gate from Identity to Hadamard allows us to observe a Hong-Ou-Mandel dip of visibility of 97%.

Chapter 5

Conclusion and perspectives

5.1 Summary of results

In this manuscript, we harnessed photonics qubits to process quantum information in the frequency domain at telecom wavelengths. Spectral encoding offers advantages toward more scalable quantum information processing. Our investigation includes theoretical, numerical, and experimental advances. We characterized two novel photon pair sources at telecom wavelength and demonstrated their performances as heralded single photon sources. We described the theoretical framework for synthesizing single qubit gates with time-bin and frequency-bin encoding. We experimentally synthesized single qubit gates for frequency-bin qubits. We used the synthesized gates on quantum states generated by integrated photon pair sources, leveraging the resource efficiency and flexibility offered by frequency-domain quantum information processing.

In more details, we investigated photon pair generation at telecom wavelength using two novel integrated sources: thin-film lithium niobate waveguides and a silicon-on-insulator micro-resonator. Compared to other sources based on LN thin film where the LN is etched, here the waveguide is defined by first depositing a thin layer of SiN on top of LN, followed by a shallow etching of SiN, leveraging the well-established etching technics for silicon nitride. With this structure, we report the generation of photon pairs at telecom wavelength on more than 170 nm (21 THz), obtaining an internal brightness of 3×10^5pairs.s^{-1}.mW^{-1}.GHz^{-1} . For the silicon-on-insulator micro-resonator, we measured the spectral properties of the cavity. We assessed a free spectral range of 21.25 GHz, smaller than previous works on the generation of frequency-bin qubits in a single ring, making the generated photons fit for encoding frequency-bin qubits. Despite the high cavity perimeter, necessary for the low free spectral range, the photon pairs are emitted efficiently due to the high quality factor of 4.75×10^5, reaching an internal brightness of 5×10^7

pairs.s^{-1}.mW^{-2}.GHz^{-1} comparable to the state of the art for silicon micro-resonators with higher free spectral range. For both sources, we assessed values of $g^{(2)}(0) = 0.03$ showing good single photon purity.

We then performed a theoretical study of all the possibilities to manipulate time and frequency bin qubits using electro-optic phase modulators and programmable filters in a 3-device configuration. The EOM is a scatterer in the frequency domain whereas the PF is a scatterer in the time domain. For each device, the scattering is controlled through Fourier transform manipulation in the conjugate space. In particular, we demonstrated that the PF acts as a two-scattering matrix coupling time bins in pairs, and enabling a unitary tunable rotation of time-bin qubits around the y axis of the Bloch sphere. We investigated two combinations of devices, [EOM-PF-EOM] and [PF-EOM-PF], acting on time-bin and frequency-bin qubits. The synthesis of arbitrary single-qubit gates is possible for each configuration and both encodings. We then investigated the parallelization of such qubit gates to independent qubits. For frequency encoding, guard modes between qubits are necessary to minimize the crosstalk. For time-bin qubits, the two-scattering operation performed by the PF in the time domain allows to suppress crosstalk between contiguous qubits, necessitating therefore no guard modes. We demonstrated the ability to parallelize 24 Hadamard gates with the [EOM-PF-EOM] configuration, and 28 for the [PF-EOM-PF] configuration for time-bin qubits. Finally, we showed that increasing the complexity of the RF signal driving the EOMs increases the number of successful parallelized operations. For time-bin encoded qubits, a square wave is the optimal form of signal for the exact parallelization of single-qubit gates.

We experimentally realized single qubit operations for frequency-bin qubits, performing a rotation around the x axis of the Bloch sphere, tunable from identity and Hadamard gate. These gates are core building blocks of quantum information protocols. We investigated the crosstalk of the synthesized gates and found that 2 frequency modes were sufficient to ensure a minimal crosstalk of 10^{-3} between each qubit. Under this condition, these tunable qubit gates can be applied independently to parallel qubits. We then used the tunable single qubit gates on frequency-bin quantum states generated by the SOI micro-resonator and the LNOI waveguide. We conducted a frequency-domain version of the Hong-Ou-Mandel experiment, measuring a visibility of 0.98±0.02, showing high indistinguishability of the interacting photons. We performed two-photon interferences and quantum state tomography, reaching a fidelity to a $|\phi^+\rangle$ of 0.961±0.007. The broadband generation of photon pairs offered by our SOI micro-resonator, and the ability to parallelize tunable single quantum gates allowed us to assess the fidelity to a $|\phi^+\rangle$ entangled state for 17 frequency-bin entangled states. We proposed for the first time a proof-of-concept of a trusted-node-free fully-connected network with frequency-encoded qubits, leveraging the intrinsic advantages of frequency-encoding stability for such applications.

All these results represent a step toward more scalable frequency-domain information processing. The sources presented in this manuscript demonstrated a scalable way to generate frequency-bin qubits, defined in tightly spaced frequency modes, and enabling an easier manipulation using standard off-the-shelf electro-optic modulators. At the start of my Ph.D. in 2020, the manipulation of frequency-bin qubits using EOMs and PFs was only investigated by two groups. Only one group had reported the experimental arbitrary synthesis of single-qubit gates with classical light. Since then, the work in this domain has experienced a very fast growth, mostly in the domain of quantum computation. This manuscript reports the generation and manipulation of frequency-bin qubits. Together with photon pair generation in state-of-the-art integrated sources, we performed reconfigurable experiments and proposed a concrete application of frequency-encoding to the domain of quantum communication.

The last sections of this manuscript aim to give an insight into the perspectives of this work, through preliminary results on experiments that I initiated during my Ph.D. and are now the backbones of the next Ph.D. projects. Finally, I present perspectives on the integration of frequency-bin manipulation schemes.

In Section 5.2, we investigate a protocol of entanglement swapping for frequency-bin qubits. Section 5.4 will present the perspective of using frequency-bin entangled qudits, quantum states in a superposition of more than two frequency bins, to reach longer distances between two quantum nodes in quantum communication protocols. We then discuss in Section 5.5 the perspective for frequency-bin manipulation, with integrated photonics. We discuss about promising experimental works and theoretical proposals realizing the manipulation of frequency-bin qubits and frequency-bin qudits.

5.2 Entanglement swapping of frequency-bin qubits

In Chapter 4, we performed a quantum key distribution protocol based on the distribution of a two-photon frequency-bin entangled state. A perspective to the results presented in this thesis is the realization of more complex quantum communication protocols. In this section, we present preliminary results on a frequency-domain version of an entanglement swapping protocol realized with frequency-bin qubits.

Entanglement swapping aims to entangle two photons that never interacted. This application plays a pivotal role in quantum communications, as it is an essential component of quantum repeaters [179]. Such a device would help to achieve longer-distance quantum communication between two parties. Entanglement swapping is usually implemented with polarization-encoded qubits [180] or time-bin qubits [148, 181]. Recently, entanglement swapping has been demonstrated for frequency entangled qubits, where the Bell state measurement is performed by a spatial beam splitter [65]. In this section, we present a method to realize entanglement swapping using electro-optic quantum gates. We perform the calculation leading to the entanglement swapping and present the preliminary results of the experiment. Combining EOMs and PF, it is possible to realize a complete Bell-state analyzer for frequency bin qubits [67].

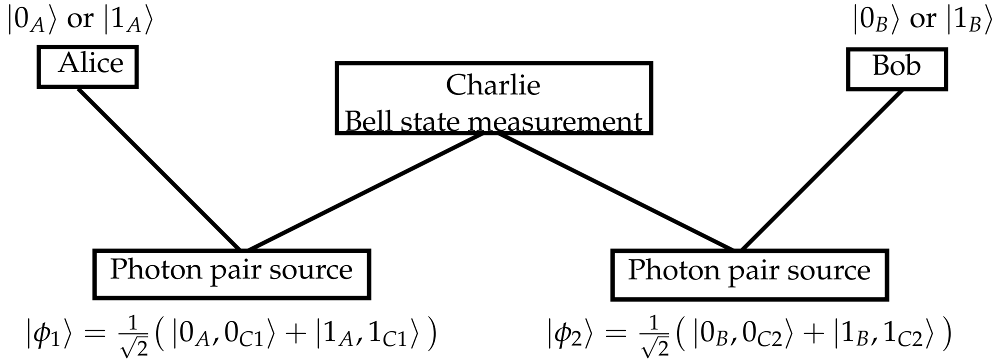

Figure 5.1: Representation of the entanglement swapping protocol: two sources of two-qubit entangled states.

Fig. 5.1 shows the principle of this protocol. Alice and Bob are two parties that wish to communicate but are too far apart for a direct quantum link, and Charlie is at an intermediate node. Two independent sources produce two-photon entangled states, $|\phi_1\rangle = \frac{1}{\sqrt{2}}\big(|0_A, 0_{C1}\rangle + |1_A, 1_{C1}\rangle \big)$ and $|\phi_2\rangle = \frac{1}{\sqrt{2}}\big(|0_B, 0_{C2}\rangle + |1_B, 1_{C2}\rangle \big)$. The first pair is shared between Alice and Charlie, and the second one between Charlie and Bob. When Charlie performs a Bell-state measurement on the two photons belonging to different pairs, the photons of Alice and Bob are projected on an entangled state.

Entanglement swapping experiments involve the measurement of four-photon coincidences. As such, any source of loss in the setup is detrimental to the measured counts. For instance, the setup proposed in [67] based on the [EOM-PF-EOM] configuration induces a transmission of 11%, if we calculate it from the insertion loss of our own devices. Here we wish to perform a more resource-efficient version of the Bell-state measurement performed by a single EOM with a transmission of 56%.

To perform this proof-of-principle of the entanglement swapping protocol, we generate frequency-bin entangled states from the SOI micro-resonator. The two pairs originate from the same source and are encoded on interleaved frequency modes as

$$|\phi_1\rangle = \frac{1}{\sqrt{2}}\left(|I_{10}, S_{10}\rangle + |I_{12}, S_{12}\rangle\right), \tag{5.1}$$

$$|\phi_2\rangle = \frac{1}{\sqrt{2}}\left(|I_{11}, S_{11}\rangle + |I_{13}, S_{13}\rangle\right) \tag{5.2}$$

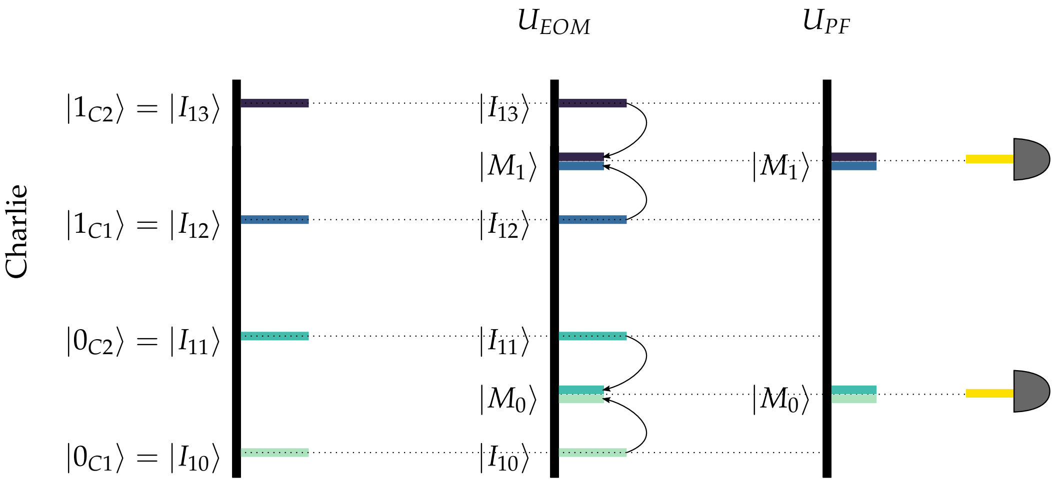

Figure 5.2: Sketch of the frequency-domain action of the devices for the Bell state measurement EOM: electro-optic modulator, PF: programmable filter.

The four-photon state is then the tensor product

$$\begin{aligned} |\phi_1\rangle \otimes |\phi_2\rangle = \frac{1}{2}(&|I_{10}, S_{10}\rangle |I_{11}, S_{11}\rangle \\ &+ |I_{10}, S_{10}\rangle |I_{13}, S_{13}\rangle \\ &+ |I_{12}, S_{12}\rangle |I_{11}, S_{11}\rangle \\ &+ |I_{12}, S_{12}\rangle |I_{13}, S_{13}\rangle) \end{aligned} \tag{5.3}$$

Alice receives the signal photon from the photon pair $|\phi_1\rangle$, encoded on the frequency modes $|S_{10}\rangle$ and $|S_{12}\rangle$. Bob receives the signal photon coming from the photon pair $|\phi_2\rangle$, encoded on the frequency modes $|S_{11}\rangle$ and $|S_{13}\rangle$. The two idler photons are sent to Charlie who performs a Bell state measurement.

Fig. 5.2 illustrates a frequency-domain representation of the Bell state measurement setup. An EOM converts light from the modes I_{10} and I_{11} to a frequency mode $|M_0\rangle$, and from the modes I_{12} and I_{13} to a frequency mode $|M_1\rangle$. The modulation index $\mu = 1.2$ of the RF driving is such that only frequency conversion to the first neighbors is significant. Under these considerations, the action of the EOM on the initial state of Eq. 5.3 is

$$\begin{gathered} U_{EOM_I} |\phi_1\rangle |\phi_2\rangle = \\ \frac{J_1 J_{-1}}{2} \left[\, |M_0, S_{10}\rangle |M_0, S_{11}\rangle + |M_0, S_{10}\rangle |M_1, S_{13}\rangle + \right. \\ \left. |M_1, S_{12}\rangle |M_0, S_{11}\rangle + |M_1, S_{12}\rangle |M_1, S_{13}\rangle \, \right] \end{gathered} \tag{5.4}$$

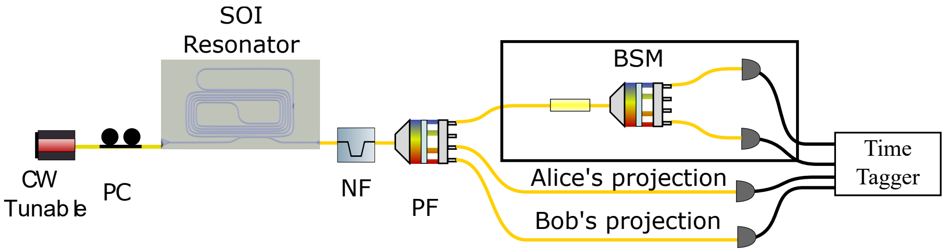

Figure 5.3: Setup for the measurement in the natural basis of the entanglement swapping. NF: notch filter, PF: programmable filter, BSM: Bell state measurement (cf Fig. 5.2).

Where J_1 and J_{-1} are the probability amplitudes of converting a photon from its original frequency mode to the first neighbors. Subsequently, a programmable filter (PF) is used for postselecting the modes $\langle M_0|$ and $\langle M_1|$, and spatially separating them into two distinct fibers.

$$\begin{gathered} U_{PF}\, U_{EOM_I}\, |\phi_1\rangle\, |\phi_2\rangle = \langle M_0|\, \langle M_1|\, U_{EOM_I}\, |A\rangle\, |B\rangle = \\ \frac{J_1 J_{-1}}{2} \left[\, \langle M_0|\, \langle M_1|\, |M_0, S_{10}\rangle\, |M_1, S_{13}\rangle + \right. \\ \left. \langle M_0|\, \langle M_1|\, |M_1, S_{12}\rangle\, |M_0, S_{11}\rangle \,\right] \end{gathered} \tag{5.5}$$

The state $|\psi_{post}\rangle$ shared between Alice and Bob is maximally entangled.

$$|\psi_{post}\rangle = \frac{J_1 J_{-1}}{2} \left[\, |S_{10}\rangle\, |S_{13}\rangle + |S_{12}\rangle\, |S_{11}\rangle \,\right] \tag{5.6}$$

The experimental setup to perform the entanglement swapping experiment is presented in Fig. 5.3. The four photons are generated by the silicon on insulator micro-resonator, and the residual pump is filtered by a Notch filter. The programmable filter (PF) prepares the four photons by selecting the respective signal and idler modes. The two idler photons are sent to Charlie for the BSM. Our first measurement to verify entanglement swapping is a correlation measurement between Alice and Bob, conditioned on Charlie's coincidence detection. A time tagger computes the four-fold coincidences between Charlie, Alice, and Bob.

From Eq. 5.6, we expect that two combinations of projective measurement give rise to coincident clicks between Alice and Bob, while the two other projective measurements are expected to give no coincident clicks. The results of the measurement are given in Fig. 5.4. The coincidences are measured for four hours for each measurement, with a maximum number of 21 four-fold coincidences for the projection $\langle S_{10}, S_{13}|\psi_{post}\rangle$.

The figure shows the normalized coincidences for the four possible outputs. The bars correspond to the measurement and the dashed outline corresponds to the expected values. We see clear correlations as expected from the theoretical results, which means that

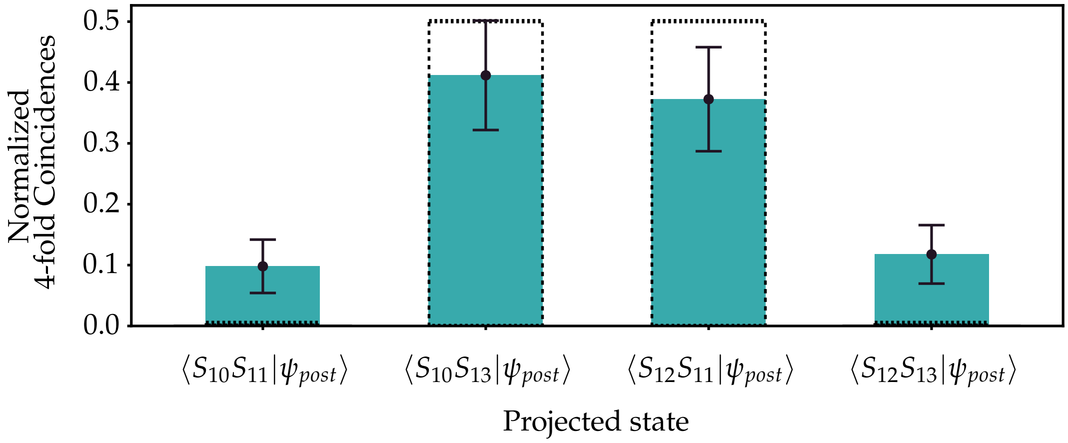

Figure 5.4: Projective measurement in the natural basis for Alice and Bob, conditioned by the coincidence detection of Charlie.

the two signal photons, initially uncorrelated, are now correlated in frequency. The error bars are calculated using the square roots of the measured coincidences. Improving the measurement would necessitate a longer integration time, which is challenging for setup stability reasons.

While this measurement shows a clear correlation sign, measuring coincidences on the superposition basis is necessary to assess entanglement. For this purpose, the setup for Alice and Bob needs to be modified, with at least one EOM and one PF each. We have implemented the proposed setup in Fig. 5.5. No significant results were obtained so far because of the low number of events recorded. In the coming months, we plan to improve the setup stability and control the losses to increase the number of events.

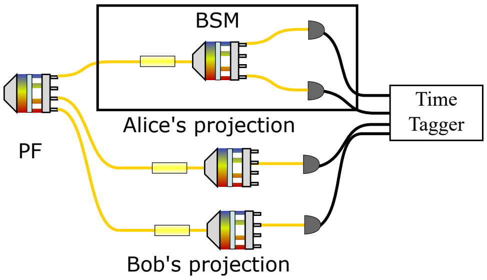

Figure 5.5: Setup for the correlation measurement in the superposition basis.

This experiment would enable for the first time a full frequency-domain entanglement swapping experiment, contrary to the work in [65], where the Bell state is performed with a spatial beam splitter.

5.3 Further applications of frequency encoding

Our first successful manipulation of frequency-bin qubits motivated us to try more transpositions of data processing to the frequency domain. We briefly mention here two experiments for which our preliminary results were encouraging.

5.3.1 Frequency-domain ghost imaging

The ghost imaging technique combines information from two detectors to reconstruct an object's image when resolving detectors are unavailable in the desired wavelength range. One detector collects photons that illuminate the object but cannot resolve it. The other detector collects photons that do not interact with the object but instead provides the necessary degree of freedom for imaging it. The light measured by each detector needs to be correlated so that we can reconstruct the image using the information from the two detectors. Therefore, photon pair sources are particularly suited, as the two generated photons possess correlation in various degrees of freedom. As such, several ghost imaging experiments have been demonstrated with photon pairs in degrees of freedom such as space [182] and time [183].

In the spectral domain, the object can be a spectral intensity pattern produced with a programmable filter. We reconstruct the spectral pattern using the spectral correlation [184]. Fig 5.6 displays the setup and findings of our frequency-domain ghost imaging experiment. A periodically poled lithium niobate waveguide generates frequency-correlated signal and idler pairs. The signal photon sees the object that we wish to reconstruct and is then measured by a non-frequency-resolving detector. The idler photon can be resolved with a resolution of up to 20 GHz. We conducted the ghost imaging experiment using two techniques to resolve the idler photon spectrum and check how it images the object with which it did not interact. First, we measured the two-photon coincidences between the non-resolved signal and the idler photon for each 20 GHz idler frequency bin. The results of this experiment are presented in Fig. 5.6.(a). Secondly, we applied 11981 random filters to the idler photon. The results of this experiment are shown in Fig. 5.6.(b). Both methods were successful in reconstructing the spectral object. Therefore, our implementation represents a first-of-a-kind realization of a ghost imaging experiment in the frequency domain.

5.3.2 Data classification with an optical processor

In integrated photonics, machine learning applications have been demonstrated with degrees of freedom such as space [185], and transverse modes [186]. The optical processor

(a) scanning idler filter central frequency

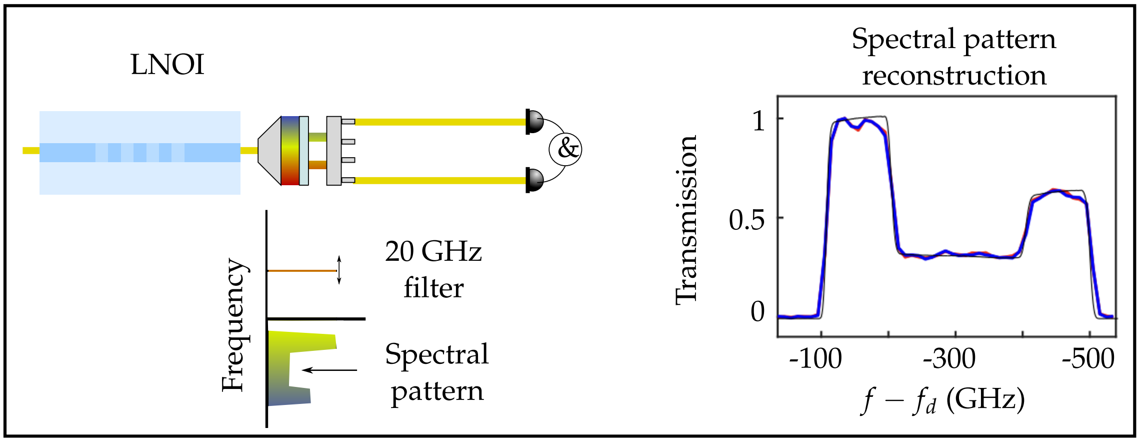

(b) Sampling with random idler filters

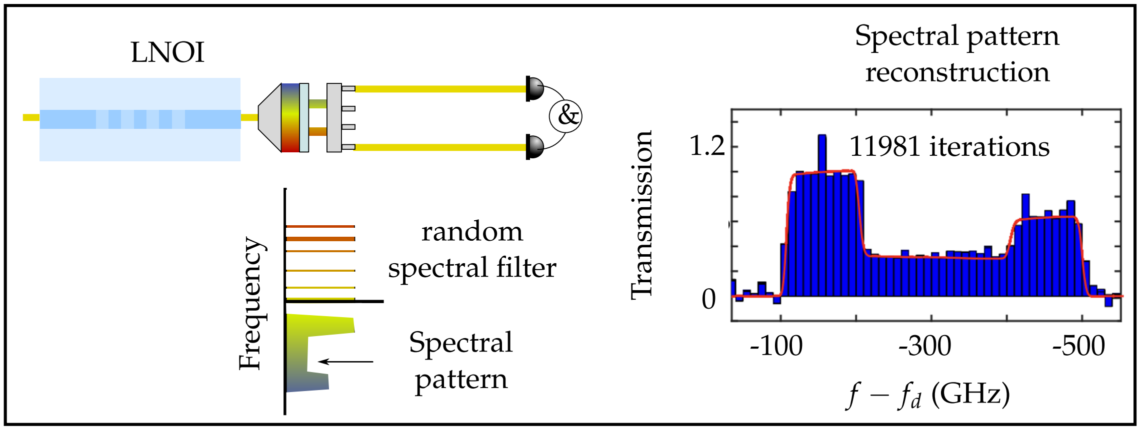

Figure 5.6: Setup and results of ghost imaging experiments. Broadband photons are generated by the LNOI waveguide, and directed to a PF where the spectral pattern is applied to the signal photon. The idler photon can be spectrally resolved with narrow-band filters with a minimal bandwidth of 20 GHz. (a): A first way to reconstruct the spectral pattern is to continuously scan the central frequency of the idler's narrow filter and collect the two-photon coincidences between the two detectors. (b): Alternatively, we randomly select 20 GHz wide bins from the idler spectrum and measure the resulting two-photon coincidences. With a large number of trials, it is possible to reconstruct the spectral pattern by pondering the random filters with the number of obtained coincidences. Here we show a reconstruction with 11981 trials. $f_d = 192.113$ THz is the degeneracy frequency

is composed either of beam splitters and phase shifters for the spatial degree of freedom, or of phase masks and spatial light modulators for transverse modes.

We performed a proof-of-concept modelization and experiment to classify data using an optical frequency processor with EOMs and PFs. The experimental setup and preliminary results are shown in Fig. 5.7. The implemented algorithm classifies two types of flowers based on the length and width of their petals and sepals, which compose a four-parameter space. We generate a four-frequency mode comb by sending a laser into an EOM and a PF. Each of the four flower parameter is then encoded as a phase on a frequency mode via this first PF. After data encoding, the light passes through an optical frequency processor consisting of EOMs and PFs arranged in a [EOM-PF-EOM-PF-EOM] configuration. We measure the intensity in each frequency mode and normalize the intensities to obtain a probability distribution $\{P_i\}$ to find light in a given frequency mode. We associate a weight W_i to each P_i. These weights are part of the optimized parameters along with PFs phases, EOMs modulation indices and phases. The output of the machine learning algorithm is a single number, $S = \sum_{i=0}^{3} P_i \times W_i$.

We split the flower dataset into two sections. One section is used to train the optical frequency processor, and the other section is used to test the trained system. For the training phase, we used the Scikit library in Python. The training set is processed by the optical processor, which provides new parameters and weights based on the success rate of trained objects for each iteration. This process continues until the optimization is complete and the best parameters are found. Results from numerical simulation and experimental implementation after optimization when fed with the test part of the dataset are shown in Fig. 5.7.(b) and (c). We managed to classify successfully two types of flowers, both numerically and experimentally, offering a first-of-a-kind application of optical frequency-encoding to a machine-learning problem.

5.4 Quantum key distribution protocol with frequency-entangled qudits

In quantum key distribution, harnessing high-dimensional quantum states defined as qudits offers advantages compared to qubits.

Encoding information on more than two quantum states allows to carry more than one bit per photon [187]. The main feature of using qudits for quantum key distribution is the robustness of such states to the environment [188, 189]. The amount of information shared between Alice and Bob, exchanging a pair of frequency-entangled qudits of dimension D, generalized from Eq. 4.32 is expressed as [190]

$$R^{D}_{sift} = \frac{1}{2} R_{raw} \left(log_2(D) - H_D(e) f(e) - H_D(e) \right). \tag{5.7}$$

$H_D(e) = -e \times log(\frac{e}{1-D}) - (1-e)log(1-e)$ is the binary entropy function generalized to D dimensions. The impact of expanding the dimension of the quantum state on the

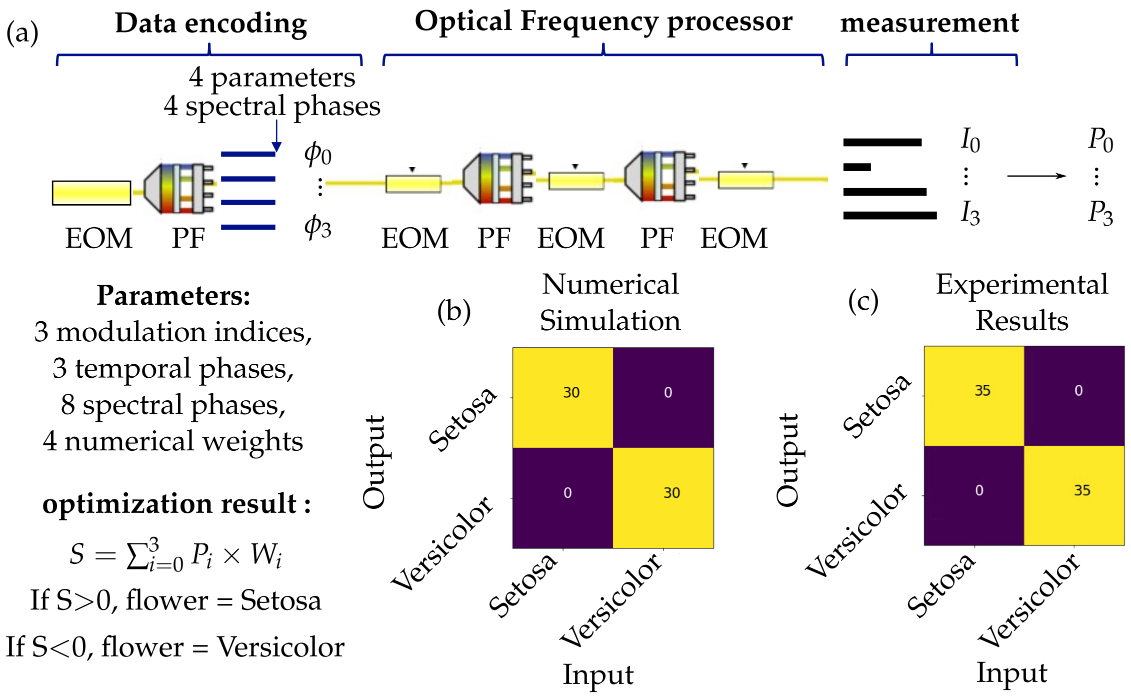

Figure 5.7: (a): Experimental setup for the classification algorithm. A comb of four frequency modes is created by sending a laser in a combination of EOM and PF. Each of the four parameters is encoded as a phase on each frequency mode. The data is then processed by the optical frequency processor. After that, the intensity is measured and transformed into a probability distribution. (b): numerical optimization performed using EOMs and PFs modelized with the Fourier transform model of Chapter 3. (c): Experimental results.

information per photon exchanged by two parties is given in Fig. 5.8. The quantity of information per photon increases with the dimensionality of the qudit. The QBER threshold over which the communication rate vanishes also increases. This increase in the QBER threshold would enable a higher tolerance for environmental noise and ultimately an increase in the achievable distance in a quantum key distribution protocol.

To manipulate frequency-bin qudits, it is possible to use setups as simple as a single electro-optic modulator [68, 73, 75, 76, 86, 88]. The manipulation of frequency-bin qudits is possible if electro-optic bandwidth is high enough, using the [EOM-PF-EOM] configuration [75]. This perspective is being investigated by George Crisan in his Ph.D. in the GOSS group at C2N as a continuation of this Ph.D. thesis. A very promising outcome would be the possibility of harnessing the high density of frequency modes offered by the SOI micro-resonator for both high-dimensional frequency encoding and spectral demul-

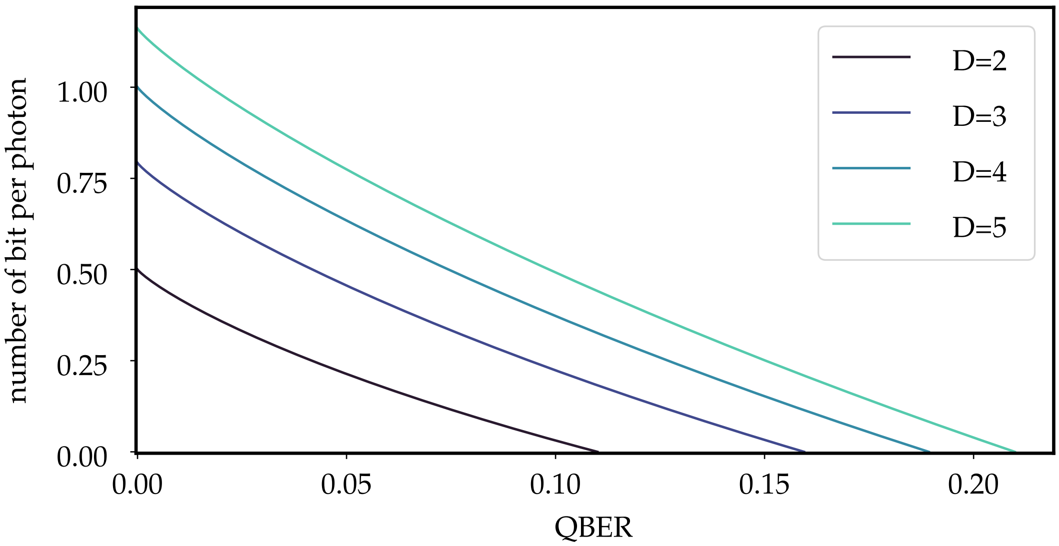

Figure 5.8: Number of bit per photon shared between Alice and Bob as a function of the QBER for 5 qudit dimensions D.

tiplexing.

5.5 Recent progress of on-chip integration for the manipulation of frequency bin quantum states

This work presented the ability to manipulate quantum states in the frequency domain, using fibered off-the-shelf devices. Two main limitations appeared, however.

Insertion loss:
The devices used in this manuscript exhibit an insertion loss of 2.5 dB for the modulators, mainly due to fiber-to-waveguide coupling, and 3.3 dB for the programmable filters. For instance, the [EOM-PF-EOM] configuration has an insertion loss of around 9 dB (11% transmission).

Resolution and bandwidth:
The technical limitations of the devices restrict the frequency spacing that can be accessed. On the one hand, the limited bandwidth of the EOM does not allow to couple frequency modes spaced by more than a few tens of GHz. On the other hand, the limited resolution of the PF does not allow to resolve frequency modes spaced by less than 10 GHz.

Integrating the tools needed for frequency-domain manipulation on a single chip would allow overcoming these limitations. Some interesting designs have been recently reported:

Integrating the [EOM-PF-EOM] configuration

In the direct continuity of the work presented in this manuscript, a design was proposed in [62] in order to integrate into a single photonic chip the [EOM-PF-EOM] configuration. In this design, modulators would consist of the hybrid integration of the lithium niobate on silicon. The integration of the PF relies on arrays of resonators acting as add-drop filters to separate and recombine frequencies. Thermal or electro-optic phase shifters would apply a spectral phase on each frequency mode. Such a design would enable lower mode spacing, limited only by the ability to realize micro-resonators with high quality factors. As a consequence, the EOMs could be driven by arbitrary waveform generators.

Another example of recent progress is the realization of electro-optic modulators with bandwidths of >100 GHz, harnessing wider mode spacing between the qubit modes [44, 46]. This integrated approach would thus increase the overall transmission from 11% for the fibered devices in our implementation to 75%.

Other integration possibilities

Other groups have proposed designs and performed experiments to manipulate frequency-bin qubits, using only electro-optic manipulation with no PF devices. In [191], a tunable frequency beam-splitter is realized by using a pair of modulated LNOI ring resonators. The coupling between the two frequency modes is tuned by the power of the RF driving. The success probability and fidelity of the tunable operation exceed 0.9 for all rotation angles. The work expands by showing the ability to realize wider frequency shifts using a more complex design, and experimentally demonstrate frequency shifting between modes 120 GHz apart. In [60], a similar approach is proposed to perform arbitrary linear transformation in the frequency domain. They show the possibility to perform any given NxN transformation with high fidelity using a combination of N rings. Third-order non-linearities can also be harnessed for the on-chip processing of frequency-bin qubits. A proposed design in [63] demonstrates the possibility of both generating photon pairs and processing them in the frequency domain using a silicon-nitride integrated circuit. In this case, the frequency-bin operation is tuned by an optical pump, through four-wave mixing. The on-chip generation of more complex frequency-domain quantum states has also been proposed using silicon photonics. In [192], a design based on multiple silicon-micro-resonator photon pair sources, and add-drop filters would enable the generation of three-photons and four-photons frequency-bin entangled states. Finally, recent experimental work showed the possibility of harnessing the LNOI technology for both the generation and frequency-domain manipulation of frequency-bin qubits [193]. In this work, a modulated lithium niobate on insulator microresonator with a periodically poled section is used both for the generation of frequency-entangled pairs and for their manipulation.

A notable advantage of integrated frequency-domain manipulation is the ability to realize complex linear interferometers. In the frequency domain, the number of integrated optical components needed to realize an N modes interferometer scales as $O(\mathcal{N})$. This is in contrast to standard path-encoded interferometers, which scale as $O(\mathcal{N}^2)$[60].

All these works offer bright perspectives for the integration of frequency domain processing.

Bibliography

[1] Yuchen Wang, Klaus D. Jöns, and Zhipei Sun. Integrated photon-pair sources with nonlinear optics. *Applied Physics Reviews*, 8(1):011314, March 2021.

[2] Morten Kjaergaard, Mollie E. Schwartz, Jochen Braumüller, Philip Krantz, Joel I.-J. Wang, Simon Gustavsson, and William D. Oliver. Superconducting Qubits: Current State of Play. *Annual Review of Condensed Matter Physics*, 11(1):369–395, March 2020.

[3] Jan Benhelm, Gerhard Kirchmair, Christian F. Roos, and Rainer Blatt. Towards fault-tolerant quantum computing with trapped ions. *Nature Physics*, 4(6):463–466, June 2008.

[4] P. Scholl, H. J. Williams, G. Bornet, F. Wallner, D. Barredo, L. Henriet, A. Signoles, C. Hainaut, T. Franz, S. Geier, A. Tebben, A. Salzinger, G. Zürn, T. Lahaye, M. Weidemüller, and A. Browaeys. Microwave Engineering of Programmable X X Z Hamiltonians in Arrays of Rydberg Atoms. *PRX Quantum*, 3(2):020303, April 2022.

[5] Emanuele Pelucchi, Giorgos Fagas, Igor Aharonovich, Dirk Englund, Eden Figueroa, Qihuang Gong, Hübel Hannes, Jin Liu, Chao-Yang Lu, Nobuyuki Matsuda, Jian-Wei Pan, Florian Schreck, Fabio Sciarrino, Christine Silberhorn, Jianwei Wang, and Klaus D. Jöns. The potential and global outlook of integrated photonics for quantum technologies. *Nature Reviews Physics*, 4(3):194–208, December 2021.

[6] Jeremy L. O'Brien. Optical Quantum Computing. *Science*, 318(5856):1567–1570, December 2007.

[7] Jeremy L. O'Brien, Akira Furusawa, and Jelena Vučković. Photonic quantum technologies. *Nature Photonics*, 3(12):687–695, December 2009.

[8] Stephanie Wehner, David Elkouss, and Ronald Hanson. Quantum internet: A vision for the road ahead. *Science*, 362(6412):eaam9288, October 2018.

[9] Lars S. Madsen, Fabian Laudenbach, Mohsen Falamarzi. Askarani, Fabien Rortais, Trevor Vincent, Jacob F. F. Bulmer, Filippo M. Miatto, Leonhard Neuhaus,

Lukas G. Helt, Matthew J. Collins, Adriana E. Lita, Thomas Gerrits, Sae Woo Nam, Varun D. Vaidya, Matteo Menotti, Ish Dhand, Zachary Vernon, Nicolás Quesada, and Jonathan Lavoie. Quantum computational advantage with a programmable photonic processor. *Nature*, 606(7912):75–81, June 2022.

[10] Nicolas Maring, Andreas Fyrillas, Mathias Pont, Edouard Ivanov, Petr Stepanov, Nico Margaria, William Hease, Anton Pishchagin, Thi Huong Au, Sébastien Boissier, Eric Bertasi, Aurélien Baert, Mario Valdivia, Marie Billard, Ozan Acar, Alexandre Brieussel, Rawad Mezher, Stephen C. Wein, Alexia Salavrakos, Patrick Sinnott, Dario A. Fioretto, Pierre-Emmanuel Emeriau, Nadia Belabas, Shane Mansfield, Pascale Senellart, Jean Senellart, and Niccolo Somaschi. A general-purpose single-photon-based quantum computing platform. 2023. Publisher: arXiv Version Number: 1.

[11] C. L. Degen, F. Reinhard, and P. Cappellaro. Quantum sensing. *Reviews of Modern Physics*, 89(3):035002, July 2017.

[12] Axel Kuhn, Markus Hennrich, and Gerhard Rempe. Deterministic Single-Photon Source for Distributed Quantum Networking. *Physical Review Letters*, 89(6):067901, July 2002.

[13] Clarisse Fournier, Alexandre Plaud, Sébastien Roux, Aurélie Pierret, Michael Rosticher, Kenji Watanabe, Takashi Taniguchi, Stéphanie Buil, Xavier Quélin, Julien Barjon, Jean-Pierre Hermier, and Aymeric Delteil. Position-controlled quantum emitters with reproducible emission wavelength in hexagonal boron nitride. *Nature Communications*, 12(1):3779, June 2021.

[14] Toan Trong Tran, Kerem Bray, Michael J. Ford, Milos Toth, and Igor Aharonovich. Quantum emission from hexagonal boron nitride monolayers. *Nature Nanotechnology*, 11(1):37–41, January 2016.

[15] Shuliang Ren, Qinghai Tan, and Jun Zhang. Review on the quantum emitters in two-dimensional materials. *Journal of Semiconductors*, 40(7):071903, July 2019.

[16] Daniel Huber, Marcus Reindl, Yongheng Huo, Huiying Huang, Johannes S. Wildmann, Oliver G. Schmidt, Armando Rastelli, and Rinaldo Trotta. Highly indistinguishable and strongly entangled photons from symmetric GaAs quantum dots. *Nature Communications*, 8(1):15506, May 2017.

[17] Pascale Senellart, Glenn Solomon, and Andrew White. High-performance semiconductor quantum-dot single-photon sources. *Nature Nanotechnology*, 12(11):1026–1039, November 2017.

[18] Robert Fickler, Radek Lapkiewicz, William N. Plick, Mario Krenn, Christoph Scha-

eff, Sven Ramelow, and Anton Zeilinger. Quantum Entanglement of High Angular Momenta. *Science*, 338(6107):640–643, November 2012.

[19] Jonas H. Weber, Benjamin Kambs, Jan Kettler, Simon Kern, Julian Maisch, Hüseyin Vural, Michael Jetter, Simone L. Portalupi, Christoph Becher, and Peter Michler. Two-photon interference in the telecom C-band after frequency conversion of photons from remote quantum emitters. *Nature Nanotechnology*, 14(1):23–26, January 2019.

[20] Sebastian Zaske, Andreas Lenhard, Christian A. Keßler, Jan Kettler, Christian Hepp, Carsten Arend, Roland Albrecht, Wolfgang-Michael Schulz, Michael Jetter, Peter Michler, and Christoph Becher. Visible-to-Telecom Quantum Frequency Conversion of Light from a Single Quantum Emitter. *Physical Review Letters*, 109(14):147404, October 2012.

[21] Mathias Pont, Giacomo Corrielli, Andreas Fyrillas, Iris Agresti, Gonzalo Carvacho, Nicolas Maring, Pierre-Emmanuel Emeriau, Francesco Ceccarelli, Ricardo Albiero, Paulo H. D. Ferreira, Niccolo Somaschi, Jean Senellart, Isabelle Sagnes, Martina Morassi, Aristide Lemaitre, Pascale Senellart, Fabio Sciarrino, Marco Liscidini, Nadia Belabas, and Roberto Osellame. High-fidelity generation of four-photon GHZ states on-chip, November 2022. arXiv:2211.15626 [quant-ph].

[22] F. Basso-Basset, M.B. Rota, C. Schimpf, D. Tedeschi, K.D. Zeuner, S. F. Covre Da Silva, M. Reindl, V. Zwiller, K. D. Jöns, A. Rastelli, and R. Trotta. Entanglement Swapping with Photons Generated on Demand by a Quantum Dot. *Physical Review Letters*, 123(16):160501, October 2019.

[23] Jianwei Wang, Fabio Sciarrino, Anthony Laing, and Mark G. Thompson. Integrated photonic quantum technologies. *Nature Photonics*, 14(5):273–284, May 2020.

[24] Jueming Bao, Zhaorong Fu, Tanumoy Pramanik, Jun Mao, Yulin Chi, Yingkang Cao, Chonghao Zhai, Yifei Mao, Tianxiang Dai, Xiaojiong Chen, Xinyu Jia, Leshi Zhao, Yun Zheng, Bo Tang, Zhihua Li, Jun Luo, Wenwu Wang, Yan Yang, Yingying Peng, Dajian Liu, Daoxin Dai, Qiongyi He, Alif Laila Muthali, Leif K. Oxenløwe, Caterina Vigliar, Stefano Paesani, Huili Hou, Raffaele Santagati, Joshua W. Silverstone, Anthony Laing, Mark G. Thompson, Jeremy L. O'Brien, Yunhong Ding, Qihuang Gong, and Jianwei Wang. Very-large-scale integrated quantum graph photonics. *Nature Photonics*, 17(7):573–581, July 2023.

[25] Fulvio Flamini, Nicolò Spagnolo, and Fabio Sciarrino. Photonic quantum information processing: a review. *Reports on Progress in Physics*, 82(1):016001, January 2019.

[26] Sergei Slussarenko and Geoff J. Pryde. Photonic quantum information processing: A concise review. *Applied Physics Reviews*, 6(4):041303, December 2019.

[27] Jonathan C. F. Matthews, Alberto Politi, André Stefanov, and Jeremy L. O'Brien. Manipulation of multiphoton entanglement in waveguide quantum circuits. *Nature Photonics*, 3(6):346–350, June 2009.

[28] Chao Xiang, Warren Jin, and John E. Bowers. Silicon nitride passive and active photonic integrated circuits: trends and prospects. *Photonics Research*, 10(6):A82, June 2022.

[29] F. Baboux, G. Moody, and S. Ducci. Nonlinear integrated quantum photonics with AlGaAs. *Optica*, 10(7):917, July 2023.

[30] Sina Saravi, Thomas Pertsch, and Frank Setzpfandt. Lithium Niobate on Insulator: An Emerging Platform for Integrated Quantum Photonics. *Advanced Optical Materials*, n/a(n/a):2100789, December 2021.

[31] S. Tanzilli, H. De Riedmatten, W. Tittel, H. Zbinden, P. Baldi, M. De Micheli, D. B. Ostrowsky, and N. Gisin. Highly efficient photon-pair source using periodically poled lithium niobate waveguide. *Electronics Letters*, 37(1):26–28, January 2001.

[32] Sridhar Majety, Pranta Saha, Victoria A. Norman, and Marina Radulaski. Quantum information processing with integrated silicon carbide photonics. *Journal of Applied Physics*, 131(13):130901, April 2022.

[33] Jay E. Sharping, Kim F. Lee, Mark A. Foster, Amy C. Turner, Bradley S. Schmidt, Michal Lipson, Alexander L. Gaeta, and Prem Kumar. Generation of correlated photons in nanoscale silicon waveguides. *Optics Express*, 14(25):12388, 2006.

[34] S. Clemmen, K. Phan Huy, W. Bogaerts, R. G. Baets, Ph Emplit, and S. Massar. Continuous wave photon pair generation in silicon-on-insulator waveguides and ring resonators. *Optics Express*, 17(19):16558–16570, September 2009.

[35] J. Brendel, N. Gisin, W. Tittel, and H. Zbinden. Pulsed Energy-Time Entangled Twin-Photon Source for Quantum Communication. *Physical Review Letters*, 82(12):2594–2597, March 1999.

[36] Marius A. Albota and Eric Dauler. Single photon detection of degenerate photon pairs at 1.55 um from a periodically poled lithium niobate parametric downconverter. *Journal of Modern Optics*, 51(9-10):1417–1432, June 2004.

[37] S. Tanzilli, W. Tittel, H. De Riedmatten, H. Zbinden, P. Baldi, M. DeMicheli, D.B. Ostrowsky, and N. Gisin. PPLN waveguide for quantum communication. *The European Physical Journal D - Atomic, Molecular, Optical and Plasma Physics*, 18(2):155–160, February 2002.

[38] G. Poberaj, H. Hu, W. Sohler, and P. Günter. Lithium niobate on insulator (LNOI) for micro-photonic devices. *Laser & Photonics Reviews*, 6(4):488–503, July 2012.

[39] Bing-Xi Xiang, Lei Wang, Yu-Jie Ma, Li Yu, Huang-Pu Han, and Shuang-Chen Ruan. Supercontinuum Generation in Lithium Niobate Ridge Waveguides Fabricated by Proton Exchange and Ion Beam Enhanced Etching. *Chinese Physics Letters*, 34(2):024203, February 2017.

[40] Di Zhu, Linbo Shao, Mengjie Yu, Rebecca Cheng, Boris Desiatov, C. J. Xin, Yaowen Hu, Jeffrey Holzgrafe, Soumya Ghosh, Amirhassan Shams-Ansari, Eric Puma, Neil Sinclair, Christian Reimer, Mian Zhang, and Marko Lončar. Integrated photonics on thin-film lithium niobate. *Advances in Optics and Photonics*, 13(2):242, June 2021.

[41] Antoine Henry, David Barral, Isabelle Zaquine, Andreas Boes, Arnan Mitchell, Nadia Belabas, and Kamel Bencheikh. Correlated twin-photon generation in a silicon nitride loaded thin film PPLN waveguide. *Optics Express*, 31(5):7277, February 2023.

[42] Bradley S. Elkus, Kamal Abdelsalam, Sasan Fathpour, Prem Kumar, and Gregory S. Kanter. Quantum-correlated photon-pair generation via cascaded nonlinearity in an ultra-compact lithium-niobate nano-waveguide. *Optics Express*, 28(26):39963, December 2020.

[43] Jie Zhao, Chaoxuan Ma, Michael Rüsing, and Shayan Mookherjea. High Quality Entangled Photon Pair Generation in Periodically Poled Thin-Film Lithium Niobate Waveguides. *Physical Review Letters*, 124(16):163603, April 2020.

[44] Forrest Valdez, Viphretuo Mere, Xiaoxi Wang, Nicholas Boynton, Thomas A. Friedmann, Shawn Arterburn, Christina Dallo, Andrew T. Pomerene, Andrew L. Starbuck, Douglas C. Trotter, Anthony L. Lentine, and Shayan Mookherjea. 110 GHz, 110 mW hybrid silicon-lithium niobate Mach-Zehnder modulator. *Scientific Reports*, 12(1):18611, November 2022.

[45] Oguz Tolga Celik, Christopher J. Sarabalis, Felix M. Mayor, Hubert S. Stokowski, Jason F. Herrmann, Timothy P. McKenna, Nathan R. A. Lee, Wentao Jiang, Kevin K. S. Multani, and Amir H. Safavi-Naeini. High-bandwidth CMOS-voltage-level electro-optic modulation of 780 nm light in thin-film lithium niobate. *Optics Express*, 30(13):23177, June 2022.

[46] Ying Li, Tian Lan, Dengcai Yang, Jianfeng Bao, Meihua Xiang, Feng Yang, and Zhiyong Wang. High-Performance Mach–Zehnder Modulator Based on Thin-Film Lithium Niobate with Low Voltage-Length Product. *ACS Omega*, 8(10):9644–9651, March 2023. Publisher: American Chemical Society.

[47] Mingbo He, Mengyue Xu, Yuxuan Ren, Jian Jian, Ziliang Ruan, Yongsheng Xu, Shengqian Gao, Shihao Sun, Xueqin Wen, Lidan Zhou, Lin Liu, Changjian Guo, Hui Chen, Siyuan Yu, Liu Liu, and Xinlun Cai. High-performance hybrid silicon and lithium niobate Mach–Zehnder modulators for 100 Gbit s-1 and beyond. *Nature Photonics*, 13(5):359–364, May 2019.

[48] Shihao Sun, Mingbo He, Mengyue Xu, Shengqian Gao, Siyuan Yu, and Xinlun Cai. Hybrid Silicon and Lithium Niobate Modulator. *IEEE Journal of Selected Topics in Quantum Electronics*, 27(3):1–12, May 2021.

[49] Xiaoxi Wang, Forrest Valdez, Viphretuo Mere, and Shayan Mookherjea. Integrated thin-silicon passive components for hybrid silicon-lithium niobate photonics. *Optics Continuum*, 1(10):2233, October 2022.

[50] C. J. McKinstrie, J. D. Harvey, S. Radic, and M. G. Raymer. Translation of quantum states by four-wave mixing in fibers. *Optics Express*, 13(22):9131, 2005.

[51] M. G. Raymer, S. J. van Enk, C. J. McKinstrie, and H. J. McGuinness. Interference of two photons of different color. *Optics Communications*, 283(5):747–752, March 2010.

[52] Prathamesh S. Donvalkar, Vivek Venkataraman, Stéphane Clemmen, Kasturi Saha, and Alexander L. Gaeta. Frequency translation via four-wave mixing Bragg scattering in Rb filled photonic bandgap fibers. *Optics Letters*, 39(6):1557, March 2014.

[53] Chaitali Joshi, Alessandro Farsi, Avik Dutt, Bok Young Kim, Xingchen Ji, Yun Zhao, Andrew M. Bishop, Michal Lipson, and Alexander L. Gaeta. Frequency-Domain Quantum Interference with Correlated Photons from an Integrated Microresonator. *Physical Review Letters*, 124(14):143601, April 2020.

[54] Matthieu Bloch, Steven W. McLaughlin, Jean-Marc Merolla, and Frédéric Patois. Frequency-coded quantum key distribution. *Optics Letters*, 32(3):301–303, February 2007.

[55] Joseph M. Lukens and Pavel Lougovski. Frequency-encoded photonic qubits for scalable quantum information processing. *Optica*, 4(1):8–16, January 2017.

[56] Hsuan-Hao Lu, Natalie Klco, Joseph M. Lukens, Titus D. Morris, Titus D. Morris, Aaina Bansal, Andreas Ekström, Gaute Hagen, Gaute Hagen, Thomas Papenbrock, Thomas Papenbrock, Andrew M. Weiner, Martin J. Savage, and Pavel Lougovski. Subatomic Many-Body Physics Simulations on a Quantum Frequency Processor. In *Conference on Lasers and Electro-Optics (2019), paper FTh3A.6*, page FTh3A.6. Optical Society of America, May 2019.

[57] Hsuan-Hao Lu, Joseph M. Lukens, Nicholas A. Peters, Ogaga D. Odele, Daniel E. Leaird, Andrew M. Weiner, and Pavel Lougovski. Electro-Optic Frequency Beamsplitters and Tritters for High-Fidelity Photonic Quantum Information Processing. *Physical Review Letters*, 120(3):030502, January 2018. arXiv: 1712.03992.

[58] Yaowen Hu, Mengjie Yu, Di Zhu, Neil Sinclair, Amirhassan Shams-Ansari, Linbo Shao, Jeffrey Holzgrafe, Eric Puma, Mian Zhang, and Marko Lončar. On-chip electro-optic frequency shifters and beam splitters. *Nature*, 599(7886):587–593, November 2021.

[59] Anahita Khodadad Kashi and Michael Kues. Spectral Hong–Ou–Mandel Interference between Independently Generated Single Photons for Scalable Frequency-Domain Quantum Processing. *Laser & Photonics Reviews*, 15(5):2000464, 2021. [Khodadad21].

[60] Siddharth Buddhiraju, Avik Dutt, Momchil Minkov, Ian A. D. Williamson, and Shanhui Fan. Arbitrary linear transformations for photons in the frequency synthetic dimension. *Nature Communications*, 12(1):2401, April 2021.

[61] Hsuan-Hao Lu, Emma M. Simmerman, Pavel Lougovski, Andrew M. Weiner, and Joseph M. Lukens. Fully Arbitrary Control of Frequency-Bin Qubits. *Physical Review Letters*, 125(12):120503, September 2020.

[62] Benjamin E. Nussbaum, Andrew J. Pizzimenti, Navin B. Lingaraju, Hsuan-Hao Lu, and Joseph M. Lukens. Design Methodologies for Integrated Quantum Frequency Processors. *Journal of Lightwave Technology*, 40(23):7648–7657, December 2022.

[63] A. L. Aguayo-Alvarado, F. Domínguez-Serna, W. De La Cruz, and K. Garay-Palmett. An integrated photonic circuit for color qubit preparation by third-order nonlinear interactions. *Scientific Reports*, 12(1):5154, March 2022.

[64] Poolad Imany, Jose A. Jaramillo-Villegas, Mohammed S. Alshaykh, Joseph M. Lukens, Ogaga D. Odele, Alexandria J. Moore, Daniel E. Leaird, Minghao Qi, and Andrew M. Weiner. High-dimensional optical quantum logic in large operational spaces. *npj Quantum Information*, 5(1):1–10, July 2019.

[65] Sofiane Merkouche, Valerian Thiel, AlexO.C. Davis, and BrianJ. Smith. Heralding Multiple Photonic Pulsed Bell Pairs via Frequency-Resolved Entanglement Swapping. *Physical Review Letters*, 128(6):063602, February 2022.

[66] Hsuan-Hao Lu, Joseph M. Lukens, Nicholas A. Peters, Brian P. Williams, Andrew M. Weiner, and Pavel Lougovski. Quantum interference and correlation control of frequency-bin qubits. *Optica*, 5(11):1455–1460, November 2018. [lu18].

[67] Navin B. Lingaraju, Hsuan-Hao Lu, Daniel E. Leaird, Steven Estrella, Joseph M. Lukens, and Andrew M. Weiner. Bell state analyzer for spectrally distinct photons. *Optica*, 9(3):280, March 2022.

[68] Michael Kues, Christian Reimer, Piotr Roztocki, Luis Romero Cortés, Stefania Sciara, Benjamin Wetzel, Yanbing Zhang, Alfonso Cino, Sai T. Chu, Brent E. Little, David J. Moss, Lucia Caspani, José Azaña, and Roberto Morandotti. On-chip generation of high-dimensional entangled quantum states and their coherent control. *Nature*, 546(7660):622–626, June 2017.

[69] Toshiki Kobayashi, Rikizo Ikuta, Shuto Yasui, Shigehito Miki, Taro Yamashita, Hi-

rotaka Terai, Takashi Yamamoto, Masato Koashi, and Nobuyuki Imoto. Frequency-domain Hong–Ou–Mandel interference. *Nature Photonics*, 10(7):441–444, July 2016.

[70] Laurent Olislager, Erik Woodhead, Kien Phan Huy, Jean-Marc Merolla, Philippe Emplit, and Serge Massar. Creating and manipulating entangled optical qubits in the frequency domain. *Physical Review A*, 89(5):052323, May 2014.

[71] Laurent Olislager, Ismaël Mbodji, Erik Woodhead, Johann Cussey, Luca Furfaro, Philippe Emplit, Serge Massar, Kien Phan Huy, and Jean-Marc Merolla. Implementing two-photon interference in the frequency domain with electro-optic phase modulators. *New Journal of Physics*, 14(4):043015, April 2012.

[72] L. Olislager, J. Cussey, A. T. Nguyen, P. Emplit, S. Massar, J.-M. Merolla, and K. Phan Huy. Frequency-bin entangled photons. *Physical Review A*, 82(1):013804, July 2010.

[73] Hatam Mahmudlu, Robert Johanning, Albert van Rees, Anahita Khodadad Kashi, Jörn P. Epping, Raktim Haldar, Klaus-J. Boller, and Michael Kues. Fully on-chip photonic turnkey quantum source for entangled qubit/qudit state generation. *Nature Photonics*, 17(6):518–524, June 2023.

[74] Antoine Henry, Ravi Raghunathan, Guillaume Ricard, Baptiste Lefaucher, Filippo Miatto, Nadia Belabas, Isabelle Zaquine, and Romain Alléaume. Parallelizable synthesis of arbitrary single-qubit gates with linear optics and time-frequency encoding. *Physical Review A*, 107(6):062610, June 2023.

[75] Hsuan-Hao Lu, Navin B. Lingaraju, Daniel E. Leaird, Andrew M. Weiner, and Joseph M. Lukens. High-dimensional discrete Fourier transform gates with a quantum frequency processor. *Optics Express*, 30(6):10126, March 2022.

[76] Poolad Imany, Jose A. Jaramillo-Villegas, Ogaga D. Odele, Kyunghun Han, Daniel E. Leaird, Joseph M. Lukens, Pavel Lougovski, Minghao Qi, and Andrew M. Weiner. 50-GHz-spaced comb of high-dimensional frequency-bin entangled photons from an on-chip silicon nitride microresonato. *Optics Express*, 26(2):1825–1840, January 2018.

[77] Michael Kues, Christian Reimer, Joseph M. Lukens, William J. Munro, Andrew M. Weiner, David J. Moss, and Roberto Morandotti. Quantum optical microcombs. *Nature Photonics*, 13(3):170–179, March 2019.

[78] Antoine Henry, Dario Fioretto, Lorenzo M. Procopio, Stéphane Monfray, Frédéric Boeuf, Laurent Vivien, Eric Cassan, Carlos Ramos, Kamel Bencheikh, Isabelle Zaquine, and Nadia Belabas. Parallelization of frequency domain quantum gates: manipulation and distribution of frequency-entangled photon pairs generated by a 21 GHz silicon micro-resonator, May 2023. arXiv:2305.03457 [quant-ph].

[79] Meritxell Cabrejo-Ponce, André Luiz Marques Muniz, Marcus Huber, and Fabian Steinlechner. High-Dimensional Entanglement for Quantum Communication in the Frequency Domain. *Laser & Photonics Reviews*, page 2201010, July 2023.

[80] Hsuan-Hao Lu, Muneer Alshowkan, Karthik V. Myilswamy, Andrew M. Weiner, Joseph M. Lukens, and Nicholas A. Peters. Generation and characterization of ultrabroadband polarization-frequency hyperentangled photons, August 2023. arXiv:2308.16285 [physics, physics:quant-ph].

[81] Federico Andrea Sabattoli, Linda Gianini, Angelica Simbula, Marco Clementi, Antonio Fincato, Frederic Boeuf, Marco Liscidini, Matteo Galli, and Daniele Bajoni. A silicon source of frequency-bin entangled photons. *Optics Letters*, 47(23):6201, December 2022.

[82] Christian Reimer, Stefania Sciara, Piotr Roztocki, Mehedi Islam, Luis Romero Cortés, Yanbing Zhang, Bennet Fischer, Sébastien Loranger, Raman Kashyap, Alfonso Cino, Sai T. Chu, Brent E. Little, David J. Moss, Lucia Caspani, William J. Munro, José Azaña, Michael Kues, and Roberto Morandotti. High-dimensional one-way quantum processing implemented on d-level cluster states. *Nature Physics*, 15(2):148–153, February 2019.

[83] Suparna Seshadri, Hsuan-Hao Lu, Daniel E. Leaird, Andrew M. Weiner, and Joseph M. Lukens. Complete Frequency-Bin Bell Basis Synthesizer. *Physical Review Letters*, 129(23):230505, December 2022.

[84] Marco Clementi, Federico Andrea Sabattoli, Massimo Borghi, Linda Gianini, Noemi Tagliavacche, Houssein El Dirani, Laurene Youssef, Nicola Bergamasco, Camille Petit-Etienne, Erwine Pargon, J. E. Sipe, Marco Liscidini, Corrado Sciancalepore, Matteo Galli, and Daniele Bajoni. Programmable frequency-bin quantum states in a nano-engineered silicon device. *Nature Communications*, 14(1):176, January 2023.

[85] Hsuan-Hao Lu, Joseph M. Lukens, Brian P. Williams, Poolad Imany, Nicholas A. Peters, Andrew M. Weiner, and Pavel Lougovski. A controlled-NOT gate for frequency-bin qubits. *npj Quantum Information*, 5(1):1–8, March 2019.

[86] Hsuan-Hao Lu, Karthik V. Myilswamy, Ryan S. Bennink, Suparna Seshadri, Mohammed S. Alshaykh, Junqiu Liu, Tobias J. Kippenberg, Daniel E. Leaird, Andrew M. Weiner, and Joseph M. Lukens. Bayesian tomography of high-dimensional on-chip biphoton frequency combs with randomized measurements. *Nature Communications*, 13(1):4338, July 2022.

[87] Poolad Imany, Ogaga D. Odele, Mohammed S. Alshaykh, Hsuan-Hao Lu, Daniel E. Leaird, and Andrew M. Weiner. Frequency-domain Hong–Ou–Mandel interference with linear optics. *Optics Letters*, 43(12):2760–2763, June 2018. [Imany18].

[88] Massimo Borghi, Noemi Tagliavacche, Federico Andrea Sabattoli, Houssein El Dirani, Laurene Youssef, Camille Petit-Etienne, Erwine Pargon, J.E. Sipe, Marco Liscidini, Corrado Sciancalepore, Matteo Galli, and Daniele Bajoni. Reconfigurable Silicon Photonic Chip for the Generation Of Frequency-Bin-Entangled Qudits. *Physical Review Applied*, 19(6):064026, June 2023.

[89] Jianwei Wang, Stefano Paesani, Yunhong Ding, Raffaele Santagati, Paul Skrzypczyk, Alexia Salavrakos, Jordi Tura, Remigiusz Augusiak, Laura Mančinska, Davide Bacco, Damien Bonneau, Joshua W. Silverstone, Qihuang Gong, Antonio Acín, Karsten Rottwitt, Leif K. Oxenløwe, Jeremy L. O'Brien, Anthony Laing, and Mark G. Thompson. Multidimensional quantum entanglement with large-scale integrated optics. *Science*, 360(6386):285–291, April 2018.

[90] Shi-Hai Wei, Bo Jing, Xue-Ying Zhang, Jin-Yu Liao, Chen-Zhi Yuan, Bo-Yu Fan, Chen Lyu, Dian-Li Zhou, You Wang, Guang-Wei Deng, Hai-Zhi Song, Daniel Oblak, Guang-Can Guo, and Qiang Zhou. Towards Real-World Quantum Networks: A Review. *Laser & Photonics Reviews*, 16(3):2100219, March 2022.

[91] Rune S. Jacobsen, Karin N. Andersen, Peter I. Borel, Jacob Fage-Pedersen, Lars H. Frandsen, Ole Hansen, Martin Kristensen, Andrei V. Lavrinenko, Gaid Moulin, Haiyan Ou, Christophe Peucheret, Beáta Zsigri, and Anders Bjarklev. Strained silicon as a new electro-optic material. *Nature*, 441(7090):199–202, May 2006.

[92] M. Dinu, F. Quochi, and H. Garcia. Third-order nonlinearities in silicon at telecom wavelengths. *Applied Physics Letters*, 82(18):2954–2956, May 2003.

[93] Guoliang Li, Jin Yao, Hiren Thacker, Attila Mekis, Xuezhe Zheng, Ivan Shubin, Ying Luo, Jin-hyoung Lee, Kannan Raj, John E. Cunningham, and Ashok V. Krishnamoorthy. Ultralow-loss, high-density SOI optical waveguide routing for macrochip interconnects. *Optics Express*, 20(11):12035, May 2012.

[94] Abdul Rahim, Eva Ryckeboer, Ananth Z. Subramanian, Stephane Clemmen, Bart Kuyken, Ashim Dhakal, Ali Raza, Artur Hermans, Muhammad Muneeb, Soren Dhoore, Yanlu Li, Utsav Dave, Peter Bienstman, Nicolas Le Thomas, Gunther Roelkens, Dries Van Thourhout, Philippe Helin, Simone Severi, Xavier Rottenberg, and Roel Baets. Expanding the Silicon Photonics Portfolio With Silicon Nitride Photonic Integrated Circuits. *Journal of Lightwave Technology*, 35(4):639–649, February 2017.

[95] Martin H. P. Pfeiffer, Junqiu Liu, Arslan S. Raja, Tiago Morais, Bahareh Ghadiani, and Tobias J. Kippenberg. Ultra-smooth silicon nitride waveguides based on the Damascene reflow process: fabrication and loss origins. *Optica*, 5(7):884, July 2018.

[96] Kevin Luke, Avik Dutt, Carl B. Poitras, and Michal Lipson. Overcoming Si_3n_4 film

stress limitations for high quality factor ring resonators. *Optics Express*, 21(19):22829, September 2013.

[97] Y. Fujii, S. Yoshida, S. Misawa, S. Maekawa, and T. Sakudo. Nonlinear optical susceptibilities of AlN film. *Applied Physics Letters*, 31(12):815–816, December 1977.

[98] Hojoong Jung, Chi Xiong, King Y. Fong, Xufeng Zhang, and Hong X. Tang. Optical frequency comb generation from aluminum nitride microring resonator. *Optics Letters*, 38(15):2810, August 2013.

[99] Chi Xiong, Wolfram H P Pernice, Xiankai Sun, Carsten Schuck, King Y Fong, and Hong X Tang. Aluminum nitride as a new material for chip-scale optomechanics and nonlinear optics. *New Journal of Physics*, 14(9):095014, September 2012.

[100] Ichiro Shoji, Takashi Kondo, and Ryoichi Ito. Second-order nonlinear susceptibilities of various dielectric and semiconductor materials. *Optical and Quantum Electronics*, 34(8):797–833, 2002.

[101] R. DeSalvo, A.A. Said, D.J. Hagan, E.W. Van Stryland, and M. Sheik-Bahae. Infrared to ultraviolet measurements of two-photon absorption and n/sub 2/ in wide bandgap solids. *IEEE Journal of Quantum Electronics*, 32(8):1324–1333, August 1996.

[102] Jintian Lin, Junxia Zhou, Rongbo Wu, Min Wang, Zhiwei Fang, Wei Chu, Jianhao Zhang, Lingling Qiao, and Ya Cheng. High-Precision Propagation-Loss Measurement of Single-Mode Optical Waveguides on Lithium Niobate on Insulator. *Micromachines*, 10(9):612, September 2019.

[103] David J. Moss, Roberto Morandotti, Alexander L. Gaeta, and Michal Lipson. New CMOS-compatible platforms based on silicon nitride and Hydex for nonlinear optics. *Nature Photonics*, 7(8):597–607, August 2013.

[104] Hui Wang, Jian Qin, Xing Ding, Ming-Cheng Chen, Si Chen, Xiang You, Yu-Ming He, Xiao Jiang, L. You, Z. Wang, C. Schneider, Jelmer J. Renema, Sven Höfling, Chao-Yang Lu, and Jian-Wei Pan. Boson Sampling with 20 Input Photons and a 60-Mode Interferometer in a 1 0 14 -Dimensional Hilbert Space. *Physical Review Letters*, 123(25):250503, December 2019.

[105] Jeremy C. Adcock, Jueming Bao, Yulin Chi, Xiaojiong Chen, Davide Bacco, Qihuang Gong, Leif K. Oxenlowe, Jianwei Wang, and Yunhong Ding. Advances in Silicon Quantum Photonics. *IEEE Journal of Selected Topics in Quantum Electronics*, 27(2):1–24, March 2021.

[106] Q. Lin and Govind P. Agrawal. Silicon waveguides for creating quantum-correlated photon pairs. *Optics Letters*, 31(21):3140, November 2006.

[107] Ken-ichi Harada, Hiroki Takesue, Hiroshi Fukuda, Tai Tsuchizawa, Toshifumi

Watanabe, Koji Yamada, Yasuhiro Tokura, and Sei-ichi Itabashi. Indistinguishable photon pair generation using two independent silicon wire waveguides. *New Journal of Physics*, 13(6):065005, June 2011.

[108] V. Ansari, E. Roccia, M. Santandrea, M. Doostdar, C. Eigner, L. Padberg, I. Gianani, M. Sbroscia, J. M. Donohue, L. Mancino, M. Barbieri, and C. Silberhorn. Heralded generation of high-purity ultrashort single photons in programmable temporal shapes. *Optics Express*, 26(3):2764, February 2018.

[109] Stefano Azzini, Davide Grassani, Matteo Galli, Lucio Claudio Andreani, Marc Sorel, Michael J. Strain, L. G. Helt, J. E. Sipe, Marco Liscidini, and Daniele Bajoni. From classical four-wave mixing to parametric fluorescence in silicon microring resonators. *Optics Letters*, 37(18):3807–3809, September 2012.

[110] Erman Engin, Damien Bonneau, Chandra M. Natarajan, Alex S. Clark, M. G. Tanner, R. H. Hadfield, Sanders N. Dorenbos, Val Zwiller, Kazuya Ohira, Nobuo Suzuki, Haruhiko Yoshida, Norio Iizuka, Mizunori Ezaki, Jeremy L. O'Brien, and Mark G. Thompson. Photon pair generation in a silicon micro-ring resonator with reverse bias enhancement. *Optics Express*, 21(23):27826, November 2013.

[111] Yuan Guo, Wei Zhang, Shuai Dong, Yidong Huang, and Jiangde Peng. Telecom-band degenerate-frequency photon pair generation in silicon microring cavities. *Optics Letters*, 39(8):2526–2529, April 2014.

[112] Nicholas C. Harris, Davide Grassani, Angelica Simbula, Mihir Pant, Matteo Galli, Tom Baehr-Jones, Michael Hochberg, Dirk Englund, Daniele Bajoni, and Christophe Galland. Integrated Source of Spectrally Filtered Correlated Photons for Large-Scale Quantum Photonic Systems. *Physical Review X*, 4(4):041047, December 2014.

[113] Ryota Wakabayashi, Mikio Fujiwara, Ken-ichiro Yoshino, Yoshihiro Nambu, Masahide Sasaki, and Takao Aoki. Time-bin entangled photon pair generation from Si micro-ring resonator. *Optics Express*, 23(2):1103, January 2015.

[114] Davide Grassani, Stefano Azzini, Marco Liscidini, Matteo Galli, Michael J. Strain, Marc Sorel, J. E. Sipe, and Daniele Bajoni. Micrometer-scale integrated silicon source of time-energy entangled photons. *Optica*, 2(2):88, February 2015.

[115] Ranjeet Kumar, Marc Savanier, Jun Rong Ong, and Shayan Mookherjea. Entanglement measurement of a coupled silicon microring photon pair source. *Optics Express*, 23(15):19318, July 2015.

[116] J. W. Silverstone, R. Santagati, D. Bonneau, M. J. Strain, M. Sorel, J. L. O'Brien, and M. G. Thompson. Qubit entanglement between ring-resonator photon-pair sources on a silicon chip. *Nature Communications*, 6(1):7948, August 2015.

[117] Marc Savanier, Ranjeet Kumar, and Shayan Mookherjea. Photon pair generation from compact silicon microring resonators using microwatt-level pump powers. *Optics Express*, 24(4):3313, February 2016.

[118] Elizabeth Hemsley, Damien Bonneau, Jason Pelc, Ray Beausoleil, Jeremy L. O'Brien, and Mark G. Thompson. Photon pair generation in hydrogenated amorphous silicon microring resonators. *Scientific Reports*, 6(1):38908, December 2016.

[119] I N Chuprina, N S Perminov, D Yu Tarankova, and A A Kalachev. Generating pure single-photon states via spontaneous four-wave mixing in a system of coupled microresonators. *Laser Physics Letters*, 15(10):105104, October 2018.

[120] Xiaodong Shi, Kai Guo, Jesper Bjerge Christensen, Mario A. Usuga Castaneda, Xuanming Liu, Haiyan Ou, and Karsten Rottwitt. Multichannel Photon-Pair Generation with Strong and Uniform Spectral Correlation in a Silicon Microring Resonator. *Physical Review Applied*, 12(3):034053, September 2019.

[121] L. Arizmendi. Review Article: Photonic applications of lithium niobate crystals. *physica status solidi (a)*, 201(2):175–175, January 2004.

[122] Kun Liu, Jianhong Shi, and Xianfeng Chen. Linear polarization-state generator with high precision in periodically poled lithium niobate. *Applied Physics Letters*, 94(10):101106, March 2009.

[123] Xiangyu He, Yin Xu, Bo Zhang, Yue Dong, and Yi Ni. Highly efficient and tunable polarization rotator based on lithium niobate on an insulator. *Applied Optics*, 62(10):2434, April 2023.

[124] Pao-Kang Chen, Ian Briggs, Chaohan Cui, Liang Zhang, Manav Shah, and Linran Fan. Adapted poling to break the nonlinear efficiency limit in nanophotonic lithium niobate waveguides. 2023. Publisher: arXiv Version Number: 1.

[125] Jia-yang Chen, Yong Meng Sua, Zhao-hui Ma, Chao Tang, Zhan Li, and Yu-ping Huang. Efficient parametric frequency conversion in lithium niobate nanophotonic chips. *OSA Continuum*, 2(10):2914, October 2019.

[126] Zhaohui Ma, Jia-Yang Chen, Malvika Garikapati, Zhan Li, Chao Tang, Yong Meng Sua, and Yu-Ping Huang. Highly efficient and pure few-photon source on chip. *Physical Review Applied*, 20(4):044033, October 2023.

[127] Oliver Alibart. *Source de photons uniques annonc{\'e}s {\'a} 1550nm en optique guid{\'e}e pour les communications quantiques*. Theses, Universit{\'e} Nice Sophia Antipolis, 2004.

[128] Christophe Couteau. Spontaneous parametric down-conversion. *Contemporary Physics*, 59(3):291–304, July 2018.

[129] A. Szilagyi, A. Hordvik, and H. Schlossberg. A quasi-phase-matching technique for efficient optical mixing and frequency doubling. *Journal of Applied Physics*, 47(5):2025–2032, May 1976.

[130] Masakatsu Okada, Kaniharu Takizawa, and Shogo Ieiri. Second harmonic generation by periodic laminar structure of nonlinear optical crystal. *Optics Communications*, 18(3):331–334, August 1976.

[131] J. M. Chavez Boggio, D. Bodenmüller, T. Fremberg, R. Haynes, M. M. Roth, R. Eisermann, M. Lisker, L. Zimmermann, and M. Böhm. Dispersion engineered silicon nitride waveguides by geometrical and refractive-index optimization. *Journal of the Optical Society of America B*, 31(11):2846, November 2014.

[132] P. Ben Dixon, Jeffrey H. Shapiro, and Franco N. C. Wong. Spectral engineering by Gaussian phase-matching for quantum photonics. *Optics Express*, 21(5):5879, March 2013.

[133] Evan Meyer-Scott, Nicola Montaut, Johannes Tiedau, Linda Sansoni, Harald Herrmann, Tim J. Bartley, and Christine Silberhorn. Limits on the heralding efficiencies and spectral purities of spectrally filtered single photons from photon-pair sources. *Physical Review A*, 95(6):061803, June 2017.

[134] C. K. Law, I. A. Walmsley, and J. H. Eberly. Continuous Frequency Entanglement: Effective Finite Hilbert Space and Entropy Control. *Physical Review Letters*, 84(23):5304–5307, June 2000.

[135] Kevin Zielnicki, Karina Garay-Palmett, Daniel Cruz-Delgado, Hector Cruz-Ramirez, Michael F. O'Boyle, Bin Fang, Virginia O. Lorenz, Alfred B. U'Ren, and Paul G. Kwiat. Joint spectral characterization of photon-pair sources. *Journal of Modern Optics*, 65(10):1141–1160, June 2018.

[136] P J Mosley, J S Lundeen, B J Smith, and I A Walmsley. Conditional preparation of single photons using parametric downconversion: a recipe for purity. *New Journal of Physics*, 10(9):093011, September 2008.

[137] Gilbert Grynberg, Alain Aspect, and Claude Fabre. *Introduction to Quantum Optics: From the Semi-classical Approach to Quantized Light*. Cambridge University Press, Cambridge, 2010.

[138] Rodney Loudon and Rodney Loudon. *The Quantum Theory of Light*. Oxford University Press, Oxford, New York, third edition, third edition edition, September 2000.

[139] Lin Chang, Yifei Li, Nicolas Volet, Leiran Wang, Jon Peters, and John E. Bowers. Thin film wavelength converters for photonic integrated circuits. *Optica*, 3(5):531, May 2016.

[140] Ashutosh Rao, Kamal Abdelsalam, Tracy Sjaardema, Amirmahdi Honardoost, Guillermo F. Camacho-Gonzalez, and Sasan Fathpour. Actively-monitored periodic-poling in thin-film lithium niobate photonic waveguides with ultrahigh nonlinear conversion efficiency of 4600 \%.W$ˆ{-1}$.cm$ˆ{-2}$. *Optics Express*, 27(18):25920, September 2019.

[141] Farid Samara. *Integrated Si3N4 Microring Resonator: A Photon-Pair Source for Quantum Communication*. PhD thesis, Université de Genève, 2021.

[142] Dorian Oser, Sébastien Tanzilli, Florent Mazeas, Carlos Alonso-Ramos, Xavier Le Roux, Grégory Sauder, Xin Hua, Oliver Alibart, Laurent Vivien, Eric Cassan, and Laurent Labonté. High-quality photonic entanglement out of a stand-alone silicon chip. *npj Quantum Information*, 6(1):31, March 2020.

[143] F. Mazeas, M. Traetta, M. Bentivegna, F. Kaiser, D. Aktas, W. Zhang, C. A. Ramos, L. A. Ngah, T. Lunghi, E. Picholle, N. Belabas-Plougonven, X. Le Roux, E. Cassan, D. Marris-Morini, L. Vivien, G. Sauder, L. Labonté, and S. Tanzilli. High-quality photonic entanglement for wavelength-multiplexed quantum communication based on a silicon chip. *Optics Express*, 24(25):28731, December 2016.

[144] Wei C. Jiang, Xiyuan Lu, Jidong Zhang, Oskar Painter, and Qiang Lin. Silicon-chip source of bright photon pairs. *Optics Express*, 23(16):20884, August 2015.

[145] Sylvain Fasel, Olivier Alibart, Sébastien Tanzilli, Pascal Baldi, Alexios Beveratos, Nicolas Gisin, and Hugo Zbinden. High-quality asynchronous heralded single-photon source at telecom wavelength. *New Journal of Physics*, 6:163–163, November 2004.

[146] Dorian Oser. *Integrated silicon photonics for quantum optics*. phdthesis, Université Paris Saclay (COmUE), November 2019.

[147] Xin Hua, Tommaso Lunghi, Florent Doutre, Panagiotis Vergyris, Gregory Sauder, Pierrick Charlier, Laurent Labonté, Virginia D'Auria, Anthony Martin, Sorin Tascu, Marc P. De Micheli, Sebastien Tanzilli, and Olivier Alibart. Configurable heralded two-photon Fock-states on a chip. *Optics Express*, 29(1):415–424, January 2021.

[148] Farid Samara, Nicolas Maring, Anthony Martin, Arslan S. Raja, Tobias J. Kippenberg, Hugo Zbinden, and Rob Thew. Entanglement swapping between independent and asynchronous integrated photon-pair sources. *arXiv:2011.08150 [quant-ph]*, November 2020. arXiv: 2011.08150.

[149] Michael A. Nielsen and Isaac L. Chuang. *Quantum Computation and Quantum Information: 10th Anniversary Edition*. Cambridge University Press, 1 edition, June 2012.

[150] Charles H. Bennett and Gilles Brassard. Quantum cryptography: Public key distribution and coin tossing. *Theoretical Computer Science*, 560:7–11, December 2014.

[151] P.W. Shor. Algorithms for quantum computation: discrete logarithms and factoring. In *Proceedings 35th Annual Symposium on Foundations of Computer Science*, pages 124–134, Santa Fe, NM, USA, 1994. IEEE Comput. Soc. Press.

[152] David P. DiVincenzo. The Physical Implementation of Quantum Computation. *Fortschritte der Physik*, 48(9-11):771–783, September 2000.

[153] A Yu Kitaev. Quantum computations: algorithms and error correction. *Russian Mathematical Surveys*, 52(6):1191–1249, December 1997.

[154] Dorit Aharonov. A Simple Proof that Toffoli and Hadamard are Quantum Universal. 2003. Publisher: arXiv Version Number: 1.

[155] E. Knill, R. Laflamme, and G. Milburn. Efficient Linear Optics Quantum Computation. *arXiv:quant-ph/0006088*, June 2000. arXiv: quant-ph/0006088.

[156] Shikang Li, Xue Feng, Kaiyu Cui, Fang Liu, Wei Zhang, and Yidong Huang. Programmable unitary operations for orbital angular momentum encoded states. *National Science Open*, 1(3):20220019, January 2022.

[157] J. D. Franson. Bell inequality for position and time. *Physical Review Letters*, 62(19):2205–2208, May 1989.

[158] José Capmany and Carlos R. Fernández-Pousa. Quantum model for electro-optical phase modulation. *JOSA B*, 27(6):A119–A129, June 2010.

[159] Berthold-Georg Englert, Christian Kurtsiefer, and Harald Weinfurter. Universal unitary gate for single-photon two-qubit states. *Physical Review A*, 63(3):032303, February 2001.

[160] Yuchen Wang, Zixuan Hu, Barry C. Sanders, and Sabre Kais. Qudits and High-Dimensional Quantum Computing. *Frontiers in Physics*, 8:589504, November 2020.

[161] Charles H. Bennett, Gilles Brassard, and N. David Mermin. Quantum cryptography without Bell's theorem. *Physical Review Letters*, 68(5):557–559, February 1992.

[162] Daniel F. V. James, Paul G. Kwiat, William J. Munro, and Andrew G. White. Measurement of qubits. *Physical Review A*, 64(5):052312, October 2001.

[163] M Peev, C Pacher, R Alléaume, C Barreiro, J Bouda, W Boxleitner, T Debuisschert, E Diamanti, M Dianati, J F Dynes, S Fasel, S Fossier, M Fürst, J-D Gautier, O Gay, N Gisin, P Grangier, A Happe, Y Hasani, M Hentschel, H Hübel, G Humer, T Länger, M Legré, R Lieger, J Lodewyck, T Lorünser, N Lütkenhaus, A Marhold, T Matyus, O Maurhart, L Monat, S Nauerth, J-B Page, A Poppe, E Querasser, G Ribordy, S Robyr, L Salvail, A W Sharpe, A J Shields, D Stucki, M Suda, C Tamas, T Themel, R T Thew, Y Thoma, A Treiber, P Trinkler, R Tualle-Brouri, F Vannel, N Walenta, H Weier, H Weinfurter, I Wimberger, Z L Yuan, H Zbinden, and

A Zeilinger. The SECOQC quantum key distribution network in Vienna. *New Journal of Physics*, 11(7):075001, July 2009.

[164] M. Sasaki, M. Fujiwara, H. Ishizuka, W. Klaus, K. Wakui, M. Takeoka, S. Miki, T. Yamashita, Z. Wang, A. Tanaka, K. Yoshino, Y. Nambu, S. Takahashi, A. Tajima, A. Tomita, T. Domeki, T. Hasegawa, Y. Sakai, H. Kobayashi, T. Asai, K. Shimizu, T. Tokura, T. Tsurumaru, M. Matsui, T. Honjo, K. Tamaki, H. Takesue, Y. Tokura, J. F. Dynes, A. R. Dixon, A. W. Sharpe, Z. L. Yuan, A. J. Shields, S. Uchikoga, M. Legré, S. Robyr, P. Trinkler, L. Monat, J.-B. Page, G. Ribordy, A. Poppe, A. Allacher, O. Maurhart, T. Länger, M. Peev, and A. Zeilinger. Field test of quantum key distribution in the Tokyo QKD Network. *Optics Express*, 19(11):10387, May 2011.

[165] I. Herbauts, B. Blauensteiner, A. Poppe, T. Jennewein, and H. Hübel. Demonstration of active routing of entanglement in a multi-user network. *Optics Express*, 21(23):29013, November 2013.

[166] X.-Y. Chang, D.-L. Deng, X.-X. Yuan, P.-Y. Hou, Y.-Y. Huang, and L.-M. Duan. Experimental realization of an entanglement access network and secure multi-party computation. *Scientific Reports*, 6(1):29453, July 2016.

[167] Siddarth Koduru Joshi, Djeylan Aktas, Sören Wengerowsky, Martin Lončarić, Sebastian Philipp Neumann, Bo Liu, Thomas Scheidl, Guillermo Currás Lorenzo, Željko Samec, Laurent Kling, Alex Qiu, Mohsen Razavi, Mario Stipčević, John G. Rarity, and Rupert Ursin. A trusted-node-free eight-user metropolitan quantum communication network. *Science Advances*, 6(36):eaba0959, September 2020. arXiv: 1907.08229.

[168] C Autebert, J Trapateau, A Orieux, A Lemaître, C Gomez-Carbonell, E Diamanti, I Zaquine, and S Ducci. Multi-user quantum key distribution with entangled photons from an AlGaAs chip. *Quantum Science and Technology*, 1(1):01LT02, December 2016.

[169] Sören Wengerowsky, Siddarth Koduru Joshi, Fabian Steinlechner, Hannes Hübel, and Rupert Ursin. Entanglement-based wavelength multiplexed quantum communication network. *Nature*, 564(7735):225–228, December 2018. arXiv: 1801.06194.

[170] I. Marcikic, H. de Riedmatten, W. Tittel, V. Scarani, H. Zbinden, and N. Gisin. Time-bin entangled qubits for quantum communication created by femtosecond pulses. *Physical Review A*, 66(6):062308, December 2002.

[171] Farid Samara, Anthony Martin, Claire Autebert, Maxim Karpov, Tobias J. Kippenberg, Hugo Zbinden, and Rob Thew. High-rate photon pairs and sequential Time-Bin entanglement with Si $_3$ N $_4$ microring resonators. *Optics Express*, 27(14):19309, July 2019.

[172] C. Xiong, X. Zhang, A. Mahendra, J. He, D.-Y. Choi, C. J. Chae, D. Marpaung, A. Leinse, R. G. Heideman, M. Hoekman, C. G. H. Roeloffzen, R. M. Oldenbeuving, P. W. L. van Dijk, C. Taddei, P. H. W. Leong, and B. J. Eggleton. Compact and reconfigurable silicon nitride time-bin entanglement circuit. *Optica*, 2(8):724, August 2015.

[173] Felicien Appas, Florent Baboux, Maria I. Amanti, Aristide Lemaítre, Fabien Boitier, Eleni Diamanti, and Sara Ducci. Flexible entanglement-distribution network with an AlGaAs chip for secure communications. *npj Quantum Information*, 7(1):1–10, July 2021.

[174] Xiongfeng Ma, Chi-Hang Fred Fung, and Hoi-Kwong Lo. Quantum key distribution with entangled photon sources. *Physical Review A*, 76(1):012307, July 2007.

[175] Norbert Lütkenhaus. Security against individual attacks for realistic quantum key distribution. *Physical Review A*, 61(5):052304, April 2000. arXiv: quant-ph/9910093.

[176] Oscar E. Sandoval, Navin B. Lingaraju, Poolad Imany, Daniel E. Leaird, Michael Brodsky, and Andrew M. Weiner. Polarization diversity phase modulator for measuring frequency-bin entanglement of a biphoton frequency comb in a depolarized channel. *Optics Letters*, 44(7):1674, April 2019.

[177] C. K. Hong, Z. Y. Ou, and L. Mandel. Measurement of subpicosecond time intervals between two photons by interference. *Physical Review Letters*, 59(18):2044–2046, November 1987.

[178] Laura J. Wright, Michał Karpiński, Christoph Söller, and Brian J. Smith. Spectral Shearing of Quantum Light Pulses by Electro-Optic Phase Modulation. *Physical Review Letters*, 118(2):023601, January 2017.

[179] Travis R. Beals and Barry C. Sanders. Distributed Relay Protocol for Probabilistic Information-Theoretic Security in a Randomly-Compromised Network. In Reihaneh Safavi-Naini, editor, *Information Theoretic Security*, volume 5155, pages 29–39. Springer Berlin Heidelberg, Berlin, Heidelberg, 2008. ISSN: 0302-9743, 1611-3349 Series Title: Lecture Notes in Computer Science.

[180] Jian-Wei Pan, Dik Bouwmeester, Harald Weinfurter, and Anton Zeilinger. Experimental Entanglement Swapping: Entangling Photons That Never Interacted. *Physical Review Letters*, 80(18):3891–3894, May 1998.

[181] Matthäus Halder, Alexios Beveratos, Nicolas Gisin, Valerio Scarani, Christoph Simon, and Hugo Zbinden. Entangling independent photons by time measurement. *Nature Physics*, 3(10):692–695, October 2007.

[182] Mehul Malik, Heedeuk Shin, Malcolm O'Sullivan, Petros Zerom, and Robert W.

Boyd. Quantum Ghost Image Identification with Correlated Photon Pairs. *Physical Review Letters*, 104(16):163602, April 2010.

[183] Piotr Ryczkowski, Margaux Barbier, Ari T. Friberg, John M. Dudley, and Goëry Genty. Ghost imaging in the time domain. *Nature Photonics*, 10(3):167–170, March 2016.

[184] Antoine Henry, David Barral, Isabelle Zaquine, Andreas Boes, Arnan Mitchell, Nadia Belabas, and Kamel Bencheikh. Generation and manipulation of twin photons in Thin Film Lithium Niobate platform: from a single photon source to frequency ghost imaging. In *Optica Nonlinear Optics Topical Meeting 2023*, page W1A.1, Honolulu, Hawaii, 2023. Optica Publishing Group.

[185] Yichen Shen, Nicholas C. Harris, Scott Skirlo, Mihika Prabhu, Tom Baehr-Jones, Michael Hochberg, Xin Sun, Shijie Zhao, Hugo Larochelle, Dirk Englund, and Marin Soljačić. Deep learning with coherent nanophotonic circuits. *Nature Photonics*, 11(7):441–446, July 2017.

[186] Xing Lin, Yair Rivenson, Nezih T. Yardimci, Muhammed Veli, Yi Luo, Mona Jarrahi, and Aydogan Ozcan. All-optical machine learning using diffractive deep neural networks. *Science*, 361(6406):1004–1008, September 2018.

[187] S. Etcheverry, G. Cañas, E. S. Gómez, W. A. T. Nogueira, C. Saavedra, G. B. Xavier, and G. Lima. Quantum key distribution session with 16-dimensional photonic states. *Scientific Reports*, 3(1):2316, July 2013.

[188] Thomas Durt, Nicolas J. Cerf, Nicolas Gisin, and Marek Żukowski. Security of quantum key distribution with entangled qutrits. *Physical Review A*, 67(1):012311, January 2003.

[189] Mohamed Bourennane, Anders Karlsson, Gunnar Bj rk, Nicolas Gisin, and Nicolas J Cerf. Quantum key distribution using multilevel encoding: security analysis. *Journal of Physics A: Mathematical and General*, 35(47):10065–10076, November 2002.

[190] Nicolas J. Cerf, Mohamed Bourennane, Anders Karlsson, and Nicolas Gisin. Security of Quantum Key Distribution Using d -Level Systems. *Physical Review Letters*, 88(12):127902, March 2002.

[191] Yaowen Hu, Mengjie Yu, Di Zhu, Neil Sinclair, Amirhassan Shams-Ansari, Linbo Shao, Jeffrey Holzgrafe, Eric Puma, Mian Zhang, and Marko Loncar. Reconfigurable electro-optic frequency shifter. *arXiv:2005.09621 [physics]*, May 2020. arXiv: 2005.09621.

[192] Milica Banic, J. E. Sipe, and Marco Liscidini. Integrated photonic sources of frequency-bin-encoded multipartite entangled states. 2023. Publisher: arXiv Version Number: 1.

[193] Usman A. Javid, Jingwei Ling, Jeremy Staffa, Mingxiao Li, Yang He, and Qiang Lin. Ultrabroadband Entangled Photons on a Nanophotonic Chip. *Physical Review Letters*, 127(18):183601, October 2021.

Appendices

Appendix A

Calculations for Chapter 3

A.1 Generalised expressions for component action in the time Basis

Consider the action of a single PS in the time basis. For this, recall that in the spectral mode-basis, the PS-matrix has a representation of the form:

$$U_{PF} = \begin{bmatrix} 1 & 0 & \dots & 0 \\ 0 & e^{i\varphi_1} & \dots & 0 \\ \vdots & \vdots & \ddots & \vdots \\ 0 & 0 & \dots & e^{i\varphi_{M-1}} \end{bmatrix} \tag{A.1}$$

where, $\varphi_1, \dots, \varphi_{M-1}$ denote the real phases applied to the frequency modes. The equivalent expression in the time basis:

$$\begin{aligned} \tilde{U}_{PF} = F \cdot U_{PF} \cdot F^{\dagger} = \frac{1}{M} &\begin{bmatrix} 1 & 1 & 1 & \dots & 1 \\ 1 & \xi & \xi^2 & \dots & \xi^{(M-1)} \\ 1 & \xi^2 & \xi^4 & \dots & \xi^{2(M-1)} \\ \vdots & \vdots & \vdots & \ddots & \vdots \\ 1 & \xi^{(M-1)} & \xi^{2(M-1)} & \dots & \xi^{(M-1)^2} \end{bmatrix} \\ \times &\begin{bmatrix} 1 & 0 & 0 & \dots & 0 \\ 0 & e^{i\varphi_1} & 0 & \dots & 0 \\ 0 & 0 & e^{i\varphi_2} & \dots & 0 \\ \vdots & \vdots & \vdots & \ddots & \vdots \\ 0 & 0 & 0 & \dots & e^{i\varphi_{M-1}} \end{bmatrix} \begin{bmatrix} 1 & 1 & 1 & \dots & 1 \\ 1 & \xi^{-1} & \xi^{-2} & \dots & \xi^{-(M-1)} \\ 1 & \xi^{-2} & \xi^{-4} & \dots & \xi^{-2(M-1)} \\ \vdots & \vdots & \vdots & \ddots & \vdots \\ 1 & \xi^{-(M-1)} & \xi^{-2(M-1)} & \dots & \xi^{-(M-1)^2} \end{bmatrix} \end{aligned}$$

$$= \frac{1}{M}\begin{bmatrix} 1 & e^{i\varphi_1} & e^{i\varphi_2} & \dots & e^{i\varphi_{M-1}} \\ 1 & \xi e^{i\varphi_1} & \xi^2 e^{i\varphi_2} & \dots & \xi^{(M-1)} e^{i\varphi_{M-1}} \\ \vdots & \vdots & \vdots & \ddots & \vdots \\ 1 & \xi^{(M-1)} e^{i\varphi_1} & \xi^{2(M-1)} e^{i\varphi_2} & \dots & \xi^{(M-1)^2} e^{i\varphi_{M-1}} \end{bmatrix}$$

$$\times \begin{bmatrix} 1 & 1 & 1 & \dots & 1 \\ 1 & \xi^{-1} & \xi^{-2} & \dots & \xi^{-(M-1)} \\ 1 & \xi^{-2} & \xi^{-4} & \dots & \xi^{-2(M-1)} \\ \vdots & \vdots & \vdots & \ddots & \vdots \\ 1 & \xi^{-(M-1)} & \xi^{-2(M-1)} & \dots & \xi^{-(M-1)^2} \end{bmatrix} \tag{A.2}$$

where, $\xi = e^{i(2\pi/M)}$. This expression can be expressed more compactly as

$$\forall k, k' \in [0, M-1] \qquad \tilde{U}_{PF\,k,k'} = \frac{1}{M}\sum_{j_1=0}^{M-1} \xi^{(k'-k)j_1} e^{i\varphi_{j_1}}. \tag{A.3}$$

The matrix of the EOM is diagonal in the time basis

$$\forall k', k'' \in [0, M-1] \qquad \tilde{U}_{EOM\,k'',k'} = \delta_{k''k'} e^{i\phi_{k'}} \tag{A.4}$$

A.2 Derivation of the two-scattering matrix with the PF

Our goal is to use this device to act on single qubits. For frequency-bin encoded on two frequency modes $|\omega_j\rangle$ and $|\omega_j'\rangle$, U_{PF} acts as a phase gate. For time-bin qubits, $\tilde{U}_{PF}$ scatters light on several time bins. We wish to program time the scattering.For a qubit encoded on two time bins $|t_k\rangle$ and $|t_k'\rangle$, we wish the action $\tilde{U}_{PF}$ on a time bin $|t_k\rangle$ to be

$$\tilde{U}_{PF}\,|t_k\rangle = \alpha\,|t_k\rangle + \beta\,|t_{k'}\rangle\,.,\ \alpha, \beta \in \mathbb{C}, \tag{A.5}$$

with $|\alpha|^2 + |\beta|^2 = 1$, $(\alpha, \beta) \in \mathbb{C}^2$. We start with no assumption on the "distance" $k - k'$ between the two vectors of the qubit subspace. The coupling constants between time modes can be derived from the Fourier transform of the pulse shaper action in the frequency domain

$$\forall (k, k') \in \{[0, M-1]\}^2, \tilde{P}_{k',k} = \langle t_{k'}|\tilde{U}_{PF}|t_k\rangle = \frac{1}{M}\sum_j \exp\left(i\frac{2\pi}{M}(k'-k)j + i\varphi_j\right). \tag{A.6}$$

where φ_j is the phase applied by the PS to the frequency mode $|\omega_j\rangle$ that we want to determine for $j \in [0, M-1]$.

$$\begin{cases} \frac{1}{M}\sum_{j=0}^{M-1} e^{i\varphi_j} = \alpha, \\ \frac{1}{M}\sum_{j=0}^{M-1} e^{i2\pi\frac{mj}{M}} e^{i\varphi_j} = \beta, \\ \forall (p,q) \neq (k,k),(k+m,k), \qquad \frac{1}{M}\sum_{j=0}^{M-1} e^{i2\pi\frac{(p-q)j}{M}} e^{i\varphi_j} = 0. \end{cases} \tag{A.7}$$

Let $e^{i\varphi_j} = A_j\alpha + B_j\beta$. Eq. (A.7) becomes

$$\begin{cases} \sum_{j=0}^{M-1} A_j\alpha = M\alpha \\ \sum_{j=0}^{M-1} e^{i2\pi\frac{mj}{M}} B_j\beta = M\beta \end{cases} \tag{A.8}$$

These equations can be satisfied by choosing $A_j = 1$ and $B_j = e^{-i2\pi\frac{mj}{M}}$, which finally gives

$$\forall j \in [0, M-1], \qquad e^{i\varphi_j} = \alpha + \beta e^{-i2\pi\frac{mj}{M}} \tag{A.9}$$

Then the unitarity of the PS matrix enforces the following relation

$$\forall j \in [0, M-1], \qquad |\alpha|^2 + |\beta|^2 + 2\mathfrak{Re}\{\alpha\beta^* e^{-i2\pi\frac{mj}{M}}\} = 1 \tag{A.10}$$

The case $j = 0$ imposes $\alpha\beta^*$ to be purely imaginary. Therefore we can set $\alpha = |\alpha|e^{i\gamma}$ and $\beta = \pm i|\beta|e^{i\gamma}$, which yields a new unitarity condition

$$\forall j \in [0, M-1], \qquad \mathfrak{Im}\{e^{-i2\pi\frac{mj}{M}}\} = 0 \tag{A.11}$$

which sets $m = M/2$.
It is therefore possible to choose settings of the PS so that it scatters the energy of mode $|t_k\rangle$ only into the two modes $|t_k\rangle$ and $|t_{k+M/2}\rangle$. In the frequency basis

$$\forall j \in [0, M-1], \qquad \hat{U}_{PS}\,|\omega_j\rangle = \left[\alpha + \beta e^{-i\pi j}\right]|\omega_j\rangle \tag{A.12}$$

Finally, we obtain

$$\begin{cases} \forall k \in [0, M/2], \hat{U}_{PS}\,|t_k\rangle = \alpha\,|t_k\rangle + \beta\,|t_{k+M/2}\rangle \\ \forall k \in [M/2, M-1], \hat{U}_{PS}\,|t_k\rangle = \beta\,|t_k\rangle + \alpha\,|t_{k-M/2}\rangle\,. \end{cases} \tag{A.13}$$

Subsequently, the PS matrix takes the following form in the time basis:

$$\tilde{U}_{PF} = e^{i\gamma}\begin{pmatrix} |\alpha| I & \pm i|\beta| I \\ \pm i|\beta| I & |\alpha| I \end{pmatrix} \tag{A.14}$$

where I is the identity matrix of dimension $M/2$.

A.3 Phase gate

The matrix of phase gates is of the form

$$\mathcal{M} = \begin{pmatrix} 1 & 0 \\ 0 & e^{-i\nu} \end{pmatrix}. \tag{A.15}$$

From the expression of the W_k matrix corresponding to the [EOM-PF-EOM] and [PF-EOM-PF], we derive a set of conditions on the component parameters for the parallelization, first for the [EOM-PF-EOM] configuration

$$\left\{ \begin{array}{c} |\alpha| = 1; \qquad |\beta| = 0 \\ \forall k \in [0, M/2-1] \qquad \phi_{1,k} + \phi_{2,k} = \frac{\nu}{2} \quad \mathrm{mod}\ 2\pi \\ \forall k \in [0, M/2-1] \qquad \phi_{1,k+M/2} + \phi_{2,k+M/2} = -\frac{\nu}{2} \quad \mathrm{mod}\ 2\pi \\ \phi_{c_1} + \phi_{c_2} + \gamma = -\frac{\nu}{2} \quad \mathrm{mod}\ 2\pi. \end{array} \right. \tag{A.16}$$

As $\phi_{i,k+M/2} = -\phi_{i,k}$, we need only write

$$\left\{ \begin{array}{c} |\alpha| = 1; \qquad |\beta| = 0 \\ \forall k \in [0, M/2-1] \qquad \phi_{k,1} + \phi_{k,2} = \mu_1 \sin\left(\frac{2k\pi}{M} + \theta_1\right) + \mu_2 \sin\left(\frac{2k\pi}{M} + \theta_2\right) = \frac{\nu}{2} \quad \mathrm{mod}\ 2\pi \\ \phi_{c_1} + \phi_{c_2} + \gamma = -\frac{\nu}{2} \quad \mathrm{mod}\ 2\pi. \end{array} \right. \tag{A.17}$$

The two modulators act as one. It is then sufficient to consider only one modulator. We can write the previous set of equation as

$$\left\{ \begin{array}{c} |\alpha| = 1; \qquad |\beta| = 0 \\ \forall k \in [0, M/2-1] \qquad \phi_k = \mu \sin\left(\frac{2k\pi}{M} + \theta\right) = \frac{\nu}{2} \quad \mathrm{mod}\ 2\pi \\ \phi_c + \gamma = -\frac{\nu}{2} \quad \mathrm{mod}\ 2\pi. \end{array} \right. \tag{A.18}$$

In the same way, conditions can be found on the component parameters for the [PF-EOM-PF] configuration.

$$\left\{ \begin{array}{c} |\alpha_1| = |\alpha_2| = 1; \qquad |\beta_1| = |\beta_2| = 0 \\ \forall k \in [0, M/2-1] \qquad \phi_k = \mu \sin\left(\frac{2k\pi}{M} + \theta\right) = \frac{\nu}{2} \quad \mathrm{mod}\ 2\pi \\ \phi_c + \gamma_1 + \gamma_2 = -\frac{\nu}{2} \quad \mathrm{mod}\ 2\pi. \end{array} \right. \tag{A.19}$$

or

$$\left\{ \begin{array}{c} |\alpha_1| = |\alpha_2| = 0; \qquad |\beta_1| = |\beta_2| = 1 \\ \forall k \in [0, M/2-1] \qquad \phi_k = \mu \sin\left(\frac{2k\pi}{M} + \theta\right) = -\frac{\nu}{2} \quad \mathrm{mod}\ 2\pi \\ \phi_c + \gamma_1 + \gamma_2 = -\frac{\nu}{2} \quad \mathrm{mod}\ 2\pi. \end{array} \right. \tag{A.20}$$

These three sets of equations lead to the same synthesized matrix and therefore to the same formula for the fidelity. The fidelity of each qubit k undergoing a phase change ϕ_k can be computed with the parameters for phase gates using Eq. 3.25 as

$$\forall k \in [0, M/2-1] \qquad \mathcal{F}_k = \cos^2\left(\phi_k - \frac{\nu}{2}\right). \tag{A.21}$$

Each qubit will not realize the gate with the same fidelity, as this fidelity depends on the value of the phase at a each time k. We now compute the maximum number of qubits realizing the transformation with a fidelity better than a threshold $\mathcal{F}_{th}$ For each qubit k,

$$\mathcal{F}_k \geq \mathcal{F}_{th} \Rightarrow \cos^2\left(\phi_k - \frac{\nu}{2}\right) \geq \mathcal{F}_{th}. \tag{A.22}$$

Solving this inequation and replacing ϕ_k by its expression, we find

$$\frac{\nu}{2} - \arccos\left(\sqrt{\mathcal{F}_{th}}\right) \leq \mu \sin\left(\frac{2\pi k}{M} + \theta\right) \leq \frac{\nu}{2} + \arccos\left(\sqrt{\mathcal{F}_{th}}\right). \tag{A.23}$$

The maximum value that the sine can take is bounded by the upper bound. We thus set the modulation index to this upper bound $\mu = \frac{\nu}{2} + \arccos\left(\sqrt{\mathcal{F}_{th}}\right)$. Eq. (A.23) can then be rewritten as a condition on k:

$$\frac{M}{2\pi}\arcsin\left(\frac{\frac{\nu}{2} - \arccos\left(\sqrt{\mathcal{F}_{th}}\right)}{\frac{\nu}{2} + \arccos\left(\sqrt{\mathcal{F}_{th}}\right)}\right) - \theta \leq k \leq \frac{M}{2} - \frac{M}{2\pi}\arcsin\left(\frac{\frac{\nu}{2} - \arccos\left(\sqrt{\mathcal{F}_{th}}\right)}{\frac{\nu}{2} + \arccos\left(\sqrt{\mathcal{F}_{th}}\right)}\right) - \theta. \tag{A.24}$$

The number $\mathcal{N}$ of qubit k realizing the transformation with a fidelity over $\mathcal{F}_{th}$ is thus given by

$$\mathcal{N} = \left\lfloor \frac{M}{2\pi}\left[\frac{\pi}{2} - \arcsin\left(\frac{\frac{\nu}{2} - \arccos\left(\sqrt{\mathcal{F}_{th}}\right)}{\frac{\nu}{2} + \arccos\left(\sqrt{\mathcal{F}_{th}}\right)}\right)\right]\right\rfloor. \tag{A.25}$$

The additional factor $\frac{1}{2}$ comes from the fact that we consider only half the the values k, as we divide our 128 dimensional sate of space in 64 two dimensional subspaces

$\mathcal{N}$ decreases with increasing ν showing that the limitation comes from the phase of the EOM.

A.4 Number of parallel Hadamard gates above fidelity threshold

The Hadamard gate requiring both phase change and energy splitting between the two modes of the qubit subspace is therefore among the most difficult to synthesize.

Let us calculate the number of qubits realizing the Hadamard gate with performances exceeding $\mathcal{P}_{th}$ and $\mathcal{F}_{th}$ in [PF-EOM-PF] and [EOM-PF-EOM] configurations: the parameters corresponding to a single Hadamard gate for qubit k are

$$\left\{ \begin{array}{ll} & |\alpha| = |\beta| = \frac{1}{\sqrt{2}} \\ \forall k \in [0, M/2-1] & \phi_k = \mu \sin\left(\frac{2k\pi}{M} + \theta\right) = \frac{\pi}{4} \mod \pi. \end{array} \right. \tag{A.26}$$

By using the same method as for the phase gates, we can determine the fidelity achieved for each qubit k as

$$\forall k \in [0, M/2-1] \qquad \mathcal{F}_k^{(EPE)} = \sin^4\left(\phi_k + \frac{\pi}{4}\right) \tag{A.27}$$

$$\forall k \in [0, M/2-1] \qquad \mathcal{F}_k^{(PEP)} = \sin^2\left(\phi_k + \frac{\pi}{4}\right) \tag{A.28}$$

for respectively [EOM-PF-EOM] and [PF-EOM-PF] configurations.

As for the phase gate, we look at the greater number of qubits that can realize the Hadamard transformation for [EOM-PF-EOM] and [PF-EOM-PF] configurations. By starting with Eqs A.27 and A.28, we find,

for the [EOM-PF-EOM] configuration

$$-\frac{\pi}{4} + \arcsin\left(\mathcal{F}_{th}^{1/4}\right) \leq \phi_k \leq 3\frac{\pi}{4} - \arcsin\left(\mathcal{F}_{th}^{1/4}\right), \tag{A.29}$$

and for the [PF-EOM-PF] configuration

$$-\frac{\pi}{4} + \arcsin\left(\mathcal{F}_{th}^{1/2}\right) \leq \phi_k \leq 3\frac{\pi}{4} - \arcsin\left(\mathcal{F}_{th}^{1/2}\right). \tag{A.30}$$

Introducing $\Delta\nu_{EPE} = \frac{\pi}{2} - \arcsin\left(\mathcal{F}_{th}{}^{1/4}\right)$ and $\Delta\nu_{PEP} = \frac{\pi}{2} - \arcsin\left(\mathcal{F}_{th}{}^{1/2}\right)$, this reads

$$\frac{\pi}{4} - \Delta\nu_{EPE} \leq \phi_k \leq \frac{\pi}{4} + \Delta\nu_{EPE}, \qquad \frac{\pi}{4} - \Delta\nu_{PEP} \leq \phi_k \leq \frac{\pi}{4} + \Delta\nu_{PEP}. \tag{A.31}$$

Similarly to the phase gate calculation, we find the maximum number of qubits achieving the Hadamard transformation with a fidelity over $\mathcal{F}_{th}$ for both configurations

$$\mathcal{N}_{\mathcal{EPE}} = \frac{M}{\pi}\left\lfloor \frac{\pi}{2} - \arcsin\left(\frac{\frac{\pi}{4} - \Delta\nu_{EPE}}{\frac{\pi}{4} + \Delta\nu_{EPE}}\right)\right\rfloor + 1; \qquad \mathcal{N}_{\mathcal{PEP}} = \frac{M}{\pi}\left\lfloor \frac{\pi}{2} - \arcsin\left(\frac{\frac{\pi}{4} - \Delta\nu_{PEP}}{\frac{\pi}{4} + \Delta\nu_{PEP}}\right)\right\rfloor + 1. \tag{A.32}$$

Appendix B

Experimental techniques

B.1 Correspondance between nominal voltage and modulation index for the electro-optic modulators

This section present the characterization done for the several modualator used in the experiments.

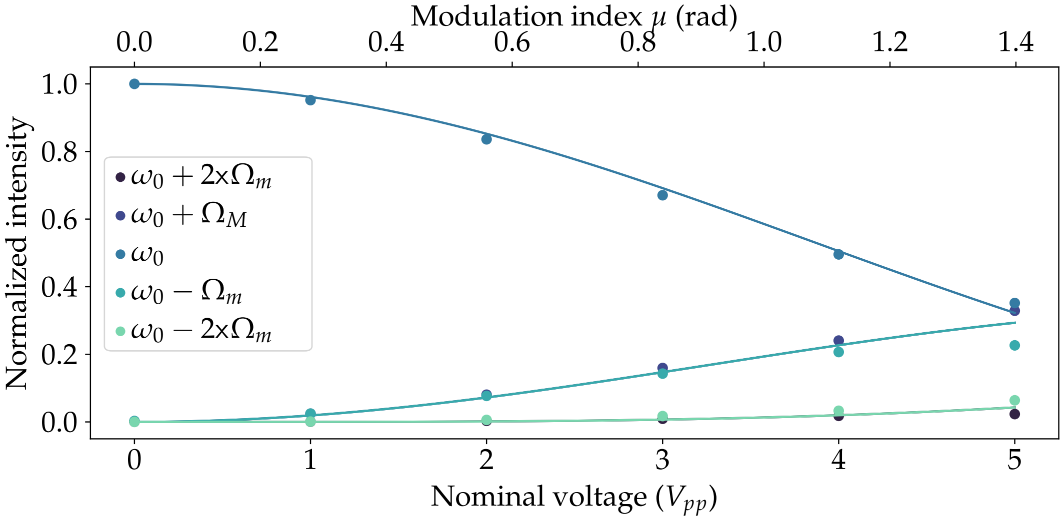

Figure B.1: Characterization of the electro-optic modulator serial number N°:118-44-15, with a meadures V_π= 11.234 V_{PP}

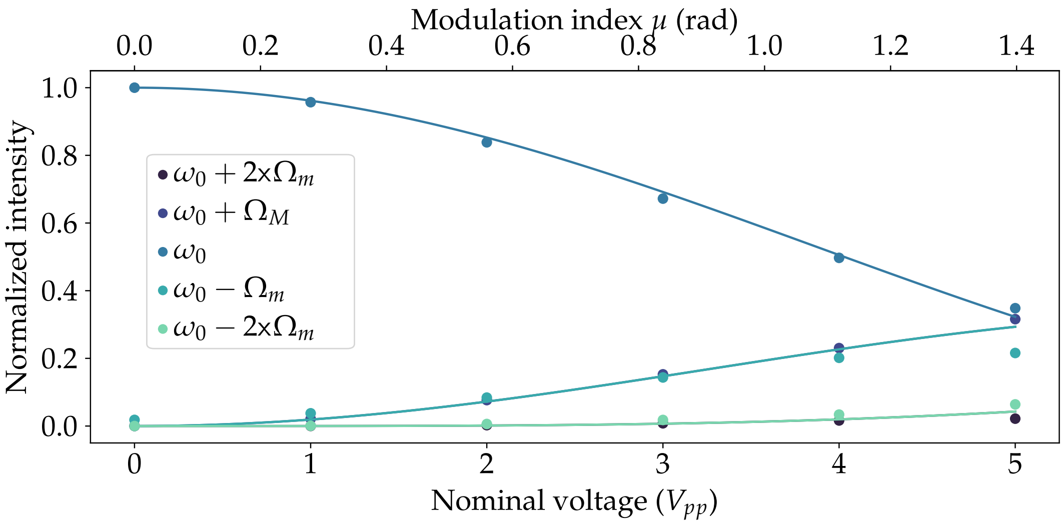

Figure B.2: Characterization of the electro-optic 188-44-13, with a meadures V_π= 11.237 V_{PP}

B.2 Transmission spectrum of the notch filters for pump rejection

This section presents the characteristics of the notch filter used to filter the residual pump laser from the photon pair stream for the silicon-on-insulator micro-resonator. Togetehr with the programmable filters, each enabling a filtering of the pump of >45 dB they ensure at least a rejection of $>$ 105 dB.

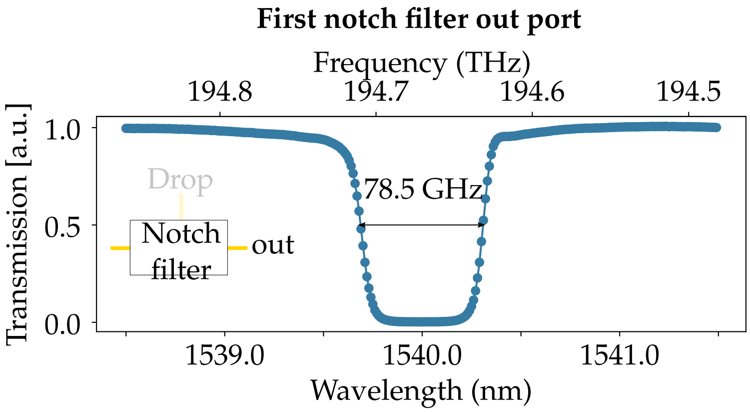

Figure B.3: Transmission spectrum of the second notch filtered centered at 1540 nm. The rejection is of **25 dB**

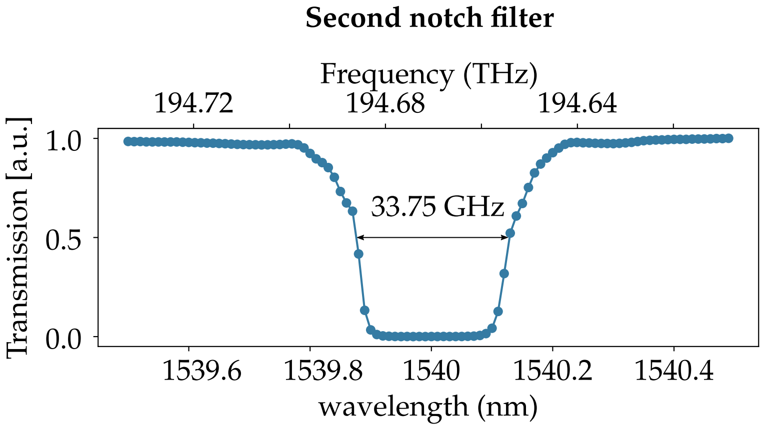

Figure B.4: Transmission spectrum of the second notch filtered centered at 1540 nm. The rejection is of **38 dB**

Titre : Traitement quantique de l'information dans le domaine des fréquences d'états photoniques quantiques multimodes générés par des sources intégrées aux longueurs d'ondes télécom

Mots clés : Information quantique, multimode, portes quantiques, optique quantique, qubits fréquentiels

Résumé : En information quantique, un encodage sur les degrés de liberté temps et fréquence donne accès à un espace de Hilbert de grande dimension pour les états photoniques ce qui autorise le traitement en parallèle d'un grand nombre de qubits voire de qudits. C'est dans ce cadre que se situe cette thèse sur la génération et la manipulation d'états quantiques photoniques aux longueurs d'onde télécom. Nous présentons trois réalisations. La première est la génération efficace de paires de photons par processus non-linéaire du second et du troisième ordre dans des sources intégrées innovantes : un guide en niobate de lithium sur isolant, en couche mince et à inversion de domaines periodique, et un micro-résonateur en silicium sur isolant possédant un intervalle spectral libre de 21 GHz. La deuxième est le développement de concepts, de modèles et d'optimisations numériques pour la manipulation de qubits et qudits photoniques dans les espaces temps fréquence avec des éléments linéaires. Nous utilisons des filtres programmables (PF) et des modulateurs de phase électro-optiques (EOM). Nous comparons les performances théoriques de portes à 1 qubit pour deux configurations de composants [EOM-PF-EOM] et [PF-EOM-PF] dans les deux types d'encodage temps et fréquence. La troisième est la démonstration expérimentale d'une telle manipulation de qubits fréquentiels issus du microrésonateur en Silicium. Nous utilisons la configuration [EOM-PF-EOM] pour implémenter une porte quantique reconfigurable et accordable. Un seul paramètre variable permet de passer d'une porte identité à une porte Hadamard, ainsi qu'à un continuum de portes intermédiaires. Nous démontrons la parallélisation de 34 de ces portes appliquées à 17 états à deux qubits intriqués en fréquence générés par le résonateur. Nous utilisons ensuite ces portes pour réaliser la tomographie quantique des états intriqués et pour mettre en oeuvre un protocole de distribution de clef quantique basé sur l'intrication des deux photons en fréquence. Nous faisons finalement la démonstration inédite d'un réseau multi-utilisateur sans nœuds sécurisés en encodage fréquentiel. Cette expérience constitue une preuve de principe pour la distribution de clé quantique dans le domaine fréquentiel avec un débit de 2 bits par seconde en simultané pour chacune des paires d'utilisateurs dans un réseau de 5 utilisateurs.

Title : Frequency-domain quantum information processing with multimode quantum states of light from integrated sources at telecom wavelengths

Keywords : Quantum information, multimode, quantum gates, quantum optics, frequency qubits

Abstract : In quantum information, encoding in time and frequency degrees of freedom gives access to a high-dimensional Hilbert space for photonic states, enabling parallel processing of a large number of qubits or even qudits. This is the scope of our work on the generation and manipulation of photonic quantum states at telecom wavelengths with three main achievements. The first one is the efficient generation of photon pairs by second and third-order nonlinear processes in innovative integrated sources: a thin-film, periodically-poled lithium niobate-on-insulator waveguide, and a silicon-on-insulator micro-resonator with a free spectral range of 21 GHz. The second one is the development of concepts, models, and numerical optimizations for the manipulation of photonic qubits and qudits in time-frequency spaces with linear devices. We use programmable filters (PF) and electro-optical phase modulators (EOM). We compare the theoretical performance of 1-qubit gates for two configurations [EOM-PF-EOM] and [PF-EOM-PF] in both time and frequency encoding. The third one is the experimental demonstration of such manipulation of frequency qubits from the silicon microresonator. We use the [EOM-PF-EOM] configuration to implement a reconfigurable and tunable quantum gate. A single tunable parameter is used to go from an identity gate to a Hadamard gate, as well as to a continuum of intermediate gates. We then use these gates to perform quantum tomography of entangled states and to implement a quantum key distribution protocol based on two-photon frequency entanglement. Finally, we demonstrate a frequency-encoded multi-user network without trusted nodes. This experiment constitutes a proof of principle for quantum key distribution in the frequency domain at a rate of 2 bits per second simultaneously for each pair of users in a 5-user network.

Institut Polytechnique de Paris
91120 Palaiseau, France